Pore-size ion-size correlations for carbon supercapacitors

A Thesis

Submitted to the Faculty

of

Drexel University

by

John Chmiola

in partial fulfillment of the

requirements for the degree

of

Doctor of Philosophy

February 2009

Acknowledgements

It's been a long road to get where I am now, and I certainly could not have done it without the love, support and inspiration of many many people. This would certainly not have been possible without the unfaltering support my colleague and advisor, Prof. Yury Gogotsi. Yury, I know I've been a pain in the butt, and I'm sorry for that. You've been outstanding in handling me all of these years. I can't imagine another advisor giving the level of professional grooming you have me, nor someone with the breadth of knowledge and ability to regurgitate it in any situation. To my committee – It is extremely humbling to have such a tremendous group of people agree to be on my committee. The past few months have been a terribly difficult and your patience is very very much appreciated.

Prof. Mun Choi, Prof. Anthony Lowman, and Vanessa Vardon – I am much obliged for you help with the NSF GRFP. Holly Burnside: Yeah, I don't even know what I would have done without you. From mid-day gripe sessions to all things IGERT, you've been boss. Dorilona Rose and Judith Trachtman have been indispensable over the decade or so I spent at Drexel. I am forever indebted to you both for the letters of recommendation, fixing my schedule, and everything else I did wrong that you both fixed.

By far the greatest joy of being in an academic environment are all of the brilliant people one gets to interact with on a daily basis. Many thanks to the Department. It has been nice watching the growth and success of all around me and pleasures me to share in everyone's success. You are truly a special group of people. Hopefully this is the start of something really awesome. Of course, the NMG Group is the best research group at

Drexel! Davide, Pia, Kris, Vadym, Mickel, Sebastian, Zarife, Liz, Svetlana, Ranjan, Tom Chobson and everyone else…Cristelle Portet – we bumped elbows in the lab for quite some time. It was an absolute pleasure. Gleb – we banged heads in the lab for quite some time. It was also an absolute pleasure. Carlos, Min and Patricia, good luck with continuing where I left off. Patrice Simon – you are truly an amazing person and researcher. Working with you gives me hope that one does not need to shed all of their youthfulness to grow up.

Inspiration can come from strange places. Milo Aukerman & Greg Graffin, of punk bands the Descendants and Bad Religion, showed me that cool kids can be scientists and scientists can be cool. Not that being cool is the coolest thing ever, but I think that it is essential to understand what makes kids tick to get them interested in learning something boring. Mrs. Barbara Stein: everyone has that one teacher who inspired them to pursue their future and you are that teacher. It gives me great hope that I can maybe someday inspire someone myself. My neighbors on 16th and Mt. Vernon, you constantly remind me that everyone on this earth has immense value, regardless of their education, income or creed. Bear & Jones & Scarlett & Max – I've always liked dogs more than people, so if you guys are my favorite dogs, then that must mean I like you a whole lot. Thanks for the long walks on summer afternoons. I look forward to many more.

The love and support of those holding the strings of my personal life have certainly been the most important factor in getting me where I am today. My parents are the 2 people who certainly gave me far more than I can ever give back. I can't even imagine the struggle of raising a kid like me. I mean, geez, I was well into school by the time they were my age, and I can barely take care of my puppy. The rest of my family has been

hugely inspirational over the course of my studies. I can't imagine how I could have made it through this without you all. My personal armada of friends trying to keep me from doing my job: Andy, Max, Mike, Gerry, Ryan, Tony, Chris, Tony, Andrew, Mike, Jon, Chris, Marvin, Matt, Dominic, Dave, Joe, Krispin, Kevin, Josh, Emily, Caity, Cathy and everyone else I forgot. Any good ideas I've had came while being with you guys and not staring at a computer, so I owe you all one.

Jared Brown, Jason Gildea, Donna Kennealy – What I wouldn't give for 5 more minutes with either of you… I'm sorry and I love you and wish this would world have kept you around a bit longer. Donna, you were there right up until the end and it breaks my heart that you couldn't see the culmination. I am so sorry.

To all of you, I dedicate this work.

Table of Contents

List of Tables

List of Figures

Abstract

Pore size ion size correlations for carbon supercapacitors

John Chmiola

Advisor: Prof. Yury Gogotsi

Carbon supercapacitors, which are energy storage devices that use ion adsorption on the surface of highly porous materials to store charge, have numerous advantages over other power-source technologies, but could realize further gains if their electrodes were properly optimized. This could lead to fleet-wide improvements in economy, performance, lifetime and environmental impact of Hybrid Electric Vehicles (HEVs), as well as enable or advance many other applications. To determine correlations between ion-size and pore-size in carbon supercapacitors, we generated a well-characterized set of porous carbide-derived carbons (CDC) with average pore sizes from 0.6 to 2.25 nm and used them to probe the limits of understanding. Performing the first systematic study of the effect of pore size on capacitance showed that, in general, decreasing the pore size below the size of the solvated ion, or to precisely the size of the ionic liquid ion, allowed higher accumulation of charge. Using CDC with properly tuned porosity showed excellent performance in H_2SO_4, ~200 F/g, and performance superior to all prior reported results in organic $(CH_3CH_2)_4NBF_4$ ($TEABF_4$) electrolytes as well as 1-ethyl-3-methyl immidazolium bis-(trifluoromethanesulfonyl)imide

(EMI-TFSI) ionic liquid, ~150 F/g. This work conclusively showed that precisely matching the pore size with the ion size is the key factor for maximizing capacitance. Understanding that pores significantly larger than the effective ion size do not have large contributions to energy storage, work on dense porous CDC films on conductive substrates showed ~100% larger volumetric capacitance than any previously reported. Depositing patterned films of carbide and electrical contacts could lead to microfabricated energy storage devices directly on a chip, or built up in layers for performances yet unrealized.

1. Survey of Literature

1.1. Introduction

As I begin to embark on a future in science and groom myself to give back as much as I have taken from my family, friends, colleagues, and, indeed, Country, I realize the interesting crossroads I am at. Looking around at the splendors of living in an industrialized society, the beautiful city of Philadelphia with its brand new 57 story Comcast Center building with 10 million pixel high definition television, it pains me to think that this era of growth and prosperity could ever come to an end. Certainly, every generation has its hurdles that it must overcome, with the scientists holding the flag of change at the front of the proverbial charge, but this future may be one like no other. It gives me great pleasure to join this brigade of like minds striving for a lofty goal, but also a bit of trepidation in realizing the long and hard struggle ahead of me.

1.2. Our BIG PROBLEM

You don't need to wear your social consciousness on your (tie-dyed) sleeve to understand that unsustainable living practices cannot continue unchecked indefinitely. At some point, the hole we are digging for ourselves (and have been for a few hundred or so years) will be deep enough that we can no longer crawl back out. It is our children that will suffer. Or is it our grandchildren that will suffer? Or their grandchildren? The fuzzy line between camps that presuppose humans as superior animals or humans as only animals is a mute

point when we consider that threats to biodiversity threaten ALL animals, humans included. “But when will this affect me?” says Average Joe. “Who says it hasn’t already,“ says I.

By focusing on economic growth as the essential human goal, and so neglecting Earth protection, we are shooting ourselves in the foot [1]. In fact, the idea of taking from the Earth without accounting for sustainability has decimated species and resulted in less than and estimated 10% of large predatory fish populations remaining [2], for example. Some scientific estimates indicate that up to half of presently existing species may become extinct by 2100 [3]. Known as the Holocene extinction event this human-induced extinction of species ranks as one of the worlds six mass extinction events and is the largest mass extinction event since the extinction of the dinosaurs [4]. Threats to biodiversity are only minimal compared to other human-induced global changes, however.

Consider oil: Understanding that millions of years go into the production of oil and we’ve been pumping it for the past hundred of so years without discretion, it should come as no surprise that we’re pumping faster than the earth is making. Oil is not going to last indefinitely. Period. Ever since M. King Hubbert used a logistic model to predict the peak in U.S. oil production occurring in the late 1960’s [5], the world became a bit wiser to the fact that oil is not a renewable resource and eventually we will run out of it. Optimists and pessimists place the exact date of declining oil production, subsequent price increases and declining global stability somewhere between now and the end of the century, depending on various factors that cannot be known *a priori*. The implications of a world

without oil are astounding and scary and are immensely further reaching than not having the luxury of driving a car to work every day. Massive losses in population due to starvation (a decrease in world population of 66% would be required for sustainability at current consumption and production levels [6]) would be seen because of the close ties between petroleum and agriculture in the worst-case scenarios. The best case scenarios involve lowered living standards due to increased cost of materials produced from petroleum, higher food prices due to transportation costs, decreased farm efficiency, and the transition of suburban sprawl into suburban slums as transportation costs force people that can afford it to move to higher population density areas where walking and public transportation are feasible leaving behind those who cannot [7]. And this is in industrialized nations…

> *"In recent years, new nations have entered enthusiastically into industrial production, thereby increasing their energy needs. This has led to an unprecedented race for available resources. Meanwhile, some parts of the planet remain backward and development is effectively blocked, partly because of the rise in energy prices. What will happen to those peoples?" – Pope Benedict XVI, 2007*

1.2.1. Transportation, petroleum and our grand challenge

> *"To provide the technology for accomplishing our energy goals, what we need to do is to find the "new oil"—a basis for energy prosperity in the 21st century that is as enabling as oil and gas have been for the past century. The sheer magnitude*

of the energy industry makes this an extremely difficult task." - Richard Smalley, 2004

In the U.S., transportation accounts for roughly 2/3 of oil consumption, and is probably the sector where the largest gains can be made [8]. Simple back of the envelope calculations by The Rocky Mountain Institute show that improving our current gas mileage by ~10 MPG is enough to displace all of the oil imported from the Persian Gulf region. Removing power from nations hostile to the U.S. and taking steps towards giving back to our Earth sounds like a pretty good motto for an army of scientists to undertake.

1.2.2. The hybrid solution

Hybrid electric vehicles (HEVs) combine the advantages of high specific energy fuels and internal combustion engines/gasoline with battery/electric motors to produce a vehicle with higher fuel economy (40% in the case of the most popular version, the Toyota Prius). Though currently a minority among traditional automobiles, most automakers look at HEVs as a core segment of the future auto market, which is evidenced by the fact that this year automakers are introducing 15 HEV models with plans on extending this in further years. Likewise, to encourage consumers to switch from conventional vehicles to HEVs, most industrialized governments offer many tax incentives or other enticements.

A 10 MPG improvement in fuel economy is still not enough when we consider that developing nations requiring efficient transportation will, likely, have oil appetites at least as large as ours in the U.S. And dumping our bastard technologies onto them in

search for a few dollars will ultimately leave us, the technologically superior, continually engaged in a battle for resources, keeping the technologically inferior, well, inferior. Already available technologies with better aerodynamics, new construction materials, ultra-lightweight construction, new ideas for propulsion and bettering energy-storage technologies have led to a 100-mpg minivan [9] at a consumer cost without government incentives of roughly the same as conventional HEVs. So where are they?

1.2.3. The battery dilemma

Though wonderful machines, batteries represent the current Achilles' Heel to HEVs [10], and pursuing other energy storage technologies could have far-reaching benefits [11]. Simply, because of the large phase changes that occur in battery electrodes upon cycling, they need to be designed to operate within a 5% depth of discharge to ensure that they do not need to be replaced during the automobile's lifetime. Basically 95% of the battery in an HEV can be thought of as dead weight. Moving from nickel metal hydride batteries (NiMH), the current standard in production automobiles, to lithium, which is the gold standard among high-energy and high-power batteries, does not help the situation much, either, because of difficulties ensuring safety and reliability over roughly 10 years. Obviously, though an elegant short-term solution, there needs to be alternatives to current batteries that better suit the cycle life requirements and power needs of HEVs.

1.3. Energy storage technologies

Numerous power source technologies exist: chemical [12], kinetic (flywheels [13] and compressed air [14]), electrochemical (batteries [15] and fuel cells), electrical (capacitors

– dielectric, electrolytic and electrochemical [16]) and solar [17], for example. Understanding the limitations of current power technologies and leveraging the benefits of others could allow device efficiencies to greatly exceed those presently achieved.

Batteries, being the technology ECs are poised to complement and maybe even displace in some applications, find themselves in a different realm than ECs. Battery electrodes undergo spontaneous chemical reactions that liberate and consume electrons. This is termed electrochemical energy storage, unlike the electrostatic energy storage of capacitors whereby charges are displaced from equilibrium positions. Electrochemical reactions store much larger amounts of energy than electrostatic ones, but they operate more slowly, hence have lower power (Figure 1.1), especially at low temperatures (which is why starting a car on a cold January day can prove difficult). Fast charging and the ability to handle high current densities without issue allow the use of ECs for recovery of energy from, say, a braking car, dropping a weight with a crane, or a falling elevator as will be discussed in Table 1.1. Many batteries also require environmentally unfriendly materials (Cobalt, Nickel and Lead for example). The most striking dissimilarity between batteries and ECs, though, is the number of charge-discharge cycles each can undergo before "running out." With batteries, phase changes during charge/discharge in the electrodes result in a decreasing amount of material available for charge transfer with increasing charge-discharge cycles. Because there are no large-scale changes in the electrodes of ECs during cycling, they have cycle lives on the order of a few hundred thousand cycles in comparison batteries have cycle lives on the order of a few hundred to a thousand.

In terms of energy storage devices for enabling the next generation of automobiles, as briefly stated above, batteries, biofuels, hydrogen, fuel cells and electrochemcial would potentially work, but understanding the limitations, benefits and potential of each is crucial for ensuring a proper match. For example, batteries are a significant environmental problem if not recycled, so using them in applications where they are inefficient not only contributes to environmental damage it also produces a complicated situation whereby it potentially takes more energy to produce a battery than can be stored in it over its lifetime and the requirement for consumer education to ensure proper recycling. Life cycle analysis of hydrogen showing a very large net energy consumption in its production and its extremely low volumetric density make it more of a pipe dream than something to take seriously. At least in the near term. Polymer electrolyte fuel cells, though approaching maturity, still suffer from problems associated with hydrogen, in the case of hydrogen fuel cells or distributed CO_2 emissions in the case of direct methanol fuel cells. Solid oxide fuel cells suffer from high start-up costs and safety issues in distributed scenarios due to high operation temperatures. Basically, at this juncture, there is no perfect technology for all applications, so understanding the requirements of the application is essential for maximizing efficiency. This is just a very short list of issues to consider when choosing energy storage technologies for powering our cars. With 20% of the world population living without adequate food, decisions to place driving our cars over preventing global starvation, should be approached carefully.

1.3.1. Energy vs. Power – What is really important?

In understanding energy storage technologies, Joules is not the only important thing to consider. The rate at which energy is withdrawn from the device, joules per time, watts or power, is as equally important as the total energy in a device and is a function of the rate at which energy is withdrawn. The Ragone Plot (Figure 1.1) was first used to compare the performance of different battery families, but can also be used to show how the total energy stored and how the performance is affected by the rate at which it is withdrawn. Electrical and electrochemical energy storage devices essentially exist as a continuum over a range of time scales from much less than a second to hours. Operating the energy storage device outside of this time window is inefficient and leads to failure in the case of too fast a discharge rate and excess mass if too slow. For example, considering that an ICE scenario, gasoline has an energy density of ~1,500 Wh kg^{-1} (assuming a mass of ICE motive components of 500 kg), it can be easily appreciated that batteries have large shoes to fill in order to replace internal combustion engines in automobiles. Of course, it takes Earth millions of years to produce our precious oil and Humans do not have that luxury – therefore finding solutions that can be pursued in the short term (<1,000,000 years, or so) is essential.

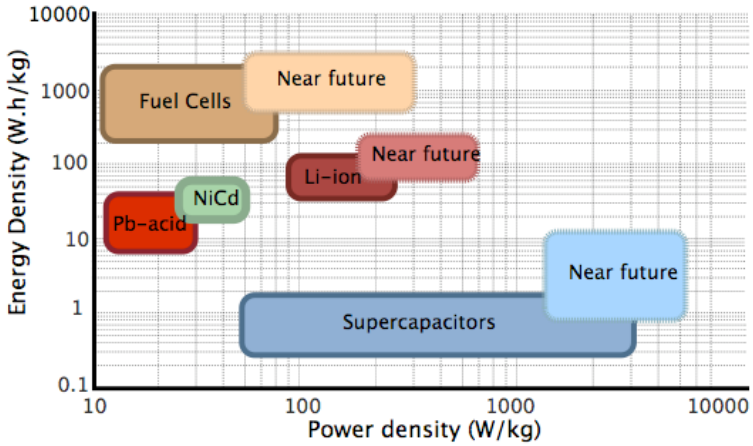

Figure 1.1: Ragone plot of battery, fuel cell and supercapacitor technologies [11].

The hybrid arrangement of a high energy device (internal combustion engine) with a high power device (battery) is what allows HEVs to increase their efficiency [18]. Moving to even better suited energy storage devices would make energy gains even greater [10, 19]. To supply a large enough power, a battery is configured to offer high power, but at a cost to total energy density. For instance, in the current production Toyota Prius, the energy density of the cells is ~30 W-h/kg with a peak power density of ~1 kW/kg. This makes a ~50 horsepower device that weighs ~50 kg. Moving to competing technologies, such as supercapacitors [10, 20, 21] could decrease the size of this battery an order of magnitude and improve cycle lives [22]. Yes, an HEV running off of a "battery" (if I were in charge of marketing, I think "Bettery" would be a wonderful product name) the size of a standard lead-acid battery with a lifetime longer than the car it is powering is far from a pipe dream. Simply understanding technological limitations and places for improvement is key to implementing these devices [21].

1.3.2. Electrochemical capacitors (ECs)

Currently, there are a dozen or so manufacturers of electrochemical capacitors (ECs) around the world offering modules in a variety of form-factors and performances (Figure 1.2). Nippon Electric Company was the first to develop and market the devices as Supercapacitors (hence the reason why the terms Electrochemical Capacitor and Supercapacitor are used interchangeable), which were intended for computer memory backup applications [23]. Currently, Japan is leading EC production with companies such as Nippon Chemicon Corporation (NCC), Power Systems Co. Ltd., NEC-Tokin Corporation, Advanced Capacitor Technologies Inc., Matsushita Electric Industrial Co. Ltd. (Panasonic) being key players in the industry. Nesscap Co. Ltd. (Korea), ESMA (Russia), and CAP-XX Inc., (Australia) are three other powerhouses in the Asian region. In Europe and North America, EPCOS (Germany), Evans Capacitor Company (US), Maxwell Technologies Inc. (US), Cooper Bussman Electronic Technologies (US), and Axion Power International (US) are among the leading producers [24].

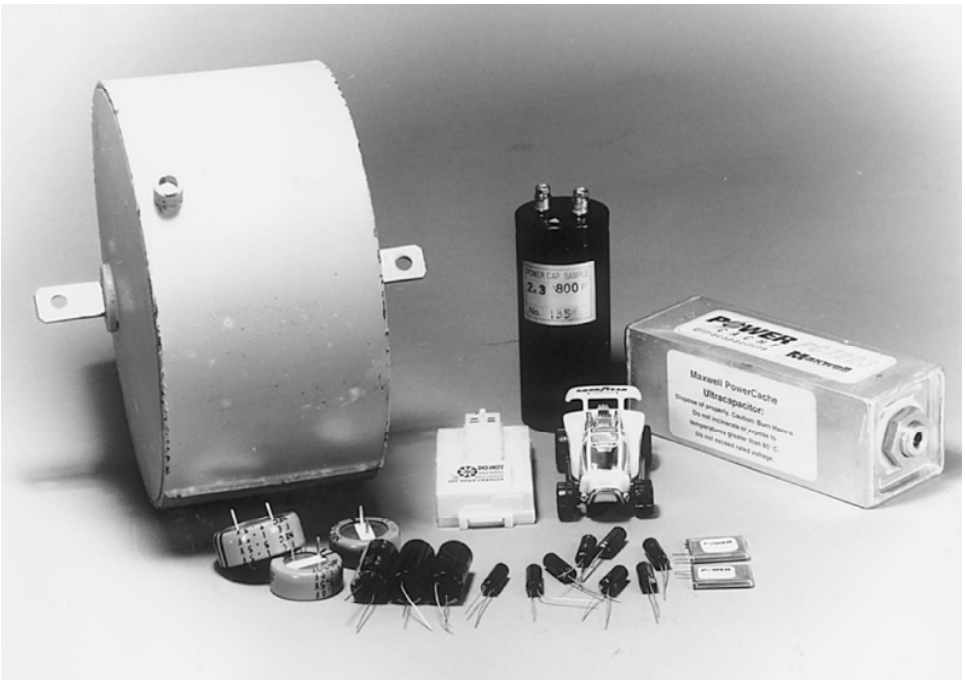

Figure 1.2: Several commercially available electrochemical capacitors [25].

At the industrial level, work is being done to decrease the cost of components to drive the overall device price down. Costs per Farad have decreased around an order of magnitude over the past decade to 20 cents as an increasing number of manufacturers are fueling competition. Additionally, energy and power density have improved by about 100% over the last 5 years with a concurrent drop in price per Farad by a factor of 10 with automated volume manufacturing. It is predicted that with increasing production their costs will continue to drop to 0.5 cents per Farad in the near future.

Realizing that, potentially, many applications can be improved or new applications can be opened because of the combination of moderate power and high power, along with very high cyclibility offered by ECs, it is important to understand how they work.

As an example of other potential applications, consider a 500 kg elevator falling 15 floors (50 m) in 1 minute. Table 1.1 shows the mass of electrostatic capacitors, ECs and batteries needed to recover the energy of the falling elevator assuming no conversion losses and the nominal power and energy values shown. For a perfectly optimized device, the mass required in terms of both power ($Mass_P$) and energy ($Mass_E$) would be equal, but in real terms, the power device must be at least as large as the largest mass required in either power or energy terms. From Table 1.1 it is apparent that ECs would be the optimal choice. Also important is the consideration that in the event that more power is generated than what the elevator is designed for, the battery would be forced to work in a regime of low efficiency where degradation is enhanced. Therefore, in realistic terms, the cost per cycle of the EC would make it the obvious choice.

Table 1.1: Mass of electrostatic capacitors, ECs or batteries needed to lift a 500 kg load 50 m in 1 min.

	Power density (kW kg^{-1})	Energy density (W-h kg^{-1})	$Mass_P$ (kg)	$Mass_E$ (kg)
Electrostatic capacitor	1000	0.05	0.02	6000
Electrochemical capacitor	10	5	2	60
Battery	0.1	300	200	1

1.3.3. Capacitive energy storage

Though ECs look very similar to batteries from the outside [26] their charge storage mechanism and implementation are different [25].

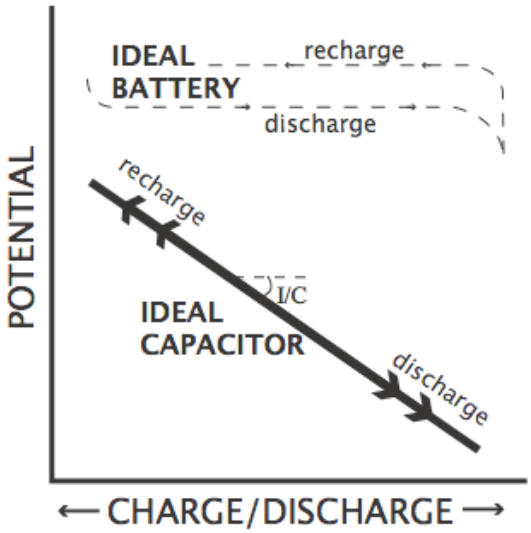

Figure 1.3: Charge-discharge curves of ideal batteries and capacitors

The defining characteristic of an EC is a sloping discharge curve upon constant current discharge (Figure 1.3). Though considered formally as electrochemical energy storage devices, this behavior is capacitive in nature and thus beginning with a short description of capacitors should aid in understanding EC operation. For dielectric capacitors, initially with no voltage applied across the capacitor, there is an equal amount of charge on each plate (Figure 1.4a). As voltage is increased across the capacitor, increasing amounts of energy are needed to transport charges. As charges, q, are continually added to the plates of the capacitor the voltage, V, increases linearly.

$$V = \frac{q}{C} \tag{1.1}$$

The proportionality constant that relates the amount of charge stored with the voltage is the capacitance, *C*, which has units of Farads (Coulombs per Volt). The energy stored in a capacitor, *E*, is then simply the integral under the *V*-*q* curve (Figure 1.3), or

$$E = \int V dq = \int \frac{q}{C} dq \tag{1.2}$$

Decreasing the slope of the curve or increasing the capacitance increases the energy stored. Immediately, it is evident that batteries, because of their flat discharge profile (Figure 1.3), will have superior energy density, all other factors being held constant. In real terms, however, the formal charge transfer in a battery give it even higher energy than a capacitor (Figure 1.1 and Table 1.1).

The capacitance of a parallel plate capacitor is directly proportional to the area, *A*, of the plates and inversely proportional to the separation between counter charges, *d*.

$$C = \frac{\varepsilon \varepsilon_0 A}{d} \tag{1.3}$$

The dielectric constant, ε, is a measure of the ability of the materials inserted between the plates to store charge (vacuum is 1). ε_0, is the permittivity of free space and is constant. Inserting high dielectric materials between the plates increases the capacitance, but a limitation on the thickness of this layer (a few fractions of a millimeter) and geometric area, limit the useful capacitance to pico-, nano- or microFarads.

Energy stored in a capacitor is then calculated using

$$E = \frac{1}{2}CV^2 \tag{1.4}$$

where V is the voltage that the capacitor is charged to and typically corresponds to the voltage where there is some irreversible change in the capacitor (breakdown voltage).

Supercapacitor, the moniker given to the technology by NEC, comes from the magnitude of capacitance stored – tens of Farads per gram of device weight, compared with micro (0.000001) Farads demonstrated by traditional dielectric capacitors [27]. There exists an interesting evolution in capacitance and, indeed, capacitors. Dielectric capacitors, which were already briefly described, were first envisaged with the Leyden Jar, invented by Pieter van Muschenbroek in 1745 and store energy as charges on parallel plates (Figure 1.4a).

Electrolytic capacitors (Figure 1.4b) are fabricated from two sheets of aluminum, one with a thin aluminum oxide layer, both separated by a layer of electrolyte soaked paper. Charge is stored between the few microns thin oxide-covered aluminum and electrolyte, which decreases the charge separation distance past dielectric capacitors. Electrode etching treatments create a rough surface, increasing the surface area above that of the geometric surface area. The decreasing charge separation and increased surface area lead to capacities up to a few hundred microFarads. Even though large voltages can be used with electrolytic capacitors, their low energy density still precludes their usage in applications besides filtering and pulse applications that operate on time scales on the order of microseconds or less.

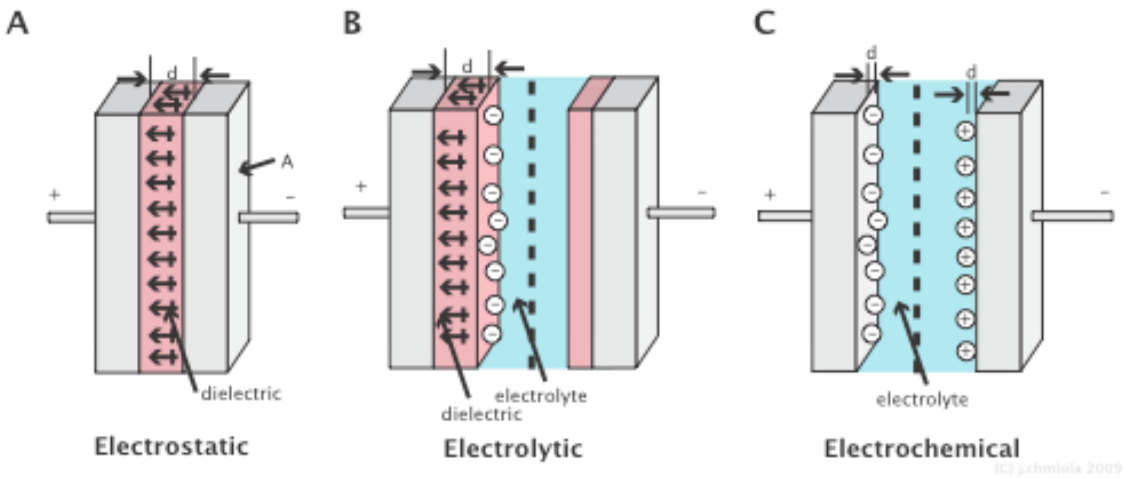

Figure 1.4: Schematic of a.) dielectric capacitors, b.) electrolytic capacitors and c.) ECs.

ECs (Figure 1.4c) further decrease the charge separation and area past what is offered by electrolytic capacitors [20, 25, 28]. ECs are charged up to the decomposition voltage of the electrolyte (which is ~1 V in aqueous systems, ~2.5 V in organic systems and >3 V in ionic liquids). Increasing the voltage is beneficial because the energy scales with the square of voltage (Eq. (1.4)). Even though ECs can only operate at voltages less than ~3V with currently available electrolytes, their moderate energy density makes them interesting for a myriad of applications where batteries are currently used [29].

1.3.4. Electrochemical capacitor energy storage

ECs exist in two main classes, those based on highly reversible redox reactions that exist over a continuum of potentials (so-called pseudocapacitors) and those based on reversible adsorption of counterions on high surface area charged interfaces (so called electrical

double-layer capacitors (EDLCs)). Briefly, because it will be covered more in-depth in Section 1.5, in EDLCs, symmetric positive and negative electrodes made from ultra high surface area carbon are immersed in an electrolyte solution, with the entire construct housed in a hermetic can (Figure 1.4). EDLCs store charge at the interface between their charged electrodes and oppositely charged electrolyte ions in solution. As the voltage between the electrodes increases, charge is balanced by an increasing number of oppositely charged ions moving to this electrode/electrolyte interface. By either increasing the size of the electrode/electrolyte interface (increasing the surface area of the electrodes) or decreasing the separation between the ions and electrode (a distance more or less dictated by nature) the capacitance stored increases. With the surface area of carbon being on the order of 2000 m^2 g^{-1} and charge separation of atomic dimensions, it is not surprising that capacitance of a few thousand Farads for assembled devices have been realized. This decrease in charge separation and increase in surface area in moving from dielectric capacitors to EDLCs spans a few order of magnitude each and results in 1,000,000 times larger energy stored for the latter.

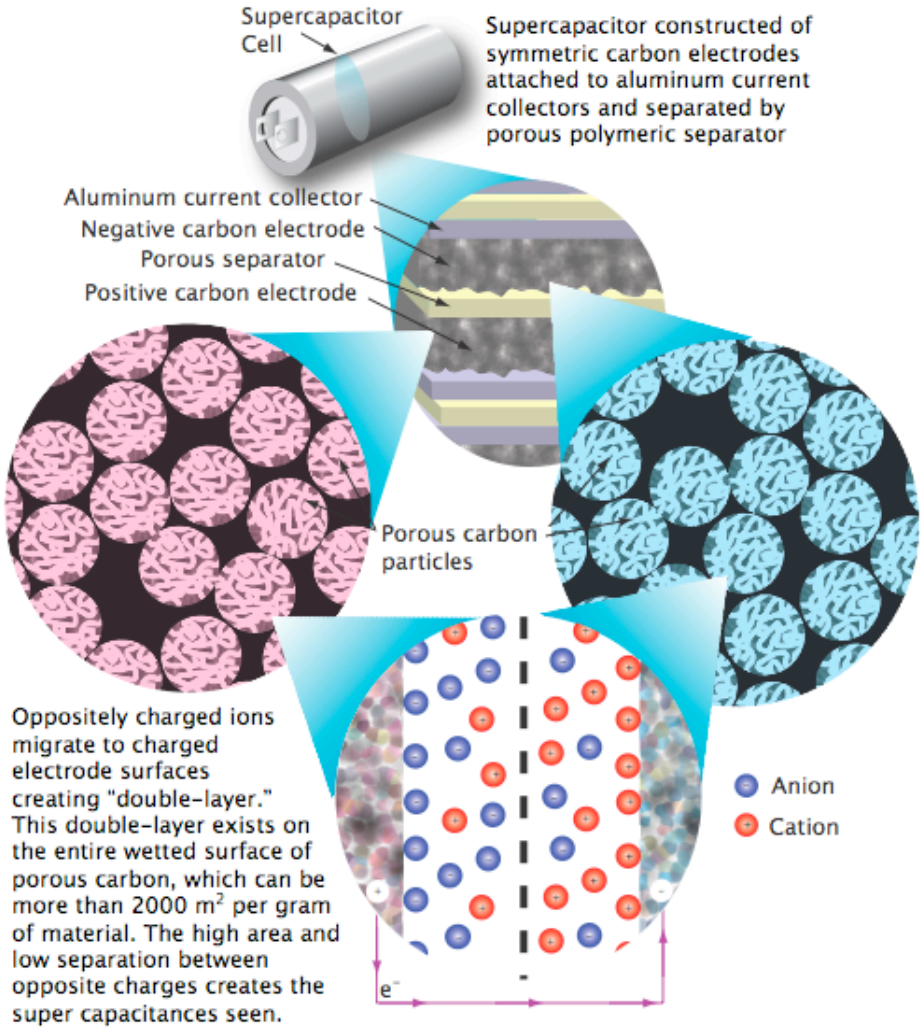

Figure 1.5: Schematic of an electrochemical double-layer capacitor [30].

Certain transition metal oxides (indium, ruthenium, indium and titanium, for example) as well as certain conductive polymers exhibit fast redox reactions that appear capacitive in nature [31, 32]. The reasons for this, in general, are dependent of the system being study, but a few generalizations can be made to simplify understanding. This charge storage behavior can be understood by considering the following derivation. Pseudocapactors

require the electro-adsorption of charges from solution, which can be thought of as following Langmuir-type adsorption isotherm [32], whereby at increasing electrode potentials increasing amounts of charge are passed as ions adsorb on the electrode surface. In real terms, this can be extrapolated to the behavior of the well-studied underpotential adsorption of atomic hydrogen on platinum [16], in much the same way double-layer capacitors use double-layers adsorbed on well-defined electrodes as a test-case [33]. A Langmuir isotherm can be described by:

$$\frac{y}{1-y} = K\exp\left(\frac{VF}{RT}\right) \tag{1.5}$$

where the fraction of sites occupied *(y/y-1)* correlates to some energy function that follows a Boltzman distribution, V is voltage, F is Faraday's constant, R is the ideal gas constant, and T is temperature. Including charge, q, in the right side of the equation and differentiating with respect to voltage, one obtains a relation for capacitance, C_ϕ

$$C_\phi = \frac{qF}{RT}\cdot\theta(1-\theta) \tag{1.6}$$

where

$$\theta = \frac{K_{C_{H^+}}\exp\left(\frac{VF}{RT}\right)}{1+K_{C_{H^+}}\exp\left(\frac{VF}{RT}\right)} \tag{1.7}$$

This simple derivation ignoring all kinetic effects and assuming steady-state exists during the entire experiment shows the theoretical basis for experimentally measured

capacitance phenomena using potential sweep experiments. At half coverage, there is a maximum in capacitance as seen in Figure 1.6 and would be predicted from Eq. (1.6).

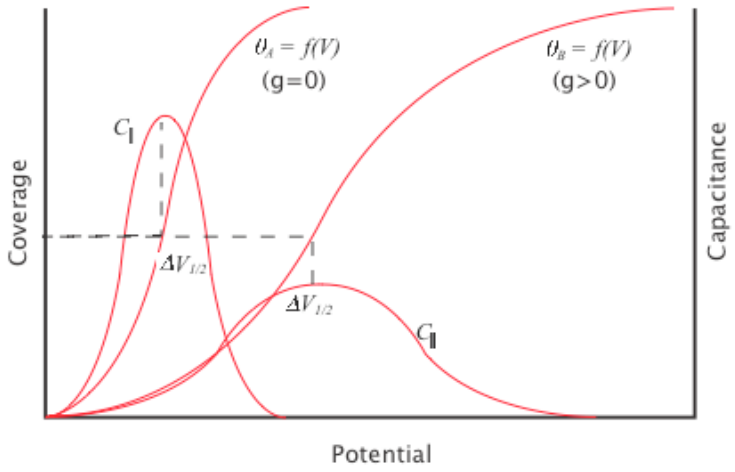

Figure 1.6: Plot of electrode coverage or capacitance as a function of potential assuming Langmuir adsorption with no interaction (g = 0) between adsorbed species and with repulsive interaction (g > 0) between species.

Introducing a lateral configuration energy term, $g\theta$, into an isotherm having the same configurational entropy term $RT\ln(\theta/1-\theta)$ results in an isotherm with a decreased, but more broad capacitance peak that is shifted to higher potentials (Figure 1.6).

$$C_{\phi 2} = \frac{qF}{RT} g\theta(1-\theta) \tag{1.8}$$

As this lateral interaction term increases, the peak width increases while the height decreases. As a real world example, ruthenium oxide is the most well-studied pseudocapacitor material [34-36]. 3 distinct oxidation states of ruthenium are accessible within the decomposition potential range of water, which when added lead to a quasi-ideal capacitive behavior over ~1 V [37]. By insertion/removal of hydrogen ions into the tetrahedral sites of the lattice and concurrent oxidation/reduction of the ruthenium, capacitive discharge is realized [38]. Protons are inserted in a quasi-staged behavior because they are not completely reduced [39], which makes additional proton insertion more difficult. This is tantamount to the $g\theta$ term in Eq. (1.8) and as shown in Figure 1.6, leads to broadening of the peaks seen in potentiodynamic experiments. In ruthenium oxide, in particular, there is enough broadening that the redox peaks actually overlap, giving rise to a constant capacitance over ~1V, like shown in Figure 1.7. Polymer pseudocapacitors resemble oxide pseudocapacitors because they require "doping" of electroactive groups to store charge [40-42], which, in general, has peak broadening because of interactions between adjacent electroactive groups as well as potentially overlapping redox peaks if there are multiple charge transfer events possible over the electrolyte voltage window. It should be noted that because pseudocapacitors utilize chemical reactions, instead of purely physical adsorption, they have the potential to store much larger amounts of energy than their EDLC counterparts [32, 43, 44]. The drawback in terms of cycling stability and cost have kept carbon EDLC's the major market players, though [26].

In actuality, in ECs, each electrode is a discrete capacitor, connected to the other in a series configuration. This must be accounted for in designing ECs, because if the capacitance of the positive and negative electrodes are not matched, the total capacitance will be lowered (Eq. (1.9)).

$$\frac{1}{C_{total}} = \frac{1}{C_{positive}} + \frac{1}{C_{negative}} \tag{1.9}$$

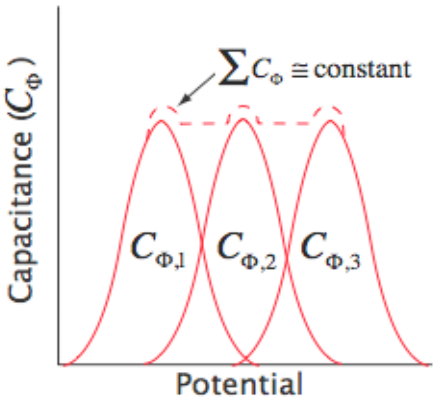

Figure 1.7: Schematic showing the overlap of redox peaks giving rise to a constant capacitance

1.4. Electrochemical capacitor construction

Though they resemble batteries on the inside and utilize many of the same components (if not the EXACT same components) it is instructive to look at the assembly of ECs to understand how this materials system performs. In general an EC is made of various interacting components: the electrodes, electrolyte, separator, current collectors and can. In what follows I will address each individually.

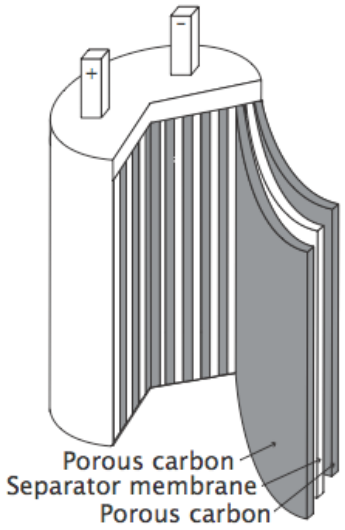

Figure 1.8: Schematic of an EC constructed in the "jellyroll" configuration showing the major parts (the electrodes, electrolyte (not shown), current collectors, separator and can).

1.4.1. Electrodes

In general, the electrodes are the most important part of an EC, because they dictate whether the device exhibits capacitor-type discharge (as in an EC), battery-type discharge (as in batteries), or some intermediate behavior (such as is seen in Li-ion batteries) [45]. In general, 3 types of materials are used for ECs – carbon [46], conductive transition metal oxides [47-52], and/or conductive polymers [53-58]. Hybrid configurations employing one capacitive electrode and one battery electrode have been increasingly explored [31, 59-62].

The primary factors of merit of electrodes are that they provide high capacitance, high conductivity and are stable over high cycle lives. Of course, cost provides probably the primary factor of merit as far as practical applications are concerned, but in the case of this thesis, cost will remain secondary and science will remain the central point. In

general, carbon has the lowest capacitance values, but provides the highest conductivity (a sum of any charge transfer resistance, ionic resistance and bulk material resistance) [26, 27]. In terms of stability, in a system precisely optimized for all other criteria, carbon is the least electrochemically stable, followed by polymers and finally metal oxides, which are the most stable [63-66]. The reasons behind all of these statements will become clear in subsequent sections after sufficient treatment.

1.4.2. Electrolyte

The electrolyte is the second most important part of the EC, as it dictates its operational voltage window. As energy in a capacitor increases with the square of voltage (Eq. (1.4)) improving a capacitor's voltage window is paramount.

Figure 1.9 shows a plot of Energy as a function of Voltage. In terms of real-world engineering, only 2/3 of the energy is available [67], considering that power from voltages below a few tens of millivolts is useless.

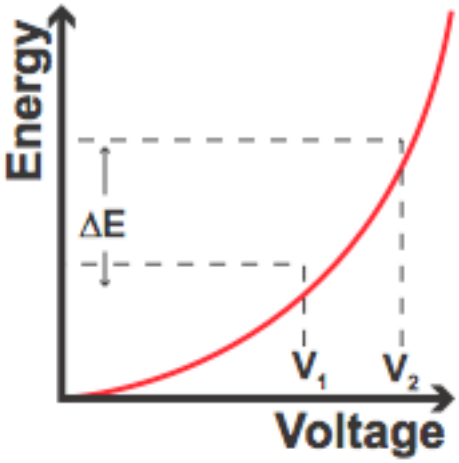

Figure 1.9: Plot of energy as a function of voltage for a capacitor

Essentially, the capacitor can be charged only below a voltage where there are irreversible changes in one of the cell components, the electrolyte being by far the most notable. For instance, capacitors utilizing aqueous solutions have voltage windows of, typically, 1 V (Figure 1.10). This is because at the cathodic limits water is oxidized, generating oxygen gas, and at the anodic limits, water is reduced generating hydrogen.

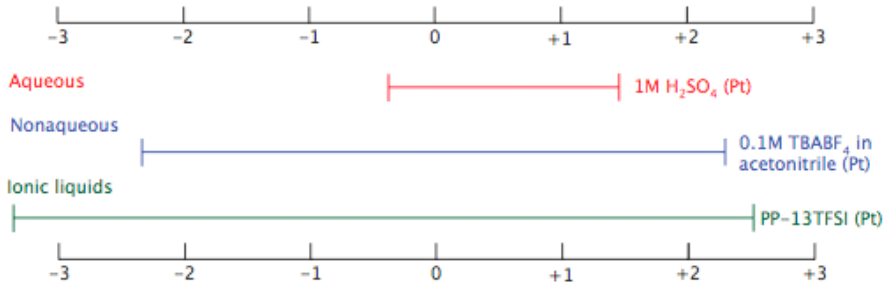

Figure 1.10: Voltage stability window for various electrolytes at a platinum working electrode. In general the stability window is smaller for carbon electrodes. [68, 69]

In contrast, many aprotic (nonaqueous) organic solvents have decomposition limits that are substantially larger than 1 V. For instance, the electrolyte tetraethylammonium tetrafluoroborate (TEABF4) in acetonitrile has a voltage window greater than 4 V versus a platinum electrode or ~2.7 V versus a carbon electrode [70]. This leads to realizable energy densities almost 5 times greater for organic electrolytes than aqueous electrolytes. Using ionic liquid-based electrolytes has the benefit of further increasing this energy density [66, 71, 72].

Of equal importance to the voltage window is the ionic conductivity of the electrolyte [73, 74]. To have a device with high power density, the overall resistance must be decreased to a minimum [67, 75]. As the electrolyte resistance makes up one of the most significant parts of the overall EC resistance, in most cases, using electrolytes with maximum conductivity results in devices with maximum performance.

To maximize capacitance, it is desirable to ensure that each electrode carries the same amount of current. Therefore, if possible, electrolytes should be chosen that have similar molar conductivity of the anions and cations. Also, conductivity increases with increasing electrolyte concentration. Because of this, electrolytes are typically saturated solutions. Other electrolyte effects, such as ion size, will be discussed in the following chapters where they are most relevant.

1.4.3. Separator

To prevent short-circuiting the device while maintaining functionality, a separator must be inserted between the anode and cathode that resists electron passage but still provides electrolyte ion passage [76]. In reality, only a thin layer of electrolyte solution between the anode and cathode is required, but in practice, because of electrode non-uniformities and difficulties processing the cells, this is not necessarily an option, though it would provide the best performance.

In general, separators are made from thin porous membranes utilizing materials that are electrically insulating, most notably polymers [77-79]. To decrease electrolyte bulk resistance, the separators are typically made as thin as possible and highly porous. Like the binder in the electrodes, electrochemical stability is very important to ensure device longevity, so it is not surprising that the same fluorinated polymers are the most widely used separator materials. Cellulose and some metal oxides are sometimes used, also, as well as thin layers of solid electrolyte or ion exchange membranes in more specialized ECs.

1.4.4. Can

Separating the electrochemical environment inside of the EC from the external environment is important for device performance, and differs in complexity depending on the electrolyte system chosen and the form factor required by the application. The most important factor for housing is chemical and electrochemical inertness. For instance, if the electrolyte is concentrated sulfuric acid, one would not use a material that would react with sulfuric acid as the housing material, such as aluminum. In general, housings for capacitors designed to operate with a cell voltage of less than 1 V are less complex because water diffusion into the cell will not affect performance, so long as water diffusion out of the cell does not dry the electrodes. In ECs utilizing nonaqueous electrolytes, the packaging can be very complex, due to the requirement that water cannot diffuse into the cell, even at parts per million concentrations. Also, because of gasses liberated during prolonged cycling, pressure valves or other safety measures are typically installed on more advanced devices to prevent accidental explosion on overcharge. Because of huge variations in packaging among different producers and the lack of importance besides those points already mentioned, an in-depth analysis of packaging will not be given.

1.4.5. Current collectors

Probably one of the most overlooked EC components, the current collectors pass charge to and from the active material and without good adherence to the electrodes, resistance is high [80]. Also, the current collectors must be stable in the chosen electrolyte at the

imposed potentials and not degrade significantly. This is especially important in highly acidic or alkaline aqueous electrolytes. A thorough analysis of problems originating from current collectors is given in the Materials and Methods chapter.

1.5. Electrical double-layer capacitors (EDLCs)

Though electrochemical capacitors exist in a variety of forms as briefly outlined in Section 1.3.2, electrochemical double layer capacitors (EDLCs), utilizing counterion adsorption on charged carbon interfaces, are the most widely-studied and, at this point, the only commercially viable electrochemical capacitor technology [81]. The fundamental processes occurring at the electrodes of these devices are very different from those taking place in batteries and utilize phenomena that have been studied for over a century [82], but still a subject of debate [83]. While batteries store the electrical energy in chemical bonds [15, 84], EDLCs store it directly in the double-layer. Attention directed towards EDLCs has greatly lagged behind that given to other power sources [85], such as batteries and fuel cells [86, 87], however, so bringing high-level understanding to these devices has the potential to influence the field greatly.

1.5.1. EDLC charge storage mechanism

As briefly stated in Section 1.3.4, EDLCs store energy through reversible ion adsorption on high specific surface area (SSA) carbons at the carbon-electrolyte interface [29]. With changes in potential, charges flow from the external circuit and within the solution only to charge the double layer and not through the double layer. As charge is increased on the electrodes, an increasing amount of counter-charge flow towards the electrodes and

within the pore structure, setting up what is classically termed a double-layer [88]. This double-layer interface is at electrostatic equilibrium rather than Faradaically at a Nernstian thermodynamic equilibrium. This electrostatic equilibrium exists over the entire range where the electrolyte and electrodes are electrochemically stable (i.e. there is no irreversible degradation of the electrodes or electrolyte). Put another way, in the absence of parasitic reactions, at every state of charge the system is in equilibrium and no currents will flow to reach some more favorable voltage. The unfortunate consequence of this is that activation energies to move the EDLC to a new state of charge are low, so self-discharge is theoretically unavoidable. In real systems, though, parasitic currents from Faradaically active impurities cause a much higher fraction of self-discharge [89]. Unlike batteries, however, this self-discharge does not lead to overall degradation of the EDLC, and when recharged the device will perform accordingly.

This surface charge mechanism explains the high power capability of these systems, because of the absence of charge-transfer resistances that cause substantial *iR* drop at large current densities. Moreover, since there are no Faradic reactions involved in the charge storage mechanism, EDLCs can sustain theoretically infinite (or more practically hundreds of thousands) charge-discharge cycles without major degradation in their performance. At this point it would be instructive to overview some basic concepts of double-layer theory.

1.5.2. Historical context

EDLCs were first worked on at General Electric and a patent detailing their invention was published in 1957 [90].

Briefly stated, in accordance with one aspect of this invention, a low voltage capacitor is provided including at least two spaced, porous carbon electrodes each having a porosity at least as great as fired tar lampblack and an electrolyte in contact with the electrodes. For higher voltage ratings a capacitor is provided having a plurality of such carbon electrode cells connected in series.

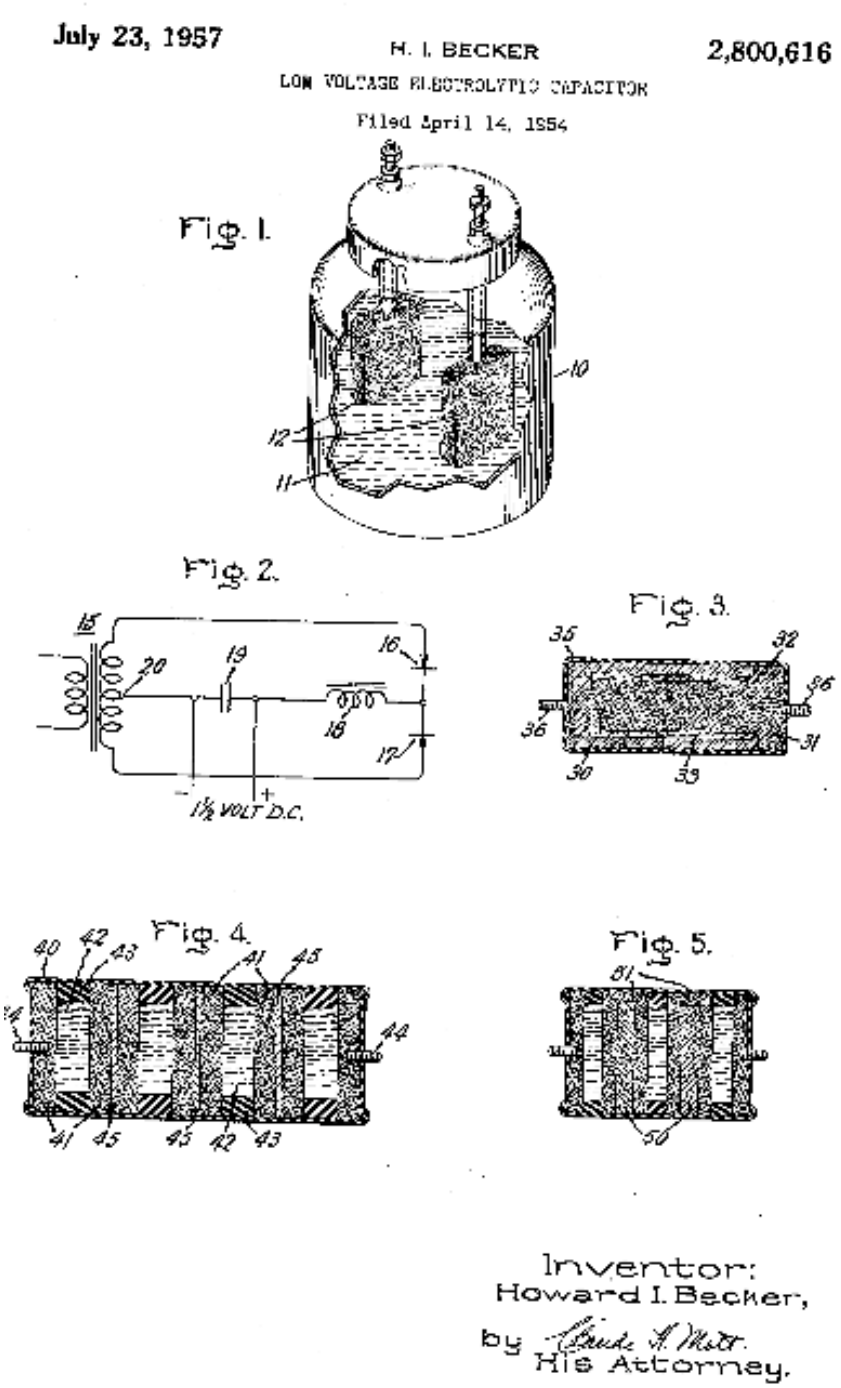

Figure 1.11: Schematic showing the first realization of an EDLC [90]

Standard Oil of Ohio (SOHIO) in 1966, made the next major contribution to electrochemical capacitors [91]. This patent marks the first mention of non-aqueous electrolytes for electrochemical capacitors.

> *The principles of this invention for exemplary purposes will be described in reference to the displacement of solute ions in aqueous medium, it being understood that these principles are applicable to other types of polar mediums (sic) as well.*

This patent is also the first official documentation relating the energy storage phenomenon in porous carbon to double-layer charging, and the importance of high surface area.

> *This invention relates generally to the utilization of an electrostatic field across the interphase boundary between an electron conductor and an ion conductor to promote the storage of energy by ionic adsorption at the interphase boundary… and, since the capacity of such a device is proportional to the effective surface area of the electron conductor, the capacity is also marginally increased.*

Interestingly, this patent points to research currently seen as "cutting-edge" as well, namely dispersing electroactive particles within the porous carbon matrix [92-96], as well as using carbon from coconut shell precursors [26, 97-99], which is currently the most widely used EDLC electrode material in commercial devices.

> *Coconut charcoal having a specific surface of 800 m^2/cc is especially useful electrode material…The amount of energy that may be drawn from such an apparatus can be*

further enhanced by providing a mechanism at the energy storage sites at each interface for promoting a reversible electrochemical reaction. The decomposition potential of the activating chemical reagent for any given electrode must be less than or equal to the applied electrode potential to provide electrochemical reconversion of the corresponding reagent. On discharge, the chemical reagent will undergo a conversion which generates electrical energy in addition to that stored in the sites.

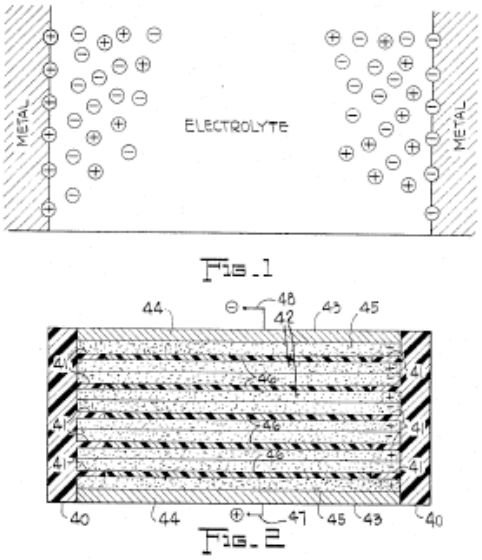

Figure 1.12 Schematics showing an idealized view of the charge storage process in EDLCs envisioned in the 1960's and coin-cell type device with multiple electrodes connected in series to allow greater voltages [91]

SOHIO was also the first to develop marketable devices based on EDLC technology [100]. These coin-cells showed good performance, even at today's standard, in terms of capacitance, resistance, cycling and low temperature performance.

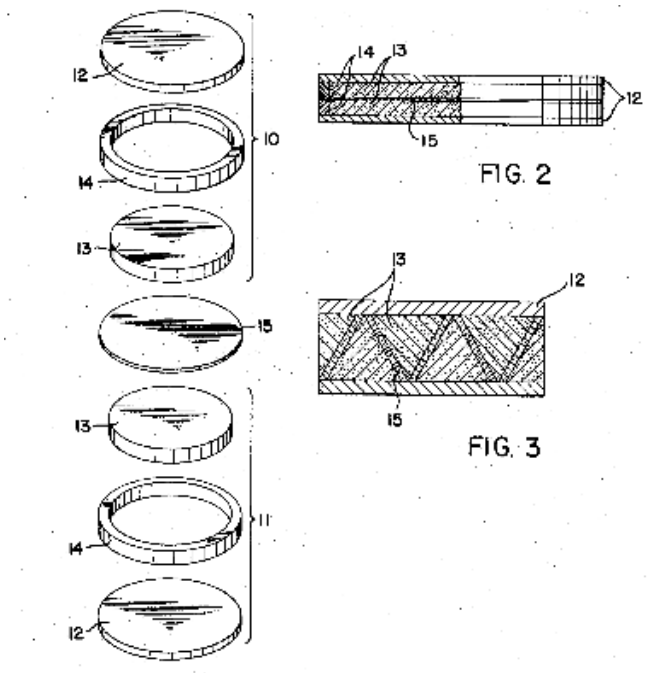

Figure 1.13: Schematic showing coin cell proposed by SOHIO[100]

1.5.3. The double-layer

The study of charged solid-liquid interfaces, manifested as "double-layers," represents a problem of both practical and scientific importance [101]. In general, ideas about the double-layer structure and implications in regards to kinetics have been based on measurements of macroscopic properties in an equilibrium state and have been traditionally studied using planar noble-metal electrodes and mercury drops [102]. It is of special interest in the field of electrochemical capacitors to understand how the double-layer changes as a function of potential as well as electrolyte conditions, both to understand EDLC limitations as well as discovering opportunities for development [103].

1.5.3.1. Classical models and structures of the double layer

At the surface of any charged electrode in solution, there exists either an excess or deficiency of electrolyte ions from that in the bulk solution (or likewise an excess or deficiency of electrons at the surface of the electrode) [68]

$$n_i^{\sigma} = n_i^S - n_i^R \tag{1.10}$$

where n_i^{σ} is the excess, and n_i^s and n_i^R are the numbers of moles of species I in the interfacial region and in the bulk, respectively. In the bulk solution, the free energy depends on temperature, pressure and molar quantities of all components:

$$\overline{G}^R = \overline{G}^R\left(T,P,n_i^R\right) \tag{1.11}$$

whereas, in the interphase, the free energy is a function of area as well.

$$\overline{G}^S = \overline{G}^S\left(T,P,A,n_i^S\right) \tag{1.12}$$

The total differentials are

$$d\overline{G}^R = \left(\frac{\partial \overline{G}^R}{\partial T}\right)dT + \left(\frac{\partial \overline{G}^R}{\partial P}\right)dP + \sum_i \left(\frac{\partial \overline{G}^R}{\partial n_i^R}\right)dn_i^R \tag{1.13}$$

$$d\overline{G}^S = \left(\frac{\partial \overline{G}^S}{\partial T}\right)dT + \left(\frac{\partial \overline{G}^S}{\partial P}\right)dP + \left(\frac{\partial \overline{G}^S}{\partial A}\right)dA + \sum_i \left(\frac{\partial \overline{G}^S}{\partial n_i^S}\right)dn_i^S \tag{1.14}$$

where $\left(\partial \overline{G}^S / \partial A\right)$ is the surface tension, γ, and $\left(\partial \overline{G} / \partial n_i\right)$ are the electrochemical potentials, $\overline{\mu}_i$, which are equal at equilibrium.

$$\bar{\mu}_i = \left(\frac{\partial \bar{G}^R}{\partial n_i^R} \right) = \left(\frac{\partial \bar{G}^S}{\partial n_i^S} \right) \tag{1.15}$$

Eq. (1.10) through Eq. (1.15) can be used to derive the change in surface tension with respect to the change in electrochemical potential and surface excess concentration of electrolyte.

$$-d\gamma = \sum_i \Gamma_i d\bar{\mu}_i \tag{1.16}$$

where Γ_i is the surface excess concentration of electrolyte ions, n_i^σ / A. Practically, what this means is that by measuring changes in surface tension, we can directly measure changes in surface excess concentration, which leads directly to information about double-layer capacitance.

In practice, a constant flux of mercury is permitted through a narrow capillary, which causes a mercury drop to grow until a combination of gravity, the mass of mercury in the drop and surface tension causes the drop to fall and a new drop begins to grow, the residence time following

$$t_{\max} = \frac{2\pi r_c}{mg}\gamma \tag{1.17}$$

where r_c is the radius of the drop, m is the mass of the drop and g is the gravitational force.

By using this growing mercury drop as the working electrode, the surface is continually renewed, which ensures any effects from surface contamination during the experiment

are marginalized [68]. Also, Hg has a large hydrogen overpotential, which extends the cathodic voltage window in aqueous electrolytes, essentially creating a larger range where only non-Faradic behavior exists.

In terms of measurement, as the surface charge density changes on the mercury, its surface tension, changes (Eq. (1.16)), which can be measured by the residence time before the drop falls Eq. (1.17), assuming constant of flux through the capillary opening. By measuring drop time relative to electrode potential, a great deal of insight about double-layer charging can be had.

To interpret the data obtained from the measurements, the Gibbs isotherm is solved for the particular system

$$SdT - VdP + d\gamma + \sigma^M dE + \sum \Gamma_i d\mu_i = 0 \tag{1.18}$$

where S is the entropy, dT is the change in temperature, V is the volume of the interphase, $d\gamma$ is the change in surface tension, and $\sigma^M dE$ is a term that multiplies the surface excess charge by the change in potential difference between the charged phases at the interphase.

For example at the surface of a mercury drop in an aqueous solution of potassium chloride

$$-d\gamma = \sigma^M dE + \Gamma_{K^+(H_2O)} d\mu_{KCl} + \Gamma_{M(H_2O)} d\mu_M \tag{1.19}$$

This allows us to determine, experimentally, the surface charge density of a mercury droplet at a constant temperature, pressure and electrolyte concentration

$$\sigma^M = -\left(\frac{\partial \gamma}{\partial E}\right)_{\mu_{KCl},P,T} \tag{1.20}$$

from which we can calculate capacitance in response to small potential perturbations

$$C_{dl} = \left(\frac{\partial \sigma^M}{\partial E}\right) \tag{1.21}$$

Because drop time is directly proportional to the surface tension, and all other parameters of Eq. (1.17) can be readily measured, ideas of surface excesses of charge and the dependence on potential can be derived. The maxima in Figure 1.14 corresponds to the case where the slope of the curve is zero (Eq. (1.20) is equal to zero) so $\sigma^M = 0$, which is the potential of zero charge (PZC).

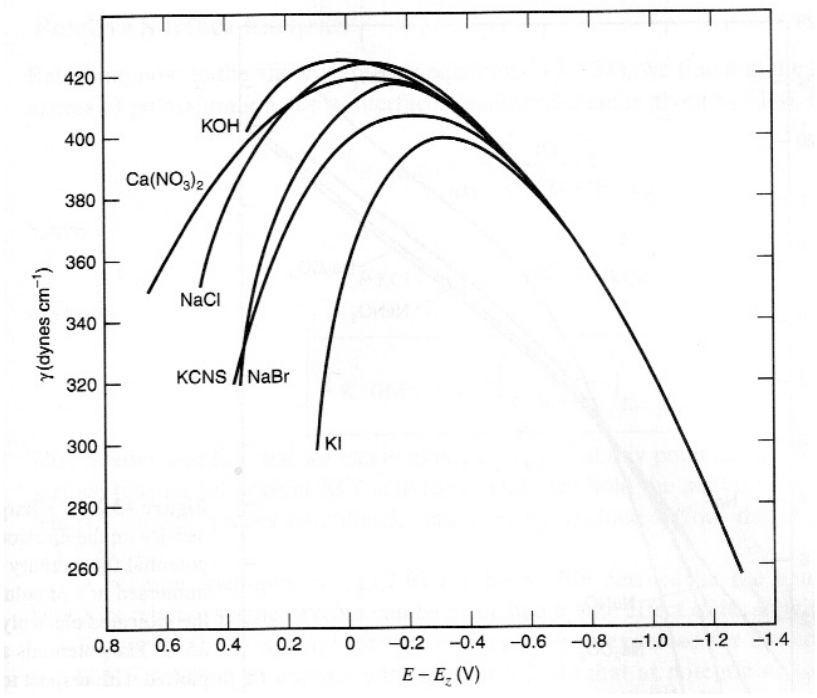

Figure 1.14: Electrocapillary curves of surface tension vs. potential for mercury in contact with solutions of the indicated electrolytes at 18ºC. The potential is plotted with respect to the PZC for NaF [68].

As shown above, from experimental measurements and simple thermodynamic considerations, we can prove that double-layers exist in electrolyte solutions with charged interfaces. Though assumptions such as the excess charge density existing in a 2-dimensional array may not be entirely accurate, the implications are clear. Excess charge density exists at the interphase, which is compensated to ensure overall electroneutrality. As seen in Figure 1.14, however, the shapes of the electrocapillary curves for different electrolytes are different, which leads to the ramification that in producing a structural model for the double-layer to relate thermodynamic quantities to a physical description, these subtle nuances must also be reproduced. In general, a structural model is proposed and tweaked to ensure that it meets the experimentally measured behaviors. It is instructive to now consider the historical development of double-layer structures

1.5.3.1.1. Helmholtz

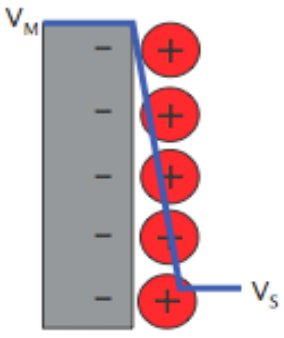

Figure 1.15: Schematic illustrating Helmholtz's treatment of double-layer structure

In the late 19th century, Helmholtz noted the adsorption of oppositely charged ions from solution on an electrode surface with an excess or deficiency of charge [82], thus coining the term "double-layer." Helmholtz, realizing that the metal side of the double-layer interface is a good conductor, when a potential is applied, charge resides on its surface, postulated that the counter charges in the electrolyte solution also reside on the surface separated by an atomic distance (Figure 1.15). These two planes of charge, having opposite charge, constitute the double-layer, which resembles a parallel plate capacitor and can be described by the same equations.

$$\frac{\partial \sigma}{\partial V} = C_d = \frac{\varepsilon \varepsilon_0}{d} \tag{1.22}$$

In Eq. (1.22), it is immediately evident that the capacitance is not a function of voltage, as was predicted by thermodynamics and measured experimentally (see Figure 1.14 for example). Therefore, though good for illustrative purposes, Helmholtz's vision of the double-layer is incomplete, though in practice, the dielectric term can change as a function of potential to account for differences in surface ion density. The dielectric term is a bulk term, however, and has no physical meaning at these length scales.

1.5.3.1.2. Gouy-Chapman

Gouy and Chapman [104] proposed the idea that, on the metal side of the double-layer interface, charge resides on the surface, though on the electrolyte side, there is a tendency for thermal fluctuations to randomize the counter charges (Figure 1.16). This creates a diffuse layer that would be affected by thermal fluctuations to the extent that kT was larger than any electrostatic or chemiosorption energies.

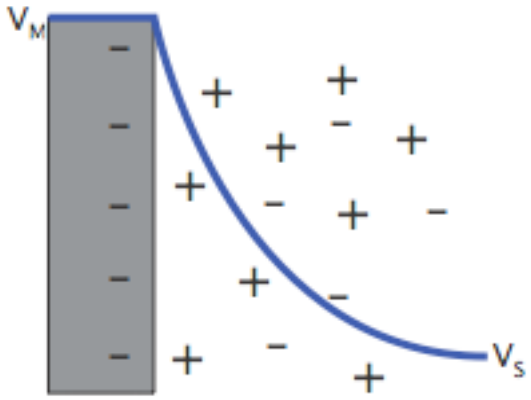

Figure 1.16: Gouy-Chapman

The Gouy-Chapman interpretation of double-layer structure begins with use of the Boltzman equation (Eq. (1.23)) to describe the concentration of electrolyte, n_i, relative to the bulk concentration, n_i^0, as the potential, ϕ, varies.

$$n_i = n_i^0 \exp\left(\frac{-z_i e\phi}{kT}\right) \tag{1.23}$$

The total charge is then just simply the sum of all ionic charges in the volume

$$\rho(x) = \sum_i n_i z_i e = \sum_i n_i^0 z_i \, e \exp\left(\frac{-z_i e\phi}{kT}\right) \tag{1.24}$$

To relate potential to charge, Gouy and Chapman made use of the Poisson equation which relates potential to a given distribution of charges

$$\rho(x) = -\varepsilon\varepsilon_0 \frac{d^2\phi}{dx^2} \tag{1.25}$$

which they combined with Eq. (1.24) to yield the Poisson-Boltzman equation

$$\frac{d^2\phi}{dx^2} = -\frac{e}{\varepsilon\varepsilon_0}\sum_i n_i^0 z_i \exp\left(\frac{-z_i e\phi}{kT}\right) \tag{1.26}$$

Eq. (1.26) can then be solved analytically at small potential perturbations and low concentrations where the equation can be linearized. Solving analytically in the case of a 1:1 electrolyte

$$\frac{2kT}{ze}\ln\left[\frac{\tanh\left(ze\phi/4kT\right)}{\tanh\left(ze\phi_0/4kT\right)}\right] = -\left(\frac{8kTn^0}{\varepsilon\varepsilon_0}\right) \tag{1.27}$$

Eq. (1.27) can be rewritten more conveniently as

$$\frac{\tanh\left(ze\phi/4kT\right)}{\tanh\left(ze\phi_0/4kT\right)} = \exp\left(-\kappa x\right) \tag{1.28}$$

This lets us describe the distance-dependant terms in the exponential, where

$$\kappa = \sqrt{\frac{2n^0 z^2 e^2}{\varepsilon\varepsilon_0 kT}} \tag{1.29}$$

κ has units of reciprocal distance and is representative of a characteristic thickness of the diffuse double-layer. Eq. (1.28) describes how the potential decays from the electrode potential to the bulk solution potential through the diffuse layer. It should be noted that, according to this treatment, as the electrode potential is increased, it decays more quickly because the diffuse layer becomes more compact at the electrode. For more realistic electrochemical conditions, the equation can be numerically integrated, as is common for molecular mechanics models in molecular modeling software.

Typical thicknesses of the diffuse layer for 1:1 electrolytes calculated from Eq. (1.29) are shown in Table 1.2. It is apparent that the κ values decrease with decreasing electrolyte concentration (diffusion layers become thicker with decreasing electrolyte concentration). At low electrolyte concentration, the diffuse layer is several nanometers thick, and in very dilute conditions can be several hundred nanometers thick. At typical concentrations for electrochemical capacitors, however, the diffuse layer is only some few Angstroms thick and corresponds to roughly the thickness of the solvation shell around an ion.

It should be noted that at concentrations $>10^{-2}$, the Poisson-Boltzman equation cannot be solved analytically, so many of the values for κ are not proper.

Table 1.2: Characteristic thickness of the diffuse layer for a 1:1 electrolyte at 25°C in water

C*(M)[b]	1/κ (Å)
1	3.0
10^{-1}	9.6
10^{-2}	30.4
10^{-3}	96.2
10^{-4}	304

[b] **$C^*=n^0/N_A$ where N_A is Avogadro's number**

Capacitance can then easily be calculated knowing the charge density. Solving to find the solution charge density, knowing

$$q = \varepsilon\varepsilon_0 A\left(\frac{d\phi}{dx}\right)_{x=0} \tag{1.30}$$

we obtain

$$\sigma^M = -\sigma^S = \sqrt{8kT\varepsilon\varepsilon_0 n^0}\sinh\left(\frac{ze\phi_0}{2kT}\right) \tag{1.31}$$

By differentiating Eq. (1.31) to find differential capacitance according to Eq. (1.21), we arrive at the sought after result

$$C_d = \frac{d\sigma^M}{d\phi_0} = \sqrt{\frac{2z^2\varepsilon\varepsilon_0 n^0}{kT}}\cosh\left(\frac{ze\phi_0}{2kT}\right) \tag{1.32}$$

Plotting the capacitance versus potential (Figure 1.17), from Eq. (1.32) leads to curves that are parabolic about the PZC. As electrolyte concentration increases, the minimum capacitance value increases and the curve becomes more narrow. In reality, what is seen experimentally is a flattening in capacitance as the electrolyte concentration increases and numerically, much lower values than those predicted by the Gouy-Chapman theory.

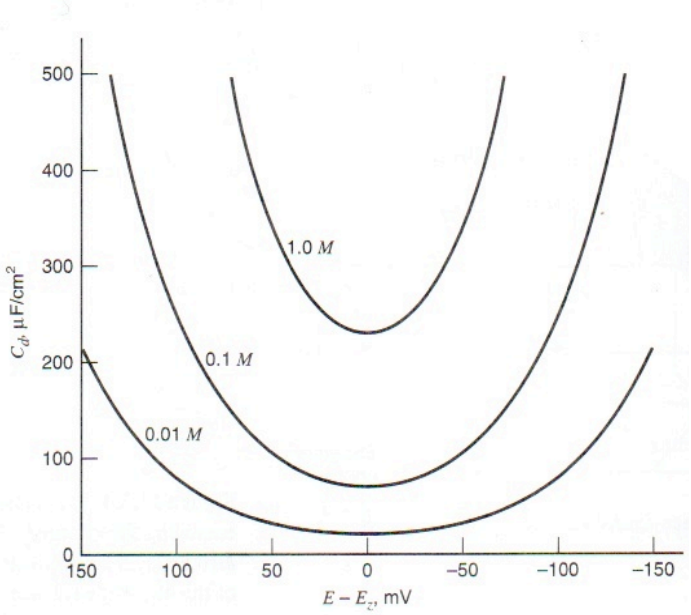

Figure 1.17: Gouy-Chapman capacitance versus potential

1.5.3.1.3. Stern

The limitation of the Gouy-Chapman model of the double-layer structure was the consideration of ions as point charges. At high surface charge densities, these point charges approach the surface very closely and lead to unrealistically high predicted capacitances.

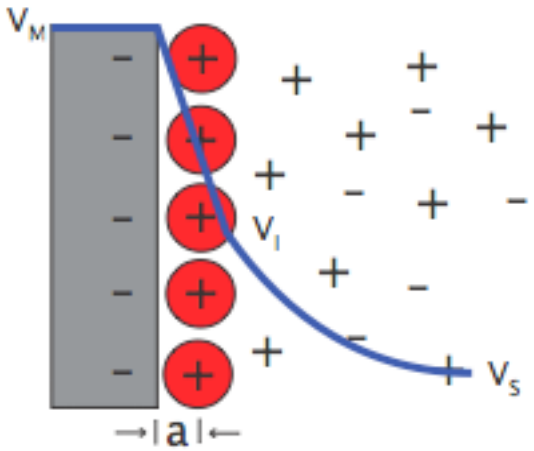

Figure 1.18: Gouy-Chapman-Stern illustration

By introducing the idea that ions have finite sizes, Stern, in effect, marginalized this limitation of the Gouy-Chapman model of the double-layer. Essentially the Stern model combines a plane of adsorbed charges, such as postulated by Helmholtz, with a diffuse layer of decaying charge density as postulated by Chapman and Gouy (Figure 1.18).

The same treatment of the diffuse layer applies as was treated by Gouy and Chapman, except there is a hard cut-off at the distance of one atomic diameter (or rather one solvated ion diameter), which can be described for a 1:1 electrolyte by

$$\frac{\tanh\left(ze\phi/4kT\right)}{\tanh\left(ze\phi_2/4kT\right)} = \exp\left(-\kappa\left(x - x_2\right)\right) \tag{1.33}$$

where x_2 is the plane of closest approach of electrolyte ions in the diffuse layer and ϕ_2 is the potential at x_2. For the compact region, the potential profile would be linear, as was shown in the case of Helmholtz's model (Figure 1.15). Therefore, the total potential drop across the double-layer would be

$$\phi_0 = \phi_2 - \left(\frac{d\phi}{dx}\right)_{x=x_2} x_2 \tag{1.34}$$

Following the same derivation in arriving at Eq. (1.31) and making use of Eq. (1.34) the charge for the diffuse layer in Stern's model can be found

$$\sigma^M = \sqrt{8kT\varepsilon\varepsilon_0 n^0}\sinh\left[\frac{ze\phi_2}{2kT}\left(\phi_0 - \frac{\sigma^M x_2}{\varepsilon\varepsilon_0}\right)\right] \tag{1.35}$$

which after differentiation and rearrangement leads to the equation for double-layer capacitance as postulated by Stern

$$C_{dl} = \frac{d\sigma^M}{d\phi_0} = \frac{\sqrt{2\varepsilon\varepsilon_0 z^2 e^2 n^0/kT}\cosh\left(ze\phi_2/2kT\right)}{1+\left(x_2/\varepsilon\varepsilon_0\right)\sqrt{2\varepsilon\varepsilon_0 z^2 e^2 n^0/kT}\cosh\left(ze\phi_2/2kT\right)} \tag{1.36}$$

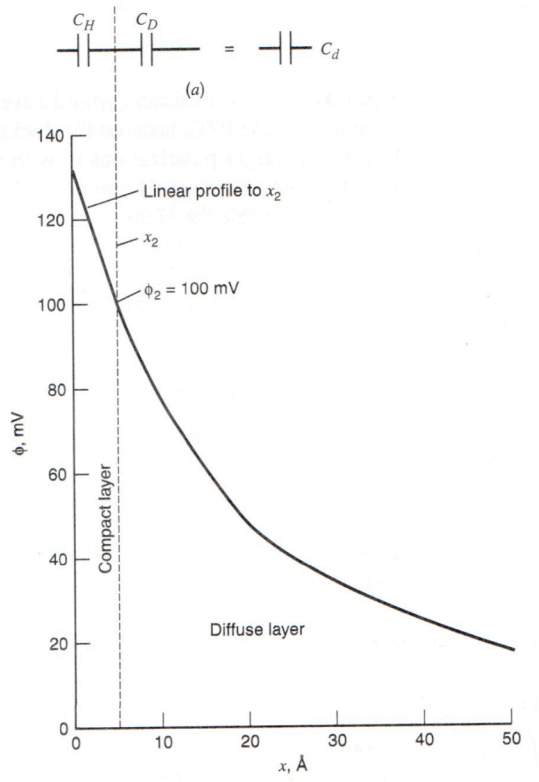

Figure 1.19: Gouy-Chapman-Stern capacitance versus distance

As capacitors in series add as the inverse (Eq. (1.9)), the inverse of Eq. (1.36) is more powerful for explaining Stern's model

$$\frac{1}{C_{dl}} = \frac{x_2}{\varepsilon\varepsilon_0} + \frac{1}{\sqrt{2\varepsilon\varepsilon_0 z^2 e^2 n^0}\cosh\left(ze\phi_2/2kT\right)} \tag{1.37}$$

which looks like the relation for adding capacitors in series (which essentially this is!)

$$\frac{1}{C_{dl}} = \frac{1}{C_H} + \frac{1}{C_D} \tag{1.38}$$

where C_H corresponds to the capacitance due to the Helmholtz plane of adsorbed coutnerions and C_D corresponds to the capacitance due to the diffuse layer. From Eq. (1.37), it is evident that the Helmholtz contribution to capacitance has no dependence on potential, as was the initial criticism of this model, and therefore only can provide, at the very most, the capacitance at the open circuit potential of the system. The capacitance from the diffuse layer follows the same behavior as was shown for the Gouy-Chapman approach, namely minimum capacitance at the PZC with an equivalent parabolic rise in capacitance positive and negative of the PZC. Because capacitance contribution from the Helmholtz plane and the diffuse layer add as the inverse, the smaller of the two determines the overall behavior. Therefore at potentials far removed from the PZC, the Helmholtz plane accounts for the capacitance and it is found to not vary with potential. Near the PZC, however, there is a valley, with minimum capacitance at the PZC. As electrolyte concentrations increase the influence of the diffuse layer diminishes and capacitance is found to vary less as a function of potential. The reciprocal nature of Eq. (1.37) and ensures that by choosing proper values for the dielectric constants, it can be used to model any double-layer phenomenon. Thus, it offers the same level of credibility as the Helmholtz model because it lacks predictive capacity without fudging bulk dielectric terms.

Also, in practice there are many things that cannot be accounted for by the Gouy-Chapman-Stern model, probably the most significant is ion specificity. Figure 1.14 shows large divergence between electrocapillary curves at potentials positive of the PZC, but convergence at potentials negative of the PZC. This indicates that double-layer processes

occurring at potentials positive of the PZC for the system studied involve some sort of chemical specificity between the electrolyte ions and electrode.

1.5.4. Carbon for EDLCs

As highlighted earlier, understanding the properties of the carbon electrode is crucial to understanding EDLC behavior. Carbon in all its forms (diamond, graphite, amorphous) is historically a technologically important material, being used in everything from graphite electrodes for metal refining, activated carbon for water purification, diamond cutting tools, jewelry and IR windows, and graphite for lubrication, for example [105]. Even in a world dominated by silicon-based electronics, carbon is the only material on the periodic table with multiple journals devoted exclusively to its study. Because of its electrochemical inertness and good conductivity, graphitic carbon also finds use in many ubiquitous electrochemical applications, such as battery and fuel cell electrodes, and in the production of many chemicals [26, 106, 107]. In recent years, more advanced applications have arisen that utilize the wide range of carbon's desirable properties, such as the carbon-carbon composites in the space shuttle's wing edges, and structural materials for next generation sport equipment, automobiles and aircrafts, for example [108]. The reason for this very wide range of potential applications arises because of the wide range of properties that carbon possesses in its different microstructures [105]. This can be appreciated by considering that diamond is one of the hardest materials known, which leads to its wide use in cutting tools, and has high dispersion and refractive index and is transparent which leads to its use in jewelry. In contrast, graphite, the most common allotrope of carbon is very soft, which leads to its use as a lubricant and is

opaque. Likewise, the electronic properties of the different allotropes are opposite, graphite being a conductor and diamond being an insulator. Discoveries of new carbon micrstructures such as nanotubes and fullerenes largely sparked the nanotechnology movement and have opened up a plethora of potential new applications [109, 110]. This has also opened up the promise of improving the performance of traditionally used carbons by tailoring their properties on the nanoscale.

In the realm of EDLCs, one significant challenge to realizing cost reductions required by industry is the current unavailability of low cost and high performance carbon materials. The breakup of costs shows that the materials used in the electrochemical capacitors account for over 50% of the cost of the total system [24, 26]. This includes high purity aluminum foil [111], sophisticated activated carbon [112], advanced separator membranes [113], high purity electrolyte [70], and complex hermetic packaging. High-performance activated carbons are currently the costliest material because they are produced in small quantities using batch processes by very few suppliers and sometimes require exotic or expensive precursors (coconut shells, phenolic resins, etc.). Finding a low-cost but high-performing porous carbon material is seen as optimal. However, the question remains – which material can provide the highest performance? To answer this, it is necessary to understand how different active material factors affect performance.

Porous (activated) carbon (charcoal) has been known for at least 3000 years and is most widely used as a low-tech material for as applications ranging from wastewater remediation, gas purification, to treating poisoning by ingestion [114]. Carbons for EDLCs must be conductive, nearly ideally polarizable (at least within the decomposition

window of most electrolytes), and have controlled pore sizes that can vary from smaller than the ionic size of electrolyte ions to many times larger than these ions [27]. The utility of using porous carbon species for studying double-layer charging was realized when using them as the active material in electrochemical capacitors, because the formation of a double-layer within their pores is assumed [115]. The conventional synthesis of porous carbon materials involves treating carbonaceous precursors in an oxidizing environment (water, CO_2, O_2, KOH, NaOH, etc.) at elevated temperature [114]. Many different activated carbons [116, 117] from precursors like bamboo [118], rice husk [119], wood [120], coconut shells [121] to phenolic resins [122] and pitch [123], aerogels [124, 125], fibers [126-128], as well as porous templated carbons [129-134], carbon nanotubes [135, 136], and more recently, carbon derived from metal carbides [137] are used in the construction of supercapacitors. Different temperatures, treatment times, oxidant concentrations, etc., lead to different carbon structures and changes in the surface chemistry [138-141] and nanotexture [142] of the resulting carbon that are difficult if not impossible to precisely and independently control [27]. Unfortunately, the pore size and structure of carbon prepared from polymer and natural precursors are difficult to control because of random orientation of polymer chains of the former and structural inhomogeneities of the latter [97]. Some generalizations can be made from the available literature data, however.

1.5.5. Pore size importance in EDLCs

The traditional understanding of how to increase the capacitance involves maximizing the surface area that is accessible to the electrolyte ions [84]. Over the past decade, the focus

was to create a carbon material with the highest surface area of the largest pores, preferably above 2 nm [30, 97, 143]. This approach was mostly born of the fact that capacitance stops being a linear function of surface area above critical surface area [124, 140, 144-147].

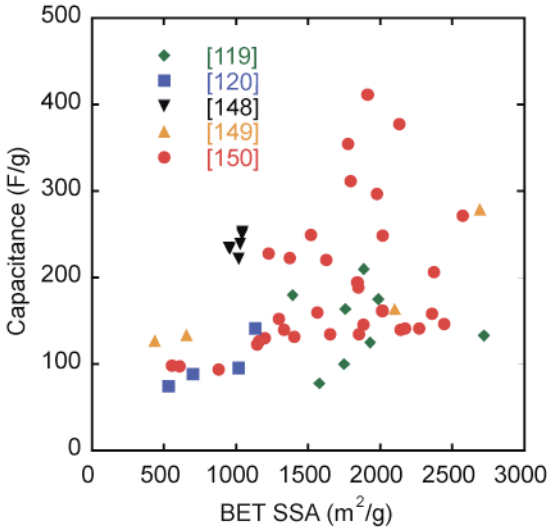

Figure 1.20: Specific capacitance in aqueous electrolytes versus specific surface area (SSA) for various carbons from different precursors and different research groups

Figure 1.20 shows the capacitance versus surface area reported by a number of different research groups [119, 120, 148-150] on the same plot. When the data is considered as a whole, there is increasing scattering with increasing surface area.

Ever since the work of Shi [150], authors have been studying the effect of pore size to reconcile this scattering (or saturation depending on who you ask) of capacitance as the surface area increases. This is explained as follows. Assuming constant pore volume, increasing the pore volume leads to diminishing surface area (Figure 1.21). At the

smallest pore size (Figure 1.21a), the surface area is effectively zero, however, as the ions are too large to effectively enter the pores. Alternatively, when pores are too large (Figure 1.21c), ions can easily access the pore surfaces, but the surface area is low. Therefore there is some ideal pore size that maximizes both surface area and pore accessibility (Figure 1.21b). A number of different groups have studied the effect of pore size on capacitance to identify this maximum. In general, the feeling amongst the community that for very high surface area carbons, the majority of the surface area lies in pores which are large enough to be accessed by gas molecules in surface area characterization experiments (~5Å), but too small to be accessed by electrolyte molecules in electrochemical experiments [115, 117, 143, 151-153].

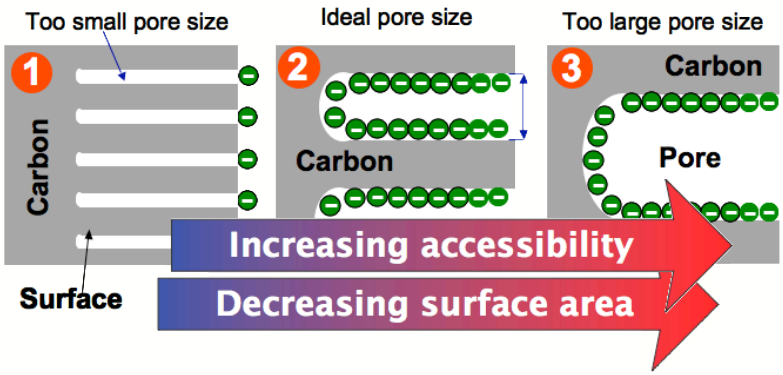

Figure 1.21: Schematic showing how pore size can effect the surface area seen by ions in electrochemical experiments.

Experiments were done by Ania, *et al* on a single carbon system in a series of ionic liquids with different ion sizes [154] ranging from 0.85 nm in the longest dimension to 2 nm in the longest dimension. The results show that, in general, the capacitance decreases with increasing ion size. The authors attributed this to pores that are too small for ions to access, much in the case of other studies that varied the pore size while keeping the ion size constant. So assuming simple ion accommodation, everything makes sense…

1.5.6. The study of pores smaller than ~2 nm

There are some limited studies in literature showing the importance of pores smaller than 2 nm in maximizing double layer capacitance [140, 155]. The group of Frackowiak showed that, in general, the capacitance for a group of mesoporous carbons scaled most reliably with the volume of CO_2 adsorption, which is a measure of the volume of pores smaller than ~1.5 nm. This indicates that the smallest pores are the most important in terms of charge storage. Lozano-Castello showed in large study on carbons with surface areas above 2500 m^2 g^{-1} that pores larger than 2 nm have little or no contribution to total capacitance, though the conclusions of the paper were quite the opposite [156]. In fact, the aim of the paper was to show how increasing the pore size increased ion accessibility at high scan rates. In fact, increasing the pore size had a much stronger influence on capacitance, which substantially decreased. Salitra showed on a series of activated carbons with different pore sizes and using K^+, Na^+, and Li^+ as probe molecules, that the minimum pore size needed for ion accessibility is ~4 Å and corresponds to the cross sectional dimension of nitrogen.

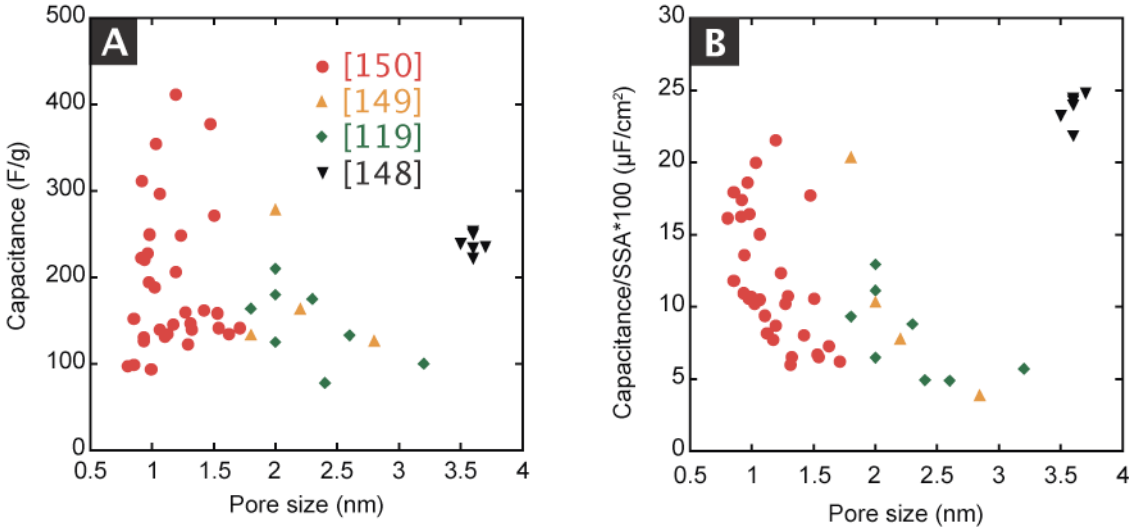

Figure 1.22: a.) Capacitance in aqueous electrolyte versus pore size for the samples shown in Figure 1.20. b.) Surface capacitance versus pore size for the samples shown in Figure 1.20.

Figure 1.22 shows the capacitance data plotted versus pore size for every study in Figure 1.20 that had pore size data available versus pore size. With data from a number of groups on the same axes (Figure 1.22a), there is not such a clear trend of increasing capacitance with increasing pore size, which is surprising because conductivity certainly increases with increasing pore size [25]. Because both increasing the surface area (Figure 1.20) increases the scatter in capacitance values and decreasing the pore size increases the scatter in capacitance values (Figure 1.22a), the capacitance was normalized by the surface are and plotted versus pore size (Figure 1.22b). As capacitance should be proportional to area (Equation 1.3), plotting the data in this way should be the best way to represent the effect of changing pore size on capacitance. A few things are apparent in

Figure 1.22b. First is decreasing the pore size seems to have a positive effect on this surface area-normalized capacitance. This is a curious result, and especially interesting because all of the data in the study were from papers that reported decreasing capacitance with decreasing pore size. Second, there is a good deal of data scatter. Oxidation of carbon causes a plethora of surface groups to be introduced that can give either a positive or negative effect of performance, depending on whom you ask [80, 125, 138, 139, 156]. This effect seems to be marginalized in organic electrolytes, however [157]. Third, the series of data from Li, *et al.* [148] are very much outliers. This can be explained by understanding that they incorrectly used the BJH model on the desorption branch of an isotherm with a broad distribution of mesopores [158]. From pore condensation effects in N_2 at 77 K, there is forced closure of the hysteresis loop at P/P_0=0.45, which gives a false pore size of ~ 3.8 nm. Thus, not only is firm understanding of the electrochemical cell effects important, also understanding and proper use of the characterization methods is equally important.

1.6. Carbide-Derived Carbon (CDC)

Carbon derived from selective etching of metals from crystalline metal carbides by chlorine has shown great promise as the active material in electrochemical capacitors [26, 159-161] because of properties that can be fine tuned [162] and potential control of functional groups [163]. In the following section, CDC research, both in our group as well as others will be outlined as well as its properties and performance. The name carbide-derived carbons was given to these materials by Y. Gogotsi [162] and is widely

used now. Previous carbons produced from carbides were called “mineral carbons” [164, 165] or nanoporous carbons [166].

1.6.1. Synthesis

In general, CDC is synthesized by high temperature extraction of metals and metalloids from carbide precursors. This can be accomplished using halogens [167, 168], vacuum decomposition [169] or etching in supercritical water [170]. High temperature chlorination Eq. (1.39) and vacuum decomposition Eq. (1.40) are the most widely used methods for CDC production:

$$MC + x/2\,Cl_2 \rightarrow MCl_x + C \tag{1.39}$$

$$MC(s) \xrightarrow[\text{vacuum, T}]{} M(g) + C(s) \tag{1.40}$$

Processing of CDC was recently reviewed by A. Nikitin et al [171]. Many different carbide precursors were chlorinated to produce CDC, ranging from complex ternary carbides [162, 172, 173], to more common carbides such as B_4C [174], Fe_3C [175], ZrC [176], SiC [167-169] and Mo_2C. The chlorination process following Eq. (1.39) was originally used to produce silicon tetrachloride from silicon carbide [177], with the carbon being burned, until pure silicon became less expensive than silicon carbide due to the semiconductor industry. This process is still used to produce a variety of metal chlorides for semiconductor industry and metal-organic synthesis, however. As the process for CDC formation is the same used in industry for synthesis of various metal chlorides and processes exist for the production of metal carbides from metal chlorides, it

can be envisioned a closed cycle process for production of both CDC and technologically important metal chlorides (Figure 1.23). Metal carbides are usually produced by reacting carbide-forming metal oxides and carbon at high temperature (Figure 1.23-1). The metal carbides can then produce CDC and metal chlorides (Figure 1.23-2) by Eq. (1.39). The metal chlorides produced in step 2 can then either be further transformed into widely used nanoscale metal oxides, such as silica or titania, (Figure 1.23-3) with sequestration of the chlorine to use in step 2 or sold as a chemical ($SiCl_4$ or $TiCl_4$). The metal oxides generated in this process can also be used in step 1 for carbide production, thus recycling the metal and theoretically making the only input carbon, which is transformed to CDC in this manufacturing process.

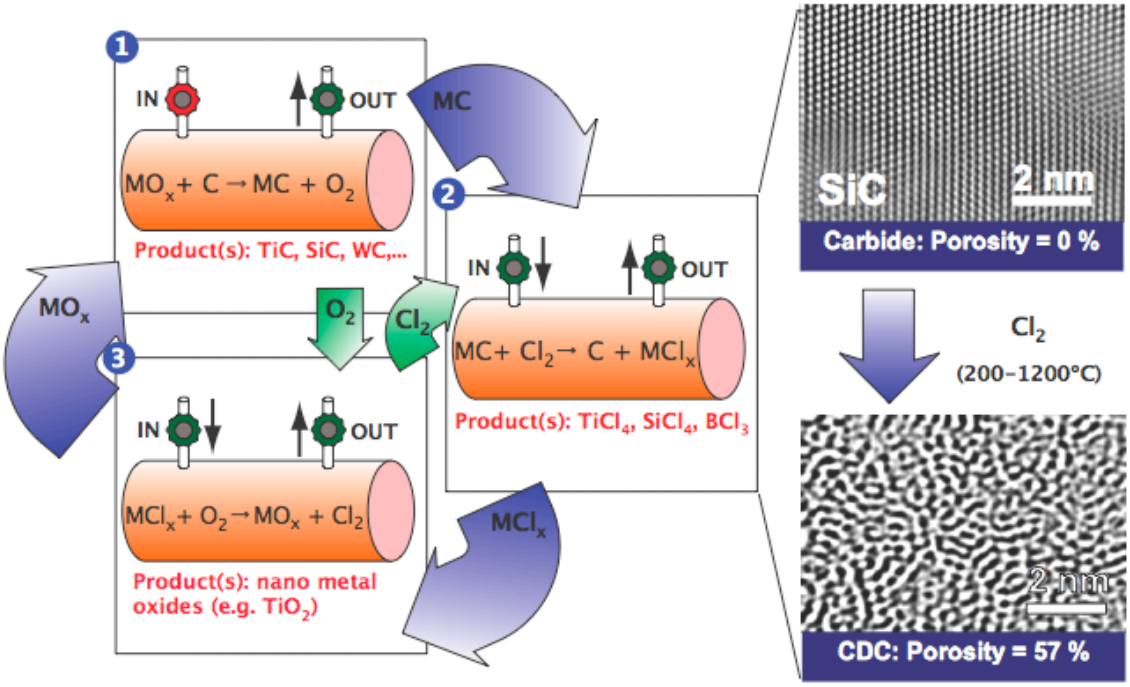

Figure 1.23: Schematic of the CDC closed cycle process and TEM micrographs showing the transformation of crystalline SiC to amorphous CDC.

1.6.2. Porosity

As first shown by Boehm in 1975 [178] on CDC synthesized from TaC and SiC, and later for most carbide precursors [163], the resulting carbons have Type I isotherms in the Brunauer classification, which are indicative of microporous carbon having pore sizes less than 2 nm and relatively high surface areas up to 2000 m^2g^{-1} [174, 176, 179]. The pore size of CDC can be tailored by selection of carbide precursors with different spatial distributions of carbon atoms in the initial carbide lattice, changing the nanotextural ordering in the CDC by varying the synthesis temperature, and post-treatment in a variety

of oxidizing atmospheres (activation) [180, 181]. Therefore, both microporous and mesoporous carbons with different pore shapes can be produced by this method.

1.6.3. Microstructure

Linear reaction kinetics for chlorination of SiC powders, whiskers and sintered ceramics to carbon coating thicknesses above 100 μm were demonstrated [169, 182], showing that there is virtually no thickness limitation to CDC coatings. Moreover, as the coating is conformal, intricate shapes can be prefabricated using the hard carbide precursor and complex morphologies can be realized. Equally important for applications is the wide range of microstructures that CDC possesses depending on the precursor carbide and synthesis conditions. Curved nanostructures ranging from onions [183, 184] to nanotubes [185] have also been produced from carbide precursors. In fact, tubular nanostructures produced from carbide precursors may have preceded Iijima's discovery of carbon nanotubes [186].

Different carbide precursors lead to different levels of graphitization for a given synthesis temperature [174, 176, 179]; however, in general, samples produced below 1000ºC are X-ray amorphous and only at synthesis temperatures of 1200ºC and above is there significant graphitization. Structure collapse leading to specific surface areas (SSA) below 100 $m^2 g^{-1}$ and formation of graphite were observed in samples produced at 1300-1800°C [187]. It was shown by Dimovski [175] and Leis [188] that iron in the precursor carbide can also cause significant graphitization at temperatures below 1000ºC. Increasing graphitization leads to increasing electrical conductivity with increasing synthesis temperature [166, 189].

In addition to porous carbons and graphite, graphene and carbon nanotubes (CNT), which possess unique electrical, mechanical and optical properties, can be produced by vacuum decomposition of SiC (Eq. (1.40)). Kusunoki et al. [190-192] observed formation of CNTs growing normally to the carbon terminated $(000\bar{1})$ C-face of hexagonal SiC with primarily zigzag chirality [193] and graphite growing on the Si terminated (0001) Si-face. Nagano *et al.* claimed CNT formation on both carbon and silicon faces of HF-etched hexagonal 6H-SiC [194] and cubic 3C-SiC [195], with tubes growing normal to the surface. CNT formation on 6H, [196] 3C, and 4H [197] SiC single crystals, powders [190, 198], as well as amorphous [199] and 3C [194] films has been reported in literature. Vacuum decomposition of SiC has also become a common method for synthesis of graphene. Ferbaux et al. [200] reported that graphite grows epitaxially on the Si-face of SiC. Our recent work on vacuum decomposition of β-SiC whiskers showed well-ordered graphene layers but no nanotube formation [169]. The most recent studies [197, 201] suggested the growth of CNTs at 1400-1700°C on both C- and Si-faces of SiC single crystals, but with different growth rates, following the reaction:

$$SiC + \tfrac{1}{2}O_2(g) \rightarrow SiO(g) + C \qquad (1.41)$$

Equally interesting for tribological applications is the possibility to create nanodiamonds during synthesis of CDC [202]. However, similar to graphene and nanotubes, those are outside the scope of my dissertation. Because of the conformal nature of the carbide-to-carbon conversion and lower theoretical density of CDC than graphite, the main feature of carbide-derived carbon is highly developed and well-controlled porosity [203]. It will be described in more details in the following sections.

1.6.4. Studies on Carbide-Derived Carbon

Porosity is important for many applications of CDC. Using CDC from SiC, TiC and Mo_2C, it has been shown that pore size is important for Li diffusion and capacity [204, 205]. The importance of pore size was also shown using CDC for cryogenic hydrogen storage [179, 203]. It was shown that tuning the pore size to have a maximum volume of pores smaller than 1 nm can increase hydrogen uptake to ~3 wt.% at 77 K and 1 atm, as well as methane uptake at room temperature. Using CDC for cytokine adsorption [206] showed that adsorption scales with the volume of pores larger than the size of the cytokine in question (5-10 nm). Porous CDC coatings have also shown good tribological properties [182, 207]. Therefore, the effect of various process parameters on the porosity of CDC will be described in detail in the following sections.

1.6.4.1. Effect of starting carbide

Using different carbide precursors for CDC synthesis essentially amounts to having a different spatial distribution of carbon atoms in the precursor and affords a degree of freedom beyond typical porous carbon synthesis techniques for tailoring properties. For example, Figure 1.24 a,b shows the layered distribution of carbon in Ti_3SiC_2 and uniform distribution of carbon in 3C-SiC [163], respectively. Upon removal of the titanium and silicon atoms, it can be seen that the different carbon distributions in the initial carbide lattice would lead to different pore sizes between Ti_3SiC_2-CDC (Figure 1.24a) and SiC-CDC (Figure 1.24b). This is reflected in experimental pore size distributions calculated from Non-Local Density Functional Theory (NLDFT) treatment of argon adsorption

isotherms taken at 77K (Figure 1.24 c,d). At the same synthesis temperature, 1200ºC (the maximum practically used), the pore size distribution of SiC-CDC is much narrower and shifted to lower average pore size than that of Ti_3SiC_2-CDC.

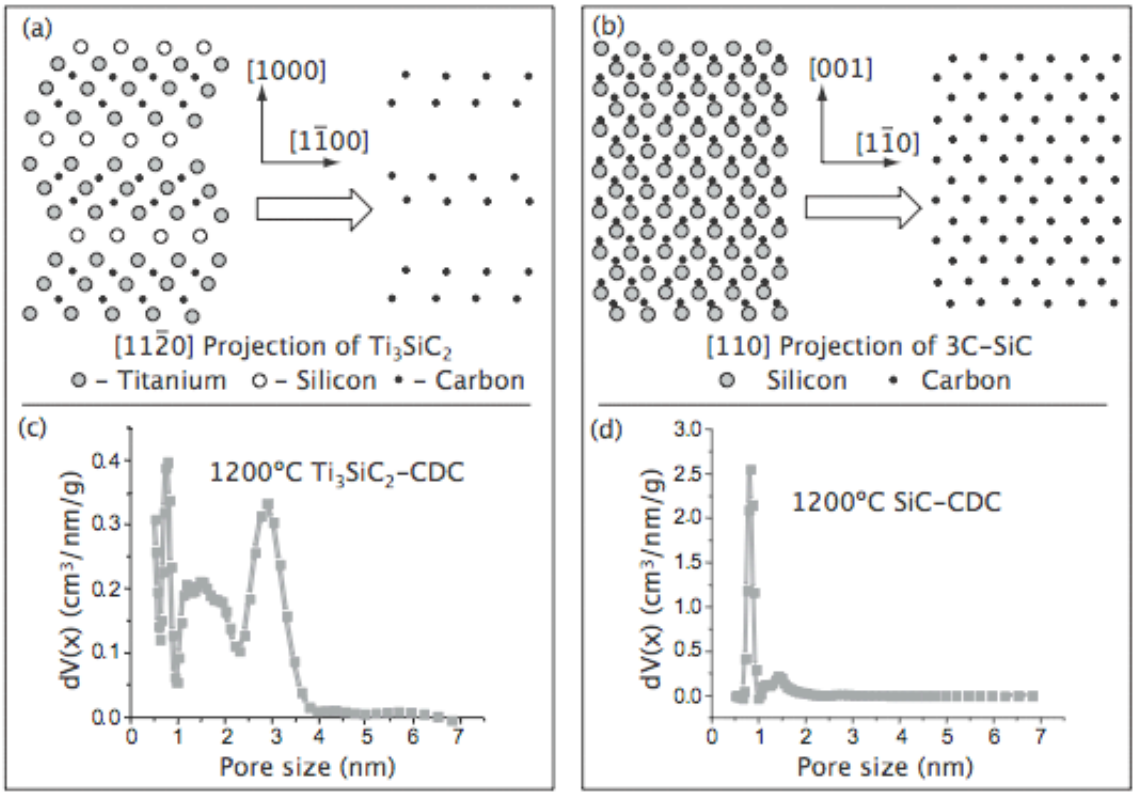

Figure 1.24: a.) [11-20] projection of Ti_3SiC_2 with removal of all Ti and Si atoms and b.) [110] projection of 3C-SiC with removal of all Si atoms removed show different distributions of carbon atoms after metal removal. c.) Pore size distribution of Ti_3SiC_2-CDC chlorinated at 1200ºC and d.) pore size distribution of SiC-CDC chlorinated at 1200ºC show much wider pore size distribution for the Ti_3SiC_2-CDC.

A wide range of carbide precursors leads to a wide range of theoretical pore volumes (Figure 1.25). Without further post treatment, pore volumes of ~55% to ~85% are potentially possible just by selecting different starting carbides and assuming conformal transformation of the carbide to CDC. Alternatively, by altering the stoichiometry of the starting carbide there is another degree of freedom for pore size control. It was shown using TiC that the average pore size was ~0.7 nm while $TiC_{0.5}$ precursors gave 2.8 nm pores [208]. A summary of data for several carbides is shown in Table 1.3.

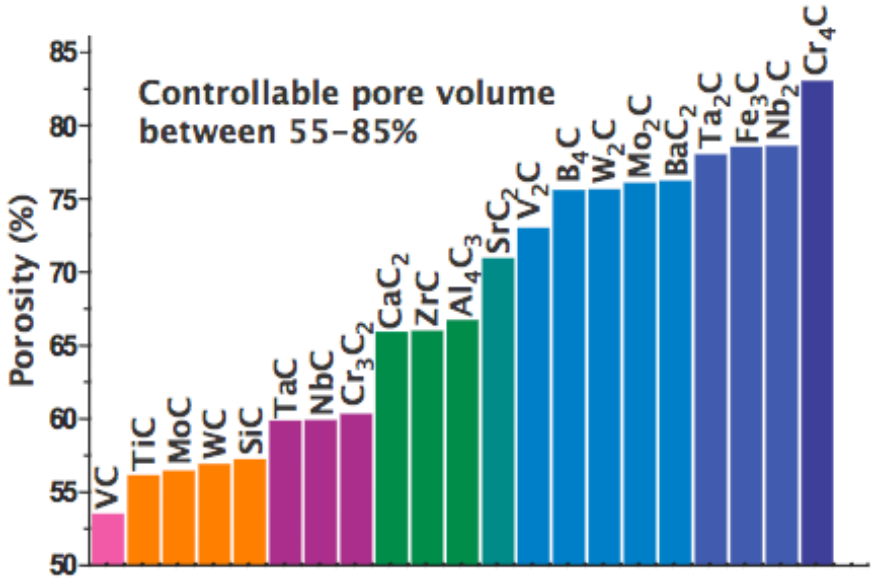

Figure 1.25: Theoretical pore volumes calculated for CDCs from various precursors [209]

Table 1.3: CDC porosity

B_4C-CDC	d (nm)	BET SSA (m^2/g)	V_{tot} (cm^3/g)	V_{meso} (cm^3/g)	V_{micro} (cm^3/g)	C_{H2SO4} (F/g)	C_{TEABF4} (F/g)
600	1.25 [210]	1150 [203]	-	-	-	95 [210]	-
750	-	1750 [203]	-	-	-	-	-
800	1.15 [210]	2000 [203]	-	-	-	140 [210]	-
850	-	2050 [203]	-	-	-	-	-
900	-	1975 [203]	-	-	-	-	-
1000	1.2 [210]	1850 [203]	-	-	-	147 [210]	-
1100	-	1750 [203]	-	-	-	-	-
1200	1.9 [210]	1525 [203]	-	-	-	120 [210]	-

SiC-CDC	d (nm)	BET SSA (m^2/g)	V_{tot} (cm^3/g)	V_{meso} (cm^3/g)	V_{micro} (cm^3/g)	C_{H2SO4} (F/g)	C_{TEABF4} (F/g)
600	-	675 [203]	-	-	-	-	-
800	-	1425 [203]	-	-	-	-	-
900	-	1275 [203]	-	-	-	-	-
1000	-	1400 [203]	-	-	-	-	-
1100	-	1450 [203]	-	-	-	-	-
1200	-	1300 [203]	-	-	-	-	-

TiC-CDC	d (nm)	BET SSA (m^2/g)	V_{tot} (cm^3/g)	V_{meso} (cm^3/g)	V_{micro} (cm^3/g)	C_{H2SO4} (F/g)	C_{TEABF4} (F/g)
500	0.678 [211]	1040 [211]	-	-	-	-	140.5 [211]
600	0.738 [211]	1269 [211]	-	-	-	110 [212]	143 [211]
700	0.764 [211]	1401 [211]	-	-	-	-	136 [211]
800	0.806 [211]	1595 [211]	-	-	-	190 [212]	130 [211]
1000	1.09 [211]	1625 [211]	-	-	-	145 [212]	98 [211]

Table 1.4: CDC porosity (continued)

Ti_2AlC-CDC	d (nm)	BET SSA (m^2/g)	V_{tot} (cm^3/g)	V_{meso} (cm^3/g)	V_{micro} (cm^3/g)	C_{H2SO4} (F/g)	C_{TEABF4} (F/g)
400	-	400 [213]	-	-	-	-	-
600	1.4 [210]	650 [213]	0.8 [173]	0.35 [173]	0.45 [173]	77 [210]	-
800	1.75 [210]	1050 [213]	1.9 [173]	1.52 [173]	0.38 [173]	120 [210]	-
1000	2.6 [210]	1125 [213]	-	-	-	175 [210]	-
1100	-	1550 [213]	-	-	-	-	-
1200	2.8 [210]	1475 [213]	1.95 [173]	1.33 [173]	0.62 [173]	160 [210]	-
Ti_3SiC_2-CDC	d (SAXS)	BET SSA (m^2/g)	V_{tot} (cm^3/g)	V_{meso} (cm^3/g)	V_{micro} (cm^3/g)	C_{H2SO4} (F/g)	C_{TEABF4} (F/g)
300	0.535 [181]	-	-	-	-	-	-
400	0.575 [181]	-	-	-	-	-	-
600	0.68 [181]	-	0.75 [214]	0.3 [214]	0.45 [214]	-	-
700	0.65 [181]	-	-	-	-	-	-
800	0.75 [181]	-	1.68 [214]	1.32 [214]	0.36 [214]	-	-
1000	0.65 [181]	-	-	-	-	-	-
1200	0.75 [181]	-	1.25 [214]	0.82 [214]	0.43 [214]	-	-

Table 1.5: CDC porosity (continued)

VC-CDC	*d (nm)*	*BET SSA (m^2/g)*	*V_{tot} (cm^3/g)*	*V_{meso} (cm^3/g)*	*V_{micro} (cm^3/g)*	*C_{H2SO4} (F/g)*	*C_{TEABF4} (F/g)*
500	0.6 [215]	1163 [215]	0.51 [215]	0.04 [215]	0.47 [215]	-	-
600	0.6 [215]	1266 [215]	0.57 [215]	0.039 [215]	0.53 [215]	-	-
700	0.6 [215]	1277 [215]	0.62 [215]	0.059 [215]	0.56 [215]	-	-
800	0.6 [215]	1286 [215]	0.65 [215]	0.06 [215]	0.59 [215]	-	-
900	0.7 [215]	1305 [215]	0.66 [215]	0.03 [215]	0.63 [215]	-	-
1000	0.75 [215]	864 [215]	0.5 [215]	0.1 [215]	0.4 [215]	-	-
1100	1.1 [215]	236 [215]	0.18 [215]	0.08 [215]	0.1 [215]	-	-

WC-CDC	*d (nm)*	*BET SSA (m^2/g)*	*V_{tot} (cm^3/g)*	*V_{meso} (cm^3/g)*	*$V_{micro-\alpha}$ (cm^3/g)*	*C_{H2SO4} (F/g)*	*C_{TEABF4} (F/g)*
700	1.27 [216]	474 [216]	-	-	0.26 [216]	-	-
1000	0.83 [216]	2036 [216]	-	-	1 [216]	-	-

TaC-CDC	*d (nm)*	*BET SSA (m^2/g)*	*V_{tot} (cm^3/g)*	*V_{meso} (cm^3/g)*	*$V_{micro-\alpha}$ (cm^3/g)*	*C_{H2SO4} (F/g)*	*C_{TEABF4} (F/g)*
700	0.82 [217]	1963 [217]	-	-	0.83 [217]	-	-
1000	0.83 [217]	2275 [217]	-	-	1.01 [217]	-	-

NbC-CDC	*d (nm)*	*BET SSA (m^2/g)*	*V_{tot} (cm^3/g)*	*V_{meso} (cm^3/g)*	*$V_{micro-\alpha}$ (cm^3/g)*	*C_{H2SO4} (F/g)*	*C_{TEABF4} (F/g)*
700	0.79 [217]	1864 [217]	-	-	0.78 [217]	-	-
1000	0.84 [217]	1721 [217]	-	-	0.78 [217]	-	-

Table 1.6: CDC porosity (continued)

HfC-CDC	*d (nm)*	*BET SSA (m^2/g)*	*V_{tot} (cm^3/g)*	*V_{meso} (cm^3/g)*	*$V_{micro-\alpha}$ (cm^3/g)*	*C_{H2SO4} (F/g)*	*C_{TEABF4} (F/g)*
700	0.79 [217]	1590 [217]	-	-	0.69 [217]	-	-
1000	0.86 [217]	1833 [217]	-	-	0.82 [217]	-	-
ZrC-CDC	*d (nm)*	*BET SSA (m^2/g)*	*V_{tot} (cm^3/g)*	*V_{meso} (cm^3/g)*	*V_{micro} (cm^3/g)*	*C_{H2SO4} (F/g)*	*C_{TEABF4} (F/g)*
350	0.76 [176]	500 [176]	0.225 [176]	0.225 [176]	0 [176]	-	-
400	0.74 [176]	500 [176]	0.225 [176]	0.224 [176]	0.001 [176]	-	-
600	0.8 [176]	875 [176]	0.475 [176]	0.45 [176]	0.025 [176]	80 [212]	-
800	0.85 [176]	1350 [176]	0.6 [176]	0.525 [176]	0.075 [176]	165 [212]	-
1000	1.21 [176]	1500 [176]	0.71 [176]	0.45 [176]	0.26 [176]	120 [212]	-
1200	1.41 [176]	1875 [176]	0.9 [176]	0.45 [176]	0.45 [176]	115 [212]	-

1.6.4.2. Effect of synthesis conditions

Increasing pore size with increasing synthesis temperature is a global trend for all CDCs (Table 1.3): TiC [179, 218, 219], B_4C [174, 210], ZrC [176, 210], and Ti_2AlC [210, 213] for example. In general, the starting carbide templates the initial pore size and then any range of average pore sizes from less than 1 nm to greater than 10 nm can be achieved by changing synthesis temperature. It was shown using Ti_3SiC_2-CDC synthesized in the 300ºC-1100ºC range that the pore texture changes considerably with synthesis temperature (Figure 1.26)[162]. The isotherms of low-temperature (600ºC synthesis temperatures and below) were all type I [220] in Brunauer classification indicating the

presence of only pores smaller than 2 nm. At synthesis temperatures above 600ºC, the isotherms were type IV, which shows the presence of pores larger than 2 nm. Considering the pore size distributions calculated using the Horvath-Kawazoe method, it can be seen that with moderate temperature control, the pore size can be tuned with sub-Angstrom accuracy (Figure 1.26). Also, the pore size distributions are narrower than that of even single-walled carbon nanotubes (SWCNT). This pore widening with increasing synthesis temperature comes about because of increasing carbon mobility with increasing temperature [221].

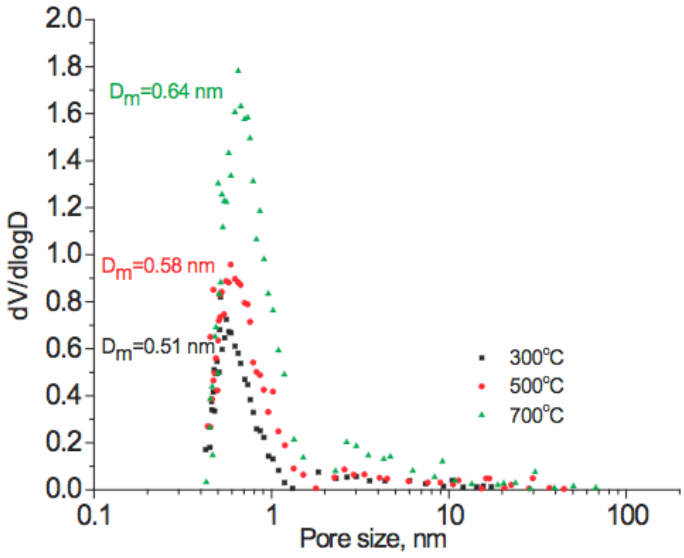

Figure 1.26: Pore size distributions from Ti_3SiC_2-CDC synthesized at 300ºC, 500ºC, and 700ºC showing the pore size is controllable with sub-Angstrom accuracy by selection of synthesis conditions [162].

Small angle X-ray scattering (SAXS) was used to corroborate porosity trends unveiled using gas adsorption techniques [162, 180]. SAXS detects density variations within the

samples and can probe pores much smaller than the 0.4 nm lower limit of gas adsorption techniques. CDC showed a monodisperse region of micropores and a lower Q region that depended systematically on the particular CDC under consideration. For rock-salt structures, TiC and ZrC, and sphalerite SiC, there is a first neighbor separation of ~0.4 nm and the SAXS profiles show narrow pore size distributions, while for rhombohedral B_4C with a larger and non-uniform nearest neighbor separation, the pore size distribution is much wider.

1.6.4.3. Effect of post treatment

Post treating CDC using physicochemical methods has been pursued in order to modify the pore texture and surface chemistry past what is achievable with chlorination alone. As CDC synthesis is a closed cycle process, it is easy to introduce post treatment gases to change porosity and surface chemistry. Considerable efforts have been given to increasing carbon pore size without compromising surface area for electrochemical capacitor applications [143]. In general, for activated carbons, widening pores is accomplished by increasing the amount of material burned during activation. As discussed above, by choosing different starting carbides and synthesis conditions, CDC can be made with very precisely tuned porosity. As the cost of some metal carbides is high, it is desirable to have some method to control the pore size of CDCs prepared from inexpensive precursors such as SiC. This is done by known methods such as exposing the carbon to an oxidizing environment at elevated temperature (activation).

A method was reported whereby CDC was produced from TiC and SiC and then subsequently treated in a water/argon mixture at 900ºC [222, 223]. This activation was found to increase the pore size, surface area and capacitance. Even though there is more complexity to the synthesis, this was a desirable method to increase the capacitance due to the fact that TiC and SiC are the least expensive carbides. Another method of pore widening involves infiltrating the pores with water and rapidly heating the infiltrated carbon above the temperature where water vapor etches carbon [224]. The objective of this method was to selectively widen only the smallest pores.

Arulepp reported an *in situ* technique of CDC activation whereby TiO_2 was mixed with TiC and chlorinated [225]. During synthesis, titanium in the TiO_2 was etched, leaving controlled amounts of oxygen to etch the carbon. It was shown that the oxidation treatment improved the volumetric capacitance but not the gravimetric capacitance. This was perhaps because of unreacted TiO_2 in the sample. The carbon was ideally polarizable at $E < 2.8$ V and showed a power density of 2.5 kW kg^{-1}.

Hydrogen treatment has been explored as a method to improve performance in a number of applications. It was shown that a treatment at 800ºC in 5% H_2/Ar increased performance of CDC coatings for tribological applications [226]. It was postulated that the mechanism responsible was due to passivation of surface with C-H bonds and elimination of high-energy dangling bonds and reactive groups. Hydrogen annealing was also shown to be beneficial for hydrogen storage. H_2 annealing at 600ºC increases surface area and pore volume by removing chlorine trapped in pores after synthesis without greatly changing the pore size distribution [179]. This increased hydrogen storage above

3 wt.% at 77 K and 1 atm. It was also shown that H_2 treatment increased hydrogen storage by up to 75% for some other CDC materials [227]. This was believed to occur because hydrogen effectively cleaned small pores of residual chlorine and metal chlorides, increasing both the volume of the smallest pores and specific surface area. This can be appreciated by considering that up to 40 wt.% chlorine has been observed in as-produced Ti_3SiC_2-CDC samples [228] at low synthesis temperatures.

1.7. Conclusions

The study of ion motion in charged confined environments presents a problem of both practical and scientific importance. Increasing EC performance by understanding the charge storage mechanisms and then designing a material system harnessing these findings is key to realizing these and future applications.

Double-layers have been known for over 100 years, but traditional models do not effectively describe the double layer. In the ionic channels in cells [229] or the small-diameter pores of electrochemical double-layer capacitors (EDLCs) [16], ions are in a very confined situation, which is different from that of a planar solid/electrolyte interface. Gaining better understanding of the physical nature of the double-layer in confined environments could have importance from supercapacitors to treating ion channel diseases such as cystic fibrosis, migranes and epilepsy, as well as selective filtering of liquids, water desalination, amongst others.

Controlling the carbon microstructure crucial for maximizing EDLC performance and probing fundamental double-layer processes inside of pores. Currently, EDLC

performance cannot be predicted in terms of surface area alone, which many authors have attributed to pores that are too small to be efficiently accessed by electrolyte ions but still contribute to surface area measured by gas sorption. However, some researchers have found that the narrowest pores contribute the largest to energy storage. Therefore, to probe this apparent contradiction in the effect of pore size on capacitance, we need a material that can offer good property (porosity) control without altering surface chemistry.

CDC allows sub-Angstrom control of pore size, with an average size being tunable between ~3 nm to ~0.5 nm. Because of the closed synthesis procedure, CDC also offers a low content of functional groups. Previously, the high performance of CDC was reported in many applications, including EDLCs, but an explanation as to why this occurs is still lacking.

2. Objectives

Objective 1: Produce a well-characterized series of CDC samples with controllable pore size having average width tailored between significantly smaller than the solvated ion size to significantly larger than the solvated ion size and use them to study ion/pore size correlations

Objective 2: Study the electrochemical behavior of a wide range of CDC samples in aqueous electrolytes and more technologically important non-aqueous electrolytes to determine the effect of varying pore size on performance

Objective 3: Understand mechanisms of ion adsorption and ion/solvent/solid interactions upon charging nanoporous electrodes

Objective 4: Use knowledge gained to intelligently design higher performance nanostructured electrodes.

3. Experimental

3.1. Materials

3.1.1. CDC precursor carbides

3.1.1.1. Powder

CDC powders were produced from a variety of metal carbides, B_4C (Alfa Aesar, #40504, 1-7 μm particle size), SiC (Superior Graphite, #1200, 0.7 μm particle size), TiC (Atlantic Equipment Engineers, #Ti-302, 1-5 μm particle size), and ZrC (Sigma Aldrich, #336351, 5 μm particle size). The powders were used as-produced, with no pre-treatments prior to chlorination. Average particle sizes of all the carbides used were similar, as to rule out effects from diffusion paths that are too long for proper electrolyte penetration. Ti_2AlC (3-ONE-2) was received in bulk form and ground into powder using a drill press and a mortar/pestle. No further characterization of the carbide precursors was done.

3.1.1.2. Bulk

To produce bulk CDC samples. TiC sputtering targets were purchased from Angstrom Scientific and cut to size (12 mm x 6 mm x 0.3 mm) using a diamond saw. Each sample was then mounted to an aluminum polishing stud using superglue. Once set, the samples were polished on one side using a Struers MD Piano grinding disc (until plane), followed by a MD Allegro fine grinding disc with 9 μm diamond suspension followed by polishing with 3 μm diamond suspension, and finally 1 μm diamond suspension. Once polished the

samples were removed from the studs by sonicating in isopropanol for a few seconds then cleaned.

3.1.2. CDC synthesis

3.1.2.1. Powder

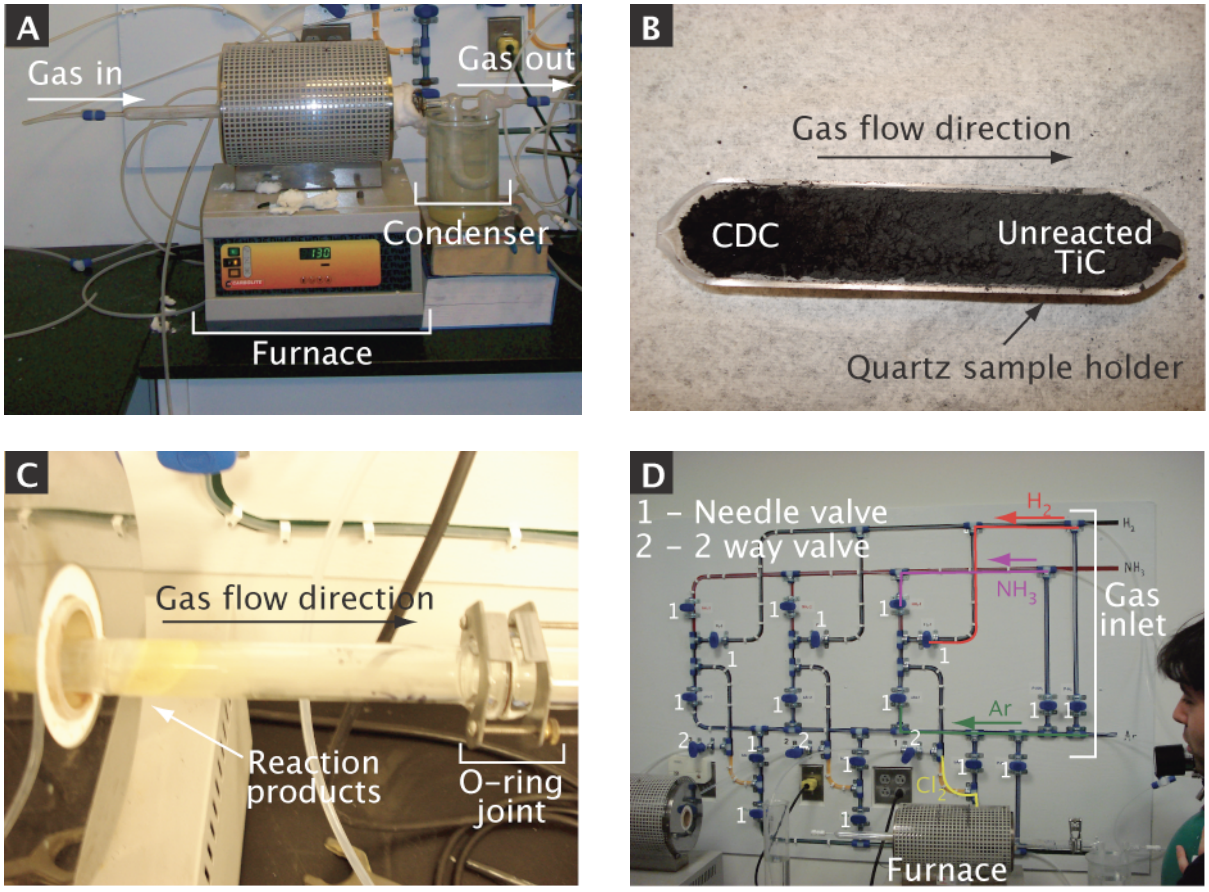

Figure 3.1: a.) Assembled chlorination setup. b.) Partially chlorinated TiC-CDC in a quartz sample boat. c.) Close-up of the furnace exit showing deposition of yellowish solid on the quartz tube as well as the o-ring joint. d.) Gas setup allowing up to 3 simultaneous experiments as well as better control over gas leaks and potential hazards.

The chlorination setup (Figure 3.1a) consisted of a Carbolite horizontal tube furnace with a maximum temperature of 1200ºC, inside of which a quartz tube was placed, one side having an o-ring connection (Figure 3.1c) to a glass condensor placed in a water bath, the other side being tapered to ¼" OD to mate with Swagelok tube fittings connected to ¼" OD PTFE tubing. The gas was bubbled though sulfuric acid to prevent any backflow of atmosphere, after which the gasses were scrubbed of chlorine by reacting with saturated potassium hydroxide solution, forming a multitude of potassium chlorates, instead of chlorinating our exhaust hood. Carbide powder (2 g) was weighed, placed into a quartz boat (Figure 3.1b) and loaded into a horizontal quartz tube furnace (Figure 3.1a). Argon was flushed through the furnace at 150ºC for 1 h to remove any oxidizing species from the setup, after which the furnace was heated to the desired temperature under argon flow. Once the desired temperature was reached (400-1200ºC), chlorine was passed through the furnace for 3 h. Excess chlorides that are vapor at elevated temperature were collected in the condenser downstream. It should be noted that the chlorides for zirconium are solid at room temperature, so other strategies needed to be devised for chlorinating them. The best success was had using a 125 cm long tube with as much exiting the furnace downstream as possible. This allows a large volume for the chlorides to solidify into, instead of clogging the PTFE tubes and causing mini disasters. After chlorination, the furnace was again flushed with argon for 1 h at the temperature of chlorination to remove excess chlorine and chlorides. Hydrogen was passed though the furnace at 600ºC for 90 minutes to remove and remaining chlorine and chlorides from the

developed pore network of the CDC powder and passivate the surface against functionalization after the samples are in atmosphere. Samples were cooled under argon flow and transferred into sealed glass vials once the tube was cool enough to handle.

3.1.2.2. Bulk

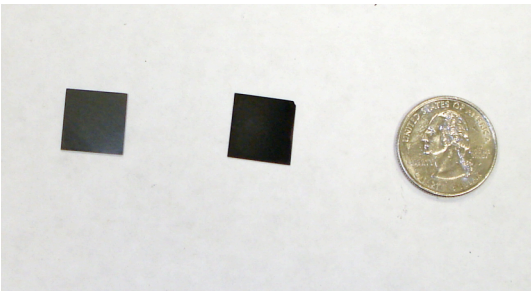

Figure 3.2: From L to R, unchlorinated bulk TiC-CDC, chlorinated TiC-CDC and a quarter for scale.

Bulk samples (Figure 3.2) were chlorinated using the same basic setup (Figure 3.1a) as used for powder CDCs. A special quartz fixture was designed to hold the bulk pieces with their polished face perpendicular to the flow of chlorine. All bulk pieces were chlorinated at 500ºC for varying times (10 s – 5 min) to give coatings in the range of ~1 µm to 150 µm. CDC along the edges and backside was carefully removed by polishing with 800 grit SiC paper and the thickness was estimated by viewing the edges under an optical microscope. After electrochemical testing the thickness was measured accurately by dicing the samples with a diamond saw, mounting them and polishing the cross section using the same procedure described in Section 3.1.1.2.

3.1.3. Electrolytes

3.1.3.1. Aqueous

Various aqueous electrolytes were used in this study: H_2SO_4 (Sigma Aldrich, #320501), KOH (Sigma, #60130), LiCl (Sigma Aldrich, #62478), NaCl (Sigma, #S7653), KCl (Sigma-Aldrich, #P9333), CsCl (Sigma-Aldrich, #289329), and RbCl (Aldrich, #215260). In all cases the solvent used was ultrapure DI water (18.2 MΩ-cm) obtained from the microfabication facility at Drexel University. Salts were used as-received. As ECs require high specific currents, saturated electrolyte solutions were used to maximize conductivity, minimizing *iR* drops. If the cell design permitted it, the electrolyte was degassed during the testing by bubbling a slow stream of argon (AirGas, UHP Grade) though the electrolyte. If the cell design did not permit this, the electrolyte was degassed prior to putting it in the cell.

3.1.3.2. Non-aqueous

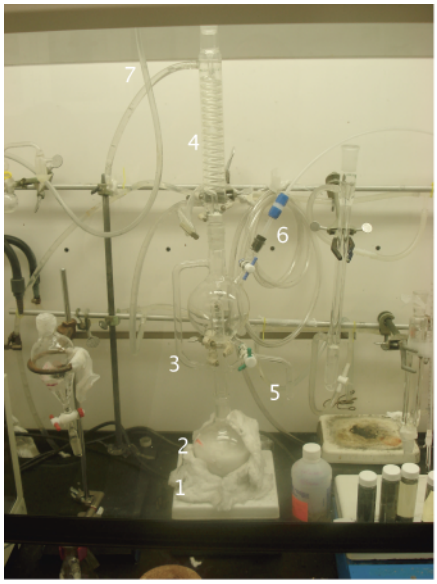

Figure 3.3: Distillation setup for purifying acetonitrile. 1 – Heating mantle, 2 – 500 mL round bottom flask, 3 – Distillation glassware, 4 – Condenser, 5 – Distillate collection, 6 – Gas inlet, 7 – Gas exit.

Tetraethylammonium tetrafluoroborate (TEA BF_4) was weighed into 15 g aliquots and dried in a vacuum oven at 90ºC for 24 h before being transferred into a glovebox (<5 ppm H_2O, nominally). The dried salt was sealed into glass vials once inside of the glovebox where it could stay until it was needed. Acetonitrile was distilled in 50 mL aliquots using the protocol outlined in Lange's Handbook [230] and transferred into the glovebox. Electrolyte solution was prepared as-needed in quantities commensurate with the cell being used. This painstaking protocol was the result of years of having cells contaminated with water. A glovebox 5 years my elder always made sure to spring a near

impossible to find leak at the most inopportune times and required constant babying. But this way works.

3.2. Methods

3.2.1. CDC microstructure and properties

3.2.1.1. Raman microspectroscopy

Both powder and bulk CDC samples were analyzed by Raman microspectroscopy using an Ar ion laser (514.5 nm) at 500x magnification (2 μm spot size). For analysis of the data, the Raman peaks were deconvoluted into 2 bands with a Gaussian distribution, the D-band (~1350 cm^{-1}) and the G-band (~1580 cm^{-1}). The ratio of the area under each curve, termed the I_D/I_G ratio gives a measure of graphene crystallite size and was used as a diagnostic to probe low-level graphitization. From prior work, we know that all CDCs are amorphous, non-graphizable carbon made of small and very distorted sp^2 clusters and no real stacking in the z-direction, but the size of these crystallites probably varies.

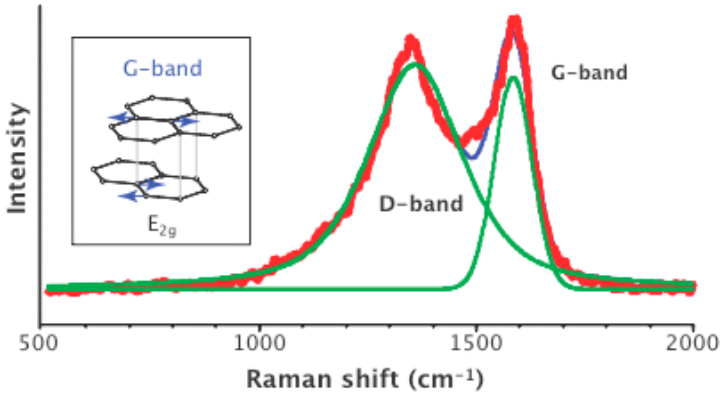

Figure 3.4: Raman spectra of CDC showing deconvolution of D and G bands

In general, the in-plane crystal size of graphite L_a (nm) can be calculated by the Tuinstra and Koenig equation, $0.44/L_a=I_D/I_G$, but in the case of CDC, the extreme amorphous nature makes this empirical relation not hold.

3.2.1.2. TEM

High resolution transmission electron microscopy (HRTEM) was used to investigate the structure of numerous powder CDCs. TEM was done by Prof. Davide Mattia (University of Bath), Prof. Gleb Yushin (Georgia Tech) and Ms. Patricia Reddington (Drexel). The TEM samples were prepared by a 1-min sonication of the CDC powder in isopropanol and deposition on a lacy-carbon coated copper grid (200 mesh). A field-emission TEM (JEOL 2010F) with an imaging filter (Gatan GIF) was used at 200 kV.

3.2.1.3. Scanning electron microscopy (SEM)

SEM was conducted on both powder and bulk CDC samples. SEM samples for powder samples were prepared by sticking CDC to an aluminum sample holder with carbon tape. CDC was conductive enough that no sputtering was necessary. Bulk CDC samples were attached to the aluminum sample stud with carbon tape as well. The resolution of SEM was too small to visualize porosity in the samples, but allowed visualization of any inclusions or impurities as well as interfaces between carbide and CDC as well as other features in the bulk samples.

3.2.1.4. Conductivity measurements

Conductivity was measured on CDC powders using a specially-constructed conductivity cell. To allow electron percolation through the powder, it was compressed at 15 kPa. To eliminate effects from contact resistance between the metal probes and carbon powder, separate probes, which are equally spaced from one another, were used for delivering current and measuring voltage. Prior to compressing the powder and measuring conductivity, the face of the probe was polished with 800 grit SiC paper.

With the 4-point probe setup, having separate current driving probes and infinite impedance voltage measuring probes allows elimination of contact resistance between the metal electrodes and carbon powder. If the sample size is semi-infinite compared to the probe spacing, *s*, in both diameter and thickness, the resistivity can be calculated by:

$$\sigma = 2\pi s \frac{V}{I} \tag{3.1}$$

where V is the measured voltage and I is the applied current. Currents were controlled in the range of 25 mA to 200 mA and voltage was measured in ~50 mA steps. If the sample cannot be considered semi-infinite, then correction factors need to be accounted for.

Initial work was conducted on commercially available activated carbon and multi walled carbon nanotubes (MWCNT), both from Arkema (Figure 3.5). The fixture was loaded with different thickness of powder from ~2 mm to ~10 mm and tested. Care was taken to ensure that the powder was flat in the text fixture and tamped down as good as possible. From Figure 3.5, it is evident that as the thickness of the powder increased, the

conductivity increases and saturates. This is most likely due to better packing of powder in thicker samples, as opposed to increased electron percolation paths, because initially the powder thickness is at least ten times greater than the probe spacing. The values that the curve saturate at are close in value to the quoted specifications of the materials, ~150 S-cm^{-1} and ~1 S-cm^{-1} for Arkema MWNTs and activated carbon, respectively.

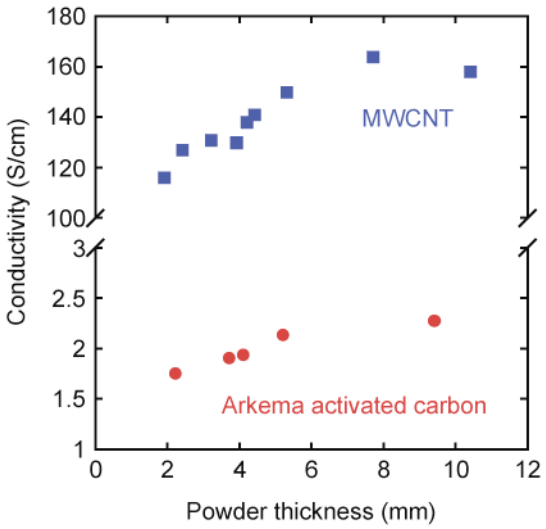

Figure 3.5: Conductivity of MWNTs and activated carbon for different thicknesses of poweder in the text fixture

As conductivity was a function of sample size, it was unavoidable to need to test several thicknesses of sample, but, in general, sample sizes thicker than ~5 mm seemed to represent the bulk properties sufficiently well.

3.2.1.5. Porosity measurements

Argon sorption was performed using an Autosorb-1 (Quantachrome Instruments) from relative pressure, P/P_0, of 10^{-6} to 1 to assess porosity and surface area data. Porosity analysis was carried out at liquid nitrogen temperature, -195.8ºC, on samples outgassed for at least 12h at 300ºC using a Quantachrome Autosorb-1. The outgassing protocol used was sufficient to remove condensed water and vapors [231, 232]. Nitrogen adsorption did not produce reliable results on samples with a pore size smaller than 1 nm.

The total pore volume was calculated from Ar adsorption isotherms at a relative pressure of 0.95. Specific surface area (SSA) was calculated according to the BET (Brunauer, Emmet and Teller) theory [233]. The BET theory assumes multilayer adsorption of gasses in determining surface area, which is certainly hindered in pores close to the atomic dimension of the adsorbate molecule, resulting in, most likely, an underestimation of the real surface area. As this is, by far, the most commonly used technique for determining surface areas, we felt comfortable in using it. For analyzing porosity, Quantachrome Instruments non-Local Density Functional Theory (NLDFT) software Autosorb V.1.50, assuming slit-shaped pores was used. This is the most advanced technique currently available for assessing porosity over the range of ~0.4 nm to ~10 nm, as verified by small-angle x-ray scattering (SAXS) measurements [234].

3.2.2. Experimental techniques and instrumentation for electrochemistry

3.2.2.1. Electrochemical instrumentation

Galvanostatic cycling was performed usign a Solartron Analytical 1287A potentiostat/galvanostat at different current densities from 5 mA/cm² to 100 mA/cm² between the initial cell potential upon assembly to the decomposition voltage of the electrolyte. The ESR was determined from the voltage drop after reversing current polarity at the maximum voltage using Ohm's law

$$R = \frac{\Delta V}{i} A \tag{3.2}$$

Where ΔV is the voltage drop over 1 ms, i is applied current and A is the are of an electrode. The capacitance of an electrode was calculated from a V-t plot using

$$C = 2\frac{i}{m\frac{dV}{dt}} \tag{3.3}$$

where $\frac{dV}{dt}$ is the slope of the discharge curve and m is the mass of one electrode (including the mass of any conductive additives and/or binders). The factor of 2 comes in because there are 2 capacitors in series (and this is what everyone in literature does – so either you comply or report values half as large!). In some cases, volumetric capacitance was also calculated. This was done by simply normalizing by the bulk volume of an electrode instead of the mass.

CVs were done by controlling the cell voltage and sweeping it at a constant rate (5 mV s^{-1} to 100 mV s^{-1}) between predefined limits (usually 0 V and slightly less than the decomposition potential of the electrolyte) using a Gamry PCl4/750to characterize the electrolyte stability window and also to gain an understanding of mechanisms. In the cyclic voltammogram, as the material approaches a pure capacitor, its current response becomes progressively more rectangular, and eventually capacitance becomes independent of linear modulation of potential in time *(dV/dt)* [16]. In this case, current can be calculated by finding the area enclosed by the curve I(V) and dividing by the voltage window scanned.

$$C = \frac{|Q|}{V} \tag{3.4}$$

$$C = \frac{|I_a - I_c|}{2\frac{dV}{dt}} \tag{3.5}$$

where I_a and I_c are anodic and cathodic current respectively, Q is the charge integrated under the voltammogram V is the voltage window and dV/dt is the scan rate (V/s).

EIS was performed on 2-electrode cells at a DC bias of 0-2.3 V by applying a 10 mV RMS sine wave at frequencies varying from 10 kHz to 10 mHz. The resulting signal was separated into a real (Z') impedance, which is completely in phase with the applied signal and imaginary (Z") impedance, which is 90º out of phase with the applied signal. High frequency data was used to characterize resistive portions of the cell and low frequency data was used to understand slower processes, such as hindered ion motion in narrow pores.

3.2.2.2. Cell construction

One of the key essentials in testing electrochemical capacitors is understanding how to construct a proper electrochemical cell on a lab scale [235, 236]. As evidence of this, an entire PhD was spent optimizing the interface between the current collector and electrode film. Further evidence are improper conclusions in literature that were made simply because a poor cell design influenced the results. In what follows, I will outline the steps I used to optimize our lab cells.

Nominally, the ideal is to produce, at the lab scale, a cell that provides maximum performance with the maximum amount of components being reusable and non-complicated assembly [111].

The experimental cell design evolved throughout the duration of this work. The main factors of merit governing this evolution are a progression in ease of use and performance. Because of the large power required for electrochemical capacitors, large currents are required, which mean that any intrinsic cell resistances need to be minimized. In industry, this is achieved by using specialized packaging equipment and large electrodes, a situation that isn't necessarily amenable to studying electrode materials that may only be available in a few milligram quantities. It is therefore of utmost importance to understand how the cell can influence results and design to minimize any of these potential difficulties.

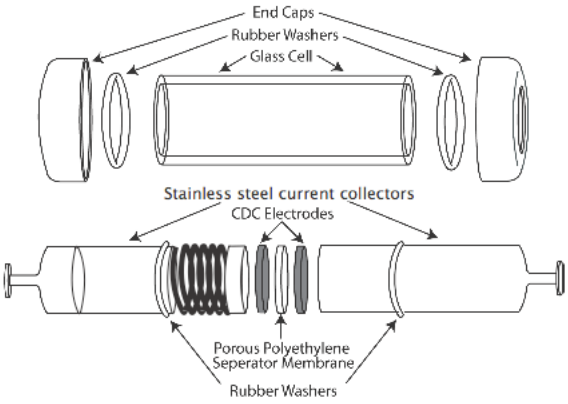

Figure 3.6: a.) Schematic of experimental cell design 1.

The first successful cell design (Figure 3.6) was developed by Prof. John Fischer [237] at the University of Pennsylvania for testing lithium battery and consisted of 1 cm^2 stainless steel current collectors housed inside of a hermetic glass cell. The electrode stack was kept under pressure by a spring that was located inside of the cell. To improve contact resistance, the face of each current collector that contacted the electrodes was polished prior to assembly to remove any surface oxides. The current collectors were stable in both aqueous and organic electrolytes, but because they were specially fabricated and limited in quantity, extensive pretreatments such as those employed by commercial electrochemical capacitor manufacturers could not be used. Likewise, pressure on the electrode stack was limited because of the combination of springs and plastic end caps – if stiffer springs were used the end caps would fracture, but less stiff springs would give lower performance at high current density. Therefore, power characteristics were not comparable to what one would expect in commercial cells, but the characteristics at low or moderate current density in both 1 M H_2SO_4 and 1 M $TEABF_4$ in acetonitrile were reasonable (Figure 3.9). From Figure 3.9, as current density is increased, the specific

capacitance decreases as Ohmic resistances limit electron percolation throughout the active material. At current densities of 5 mA cm^{-2} the measured capacitance in both electrolytes was comparable to what was achieved with more advanced cell designs and the manufacturer's quoted capacitances of 75 F g^{-1} and 140 F g^{-1} for Kuraray BP20 and Kuraray YP17 activated carbons, respectively.

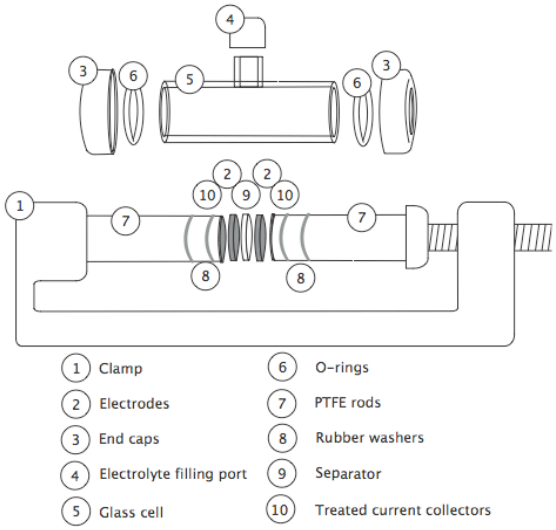

Figure 3.7: a.) Schematic of experimental cell design 2.

To allow higher pressure on the electrode stack and reasonable simplicity in current collector treatments, the cell was modified as shown in Figure 3.7. The springs were replaced by a clamp, which could apply higher pressures. Cell design #2 also replaced large stainless steel current collectors that were needed to keep the stack under pressure with a combination of electrochemically inert PTFE rods and 1 cm^2 metal foil current collectors that could be treated to allow better contact with the electrodes. To connect the

current collectors to an external circuit, wires of the same alloy were spot welded to the backside of the current collector and fed through a hole in the center of the PTFE rod. In practice, however, this spot welding proved to be the Achilles Heel of the cell, with many spoiled cells because of wires pulling off of the current collectors. Adding an electrolyte filling port to the cell allowed putting it together dry, which significantly simplified assembly. Performance was better at higher current densities than Cell design #1, as shown in Figure 3.9. Decreasing the amount of metal in the current collector, increasing the pressure on the stack, allowing for current collector pretreatments as well as assembling the cell prior to filling with electrolyte provided a more robust cell, but the number of spoiled tests encouraged a further evolution in cell design.

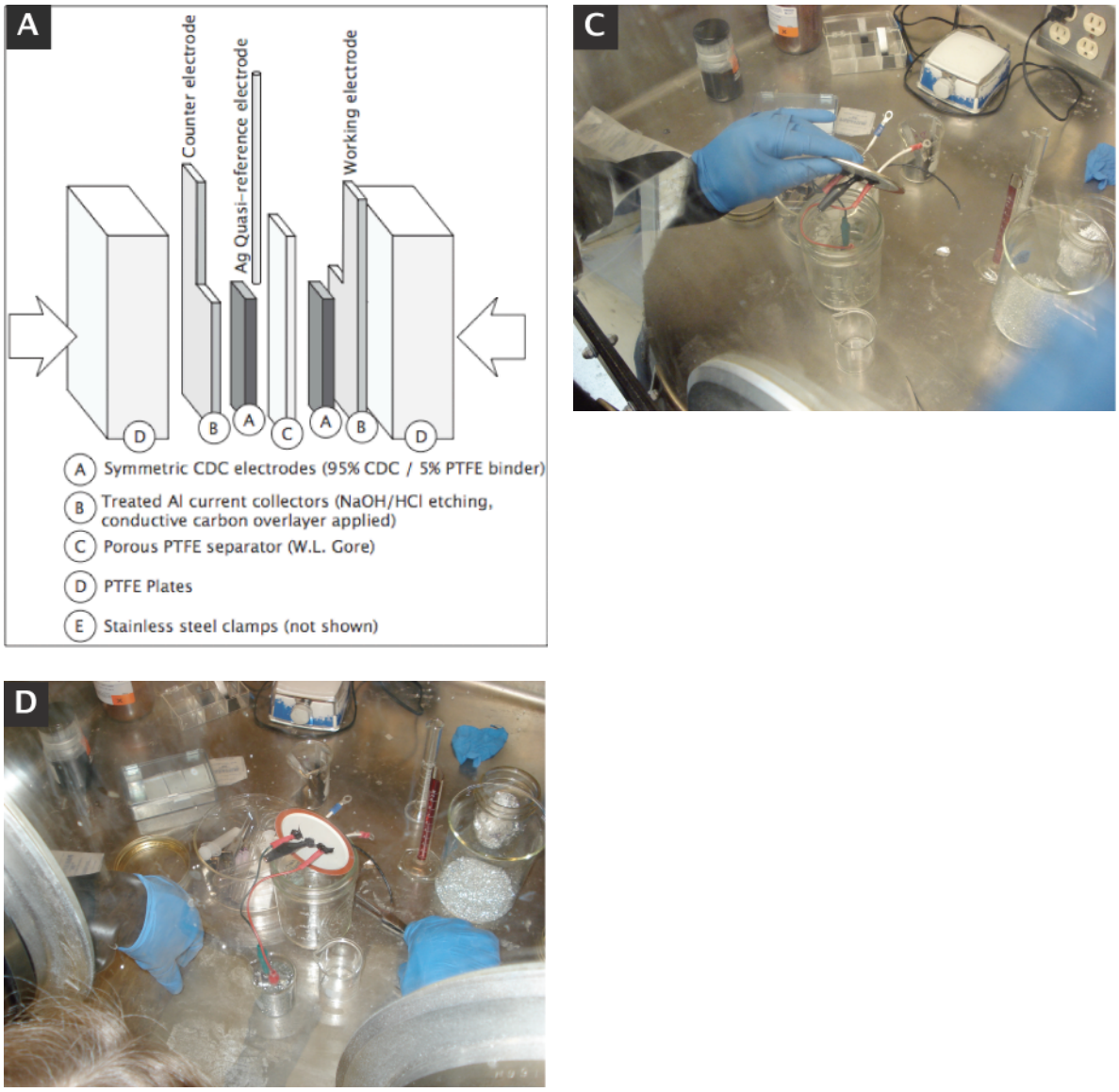

Figure 3.8: a.) Schematic of cell design 3. b.) Homemade airtight environmental chamber with electrical feedthroughs. c.) Assembled cell before placing in environmental chamber and removing from the glovebox.

Cell design #3 (Figure 3.8) took the advances in cell design #2 and simplified assembly by removing the need to spot weld contacts and enlarged the current collectors to 4 cm^2

to further simplify assembly inside of a glovebox. Enlarging the current collectors also had the added benefit of improving the contact between the electrode and current collector, decreasing the overall ESR of the cell. This design is similar to cells used by Prof. Patrice Simon (University Paul Sabatier) and developed by Dr. Cristelle Portet during her thesis. Performance of Cell Design #3 was extremely good, with capacitance in both aqueous and organic electrolytes exceeding the manufactures specifications and very good performance at high current densities (Figure 3.9). Assembly was also greatly simplified and cell spoilage was only a matter of separator failure causing short circuiting or contaminated electrolyte, factors both present in prior cell designs.

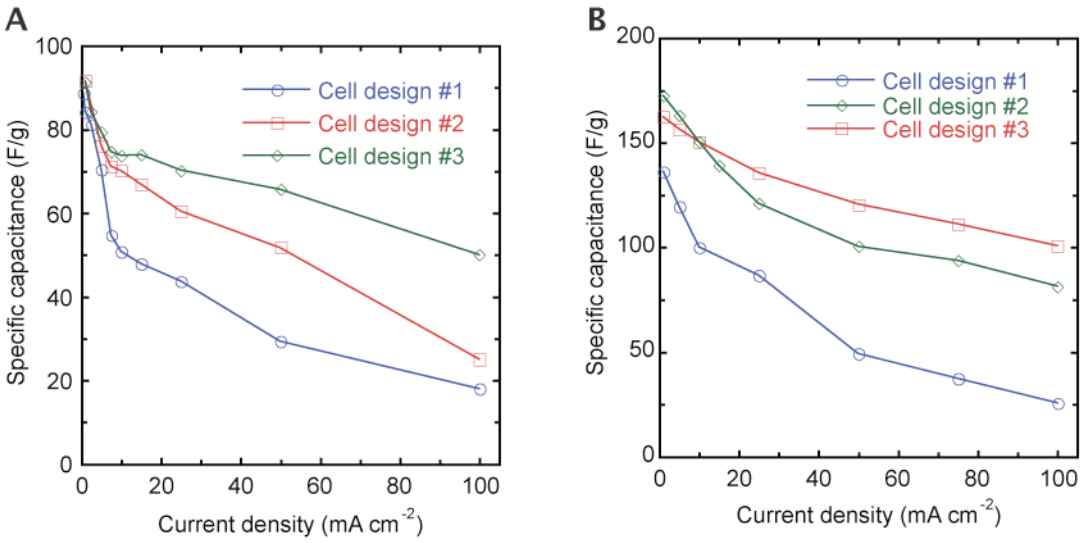

Figure 3.9: Evolution of capacitance with current density for different cell designs in a.) 1M $(CH_3CH_2)_4NBF_4$ in acetonitrile electrolyte and b.) 1M H_2SO_4 electrolyte

3.2.2.3. Binder studies – PVDF vs PTFE

To construct a robust electrode amenable to processing, a small amount (typically 5-50%) of fluorinated polymer binder, polytetrafluoroethylene (PTFE) or polyvinylidene fluoride (PVDF) is added. The requirements of the binder are that it is plastic (or can become fibrous when "worked"), and is non-interacting with any of the cell components. Processing of electrodes utilizing PTFE or PVDF binders is slightly different, but the general idea is the same – distribute the binder evenly among the carbon and then knead the mixture until it is "right." In practice, however, the processing is different. For PTFE-bound electrodes, processing is as follows: 1.) a solution of PTFE dispersed in water (Adrich) is weighed and added to a pre-weighed amount of carbon in a beaker. 2.) The carbon/PTFE mixture is diluted with ethanol, taking care to rinse any binder that accumulated on the beaker (it will look like a white haze) into the mixture. 3.) The mixture is stirred at room temperature for at least 1 hour. During this time, any binder that accumulates on the beaker at the solution surface must be rinsed into the solution with ethanol. 4.) The solution is heated to 80ºC while stirring to evaporate the ethanol. During the evaporation, any binder that accumulates at the solution surface should be washed into the mixture with ethanol. Enough extra ethanol should be added that the evaporation process takes at least an hour. 5.) Once the mixture is nearly dry, it should be taken off the hotplate and allowed to cool. When sufficiently cooled enough to handle, the carbon is then scraped from the beaker onto a sheet of clean glass. 6.) A small amount of ethanol is added to the carbon to wet it and it is kneaded with a clean spatula. Kneading should continue until the carbon forms a pliable mass, the consistency of

chewing gum. 7.) Once the carbon is of proper consistency, it is rolled into a film of ~200-250 μm thickness. The film should be self-supporting and crack/hole free. If there are any cracks or holes, the films is folded onto itself and re-rolled. This process continues until the film is of proper thickness/consistency. 8.) The film should be dried on the glass in an oven at 80ºC. If the electrodes crack during drying, repeat steps 6-8. 9.) Electrodes are then cut to the proper size to fit in the electrochemical cell and weighed. At this point they should be heavier than desired. Re-measure the thickness and calculate the thickness to reach the desired mass. 10.) Add a small amount of ethanol, roll the electrodes to the desired thickness and re-cut them to the desired shape. Re-dry and re-weigh. It should be noted at this point that it is always easier to remove electrode material to reach a smaller mass than add electrode material to reach a larger mass.

To produce PVDF-bound electrodes, the following procedure is used. 1.) Carbon and PVDF are weighed into a beaker. 2.) Isopropanol is added to the mixture and it is stirred at room temperature for at least 2 hours. 3.) The mixture is placed on a hotplate and stirred until it reaches the consistency of motor oil. Excess isopropanol is added to ensure it is heated for at least 1h. 4.) A film of ~200 μm is cast onto a sheet of clean glass using a doctor blade. 5.) The film is allowed to dry at room temperature. If the film cracks during drying, steps 2-5 should be repeated. 6.) Once dry, the film is removed from the glass very carefully using a sharp blade. If the film is brittle during removal and cannot be removed as one coherent piece, steps 1-6 should be repeated. 7.) Electrodes of proper size are cut and weighed. The thickness required for the proper mass is then calculated.

The electrodes are slightly wet with ethanol and rolled to the proper thickness, cut, re-dried and re-weighed until they are of the proper mass and size.

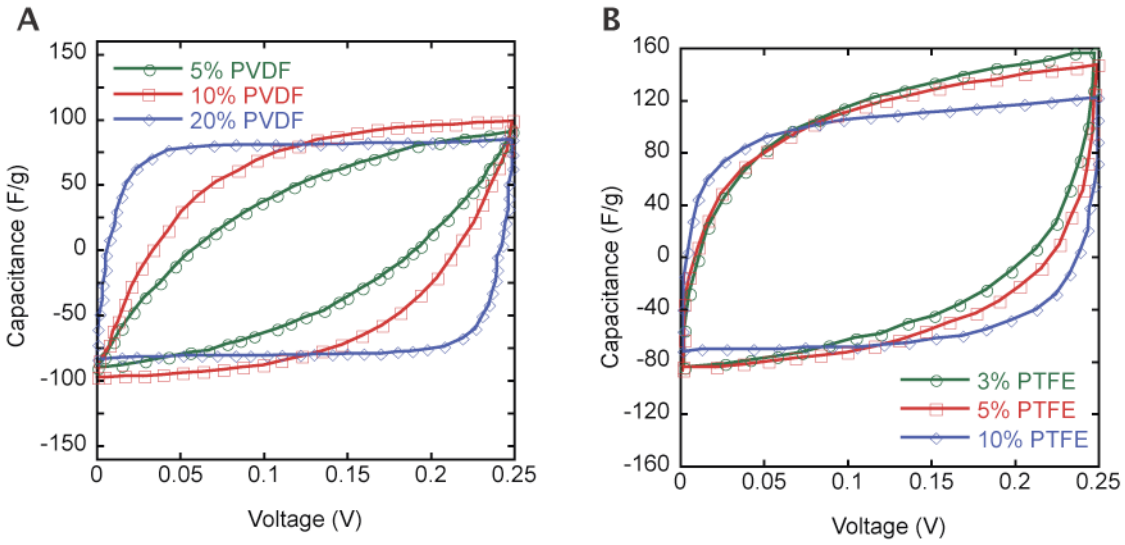

Figure 3.10: Cyclic voltammograms conducted at a scan rate of 10 mV s^{-1} in 1M H_2SO_4 of electrodes constructed of Kurarray BP 20 with different amounts of a.) PVDF binder and b.) PTFE binder.

Tests were conducted to determine the optimum amount of PTFE and PVDF for high capacitance and high conductivity electrodes. Electrodes were made from 5%, 10%, and 20% PVDF and 3%, 5%, and 10% PTFE. 3% PTFE and 5% PVDF were the lowest amount of binder that could be feasibly used and still construct a robust enough electrode for electrochemical testing. From Figure 3.10 it is evident that for all amounts of both PVDF (Figure 3.10 a) and PTFE (Figure 3.10 b), the voltammograms are capacitive in

nature, indicating no Faradaic influence from either binder. For PVDF (Figure 3.10 a), there is very poor performance at a scan rate of 10 mV s^{-1} with only 5% PVDF added. Likewise, constructing electrodes from 5% PVDF is very difficult and required reworking the electrodes many times. Adding 10% PVDF made the electrode processing slightly easier, but the electrodes still needed to be reworked multiple times. Their performance exceeded performance found using only 5% PVDF in terms of both measured capacitance (integrated charge divided by voltage scanned) and series resistance. Using 20% PVDF resulted in the best electrodes, in terms of both performance and ease of production.

PTFE was also studied as a binder material for electrochemical capacitor electrodes (Figure 3.10 b). It was found that 3% was the minimum amount of binder that could be used and still make an electrode that was self supporting. Unlike PVDF, however, producing electrodes with PTFE is slightly easier, because the consistency of the carbon and binder is monitored the entire time it is being worked into an electrode. The quality of a PVDF-bound electrode is not known until after it is cast, dried and released from the glass. 3% PTFE resulted in a CV that had lower resistance and higher capacitance than 10% PVDF (Figure 3.10 b). Increasing the amount of PTFE increased the ease of electrode processability and decreased the series resistance. The specific capacitance (in terms of electrode mass) decreased when the PTFE content increased to 10%, however.

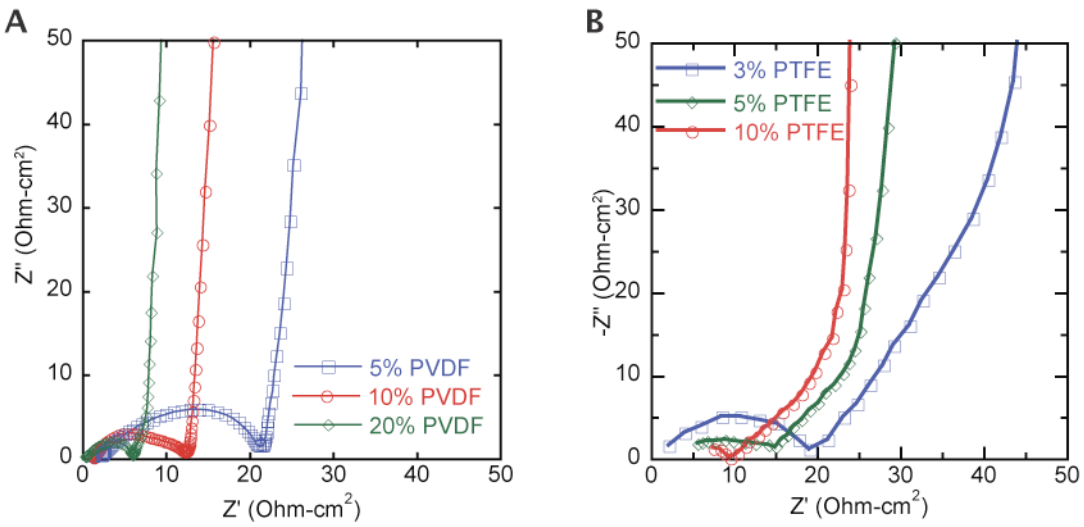

Figure 3.11: Nyquist plots for Kuraray BP20 electrodes constructed with different amounts of a.) PVDF binder or b.) PTFE binder.

Electrochemical impedance spectroscopy was also used to characterize the effect of different amounts of PVDF (Figure 3.11 a) and PTFE (Figure 3.11 b). From the intersection of the low frequency region with the Z'-axis, the series resistance of the cell can be determined. From Figure 3.11, the ESR decreases with increasing binder content for both PTFE and PVDF binders. Because the PTFE-bound electrodes were more pliable, they made better contact with the electrodes, which resulted in lower characteristic time constants (results not shown). This is evident in the more "electrochemical capacitor-like" Nyquist plot for the PTFE-bound electrodes, which have a very pronounced region with a 45º slope and low frequency region with a slope close to vertical. The PVDF-bound electrodes transition from a semi-circle to near vertical

without passing through a 45º region because very low frequencies need to be reached before the cell becomes capacitive.

Because of the ease of processability, low binder content needed, and good performance, both in AC and DC conditions, 5% PTFE was selected as the optimum amount and type of binder for characterization of materials for electrochemical capacitors.

3.2.2.4. Conductive additives

If lower conductivity materials are being used, conductive additives (typically carbon black) can be added in small fractions (typically < 30%) to improve power performance [238]. Like the binder, any conductive additive must be non-interacting with any of the cell components. The effect of adding 10% carbon black, which is a typical conductive additive for low-conductivity materials in batteries, such as the cathode materials in Li-ion batteries, was studied in 5% PTFE-bound electrodes.

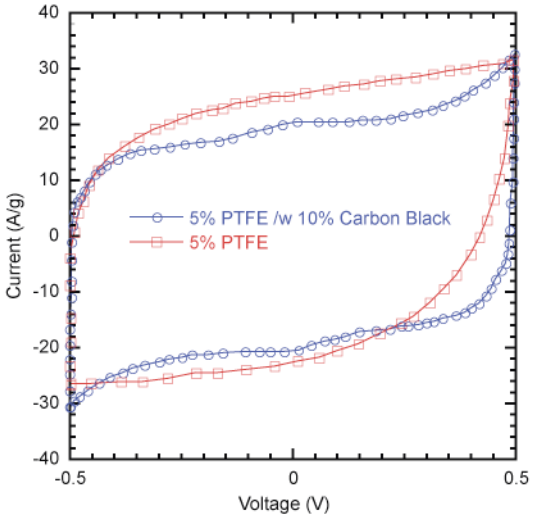

Figure 3.12: CVs of Kuraray BP20 in 1M H_2SO_4 taken at 15 mV/s showing the effect of conductive additives to PTFE-bound electrodes.

Figure 3.12 shows cyclic voltammograms that highlight the effect of adding 10 wt.% carbon black to 5% PTFE-bound Arkema activated carbon electrodes, which is a low-performing, low conductivity carbon. The CV becomes less resistive with the carbon black additive, but the capacitance also decreases, even though the scan rate is moderate. Because the electrode with conductive additive has lower resistance, at higher scan rates, there is expected to be a transition it would eventually have better performance. For more conductive activated carbons, such as those typically used in electrochemical capacitors, this effect would be further marginalized. It was therefore decided that conductive additives would not be required for our cells and only carbon and binder were used.

3.2.2.5. Current collector optimization

Choice of current collector materials and their optimization are probably the next most important issue in an electrochemical capacitor besides the electrode materials. They must be sturdy enough to ensure good mechanical robustness, extremely conductive, and as electrochemically inert as possible in the electrolyte of choice. As an example of how different electrolytes require different current collectors, compare Figure 3.13 and Figure 3.14. Figure 3.13 shows cyclic voltammograms of an activated carbon in a sulfuric acid electrolyte with both stainless steel (Figure 3.13 a) and aluminum (Figure 3.13 b) current collectors. From the voltammograms, it is apparent that there is essentially no capacitance at high scan rates in acidic electrolytes using aluminum current collectors, while stainless steel still gives moderate performance. The reason for this is simple, aluminum strongly corrodes in sulfuric acid, especially at the electrode/current collector interface, which ruins the contact and prevents charge transfer to and from the electrode.

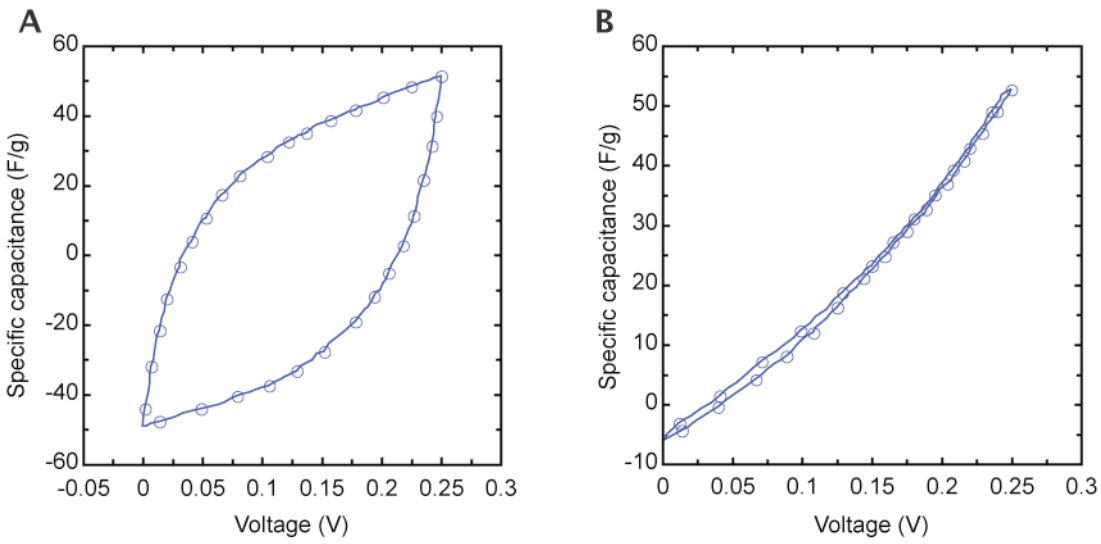

Figure 3.13: Cyclic voltammograms of Arkema activated carbon taken at a scan rate of 100 mV s^{-1} in an aqueous 1M H_2SO_4 electrolyte using a.) stainless steel current collectors and b.) aluminum current collectors.

In contrast, Figure 3.14 shows how capacitance changes with aluminum or stainless steel current collectors as a function of current density in organic electrolyte that does not attack the electrodes. Aluminum current collectors are, in general, most desirable because they can be etched to produce an extremely high surface area for very intimate contact with the electrode. The capacitance is therefore higher in cases where aluminum can be used, such as organic electrolytes and ionic liquids because there is better charge transfer to the electrode.

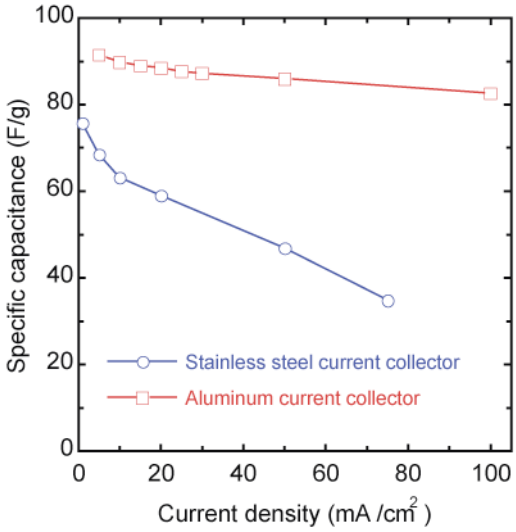

Figure 3.14: Evolution of capacitance with current density for Kuraray BP20 activated carbon in a $TEABF_4$ electrolyte using both stainless steel and aluminum current collectors

Unfortunately, there is poor adherence between carbon and bare metal current collectors, so care must be taken to prepare the current collector surface. Complex electrochemical etching treatments are seen as ideal and are commonly used in industry, sometimes coupled with electrodeposition of some other metal, in order to maximize adherence and minimize the effect of surface oxides. For both stainless steel and aluminum current collectors [239, 240], I used the following current collector treatment, 1.) The current collectors were cut to size and mechanically roughened using 240 grit SiC paper. 2.) The sized current collectors were degreased by ultrasonicating in ethanol for 5 minutes, minimum. 3.) The surface was then etched in a solution of 1 M NaOH for 10 minutes at room temperature then rinsed with DI water. 4.) Immediately following the NaOH etch, the current collectors were further etched for 10 minutes in 1 M HCl at 80ºC then rinsed with DI water. 5.) The current collectors were then dried in vacuum at 80ºC for 15 minutes to avoid re-growing a thick surface oxide layer. 6.) Once dry, the current

collectors were painted with a home-brewed conductive paint consisting of an epoxy base, ethanol carrier and 30% carbon black as the conductive agent. The thinnest coating of paint was used to maximize conductivity while still protecting the current collector surface. 7.) After painting, the current collectors were dried under vacuum at room temperature.

The effect of these treatments can be seen in Figure 3.15. The current collector that only had surface oxides removed by mechanically sanding had ESRs in excess of 10 Ω-cm^2 in both organic (Figure 3.15 a) and aqueous (Figure 3.15 b) electrolytes. By skipping the current collector etching treatment and painting the collectors immediately after sanding, the ESRs were decreased by approximately a factor of 2. The entire current collector treatment protocol allows at least a factor of 10 decrease in ESR and was used for the entirety of the work presented on CDC.

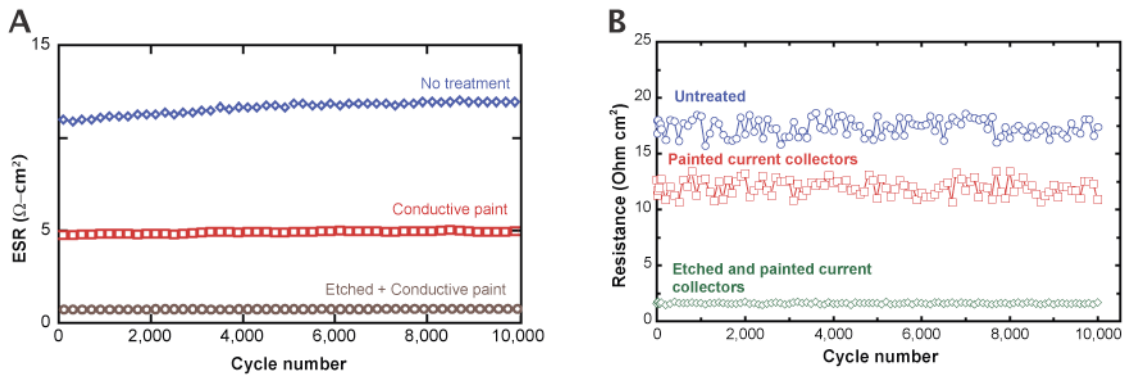

Figure 3.15: The change of equivilant series resistance with cycling at 20 mA cm^{-2} for different current collector treatments in a.) TEA BF_4 in acetonitrile with aluminum current collectors and b.) 1 M H_2SO_4 with 446-stainless steel.

3.2.2.6. Cavity microelectrode technique (CME)

3.2.2.6.1. Microelectrode construction

Microelectrodes were constructed by first sealing a 0.25 mm diameter platinum wire inside a hollow glass capillary (Figure 3.16 a). The sealed face was ground smooth with 600 grit SiC paper and finally polished with 3µm and 1µm diamond suspension. To produce a cavity in the microelectrode for housing the active material, the Pt was etched back into the polished face using aqua-regia at 80ºC. To make a connection with the potentiostat, a copper or silver wire was inserted into the capillary and a connection was made with the Pt wire by either dropping a small amount of mercury down the capillary or by spot welding. Finally, the Ag or Cu wire at the unsealed end of the capillary was immobilized with quick set epoxy. After fabrication, the volume of each microelectrode

cavity was estimated using optical microscopy. An image of 3 identical microelectrodes is shown in Figure 3.16 b.

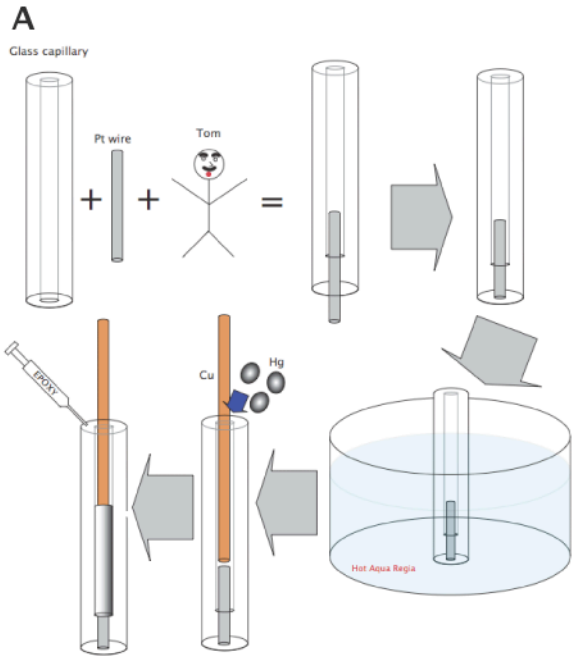

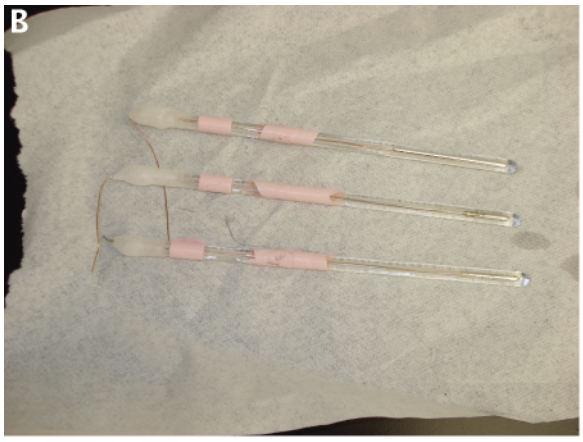

Figure 3.16: a.) Schematic showing the construction of microelectrodes. b.) Images of assembled microelectrodes.

3.2.2.6.2. Microelectrode characterization

Microelectrode cavities were filled with CDC by firmly pressing the electrode tip into a small amount of active material. Excess active material was removed by gently pressing the electrode tip onto a fresh Kimwipe to ensure a flat bottom electrode. Before testing the active materials, a scan of the empty microelectrode cells was performed to estimate background currents from the instrumentation and cell. Roughly 40 electrochemical

measurements were performed for each material to estimate the reliability of the CME technique. Any values reported are thus from a statistically significant sample set and give us high confidence in the results.

After loading the microelectrode with active material, it was inserted into a cell with an 8 cm^2 Pt counter electrode and an Ag/AgCl reference electrode. The electrolyte consisting of 1M H_2SO_4 was purged with ultra high purity argon for 10 minutes prior to testing to remove dissolved gases. CDC powders were tested using cyclic voltammetry (Gamry PCl4/750) with scan rates ranging from 5 mV/s to 5 V/s over a voltage window of -0.2 V to 1 V vs. Ag/AgCl. Volumetric capacitance of the powders was calculated by dividing the measured capacitance by the volume of the cavity recorded with a caliper and optical microscope (±5 μm accuracy).

To study the utility of CME for screening porous electrochemical capacitor materials, a set of CDC samples with a wide range of capacitance values was measured both with the CME and in traditional cells and the results were compared. Samples were selected that spanned the largest range of capacitance to show that the technique is sensitive over all ranges.

Cyclic voltammograms of TiC-CDC using the CME in 1M H_2SO_4 are capacitive in nature as shown in Figure 3.17. Note that currents arising from CDC-loaded microelectrodes are at least 1 order of magnitude greater than that of an empty microelectrode (Figure 3.17 inset). The currents from CDC loaded CME cells can be assumed to be free of artifacts attributable to the cell itself.

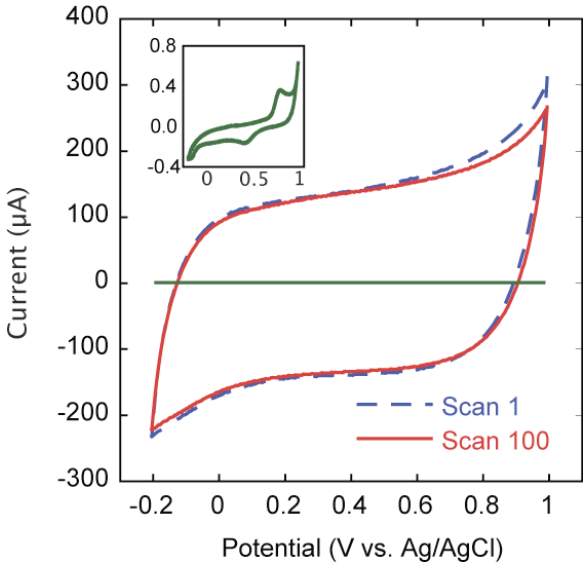

Figure 3.17: Cyclic voltammetry of TiC-CDC synthesized at 600°C post-treated in H_2 after 1 and 100 cycles for a CME cell; Scan rate = 2 V/s. Inset: cyclic voltammogram of the empty CME cell.

Figure 3.18a shows the cyclic voltammograms of TiC-CDC synthesized at different temperatures recorded at a lower scan rate than the one used in Figure 3.17; all the CVs are capacitive and very little distortion is found. Figure 3.18b shows that current measured using the microelectrode technique and volumetric capacitance measured by the traditional technique follow the same trends. In the synthesis temperature range of 600ºC to 1000ºC, TiC-CDC reaches the highest volumetric capacitance when using the traditional technique, and the maximum current, as measured using the CME technique at the same synthesis temperature. The values obtained using the traditional technique are in good agreement with those previously measured which shows that the CME can be used to highlight the same trends as previous studies, albeit with far less effort [241]. For the

same synthesis temperature, the same trend was observed for ZrC CDC exhibiting a maximum capacitance of about 80% of the TiC CDC one (Figure 4.39). The effect of annealing the TiC-CDC samples in ammonia at 500ºC for 15 minutes is also shown using both techniques. In both cases, ammonia annealing serves to decrease the current response to an almost constant value for the TiC-CDC synthesized at 600ºC and 800ºC. The microelectrode study was further extended to include B_4C-CDC synthesized at 500ºC, which was expected to have poor electrical conductivity and was difficult to measure in a conventional cell. The poor electrochemical performance of this sample was demonstrated via CME and traditional configuration. Moreover, it is important to mention that the CME study of CDC produced from SiC and ZrC (Figure 4.39) in addition to TiC and B_4C, synthesized at temperatures of 500°C to 1000°C took just 2 days of work compared to 4 weeks for studying the same materials with the traditional technique. Therefore, samples spanning a wide range of capacitance were able to be accurately described using the CME technique, showing its applicability in screening studies for materials for electrochemical capacitors. Moreover, the amount of deviation between electrodes was observed to be within 10-15%, the range typically observed in conventional electrochemical capacitor cells. The main limitation of the CME technique lies in the impossibility to determine with accuracy the mass of the active material prior to testing, but studying large numbers of samples to generate statistically relevant average data is a means around this.

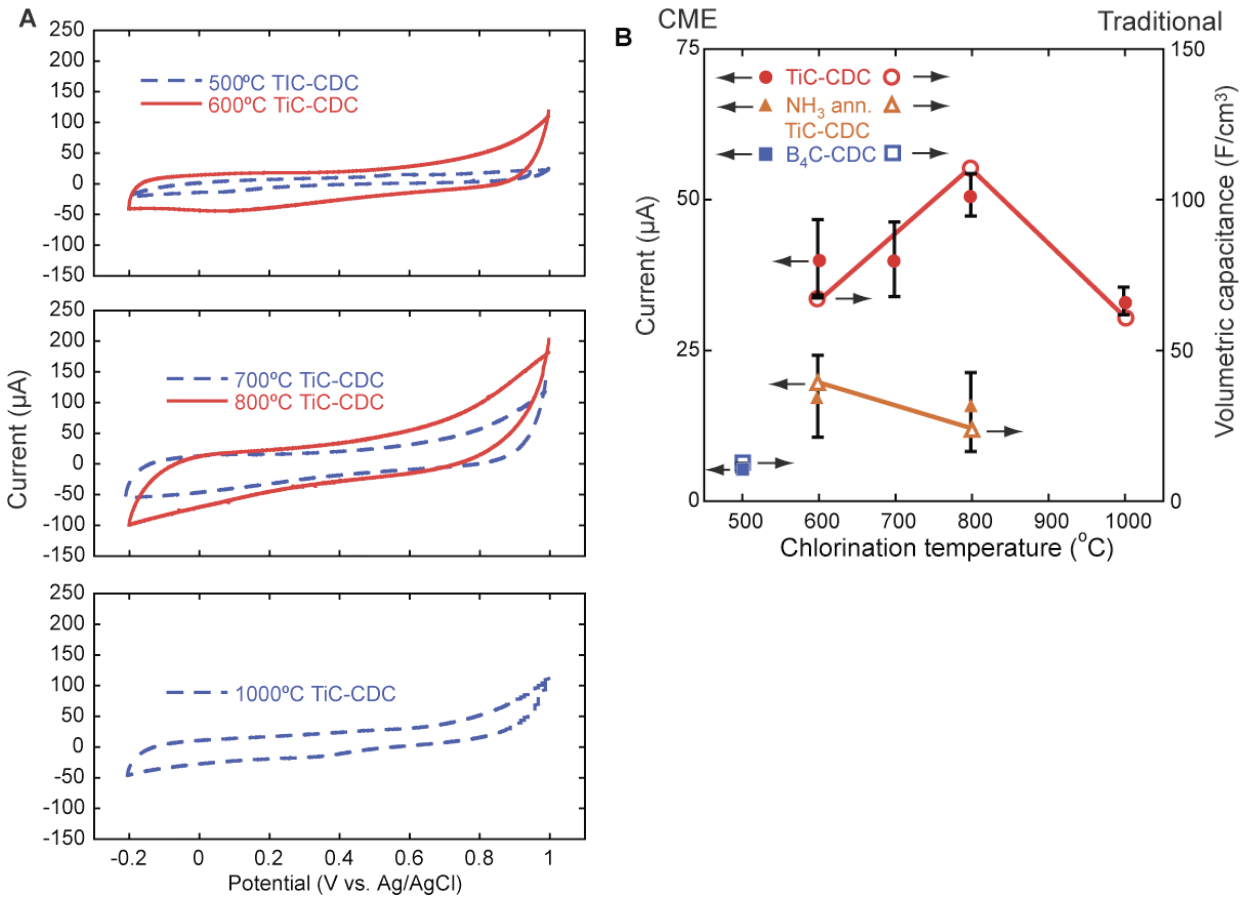

Figure 3.18: a.) Cyclic voltammograms of TiC-CDC at 50 mV/s for CME cell. b.) Capacitive currents and specific capacitance vs. chlorination temperature. CDCs analyzed using traditional cells (open symbols) and microelectrodes (closed symbols).

To rule out the possibility of material loss during cycling, 4 microelectrodes were scanned for 100 times and the average current of each cycle was calculated. The CV from the first and 100th cycle can be seen in Figure 3.17. Figure 3.19 shows the capacitance normalized by the capacitance calculated from the first cycle. During the first 5 cycles,

there is a very small (~1%) increase in current that is within the error of the technique, which may be the result of increased ion permeation into the porous carbon network. The results also show that there is very little decrease in the average current (~2%), which is again within the error of the technique, and any further decrease is more likely attributable to ageing rather than material loss.

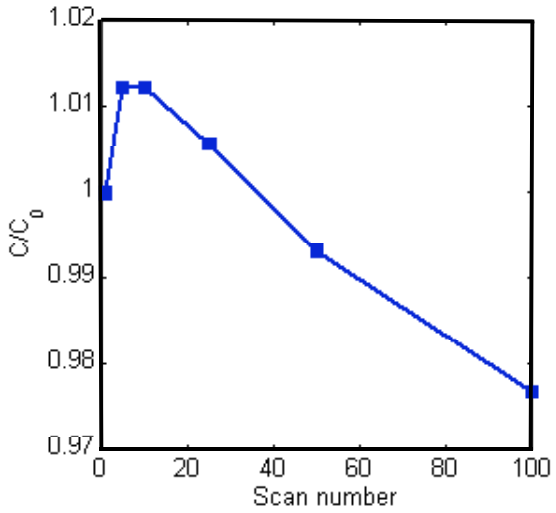

Figure 3.19: Plot of capacitance variation with scan number calculated at a scan rate of 3 V/s in a CME cell; capacitance normalized by the capacitance at cycle 1 (C_0).

The effect of the cyclic voltammetry scan rate on the measured current was determined for the CME cells. Figure 3.20 shows a linear dependence of the average current on the scan rate up to at least 1 V/s, indicating a purely capacitive behavior up to a much higher

scan rate achievable on traditionally processed cells. This demonstrates that the technique does not impart any undesirable characteristics on the test and allows high scan rates without degradation in performance. In traditional EDLC electrode assembly, corrosion of current collector, separator membrane resistance, and large *RC* constant prevent high scan rate measurement. With poor electrode optimization in the traditional case, this could potentially skew results towards materials with higher conductivity and obscure the true effect of the material pore structure on capacitance. Capacitance loss and average current variation related to the limitation of the carbon material, cannot give information on the performances such as gravimetric capacitance, resistance, ageing or self-discharge of a real device.

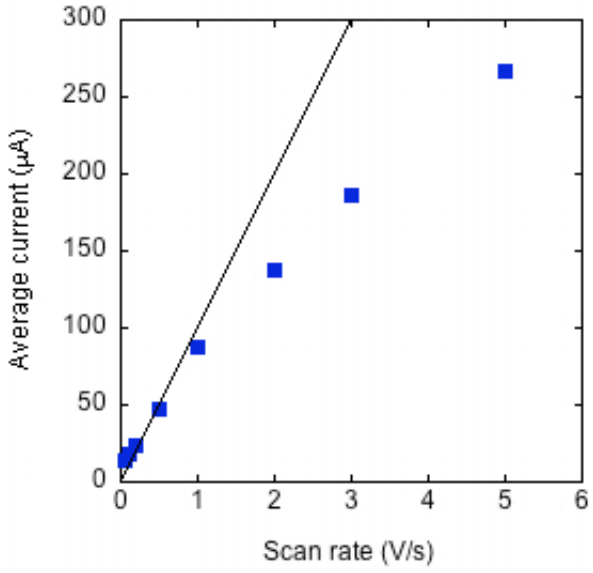

Figure 3.20: Dependence of the average current on scan rate as observed on different CDC samples tested using CME.

4. Results

4.1. CDC microstructure and properties

4.1.1. Effects of hydrogen annealing

As was previously discussed, the presence of surface functionalities, though shown to increase capacitance [139], obscures the relation between carbon pore size and capacitance. Also, residual chlorine and chlorides can potentially react with cell components and diminish performance. Therefore, hydrogen annealing was pursued to passivate the surface and remove any residual chlorine and chlorides.

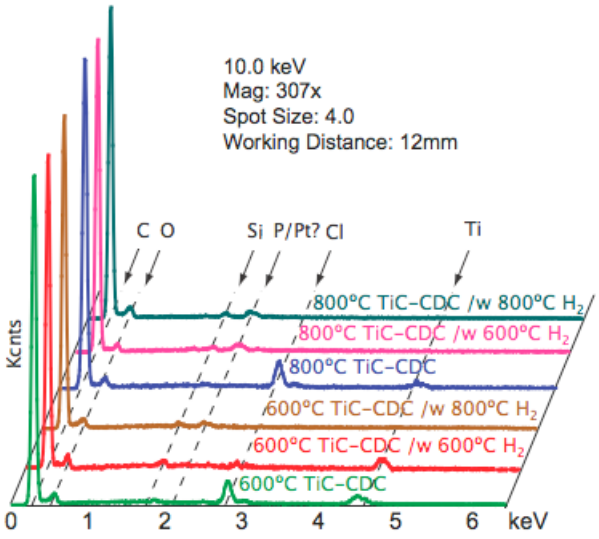

Figure 4.1: Energy dispersive spectroscopy spectra obtained for TiC-CDC chlorinated at subjected to different treatments in hydrogen.

Figure 4.1 and Table 4.1 show the elemental composition of TiC-CDCs chlorinated at moderate temperatures and subjected to hydrogen annealing at 600ºC and 800ºC for 2 h. All samples are predominantly carbon with very few impurities, as detected by EDS. The unannealed 600ºC TiC-CDC and 800ºC TiC-CDC have a large fraction of chlorine remaining after synthesis (~9 at.% and ~12 at.%, respectively). In a device, this chlorine can potentially lead to degradation in performance so removing it is seen as beneficial. Hydrogen annealing CDC samples for 2h at 600ºC was previously explored by Dash [209] and Hoffman [242] as a route to remove chlorine and passivate the surface. Likewise, Arulepp et al. [243] use hydrogen annealing at 800ºC for an undisclosed time to remove chlorine from their samples . Therefore, the effect of hydrogen annealing at 600ºC and 800ºC was explored.

Table 4.1: Chemical compositions as determined by energy dispersive spectroscopy for 600ºC TiC-CDC and 800ºC TiC-CDC with different hydrogen treatments.

Sample ID	*At. % C*	*At. % O*	*At. % Si*	*At. % P/Pt*	*At. % Cl*	*At. % Ti*
600ºC TiC-CDC	86.03	2.67±1.52	0.26±0.39	0.08±0.21	9.04±2.54	1.92±2.43
600ºC TiC-CDC // 600ºC H2	94.39	2.31±2.09	0.54±0.48	0.04±0.09	0.84±1.21	1.88±0.52
600ºC TiC-CDC // 800ºC H2	97.19	1.84±1.05	0.09±0.11	0.03±0.07	0.57±0.78	0.28±0.44
800ºC TiC-CDC	82.73	2.89±2.04	0.16±0.13	0.09±0.02	11.82±3.18	2.31±0.83
800ºC TiC-CDC // 600ºC H2	95.52	2.09±0.43	1.23±0.82	0.75±0.59	0.31±0.12	0.10±0.03
800ºC TiC-CDC // 800ºC H2	97.3	1.82±0.91	0.03±0.51	0.07±0.09	0.27±0.31	0.51±0.31

Hydrogen treating at both 600ºC and 800ºC for 2 hours serves to decrease the amount of chlorine in both 600ºC and 800ºC TiC-CDC to levels below the sensitivity limit of EDS (Table 4.1). Hydrogen treating at 800ºC seems to remove hydrogen better than treating at 600ºC, but from Figure 4.1, no peaks for Cl can be noted for any of the annealed samples, save a very minor peak in the case of the 600ºC H_2 annealed 600ºC TiC-CDC sample.

The effect of hydrogen annealing on carbon microstructural evolution was also tracked using Raman microspectroscopy. The I_d/I_g ratio for unannealed TiC-CDC decreases in increasing the synthesis temperature from 600ºC to 800ºC (Figure 4.2a). This indicates increasing order. Hydrogen annealing at 600ºC and 800ºC has no effect on the I_D/I_G ratio of 800ºC TiC-CDC, but in the case of 600ºC TiC-CDC, there is definite ordering with an 800ºC H_2 anneal.

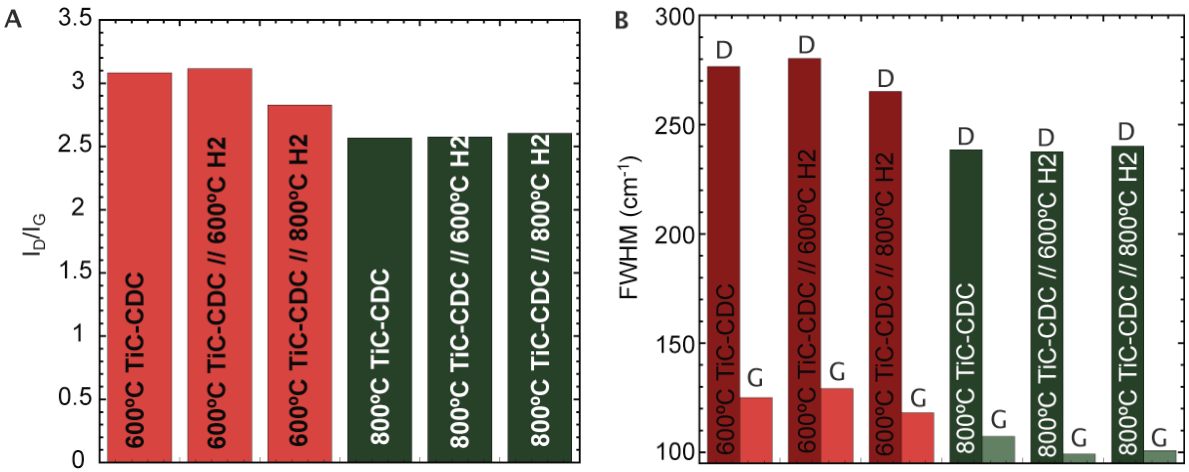

Figure 4.2: a.) I_D/I_G ratio for 600ºC and 800ºC TiC-CDC samples with different hydrogen annealing treatments. b.) FWHM

Therefore, for the duration of this work, hydrogen annealing at 600ºC was performed because it had the combination of not modifying the microstructure and removing trace amounts of chlorine.

4.1.2. TEM analysis of CDC powders

Transmission electron microscopy (TEM) was performed on all the CDC families studied. For example, see Figure 4.3, which shows the microstructural evolution of TiC-CDC and ZrC-CDC chlorinated in the temperature range of 600ºC to 1200ºC. As TEM was done on the edges of the samples, however, we must remember that the bulk microstructure may differ slightly from what we are visualizing in the micrographs. Figure 4.3 shows representative TEM micrographs highlighting structural changes in CDC depending on the precursor and synthesis conditions. For samples synthesized at low temperatures (Figure 4.3 a,d) the micrographs show a very amorphous material with little to no long range order evident. As the synthesis temperature increases to 800ºC (Figure 4.3 b,e), curved structures become evident, but the material is still largely amorphous and no stacked graphite ribbons are evident. This ordering trend continues up to synthesis temperatures of 1200ºC (Figure 4.3 c,f), but there is still no large-scale graphitization and the microstructure lacks any long-range ordering.

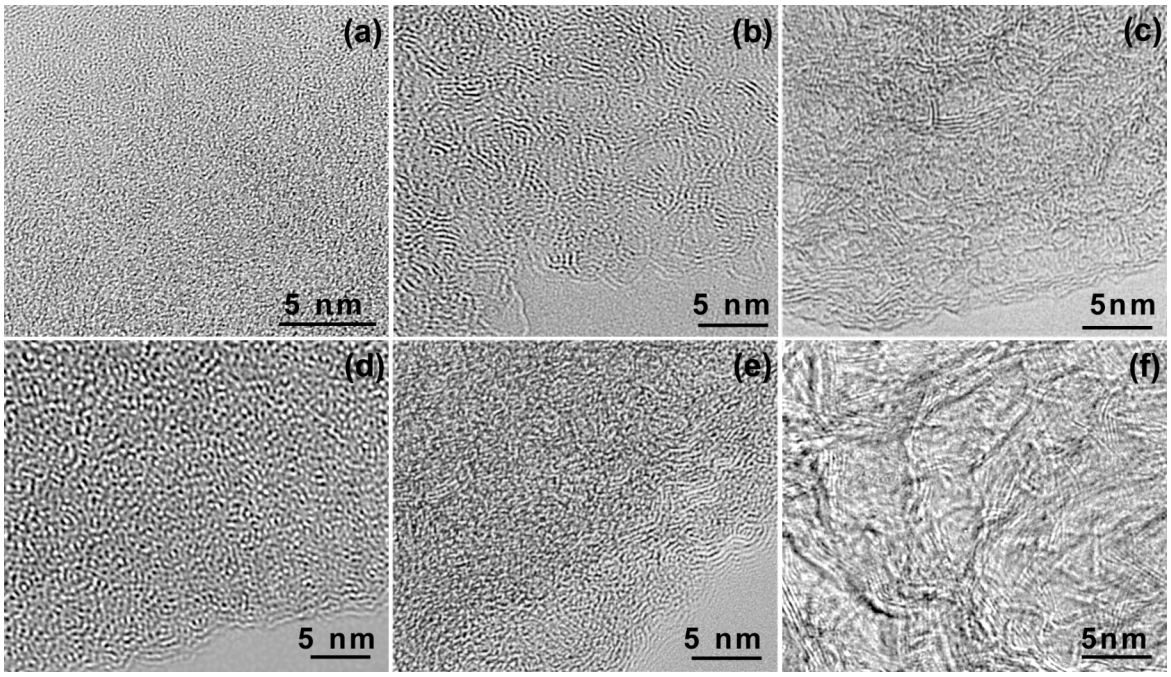

Figure 4.3: TEM micrographs of TiC-CDC synthesized at a.) 600ºC, b.) 800ºC, c.) 1200ºC and ZrC-CDC synthesized at d.) 600ºC, e.) 800ºC and f.) 1200ºC. TEM was performed by Gleb Yushin. [241]

4.1.3. Raman microspectroscopy analysis of CDC powders

Microstructural evolution can also be probed using Raman microscopy. For CDCs produced from TiC, ZrC, Ti_2AlC, and B_4C, there is a decreasing I_D/I_G ratio (Figure 4.4 a) and decreasing FWHM of the D and G bands (Figure 4.4 b) indicating increasing ordering as seen in TEM (Figure 4.3). In general, CDCs produced from all precursors follow the same trend in microstructural evolution. At synthesis temperatures less than 800ºC, the I_D/I_G ratio decreases slightly, between 800ºC and 1000ºC there is a large drop in the I_D/I_G ratio and between 1000ºC and 1200ºC, there is again only a minor drop.

There is less of a well-defined trend observed for the FWHM, though all CDCs show the same general behavior, decreasing FWHM with increasing synthesis temperature, indicating increasing ordering. Because CDC produced in the temperature range studied here is X-Ray amorphous, any data shows only diffuse scattering around ~20º and did not lead to major understandings [163], so it is not shown.

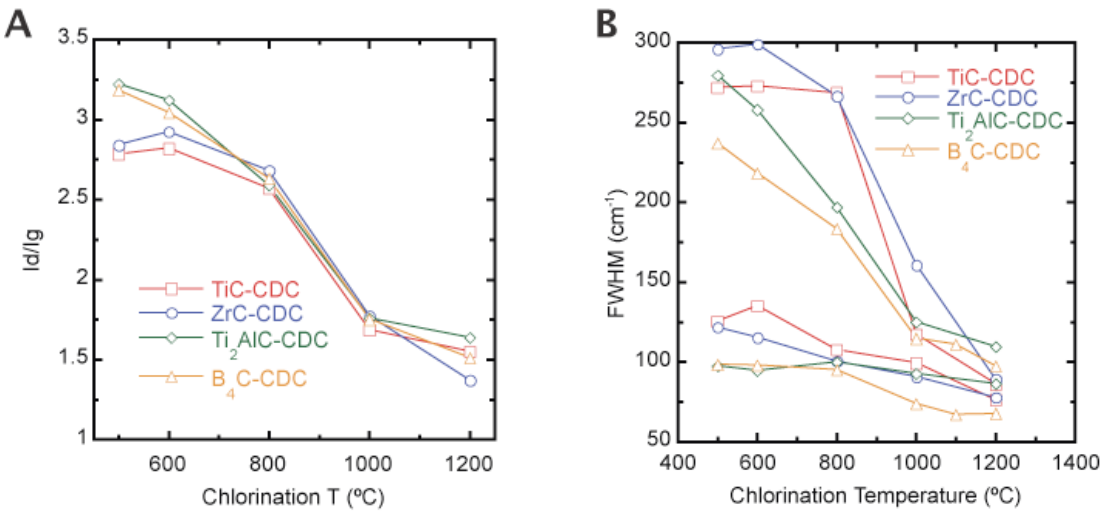

Figure 4.4: a.) Evolution of the I_D/I_G ratio and b.) full width at half maximum (FWHM) of the D and G bands with synthesis temperature for CDC produced from TiC, ZrC, Ti_2AlC and B_4C.

The microstructral evolution unveiled using Raman spectroscopy shows that at all synthesis temperatures, the structure consists of disordered carbon, as was also seen in TEM (Figure 4.3). Especially in the temperature range less than 1000ºC, the microstructure is fairly constant, allowing us to conclude that there is no large-scale graphitization that may affect results.

4.1.4. Results of porosity measurements on powder CDCs

Argon sorption isotherms obtained on CDCs chlorinated between 600ºC and 1000ºC (Figure 4.6a) are type I in the Brauner classification, which indicates the samples are completely microporous (all pores are less than 2 nm in width). At the lowest synthesis temperature, the isotherm saturates quickly, which is evident of very uniform and narrow micropores. As the synthesis temperature increases, the isotherms saturate more slowly indicating pore widening. Different shaped isotherms for different samples indicate that the pore size can be tuned by selecting either the carbide precursor or synthesis conditions.

TiC CDC synthesized at 800ºC was also studied with CO_2 sorption at 300K (Figure 4.5). NLDFT was used for obtaining pore size distributions for pores in the range of 0.4-1.5 nm. Comparing these results with those obtained using Ar sorption shows that the average pore size value obtained was very close. This was also confirmed by Jagiello in a separate study on a variety of carbonaceous materials [244]. Small angle X-ray scattering (SAXS) was used to determine the radius of gyration and confirmed the pore size values measured by gas sorption techniques [180]. The trends elucidated by SAXS mirror those realized using gas sorption. These two separate porosity studies show Ar sorption to be well-suited to studying pores in the range of interest and lend confidence to the results.

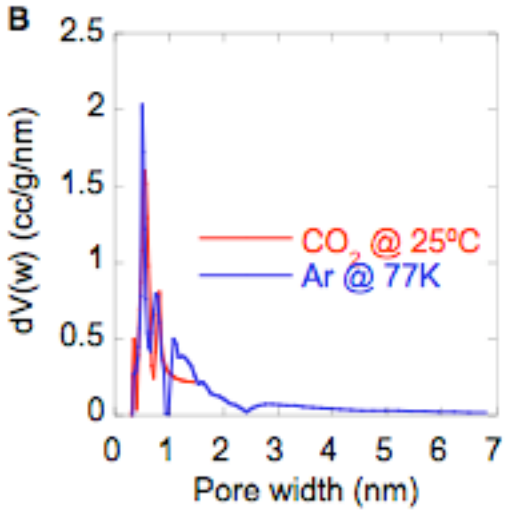

Figure 4.5: Data confirming the reliability of Ar sorption results. Comparing the pore size distributions of CO sorption and Ar sorption shows that Ar reproduces the mean pore size below 1.5 nm within 0.3 nm of CO_2 sorption [211].

BET surface area evolution with temperature for B_4C-CDC, TiC-CDC are shown in Figure 4.6 b. The values reported are averaged for samples chlorinated at different times, showing the reproducibility of the chlorination protocol. Evolution of surface area with chlorination temperature follows somewhat different trends depending on the carbide studied. For TiC-CDC with the closest distance between adjacent carbon atoms in the initial carbide lattice, there is a relatively constant increase in surface area over the entire temperature range of 600ºC to 1200ºC. As the distance between adjacent carbon atoms in the precursor lattice increases, however, the surface area saturates and then decreases with further increases in synthesis temperature. This is most likely due to structural collapse in favor of graphitization. As the distance between carbon atoms increases there is more freedom for the CDC structure to attain a lower energy structure. The surface area, in general, is a minimum of ~800 m^2/g and a maximum of ~2000 m^2/g. The standard deviation in surface area is only marginal indicating the chlorination technique

is repeatable, but large enough that porosity measurements needed to be done on each sample studied to ensure proper reporting of properties.

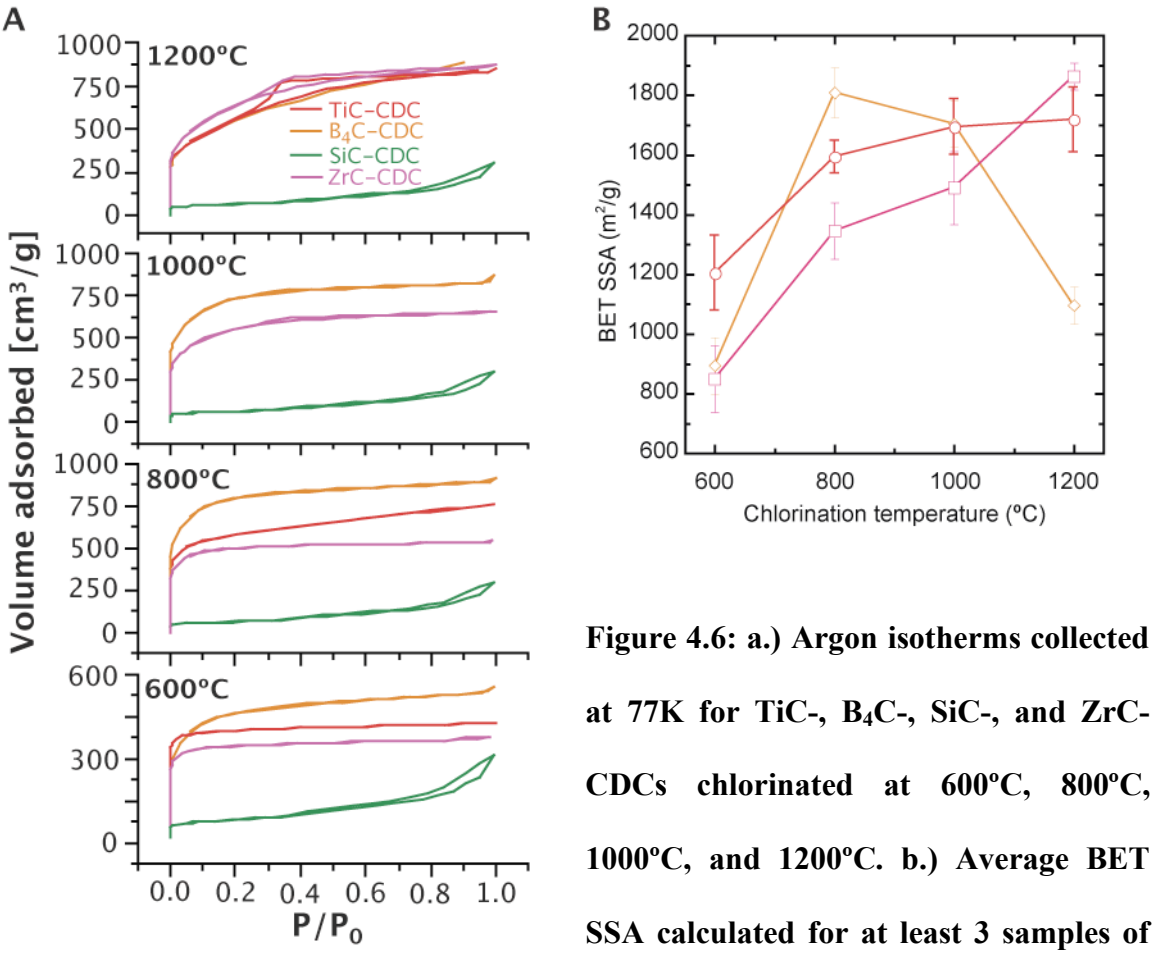

Figure 4.6: a.) Argon isotherms collected at 77K for TiC-, B_4C-, SiC-, and ZrC-CDCs chlorinated at 600°C, 800°C, 1000°C, and 1200°C. b.) Average BET SSA calculated for at least 3 samples of TiC-CDC, B_4C-CDC and SiC-CDC.

Pore size distributions calculated from NLDFT are shown in Figure 4.7. As was predicted from looking at the raw adsorption isotherms, in general the pore size increases with

increasing synthesis temperature. It should be noted that the minima in the pore size distributions are artifacts of the NLDFT model and not necessarily representative of a multimodal pore size distribution. The actual pore size distribution is expected to be a more Gaussian-like distribution around the average pore size. The average pore size for the TiC-CDCs, ZrC-CDCs, and B_4C-CDCs shown in Figure 4.6b is shown in Figure 4.8. As would be obvious from looking at Figure 4.7, the average pore size increases continually with increasing chlorination temperature. Hydrogen annealing was shown previously to have little effect on average pore size [179], and was done on all samples, so a parametric study on hydrogen annealing conditions on porosity was not done. The average pore size increases from ~0.7 nm for TiC-CDC chlorinated at 600ºC to ~ 2 nm for B_4C-CDC chlorinated at 1200ºC. The uncertainty in pore size is slightly less than the BET surface area, however.

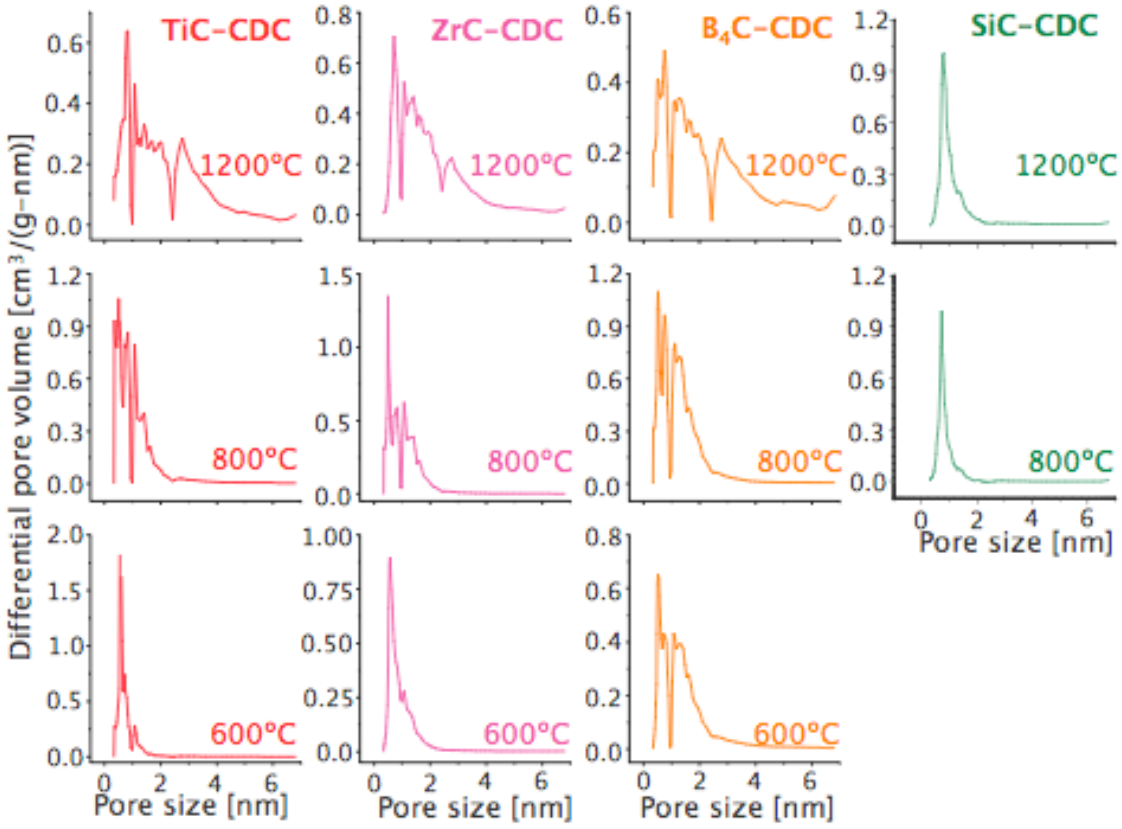

Figure 4.7: Pore size distributions calculated from density functional theory applied to Ar isotherms collected at 77 K for TiC-, ZrC-, B_4C-, and SiC-CDCs chlorinated at 600, 800, and 1200°C.

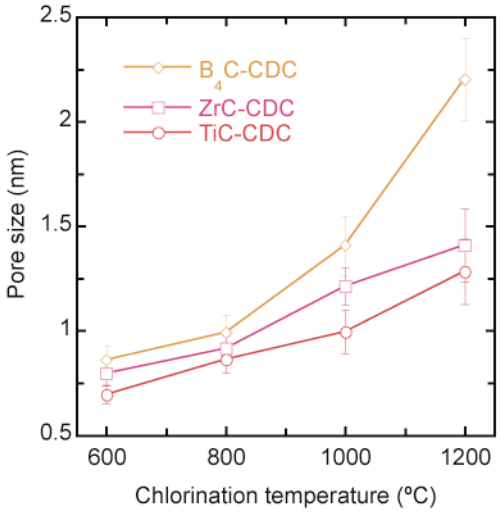

Figure 4.8: Average pore size for B_4C-, ZrC-, and TiC-CDCs calculated from DFT.

4.1.5. Conductivity measurements on CDC powders

Electrical conductivity was measured as a function of compacted powder thickness in the testing fixture for 2 commercially-available standards, Arkema activated carbon and MWCNT's. From Figure 4.9, the conductivity increases with increasing thickness of powder as it becomes more uniformly packed. Also, the conductivity of the activated carbon and MWNTs saturate at ~2 S-cm^{-1} and ~160 S-cm^{-1}, which is within the range of values quoted by the manufacturer, ~1 S-cm^{-1} and ~160 S-cm^{-1}. Confident in the quality of the results obtained using the conductivity fixture, work was extended to CDCs as well. SiC-CDC, B_4C-CDC and TiC-CDC chlorinated at temperatures of 500ºC to 1200ºC were tested with varying amounts of powder packed into the fixture for statistical reliability. Conductivity of CDC is, in general, approximately an order of magnitude greater than standard activated carbons due, probably, to a reduction in electron scattering defects with removal of surface functionality. Conductivity increases to the order of

magnitude of conductivity of MWCNTs when the synthesis temperature is increased above 1000ºC.

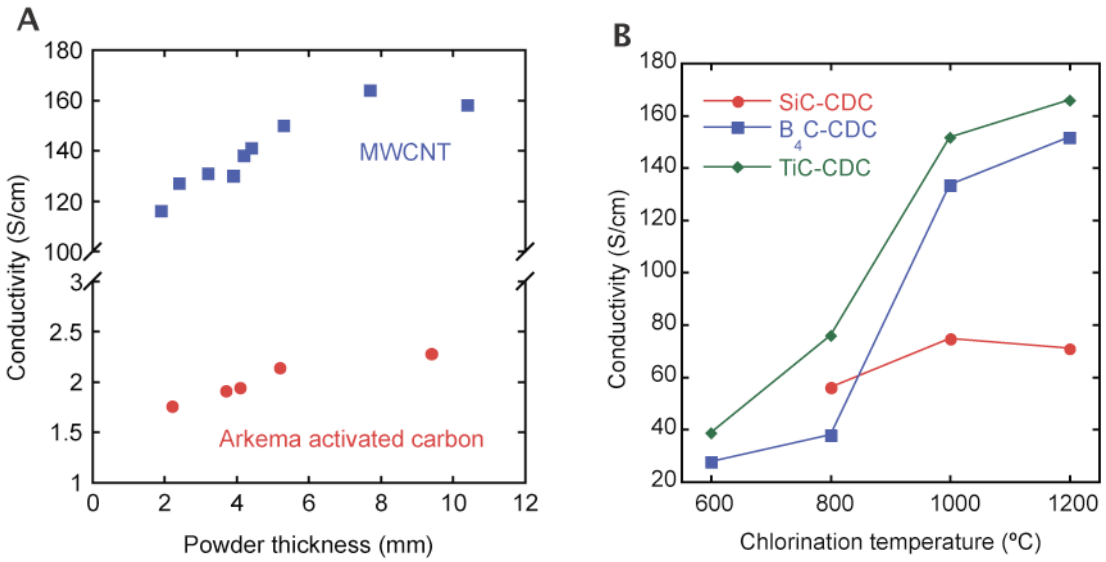

Figure 4.9: Electrical conductivity of a.) Arkema activated carbon and b.) SiC-, TiC- and B_4C-CDCs chlorinated from 600ºC to 1200ºC.

4.2. Electrochemistry: Aqueous electrolyte studies

4.2.1. Capacitance of B_4C and Ti_2AlC-CDCs in sulfuric acid

The initial electrochemical studies on CDC were conducted on Ti_2AlC and B_4C precursors in an aqueous 1M H_2SO_4 electrolyte because the carbides both offered a large spatial distribution between carbon atoms in the carbide lattice, which gave large pore sizes and sulfuric acid gave high ionic conductivity of the electrolyte. Based on the parameters outlined in literature for high performing carbon, it was expected that

studying pore sizes that were significantly larger than the solvated ion (~0.5 nm for the larger SO_4^{2-} ion [143]) would be most beneficial.

All pores for both Ti_2AlC CDC and B_4C CDC were found to be at least twice the size of the solvated SO_4^{2-} ions at chlorination temperatures as low as 600ºC, and increased to above 2 nm as the chlorination temperature increased above 1000ºC (Figure 4.8). For the purposes of this study, two commercially available activated carbons, termed low SSA activated carbon, and advanced activated carbon with surface areas of ~550 m^2/g and ~1225 m^2/g, respectively, as well as Arkema MWCNTs with a surface area of ~180 m^2/g were used as benchmark materials. They had average pore sizes of ~0.7 nm, ~1 nm and ~10 nm (based on prior TEM measurement of internal diameters), respectively.

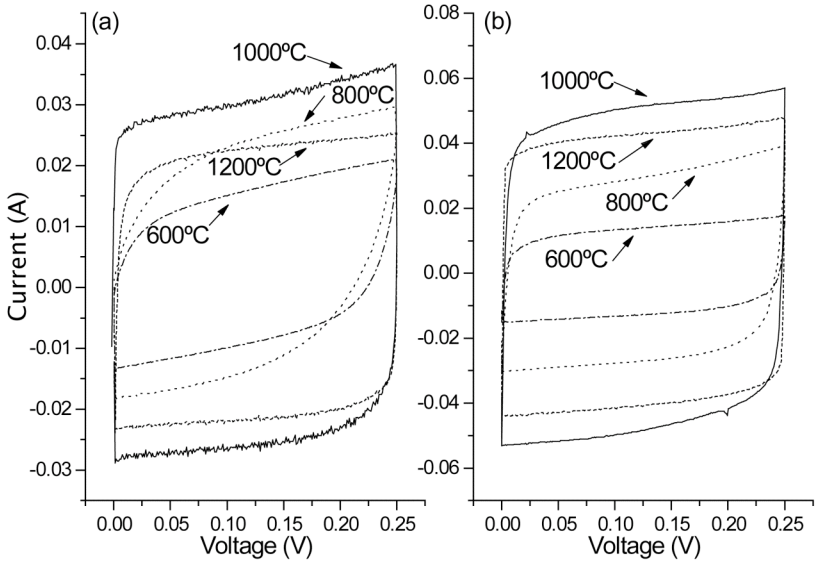

Figure 4.10: CVs obtained from tests run at a scan rate of 1 mV/s on (a) B_4C CDCs and (b) Ti_2AlC CDCs [245].

CV tests at 1 mV/s were conducted to characterize electrochemical performance of both B_4C and Ti_2AlC CDCs. Because the cell design was not perfectly optimized at this juncture (Cell design #1 was used for this study), such a low scan rate was needed to properly characterize the steady-state electrochemical behavior. No Faradic reactions were found within a 250 mV window for either material at any synthesis temperature (Figure 4.10). Also evident from Figure 4.10 are the very rectangular voltammograms, which indicates that there are no problems associated with poor percolation of charge. This again leads to good confidence in the cell design not influencing the results to a great deal. B_4C CDC synthesized at 600°C resulted in a specific capacitance of 95 F/g,

increasing to 147 F/g after 1000°C synthesis (Figure 4.11 b). The latter turned out to be the optimum synthesis temperature; at 1200°C the value dropped to 120 F/g. This trend follows that of the BET SSA, which is to be expected if the classical interpretation of the double-layer holds inside of confined pores. The observed small deviations may be connected to the incomplete accessibility of the smallest pores to the electrolyte ions or some other ill-defined phenomena. Ti_2AlC CDC's followed even closer the correlation between capacitance and SSA (Figure 4.11 a). Ti_2AlC-CDC synthesized at 600°C resulted in a specific capacitance of 77 F/g, while at 1000°C it was 175 F/g, the highest of all materials tested in this study. This high capacitance of 1000ºC B_4C CDC and 1000ºC Ti_2AlC CDC shows CDC to be a worthwhile material for study as the active material in electrochemical capacitor electrodes and the ability to tune the microstructure and follow how it effects the electrochemical performance, which shows CDC to be a good model system.

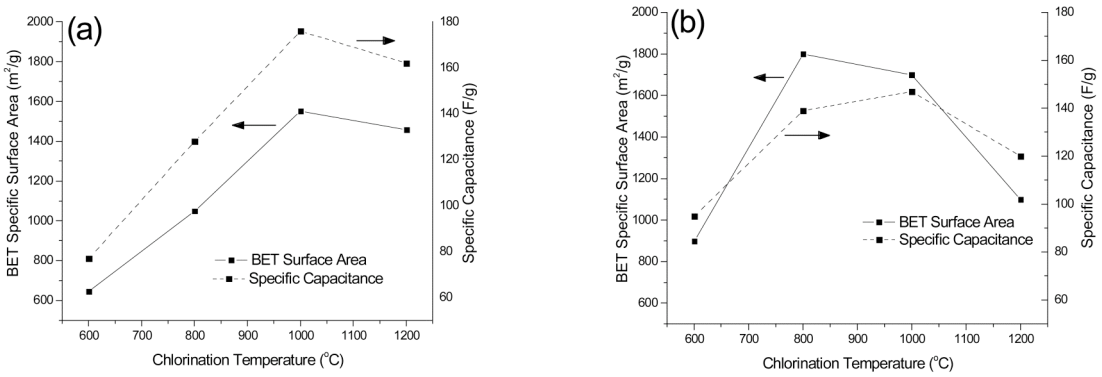

Figure 4.11: BET SSA and specific capacitance vs chlorination temperature for (a) Ti_2AlC CDC and (b) B_4C CDC. The correlation between these parameters for Ti_2AlCCDCs suggests that most of the CDC pores are accessible to the electrolyte ions, irrespective of the synthesis temperature. The small deviations from the linear dependence of the specific capacitance and the SSA seen in B_4C CDCs may be due to the incomplete accessibility of the smallest pores to the electrolyte. [241]

CV tests from 5 to 50 mV/s within a 250 mV window were performed to gain a qualitative understanding of the influence of CDC structure on the rate dependence of the charge-discharge behavior (Figure 4.12). As this study was done before the cell design was perfectly optimized, contributions from active material resistance dominate. Deviations from ideal behavior are found at the highest scan rates, where the current response is slower in more microporous electrodes. Ti_2AlC CDC and B_4C CDC synthesized at 1000°C have the largest fraction of mesopores (>2 nm width) and show only small deviations from ideal behavior at 50 mV/s (Figure 4.12c). At this juncture, however, it is impossible to separate effects from ionic conductivity in pores from electronic conductivity. So the increasing pore size of CDC with increasing synthesis

temperature may not be the dominant factor and the increasing electronic conductivity with synthesis temperature (Figure 4.9) may play a larger role.

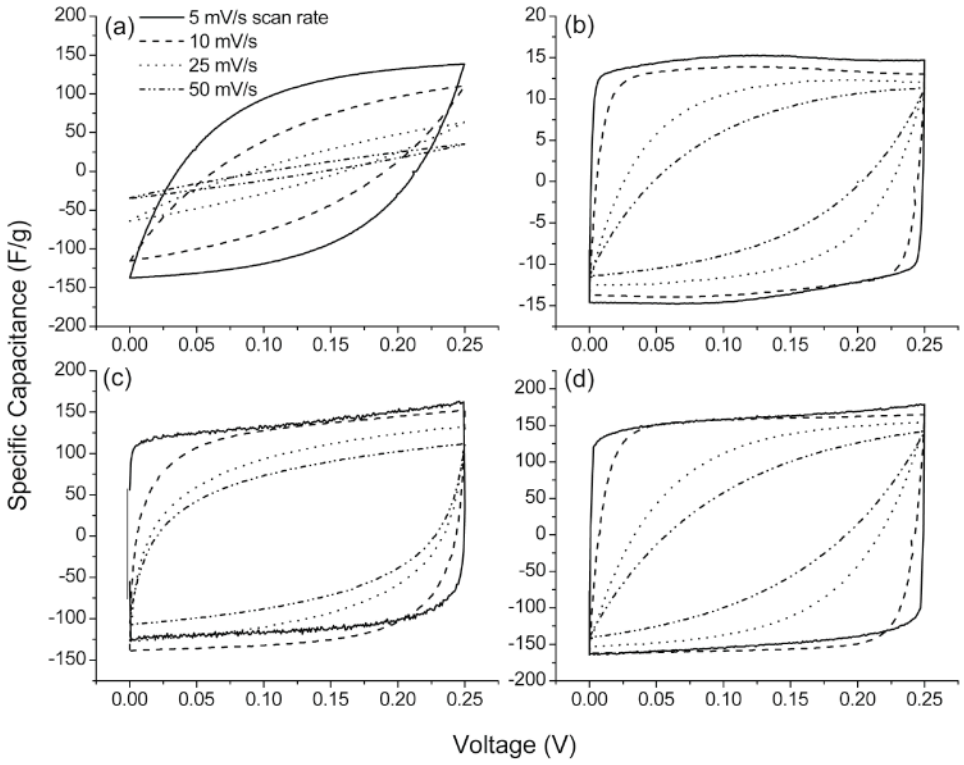

Figure 4.12: CVs taken at scan rates of 5, 10, 25, and 50 mV/s for (a) advanced activated carbon, (b) multi-wall carbon nanotubes, (c) B_4C CDC synthesized at 1000°C and (d) Ti_2AlC CDC synthesized at 1000°C. Activated carbon with the smallest pores showed the slowest current response at high scan rates. [245]

4.2.2. Capacitance of TiC-CDC and ZrC-CDC in sulfuric acid

To gain further insight into how porosity and surface contribute to capacitance of CDCs in 1M H_2SO_4, microporous TiC-CDC and ZrC-CDC synthesized in the 600ºC – 1200ºC temperature ranges were studied. As seen for B_4C-CDC and Ti_2AlC-CDC (Figure 4.10), cyclic voltammetry tests on TiC-CDC and ZrC-CDC showed an absence of any major faradic charge transfer (Figure 4.13). From Figure 4.13, it is also evident that as the synthesis temperature increases, the shape of the *I–V* loop becomes more rectangular, highlighting a decreasing equivalent series resistance with increasing synthesis temperature as was also seen in B_4C-CDC and Ti_2AlC-CDC (Figure 4.12). Also apparent is the maximum in gravimetric specific capacitance (F/g) that occurs at a synthesis temperature of 800ºC (Figure 4.13 b) for both TiC- and ZrC-CDCs. The gravimetric specific capacitance (F/g) for TiC- and ZrC-CDCs increases substantially from 108 and 81.5 F/g, respectively, to 190 and 159 F/g between synthesis temperatures of 600 and 800ºC (Figure 4.14 a).

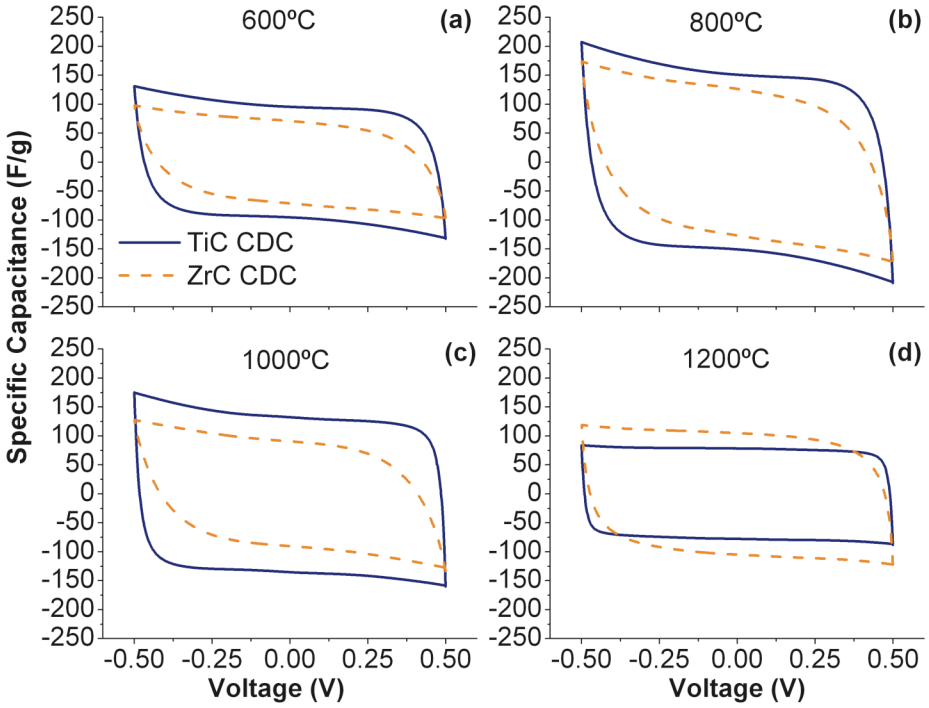

Figure 4.13: Cyclic voltammograms taken at a scan rate of 5 mV/s of TiC-CDC and ZrC-CDC synthesized at (a) 600ºC, (b) 800ºC, (c) 1000ºC and (d) 1200ºC. [241]

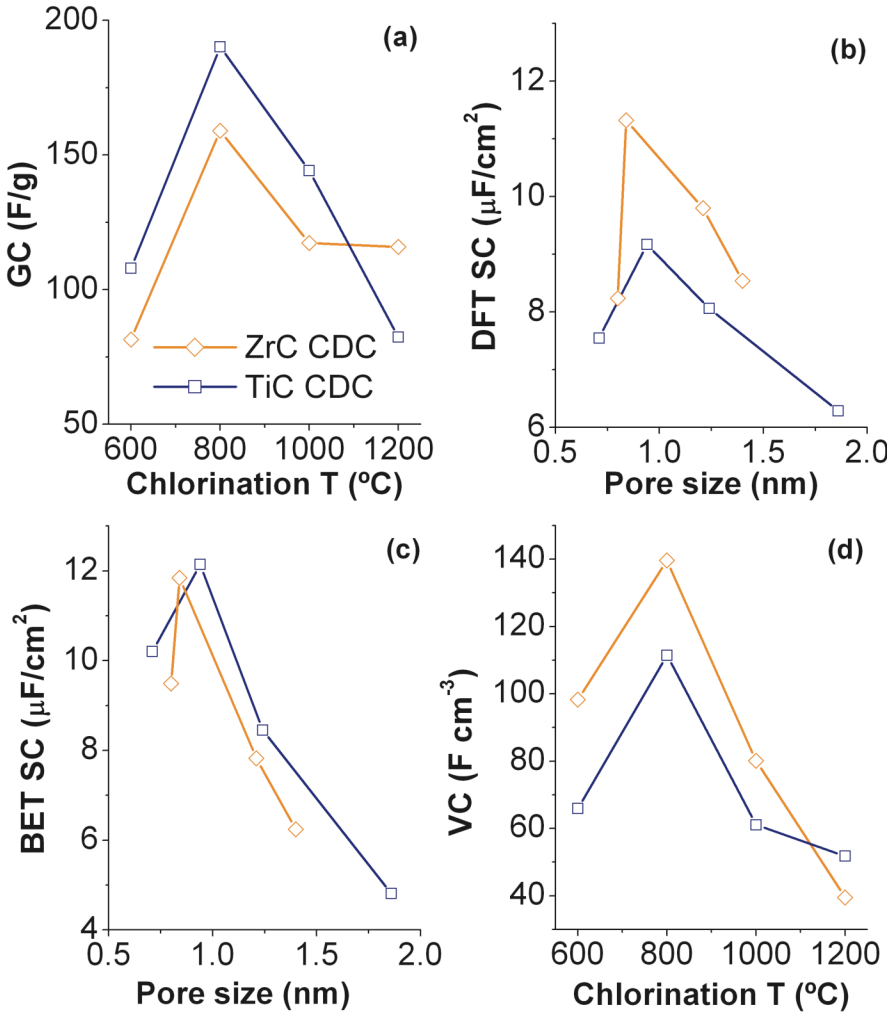

Figure 4.14: (a) Specific gravimetric capacitance (GC) vs. chlorination temperature shows maximum capacitance at a synthesis temperature of 800ºC. Specific surface caapcitance calculated using DFT SSA (DFT SC) (b) and BET SSA (BET SC) (c) vs. average pore size both show a decreasing trend with increasing pore size above 1 nm. (d) Volumetric capacitance (VC) shows a maximum at synthesis temperature of 800ºC. [241]

The volumetric capacitance (VC) of TiC-CDC and ZrC-CDC were a maximum of 140 and 110 F/cm^3 (Figure 4.14 d), showing the practical usefulness of CDC as the active material in supercapacitor electrodes. Above synthesis temperatures of 800ºC, the gravimetric specific capacitance (GC) decreases, though the BET SSA continues to increase up to synthesis temperatures of at least 1200ºC (Figure 4.14 a). The DFT SSA correlates very well with the specific capacitance, however (Figure 4.14 b). Figure 4.14 a and b shows that the surface specific capacitance (SC, F/cm^2) also has a decreasing trend with increasing pore size above 1 nm using both the DFT and BET criteria to calculate SSA. From Figure 4.13, it is evident that TiC-CDC has a larger specific capacitance than ZrC-CDC at all synthesis temperatures below 1200ºC. This is a direct result of the larger specific surface area of TiC-CDC in this temperature range.

Unlike most studies in literature that suggest increasing specific capacitance with increasing average pore size, this study shows a more complex behavior of porous carbons. Experiments on CDC demonstrate that decreasing the surface are of micropores serves to decrease both the gravimetric specific capacitance (F/g) and the specific surface capacitance (F/cm^2) in a sulfuric acid electrolyte (Figure 4.15 a and b). Even though the BET SSA continually grows with increasing synthesis temperature to the highest temperature studied, the specific capacitance decreases with decreasing micropore surface area at synthesis temperatures above 800ºC. These results corroborate those reported by Vix-Guterl *et al.* [131], which show that the non-solvated ions residing in pores smaller than 0.7 nm account for the largest portion of double-layer capacitance.

Using DFT to calculate SSA shows that even though most of the area lies in smaller pores, it still remains highly accessible to electrolyte.

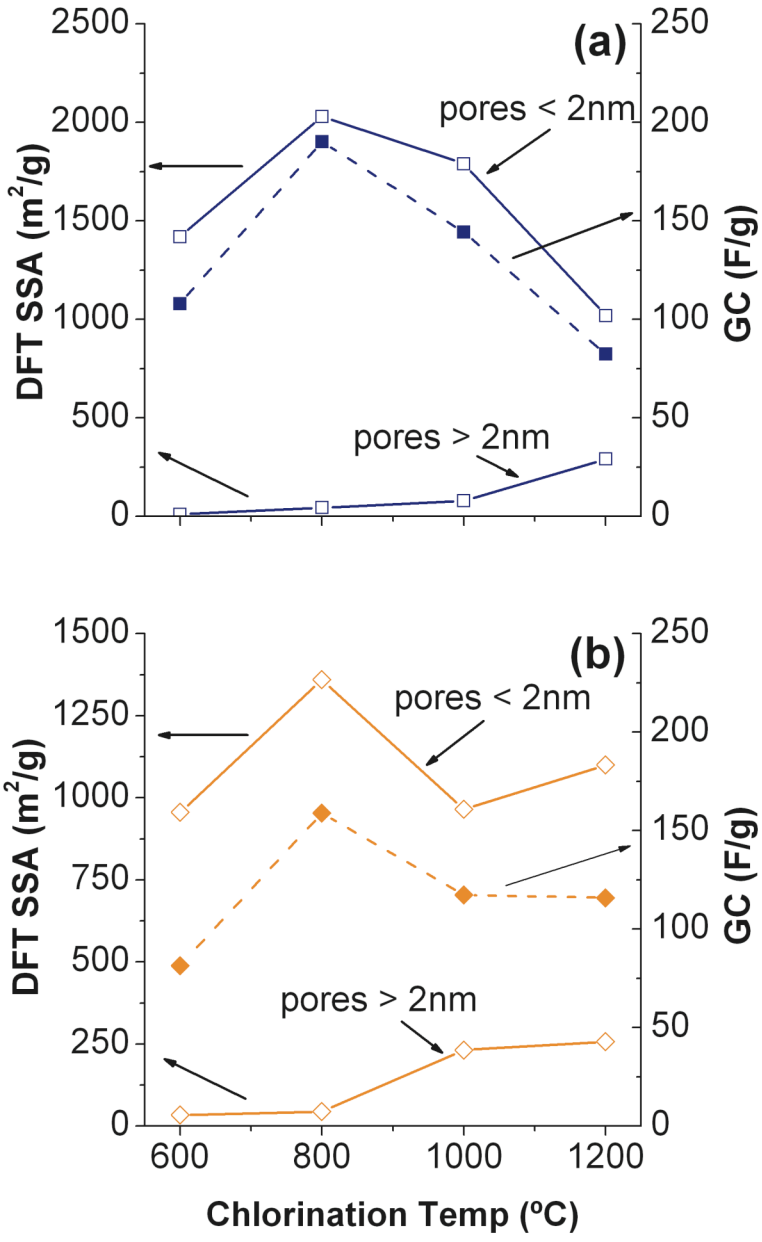

Figure 4.15: Micropore (<2 nm) and mesopore (> 2nm) surface area in comparison with gravimetric specific capacitane for (a) TiC-CDC and (b) ZrC-CDC. A direct corelation between micropore surface area and specific capacitance is evident.

The effect of the mesopore/micropore ratio on complete device performance, including charge–discharge kinetics, could not be revealed by DC measurement techniques alone. To understand the power performance of these devices, the approach taken by Taberna, *et al*. to understand impedance results was used [240]. Considering the supercapacitor behaves as a series combination of a resistance, *R*, and capacitance, *C*, and both depend on frequency, ω, the impedance can be written in complex form as:

$$Z = R(\omega) + \frac{1}{j\omega C(\omega)} \tag{4.1}$$

The total impedance is equated to a supercapacitance, *K*:

$$Z = \frac{1}{jK\omega} \tag{4.2}$$

leading to

$$K = \frac{C(\omega)}{1 + j\omega R(\omega)C(\omega)} \tag{4.3}$$
$$= \frac{C(\omega)}{1 + \omega^2 R^2(\omega)C^2(\omega)} - \frac{jC^2\omega(\omega)R(\omega)}{1 + \omega^2 R^2(\omega)C^2(\omega)}$$

or

$$K = C'(\omega) - jC''(\omega) \tag{4.4}$$

where C’(ω) and –C”(ω) are the real and imaginary components of supercapacitance, respectively:

$$C'(\omega) = \frac{C(\omega)}{1 + \omega^2 R^2(\omega) C^2(\omega)} \quad \vdots \quad C''(\omega) = \frac{\omega C^2(\omega) R(\omega)}{1 + \omega^2 R^2(\omega) C^2(\omega)} \tag{4.5}$$

Alternatively, by considering the impedance in the complex form as:

$$Z(\omega) = Z'(\omega) + jZ''(\omega) \tag{4.6}$$

it is possible to derive the real and imaginary parts of supercapacitance directly from impedance data by using Eq. (4.2) and Eq. (4.4).

$$C'(\omega) = \frac{-Z''(\omega)}{\omega |Z(\omega)|^2} \quad \vdots \quad C''(\omega) = \frac{Z'(\omega)}{\omega |Z(\omega)|^2} \tag{4.7}$$

C' (ω) corresponds to the capacitance of the cell measured under DC or low frequency AC conditions, while $C''(\omega)$ is directly proportional to resistance and corresponds to losses in the form of energy dispersion. Eq. (4.5) and Eq. (4.7) allow the expression of capacitance both as a function of electrode properties and experimentally measured parameters.

Figure 4.16a and b shows the evolution of $C'(\omega)$ normalized by C'(1 mHz) versus frequency, according to Eq. (4.3) and Eq. (4.5). This type of plot provides a convenient method to show the frequency response of supercapacitors because frequency is the dependant variable, unlike Nyquist plots that have frequency buried in both the real and imaginary impedance terms. The graph shows a transition between purely resistive behavior, where $C'(\omega)/C'$(1 mHz) is equal to zero to purely capacitive behavior where $C'(\omega)/C'$(1 mHz) is equal to 1. Ideally for applications, the capacitance should remain nearly invariant with frequency once this transition ($R^2C^2w^2 \cong 1$) is passed. TiC-CDC

(Figure 4.16 a) synthesized at temperatures above 800ºC shows this ideal behavior, while for samples synthesized at lower temperatures, capacitance continues to increase with decreasing frequency. ZrC-CDC (Figure 4.16 b) shows ideal behavior for only the 1200ºC sample.

Figure 4.16 c and d show the evolution of the imaginary capacitance with frequency according to Eq. (4.5). The maximum of the curve is a characteristic of the entire system and can be roughly described as the point where the circuit goes from purely resistive to purely capacitive. The frequency where this maximum occurs shifts to higher values with increasing synthesis temperature (Figure 4.16 c and d). The reciprocal of the characteristic frequency yields a time constant that is a quantitative measure of how fast the device can be charged and discharged reversibly. For both CDCs, this time constant decreases with increasing synthesis temperature (Figure 4.16 e). Interestingly, for TiC-CDC there is a large decrease in the time constant between synthesis temperatures of 600 and 1000ºC and little change between 1000 and 1200ºC. ZrC-CDC has a uniform decrease of time constant with synthesis temperature. For 600 and 800ºC synthesis temperatures, the values for the time constant match up pretty closely for both materials, but at higher synthesis temperatures, the time constant decreases much more for TiC-CDC. These results give valuable insight into the role of pore size on the frequency response of porous carbons. According to Eq. (4.5), there are two factors, $R(\omega)$ and $C(\omega)$, that determine the frequency response of both the real and imaginary capacitance. $R(\omega)$ can be assumed to be the sum of two contributions: a frequency independent term equal to the ESR and a frequency dependent term, $Rf(\omega)$, connected with inhibited ion motion

in small pores. As the pore structure has no influence over the ESR, the roles of increasing graphitization and increasing pore size on EIS results can be separated. For both TiC-CDC and ZrC-CDC, there is a decreasing ESR of approximately the same magnitude of ~100% from synthesis temperatures of 600 to 1200ºC. This can be directly related to the increasing graphitization with increasing synthesis temperature observed in all CDCs. From Figure 4.16e, it is apparent that the characteristic time constants for samples synthesized at 600 and 1200ºC for TiC- and ZrC-CDCs decrease by approximately a factor of 12 and 3, respectively. As the decrease in time constant is greater than that of the ESR, it can be directly inferred that widening of the pores has a positive effect on the time constant. The large difference between characteristic time constants for TiC-CDC and ZrC-CDC synthesized at 1000 and 1200ºC was surprising. As both materials have essentially the same ESR at both synthesis temperatures, explaining the result as a consequence of larger pores in TiC-CDC would seem the most plausible answer. Unfortunately, though the difference in pore sizes at 1200ºC synthesis temperatures is sufficient to make this rationalization conceivable, at a 1000ºC synthesis temperature, the average pore size and FWHM are very similar. The main difference in these two materials at these synthesis temperatures is then not the average pore sizes, but how easily accessible these pores are. This highlights the fact that basing expected supercapacitor performance simply on pore size measured by gas sorption is short sighted. Bottlenecks that may be present but not detectible by gas sorption could have major influence over the charging and discharging of supercapacitors. The discussed phenomenon creates an additional challenge to predict electrochemical performance of porous carbon materials based on their physical characteristics.

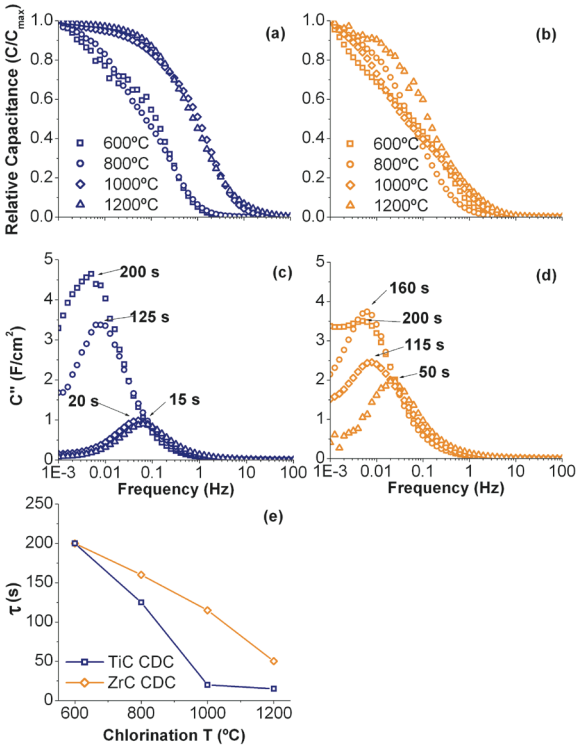

Figure 4.16: Progression of the relative real capacitance, C'(w)/C'(1 mHz) for (a) TiC-CDC and (b) ZrC-CDC, and the imaginary capacitance, C'(w) for (c) TiC-CDC and (d) ZrC-CDC with frequency for synthesis temperatures of 600, 800, 1000, and 1200ºC shows dependence on the synthesis temperature. (e) Variation of the characteristic time constant, τ, with synthesis temperature for TiC-CDC and ZrC-CDC [241]

4.2.3. Inclusive study of B_4C-, TiC-, SiC-, and ZrC-CDCs in sulfuric acid

To nullify effects from cell design potentially influencing results, the prior two electrochemical studies were repeated with cell design #3 (Section 3.2.2.2) and CDC

synthesized from SiC was added. Figure 4.17 shows cyclic voltammograms of B_4C-CDC, SiC-CDC, TiC-CDC, and ZrC-CDC synthesized in the temperature range of 600ºC to 1200ºC. As expected, there are no apparent Faradaic contributions to currents and increasing synthesis temperature makes the CV's more rectangular. Also, in general, there is no optimum synthesis temperature applicable to all CDCs and each has performance that depends differently on synthesis temperature, which is also evident from Figure 4.18 a. Also evident from Figure 4.18 is the fact that all CV's from different CDCs are very similar which lends confidence in being able to treat them as one model system.

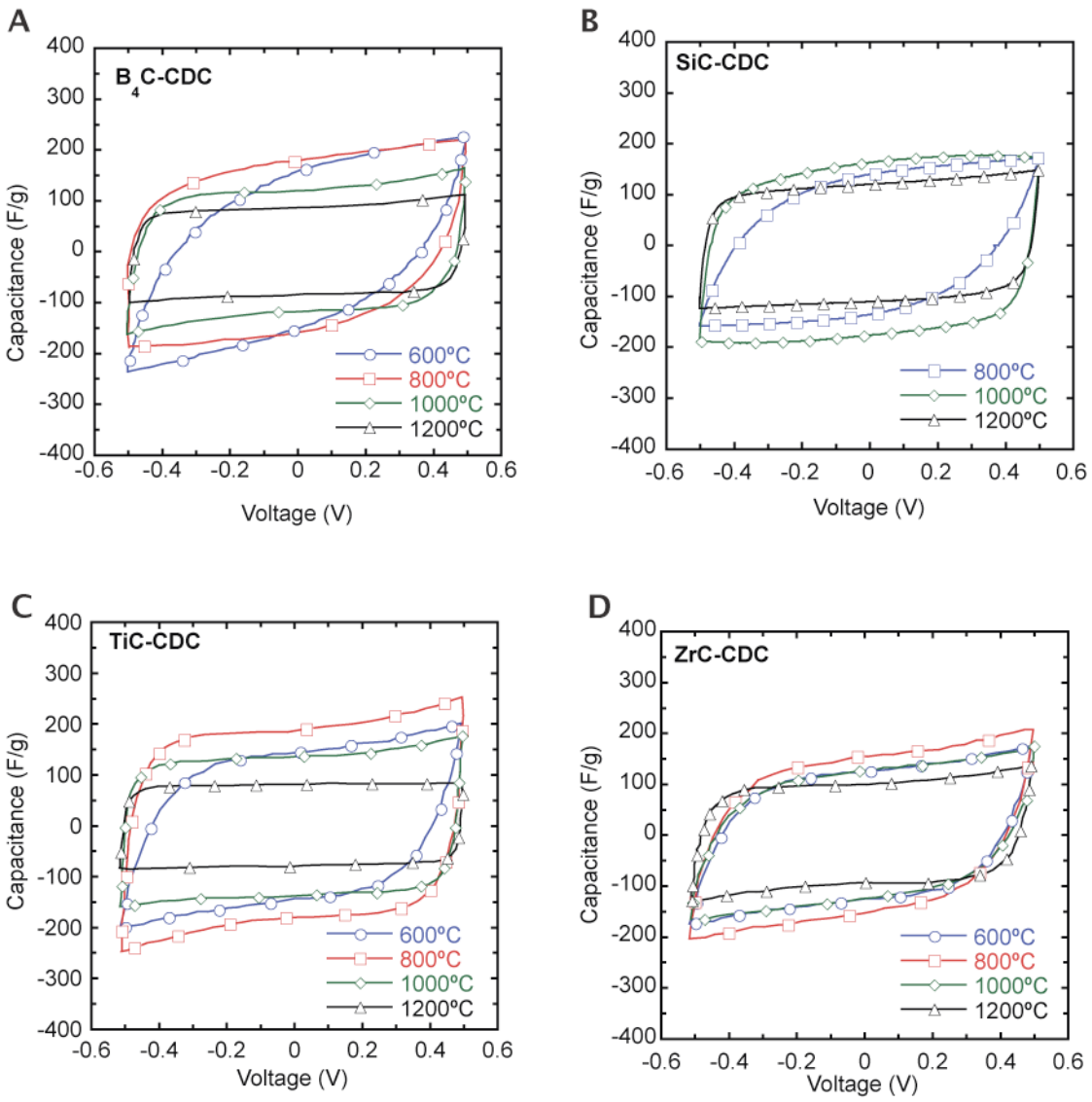

Figure 4.17: Cyclic voltammograms of a.) B_4C-CDC, b.) SiC-CDC, c.) TiC-CDC, and d.) ZrC-CDC.

Figure 4.18 a shows the specific capacitance of various CDCs in 1 M H_2SO_4. As was seen previously, and should be expected, there is a general decrease in capacitance with

increasing synthesis temperature. This is contrary to the increasing surface area and pore size with increasing synthesis temperature, as seen in Figure 4.18 b-c. Maximum specific capacitance of ~160 F/g was found for TiC-CDC and SiC-CDC at synthesis temperatures of 800ºC and 1000ºC, respectively. At higher synthesis temperatures, the capacitance, in general, converges to a fairly constant value, but at intermediate and lower synthesis temperatures there is wide divergence between capacitance values.

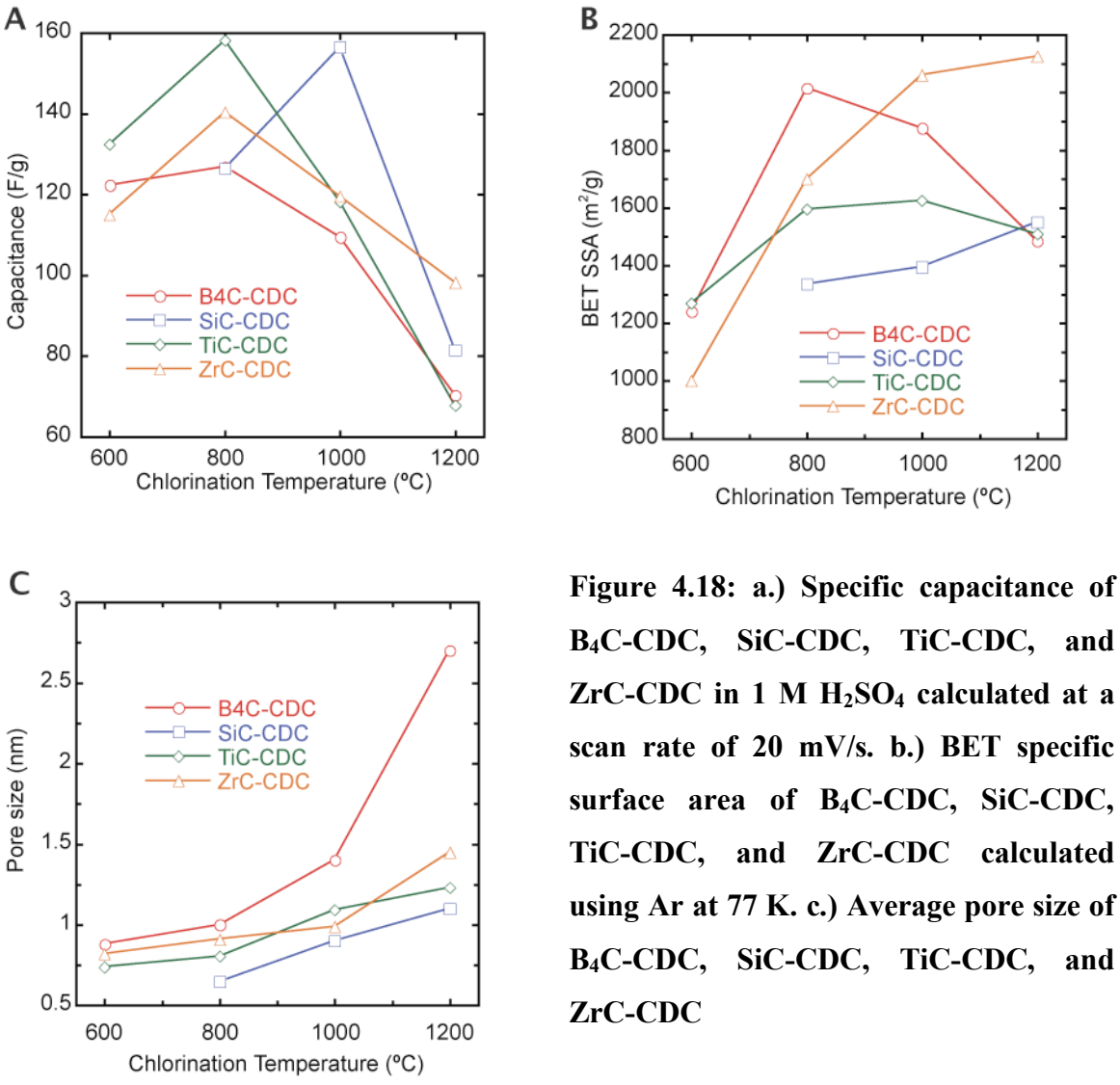

Figure 4.18: a.) Specific capacitance of B_4C-CDC, SiC-CDC, TiC-CDC, and ZrC-CDC in 1 M H_2SO_4 calculated at a scan rate of 20 mV/s. b.) BET specific surface area of B_4C-CDC, SiC-CDC, TiC-CDC, and ZrC-CDC calculated using Ar at 77 K. c.) Average pore size of B_4C-CDC, SiC-CDC, TiC-CDC, and ZrC-CDC

To gauge how effective the surface of carbon contributed to capacitance, the gravimetric capacitance was normalized by the specific surface area (Figure 4.19).

$$\frac{C}{A} = \frac{\varepsilon}{d} \tag{4.8}$$

The dependence is only a function of some dielectric term, ε, and some term that relates to charge separation, d. This allows us, in effect, to determine the optimum microstructure for carbon irrespective of the surface area to guide future material design. Not surprisingly, since the surface area and the capacitance have an opposite dependence on synthesis temperature, plotting the normalized capacitance as a function of synthesis temperature shows a decreasing dependence (Figure 4.19 a). In general, there is more of a convergence of normalized capacitance values than those in Figure 4.18 a. When the normalized capacitance is plotted versus pore size, the capacitance increases continuously with decreasing pore size, up to the smallest pore size studied, ~0.7 nm. The size of the solvated SO_4^{2-} ions is ~0.55 nm, which indicates that in the smallest pores, the ions need to enter the pores single-file.

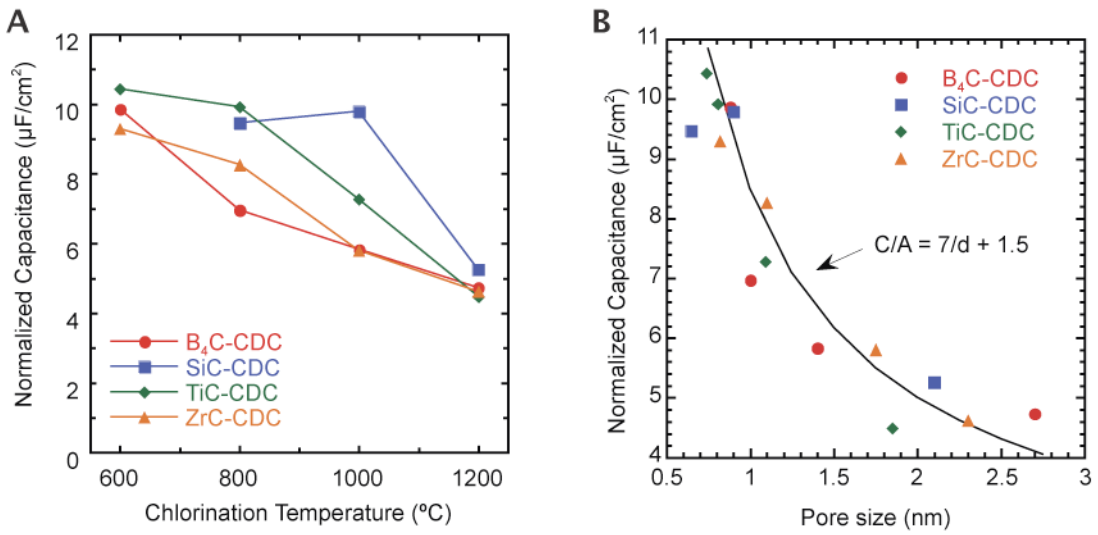

Figure 4.19: a.) Normalized capacitance for B_4C-CDC, SiC-CDC, TiC-CDC and ZrC-CDC at different chlorination temperatures. b.) Normalized capacitance versus pore size for B_4C-CDC, SiC-CDC, TiC-CDC and ZrC-CDC.

In fact, with the majority of the carbons studied, ions need to enter the pores single-file. If classical interpretations of the double-layer are to be believed, it would be expected that diffusion in the pores of these extremely nanoporous carbons would be significantly hindered. From EIS (Figure 4.16), even with a cell having an order of magnitude higher resistance than current designs, diffusion times are still on the order of what is found with even highly mesoporous carbons [132]. From Eq. (4.8), normalized capacitance should have a reciprocal dependence on the separation between counter-charges. As can be seen in Figure 4.20b, a close fit is obtained by fitting a line of the equation C/A=7/d + 1.5. From Eq. (4.8), the dielectric coefficient calculated from Figure 4.19 b is 7. This is an

order of magnitude less than the bulk dielectric coefficient of water, showing a different structure of water in the nanopores of carbon, which has been theoretically predicted. The close fit between the experimental data and classical capacitance models is curious. Why would decreasing the pore size seemingly decrease the separation between counter-charges, a distance that should be dictated by the ion size and not the pore size?

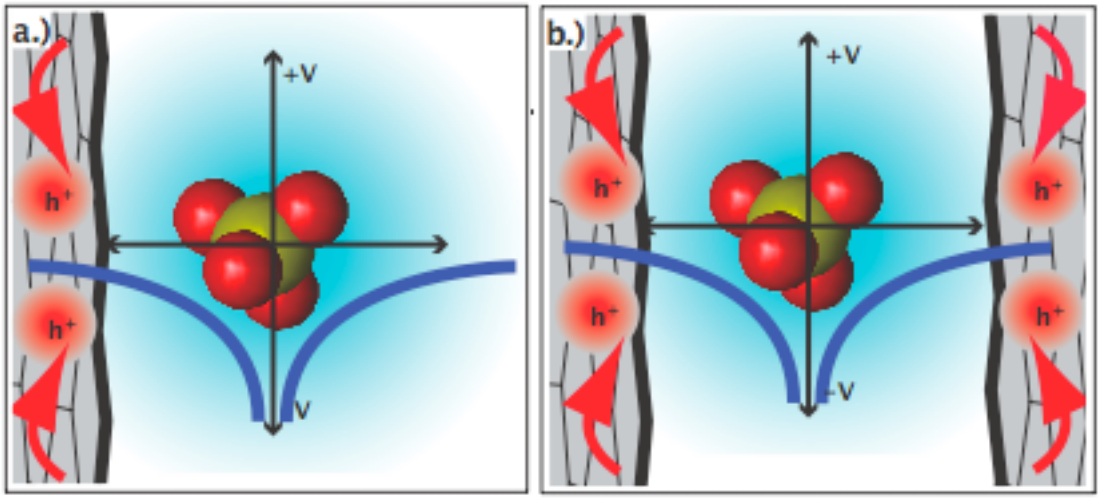

Figure 4.20: a.) Schematic showing how charge deficiency compensates for negative SO_4^{2-} anions in close proximity to a carbon electrode surface. b.) Schematic showing how when an SO_4^{2-} anion is inside of a pore with both pore walls in close proximity, there is a compensating deficiency of charge on both pore walls.

This can be appreciated by considering that ions have an electric field that decays radially away from the ion's center. As an ion approaches a plane of charge, the electric field exerted by the ion is compensated by a deficiency of charge on the electrode (Figure

4.20a) until electrostatic equilibrium is reached. As a second electrode approaches close enough that it interacts with the ion's electric field (Figure 4.20b), charge must be injected into this electrode as well for electrostatic equilibrium to be satisfied. This extra charge that needs to be added to the electrode from the circuit to compensate for pore walls in very close proximity to the counter ion accounts for the larger normalized capacitance of very nanoporous CDCs. This is tantamount to how Li^+ ions cause charge injection into a graphite electrode upon intercalation and the requisite charge storage for Li-ion battery anodes [246], though separation between "pore" walls is significantly greater in the case of electrochemical capacitor electrodes.

4.3. Electrochemistry: Non-aqueous electrolyte studies

To look at the correlation between technologically important electrolyte ions with a closer size to the size of the pores measurable using gas sorption techniques, CDC was studied in a $(CH_3CH_2)_4NBF_4$ electroltye in acetonitrile solvent. Using this electrolyte system affords high conductivity and a large voltage window [70], which is why it is the most commonly used electrolyte in electrochemical capacitors [16]. This can be seen, for example, in Figure 4.21 a for B_4C-CDC chlorinated at 600ºC, 800ºC, and 1000ºC with no solvent decomposition up to at least 2 V and very nice voltammograms at a scan rate of 20 mV s^{-1}. From a technological perspective, in moving from an aqueous electrolyte with a voltage window limited to ~1V to an organic electrolyte with a voltage window in excess of 2 V, there is a substantial increase in both energy density and power density, which is shown for TiC-CDC chlorinated at 500ºC, 600ºC, 800ºC and 1000ºC in a 1M H_2SO_4 electrolyte and 1M $(CH_3CH_2)_4NBF_4$ electrolyte in acetonitrile solvent. Even

despite the lower ionic conductivity of the organic electrolyte, in laboratory test cells, the power density is still substantially higher due to the substantially higher voltage window.

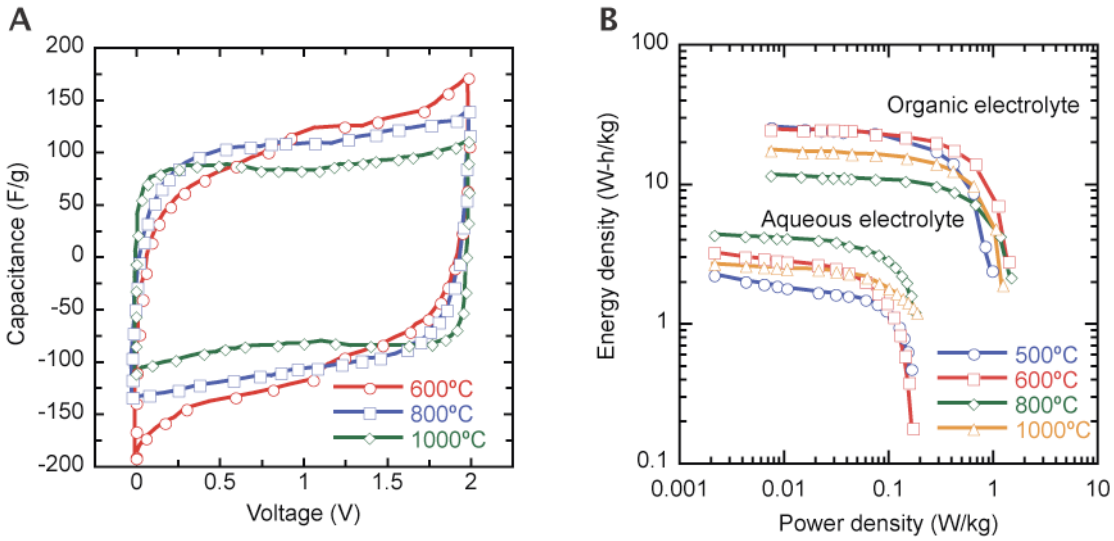

Figure 4.21: a.) Cyclic voltammograms of B_4C-CDC chlorinated at 600ºC, 800ºC, and 1000ºC at a scan rate of 20 mV s^{-1} in 1 M TEA BF_4 electrolyte with acetonitrile solvent. b.) Ragone plot for TiC-CDC chlorinated at 500ºC, 600ºC, 800ºC, and 1000ºC in an aqueous 1M H_2SO_4 electrolyte and a nonaqueous 1 M $(CH_3CH_2)_4NBF_4$ electrolyte in an acetonitrile solvent.

More importantly, in terms of this study, is a solvated ion size that is intermediate between the smallest pore size and largest pore size achievable with CDC [143]. The solvated ion size of TEA^+ and BF_4^- are ~13 Å and ~11.5 Å, respectively.

Initial electrochemical work on organic electrolytes was done by the lab of Prof. Patrice Simon of the University of Paul Sabatier, with subsequent work done at Drexel University. Like prior studies on aqueous electrolytes, CDCs with larger pore sizes were

initially studied, namely Ti_2AlC-CDC and B_4C-CDC. From Figure 4.22a, the capacitance for all CDCs studied is high, approaching or exceeding that of the best-performing commercially available activated carbon, Picactif AC. At very high current densities up to 100 mA cm^{-2}, there is no large falloff in capacitance for any material studied. Also, as the synthesis temperature is increased, there is a decreasing falloff in capacitance at higher current densities (Figure 4.22b).

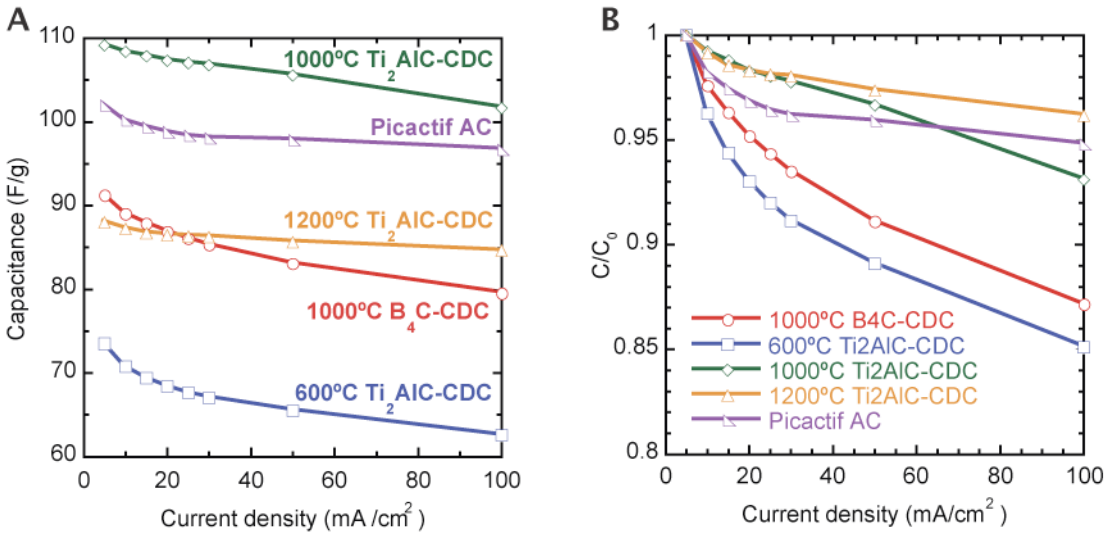

Figure 4.22: a.) Capacitance calculated from galvanostatic charge discharge experiments conducted from 5 mA/cm^2 to 100 mA/cm^2 for B_4C-CDC and Ti_2AlC-CDC chlorinated at different synthesis temperatures as well as commercially available Picactif activated carbon. b.) Capacitance normalized by the capacitance calculated at 5 mA cm^{-2}, C_0, for various CDCs and Picactif AC, highlighting the effect of current density on capacitance.

Normalizing the capacitance by the surface area and plotting it versus current density (Figure 4.23) shows that, in general, there is an increasing normalized capacitance with decreasing pore size as was also seen in work on aqueous sulfuric acid electrolyte (Figure 4.19),. Following the approach previously taken, work was extended to investigate contributions from TiC-CDCs with smaller pore sizes.

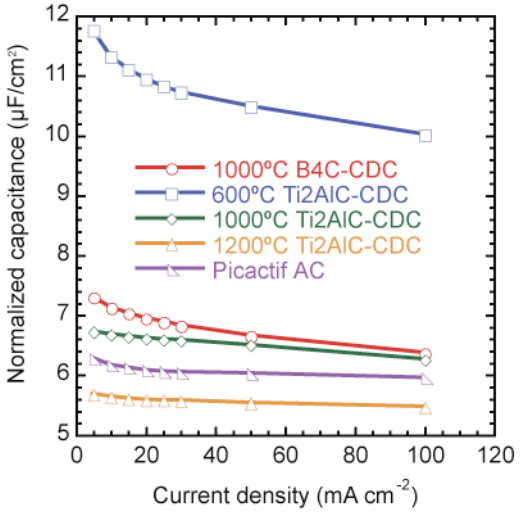

Figure 4.23: Evolution of normalized capacitance with current density for B_4C- and Ti_2AlC-CDCs and Picactif AC

4.3.1. Capacitance of TiC-CDC in $TEABF_4$

Results on aqueous electrolytes showed that CDC synthesized in the temperature range of 500ºC to 1000ºC had a pore structure representative of a wide range of activated carbons, making it a good model system to study the effect of pore size on energy storage. At this stage, no attempt was made to separate contributions from the positive and negative electrode to detect possible ion sieving because most of the pores were larger than the

diameter of the largest unsolvated ion (0.67 nm). Because the smallest pore size measured by Ar sorption was equal to the unsolvated BF_4^- electrolyte ion size, all the surface area available to the electrolyte ions for charge storage was accessible to Ar. Two advanced activated carbons used commercially in supercapacitors, referred to as NMAC (natural material precursor activated carbon) and SMAC (synthetic material precursor activated carbon), were also studied and served as a reference. They had average pore sizes of 1.45 and 1.2 nm and SSAs of 2015 and 2175 m^2/g, respectively. CDCs synthesized from B_4C and Ti_2AlC, which have pore sizes of 1.25 and 2.25 nm, respectively, and SSAs of 1850 and 1150 m^2/g, respectively, were also studied because their pore sizes are close to those of typical activated carbons.

The electrochemical behavior of TiC-CDC is shown in Figure 4.25. These results were repeated in experiments at both Drexel University and the University of Paul Sabatier with minimal deviation. Expanding the voltage to 2.7 V was done on all the cells assembled with various CDCs to test the reversibility; an example with the cell constructed from 700ºC TiC-CDC is given in Figure 4.24. The perfectly linear discharge slope up to 2.7 V is indicative of non-Faradic processes and shows CDC functioned as purely a double-layer capacitor. The capacitance calculated from the discharge slope was identical for all cases from 2.0 V to 2.7 V. Cyclic voltammograms (Figure 4.24) taken at a scan rate of 20 mV/s at increasing voltage windows from 2.0 V to 2.7 V show no obvious peaks attributable to Faradic processes.

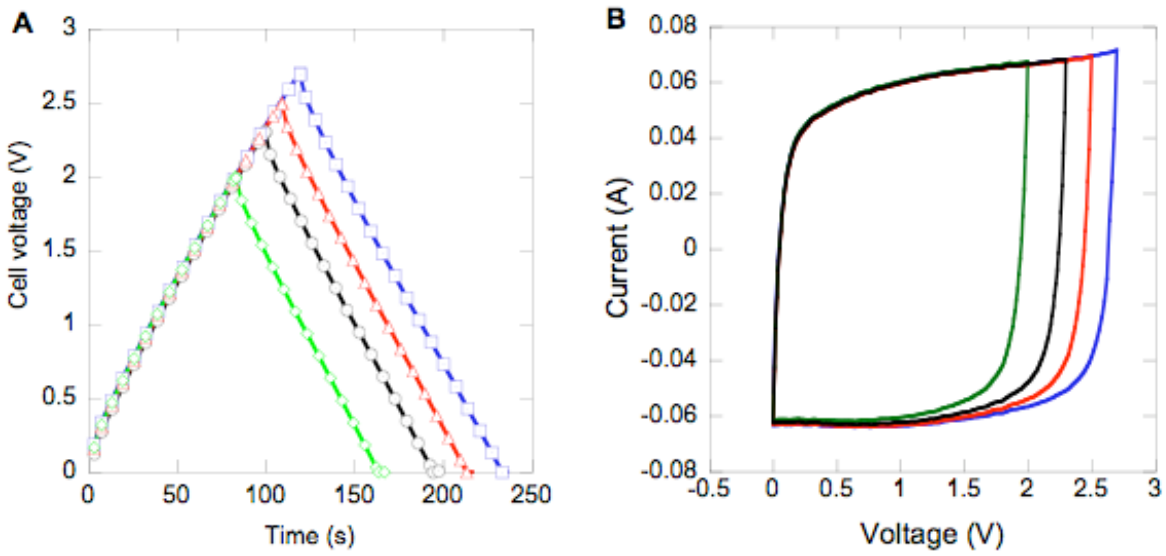

Figure 4.24: Potentiostatic and galvanostatic tests on 700ºC TiC-CDC showing the voltage window characteristic for CDC samples. a.) Charge discharge curves taken at 20 mA/cm^2 at increasing cell voltages from 2.0 V to 2.7 V. The linear discharge profile and identical slopes of the curves show non Faradic response indicating pure double-layer capacitive behavior. Cyclic voltammograms taken at 20 mV/s with increasing voltage windows show identical response and non-Faradic behavior. This shows cells constructed from CDC electrodes to be stable up to at least 2.7 V. [219]

Even for the sample with the smallest pore size (500ºC TiC-CDC), there was only a minimal decrease in specific capacitance when the current density was increased from 5 to 100 mA/cm^2 (Figure 4.25 b), which illustrates the minimal change in frequency response behavior. NMAC and SMAC, which have pore sizes similar to those of TiC-CDC at 1000ºC, had time constants similar to those of 800ºC TiC-CDC, owing to the higher bulk conductivity of CDC. The opposite trend was found in the behavior of

capacitance, however: Both the specific (gravimetric) and volumetric (capacitance per unit bulk volume of carbon) capacitances decreased with increasing synthesis temperature (Figure 4.25 a). With an increase in the chlorination temperature from 500º to 1000ºC, the specific capacitance decreased by ~40%, from ~140 to ~100 F/g, although the SSA increased by ~60%, from 1000 to 1600 m^2/g.

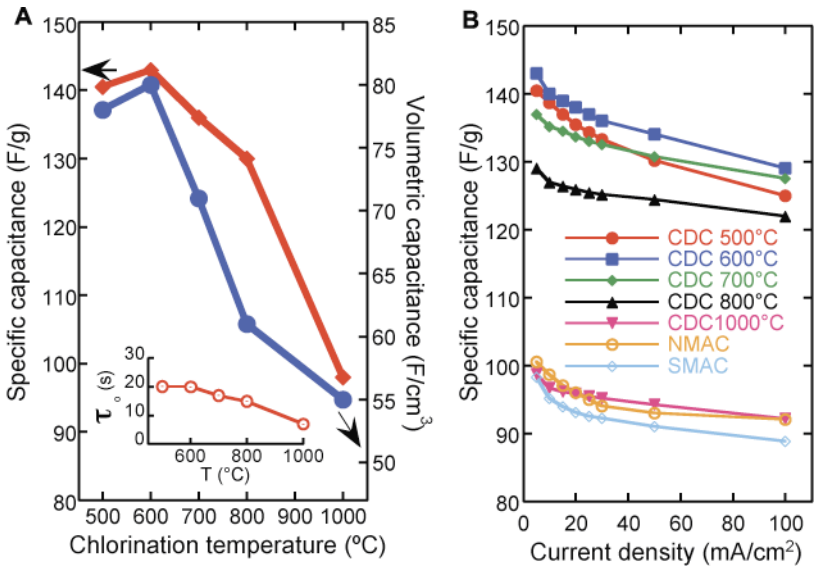

Figure 4.25: Electrochemical behavior of TiC-CDC synthesized in the range of 500ºC to 1000ºC. a.) Specific capacitance and volumetric capacitance both decreased with synthesis temperature. The maximum error reported in specific and volumetric capacitance was 2.5 and 6% , respectively. Maximum capacitance was at 600ºC synthesis temperature. NMAC and SMAC characteristics are 100 F/g, 33 F/cm^3 and 95 F/g, 45 F/cm^3, respectively, under the same conditions. The plot of characteristic time constant, τ_0, versus synthesis temperature (inset), showed slightly increasing frequency response with temperature. Comparison of TiC-CDC charge-discharge behavior with commercially available carbons (B) shows that by using rational design, a 50% improvement can be achieved. There was also very little capacitance fading at current densities up to 100 mA/cm^2, even for the 500ºC sample. [219]

As was done in Section 4.2.3 the specific capacitance was normalized by SSA, and plotted with respect to pore size (Figure 4.26 a). For TiC-CDC in a $(CH_3CH_2)_4NBF_4$ electrolyte, increasing the pore size appeared to have a detrimental effect on the normalized capacitance. These results are particularly interesting because the high capacitance of some carbons with pore sizes smaller than 1 nm has been noted before [131, 155] in this electrolyte system with relatively large ions, but a model to explain this behavior has been lacking, and large pores are still considered optimal by most [247].

As was seen in aqueous electrolytes with relatively small ions (Figure 4.19), Figure 4.26a shows that there is a trend of decreasing normalized capacitance when the pore size is reduced to ~1 nm, based on data from this study and [121, 131]. TiC-CDC synthesized at 1000ºC, B_4C-CDC, Ti_2AlC-CDC, NMAC, and SMAC all manifested this behavior, which demonstrated that this size effect was independent of the carbon material used. However, at a pore size below a critical value, as seen with TiC-CDC synthesized below 1000ºC, the trend reversed and there was a sharp increase in capacitance with decreasing pore size. Two other carbons with small pores [121] follow the same trend.

In region I of Figure 4.26A, when pores were substantially larger than twice the size of the solvated ions (Figure 4.26 b), there was a contribution to capacitance from compact layers of ions residing on both adjacent pore walls. Decreasing the pore size to less than twice the solvated ion size (Figure 4.26 c) reduced the normalized capacitance (Figure 4.26 a, region II) because compact ion layers from adjacent pore walls impinged and the surface area usable for double-layer formation was reduced.

This would largely account for the decrease in specific capacitance with pore-size reduction for pore sizes greater than ~1 nm. This trend reversed with a further decrease in the pore size to less than that of the solvated ion size (Figure 4.26 d, region III). which lends credence to understandings developed using aqueous electrolytes. Decreasing the pore size to a value approaching the crystallographic diameter of the ion led to a 100% increase in normalized capacitance for the same reasons outlined in Section 4.2.3.

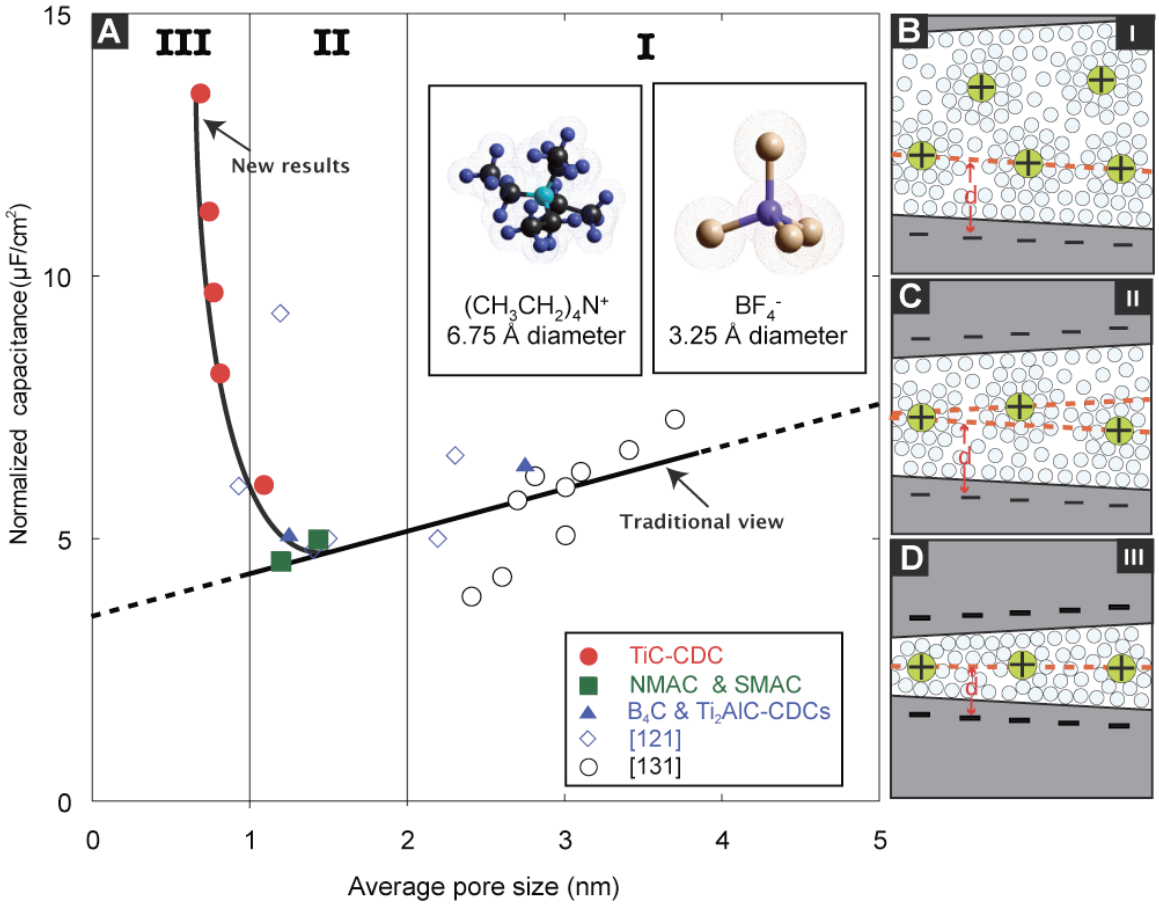

Figure 4.26: a.) Plot of specific capacitance normalized by the BET specific surface area for the carbons in this study and in two other studies with identical electrolytes. The normalized capacitance decreased with decreasing pore size until a critical value was reached, unlike the traditional view, which assumed that capacitance continually decreased. It would be expected that as the pore size becomes large enough to accommodate diffuse charge layers, the capacitance would approach a constant value. b.-d.) Schematics of solvated ions residing in pores with distance between adjacent walls b.) greater than 2 nm, c.) between 1 and 2 nm, and d.) less than 1 nm illustrate this behavior schematically. [219]

When the capacitance data from Figure 4.25 for pore sizes smaller than the size of the solvated ion (~1 nm) were plotted against the reciprocal of the pore size, a linear relation was obtained (Figure 4.27). As all the pores in this study are smaller than the size of both solvated ions, there must be at least partial desolvation, which complicates matters. From Dzubiella and Hansen showed that under a potential, there is substantial ion motion and diminished dielectric permittivity in pores less than the size of their solvation shells [248]. The distortion of solvation shells in small pores of carbon nanostructures was also reported recently [249-251].

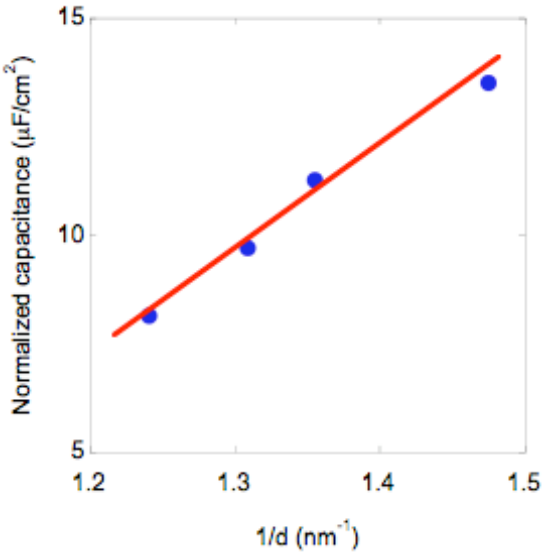

Figure 4.27: Plot of normalized capacitance versus the average distance from the charged ion center to the pore wall for samples with average pore size less than that of the solvated ion. The linear behavior indicates that the normalized capacitance is inversely proportional to this distance. [219]

Even for the organic electrolyte studied, this simplified model, which assumes planar pore surface and constant dielectric permittivity, has important implications. The effects

of surface curvature and decreasing dielectric permittivity should decrease the capacitance, which showed the dominance of the *1/d* term. A slope of ~1 F/m is commensurate with the permittivity of vacuum, more so than the permittivity of the solvent. Whereas templated carbons achieve improved specific capacitance by an increase in the pore size (Figure 4.26a, region I, and 3 b), resulting in low volumetric capacitance, our model suggests that using microporous carbons with pores smaller than 1 nm allows the volumetric capacitance to increase from 55 to 80 F/cm^3 (Figure 4.25 a).

4.3.2. Individual ion effect: 3-electrode cell for studying TEA^+ vs. BF_4^- adsorption in TiC-CDCs

Because the size of the TEA^+ cation and BF_4^- anion are different, it would be expected that their individual contribution to capacitance would be different. Whereas the prior study found an average contribution from both ions, modifying the cell design to include a silver quasi-reference electrode without compromising performance allowed us study of each ion individually. It is assumed that the silver concentration around the wire is constant therefore giving a somewhat stable reference potential, but since we are not necessarily probing formal redox potentials, this setup allows good cell performance in terms of minimizing resistances while still offering the ability to separate contributions from the anode and cathode. As expected, from the pore-size distributions for the titanium-carbide–derived carbon (TiC-CDC) used in this study, it is apparent that all samples have pores smaller than the solvated ions (see Figure 4.28), which will not allow ions to enter completely solvated.

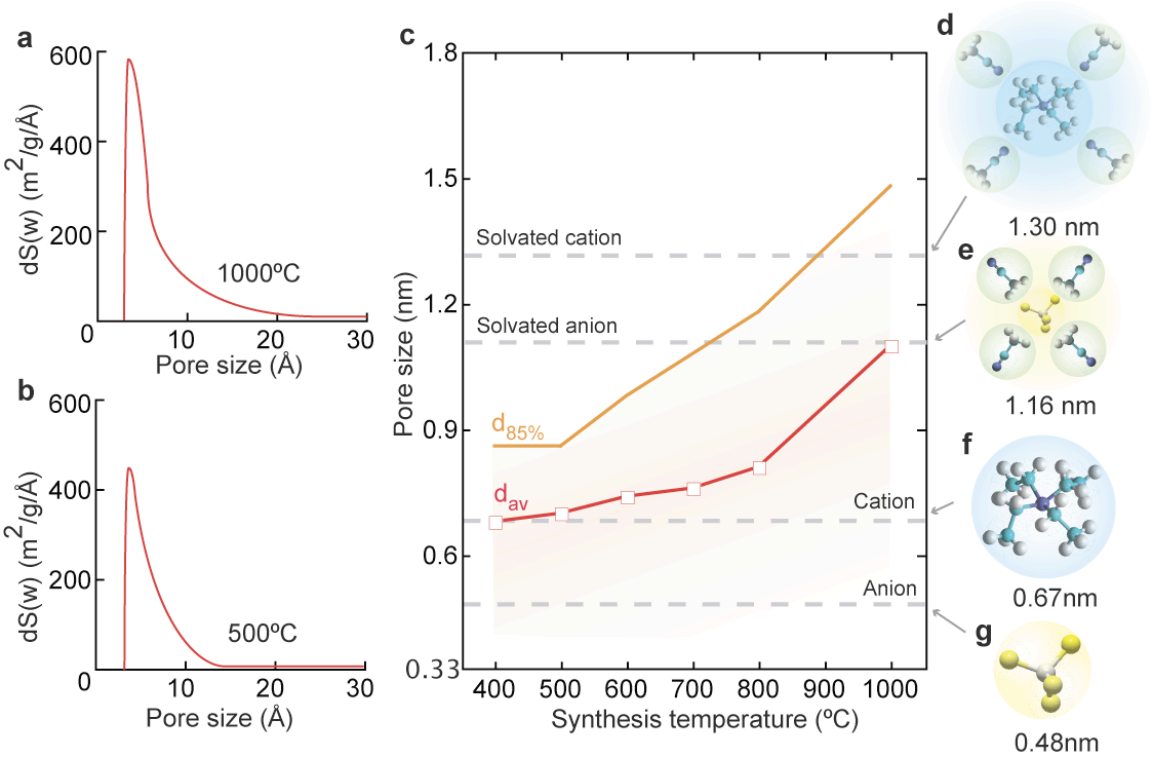

Figure 4.28: Pore size evolution and comparison with the sizes of the electrolyte ions. Pore size distributions calculated assuming slit-shaped pores for TiC-CDC synthesized at a.) 1000ºC and b.) 500ºC (fitted DFT distribution curves). A plot of the average pore size, d_{av}, versus the synthesis temperature c.) shows the pore size increase from the size of the unsolvated cation (about 0.67 nm) to about 1.0 nm. The schematic representation of the d.) solvated $(CH_3CH_2)_4N^+$ cation, e.) solvated BF_4^- anion show their sizes, in relation to the average pore sizes shown in c.). In general, the pore size distribution shifts to larger pore sizes with increasing synthesis temperature, but the majority of pores are still smaller than the size of the solvated ions. Also, at all synthesis temperatures, at least 85% of the pores, $d_{85\%}$, are smaller than the sizez of the ion with a sheath of solvent molecules around it. The smallest pore size resolvable using this technique is 0.33 nm [252].

The cyclic voltammograms obtained between 0 and 2.3 V, thereby monitoring the current response at each electrode for samples synthesized at 500 (Figure 4.29 a) and 1000ºC (Figure 4.29 b), are representative of all the samples studied. These voltammograms show no electron-transfer processes occurring on either electrode within the studied potential range. Therefore each electrolyte ion shows only capacitive currents. Also, the different potential ranges traduced for the positive and negative electrodes at different synthesis temperatures indicate different behaviors as the pore size is changed.

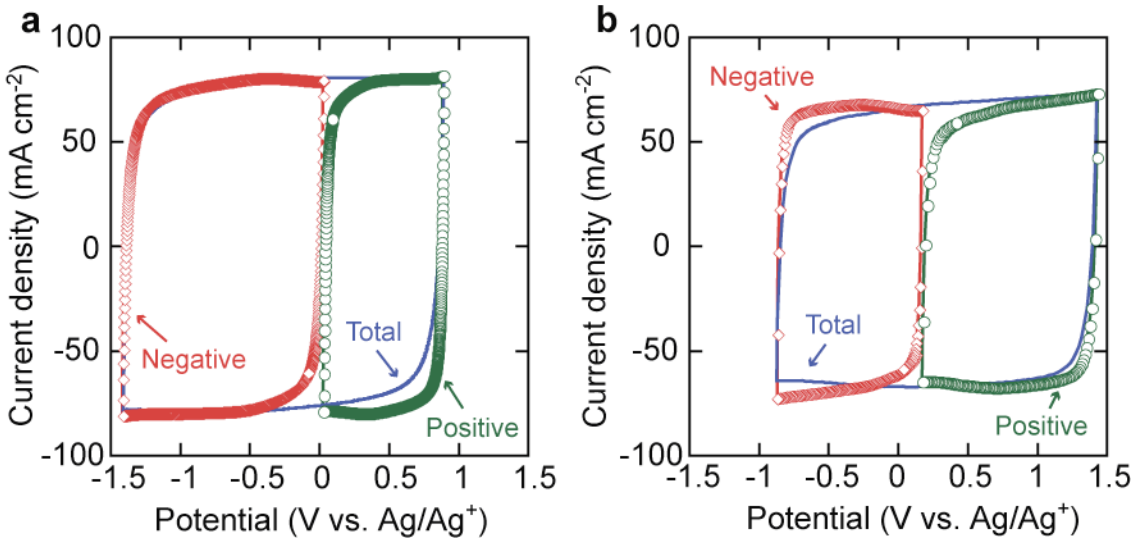

Figure 4.29: Cyclic voltammograms (CVs) taken at a scan rate of 20 mV s^{-1} on samples synthesized at a.) 500ºC and b.) 800ºC. The plot of total current density versus potential represent the response of both the positive and negative electrodes as the potential is scanned. The positive and negative electrode responses are separated from one another using a third silver quasi-reference electrode placed between the electrodes. As the current in the cell is limited by the lower capacitance electrode, the different sizes of the voltage windows in a CV plot are indicative of different capacitance values at the positive and negative electrodes. This is most clearly reflected in the TiC-CDC sample synthesized at 500ºC [252].

From Figure 4.30 it is apparent that the double-layer capacitance caused by the anion (C_-) and cation (C_+) at the positive and negative electrodes, respectively, have different behaviors with regards to the pore size. The anion/positive electrode has a relatively constant double-layer capacitance at pore sizes between 0.8 and 1.1 nm. At average pore sizes below 0.8 nm, there is a sharp increase in the double-layer capacitance. For the

cation/negative electrode, there is a slight increase in the capacitance upon decreasing the pore size from 1.1 to 0.75 nm, but at pore sizes below this value, the capacitance decreases slightly, which may be attributed to the presence of pore bottlenecks smaller than the ion or to an insufficient electrical conductivity of the CDC produced at 400ºC. This follows similar trends uncovered in 2-electrode cell configurations for both aqueous (Section 0) and organic (0) electrolyes. The maximum in capacitance for each ion/electrode system is shifted to smaller pores for the smaller ion (anion). A similar dependence was observed for the capacitance normalized by the area. It should also be noted that the sharp increase in capacitance for the anion/positive electrode system is far more profound than that of the cation/negative electrode one.

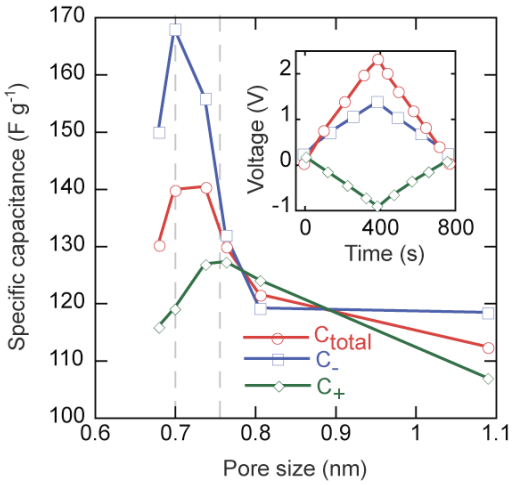

Figure 4.30: Dependence of the capacitance on the pore size. The specific capacitances calculated from a constant current discharge (inset, colors as for main plot) for the anion/positive electrode (C-) and cation/negative electrode (C+) systems show similar behaviors until a critical pore size of about 0.8 nm is reached. At pore sizes below this value, the anion/positive electrode and cation/negative electrode capacitances diverge [252].

If we used the ammonium salt $(CH_3)_4NBF_4$ instead (where the anion and cation have roughly the same size), the capacitance would be expected to be similar at both electrodes, but low solubility of this electrolyte limits its practical importance [70]. Most of the pores considered herein are equal to (or smaller than) a single ion with a single associated solvent molecule (Figure 4.31), and decreasing the pore size decreases the volume available for double-layer accumulation. Therefore, the ions must be at least partially stripped of solvent molecules to occupy the carbon pores in this study. This process can be compared to Li^+ insertion into graphite in Li-ion batteries [253], with complete removal of the solvation shell and a change in the oxidation state of carbon [254].

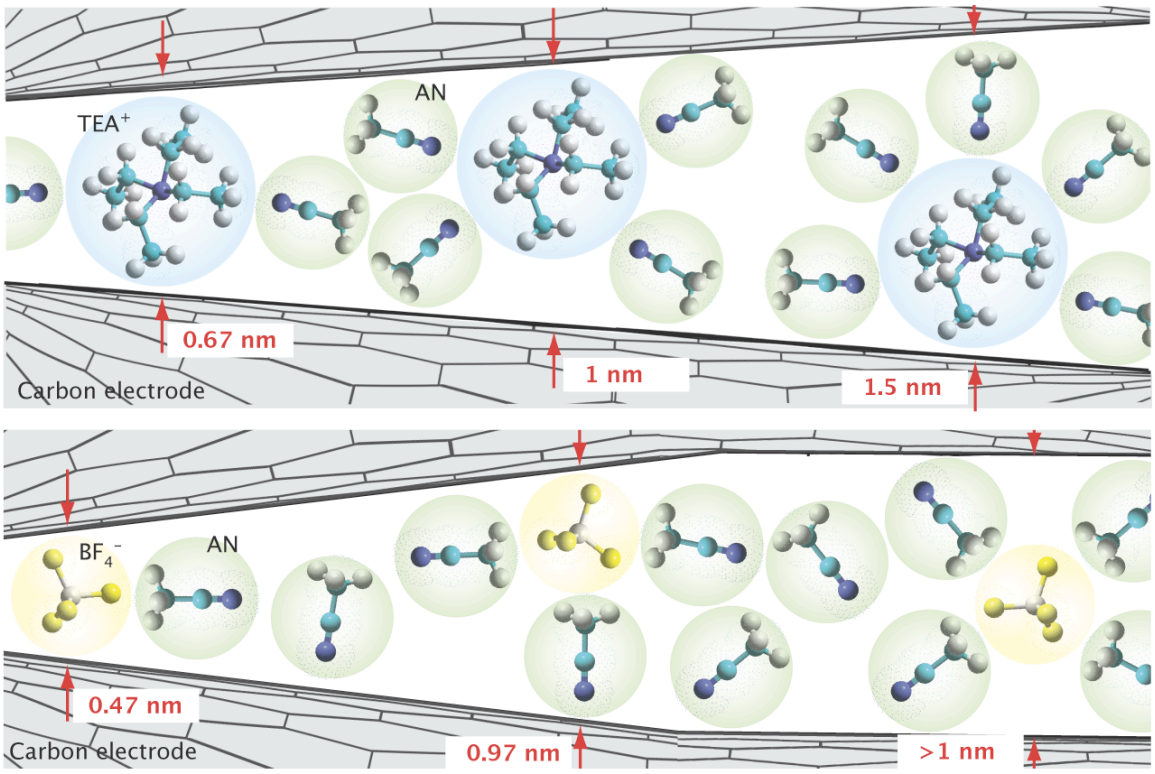

Figure 4.31: Geometric confinement of ions in extremely small pores. Both the anions and cations enter the pores with no solvent molecule screening charge at pore sizes below 1.5 and 1 nm, respectively. Therefore, it can be asserted that in all of our experiments, the ions enter the pores either bare or with partial solvent shells. (TEA^+ = tetraethylammonium, AN = acetonitrile, BF_4^- = tetrafluoroborate) [252]

Desolvation in such a weakly solvated electrolyte is not surprising, however. Recent modeling work [255] and experiments [256] suggest that the structure of water and the solvation of ions are different in nanopores than in bulk; for instance, Tanimura et al. [257, 258] showed by means of molecular dynamics simulations that alkaline cations are stripped of their hydration shells and passed into the interior of a carbon nanotube at a

charge density below 3 $mFcm^{-2}$ (at 1 V), which is a quantity that is easily accessible experimentally. This result is not surprising considering that desolvation of ions by biological voltage-gated ion channels happens readily [229] at much lower potentials. The flux of ions across these channels can be as high as 10^7 s^{-1}, which shows not only that this process happens, but also that it happens extremely quickly. Unfortunately, high-level theoretical work in the electrochemical capacitor community is still not mature enough to be able to explain this anomalous capacitance increase found in carbons with extremely small pores. The first attempt to provide an explanation of the capacitance increase in small pores observed by our group [247] used mechanistic models that simply explained the double-layer structure in terms of ions adsorbed on the inside of a cylinder instead of on a plane of charge. The model does not offer predictive capacity, though, or even the ability to determine optimum conditions for maximizing performance.

4.3.3. Ionic liquids: Capacitance of TiC-CDC in EMI-TFSI

To remove the complexity associated with ion solvation, work was done on the same TiC-CDC system in a solventless ionic liquid comprised of Ethyl-MethylImidazolium-bis(TriFluoro-methane-Sulfonyl)Imide (EMI-TFSI) (Figure 4.32). Ion sizes were calculated as 0.79 nm and 0.76 nm in the longest dimension for TFSI and EMI ions respectively. Because of thermal effects, the ion size in solution is expected to be equal to the size of a sphere carved out by a rotating ion, or the size of the ion's longest dimension. Because of the near identical size of the anion and cation, it was initially assumed that approximately the same pore size is required for carbon anode and cathode.

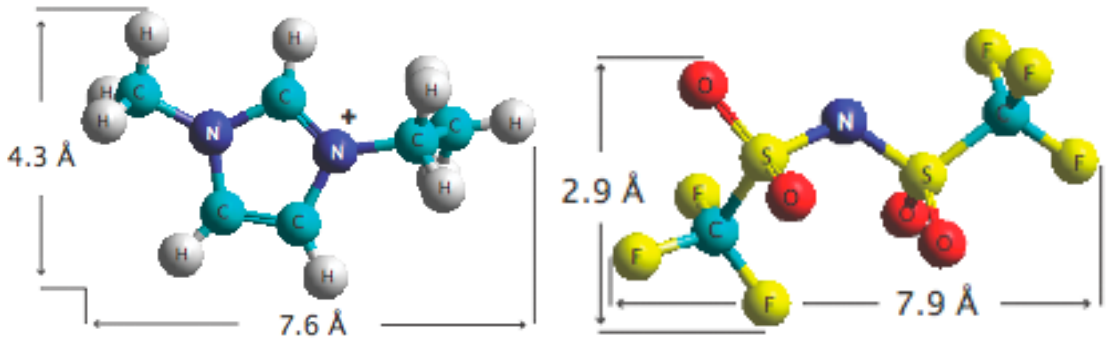

Figure 4.32: Geometrically optimized molecular models of a.) Ethyl-MethylImidazolium (EMI) cation and b.) bis(Trifluoro-methane-Sulfonyl)Imide (TFSI) anion.

Electrochemical characterization of ionic liquids was conducted at the University of Paul Sabatier at 60°C because of the very low ionic conductivity of EMI-TFSI at room temperature. Cyclic voltammetry at 20 mV/s and galvanostatic experiments (from 5 up to 100 mA/cm²) were conducted between 0 and 3 V in 2-electrode cells (Figure 4.34). The voltammogram shows fast saturation in current to a constant value, indicating no large limitations of conductivity in narrow nanopores. Even for the TiC-CDC sample chlorinated at 400ºC, the voltammogram is rectangular, which highlights the accessibility of very fine pores, even for electrolytes with large ion sizes and limited ionic conductivity. Even up to a cell voltage of 3 V, there are no Faradaic reactions visible showing the potential for very high energy density.

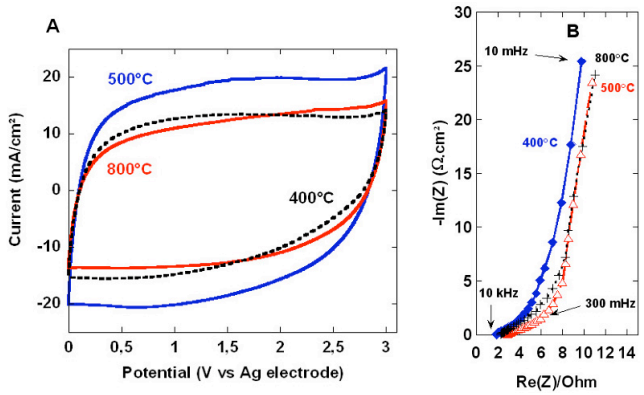

Figure 4.33: a.) Cyclic voltammetry at a scan rate of 20 mV/s and b.) Electrochemical Impedance Spectroscopy (EIS) plots between 10 kHz and 10 mHz for the 400, 500 and 800°C samples, in EMI-TFSI electrolyte at 60°C [259].

EIS plots are typical of EDLC behavior seen in traditional [260, 261] and solventless [72] electrolytes . At high frequency, the ESR is on the order of 1 $\Omega.cm^2$, which is good considering the low ionic conductivity of the electrolyte. At intermediate frequencies there is a characteristic region with a 45º slope, and at low frequency the slope is near parallel with the imaginary impedance axis, indicating good cell behavior. Galvanostatic plots for the lowest synthesis temperature samples, 400ºC TiC-CDC (Figure 4.34a) and 500ºC TiC-CDC (Figure 4.34b) are linear for both charging from 0 V to 3 V and discharging back to 0V.

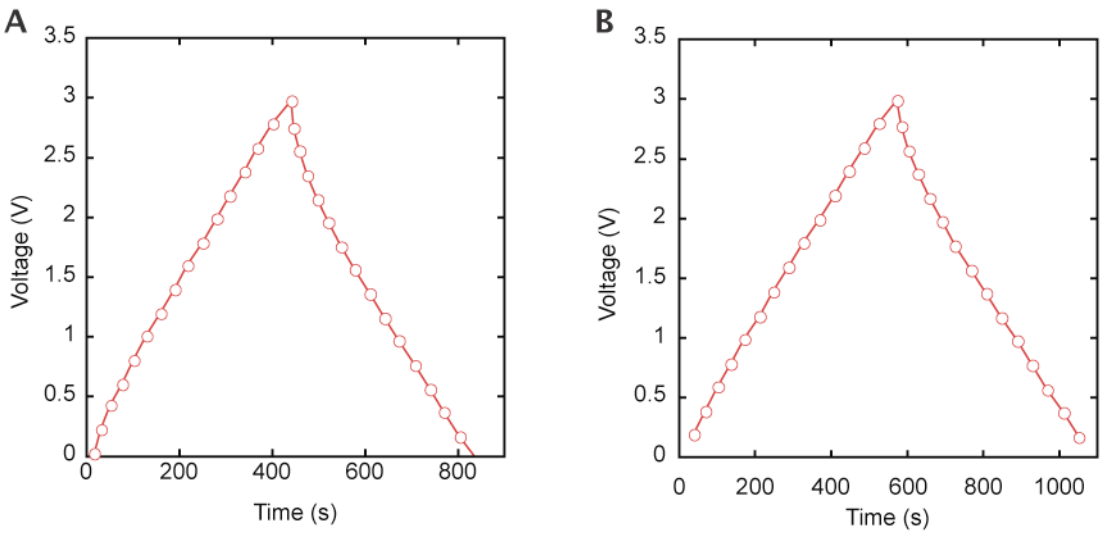

Figure 4.34: Charge-discharge plots from galvanostatic measurements of TiC-CDC chlorinated at a.) 400°C and b.) 500°C cycled from 0 V to 3 V at 5 mA/cm² [259].

Figure 4.35 shows the change of the CDC specific capacitance (F/g) with chlorination temperature, calculated from galvanostatic charge-discharge experiments conducted at 5 mA/cm². This plot is in excellent agreement with results obtained for both aqueous and organic electrolyte solutions, the capacitance decreases as the synthesis temperature increases from 500°C to 1000°C. It is also important to mention that the capacitance values of these CDCs are more than 140 F/g and 80 F/cm^3, while standard activated carbons with large and broader pore size distributions are known to have capacitance values lower than 100 F/g and 50 F/cm^3 in ionic liquids [66, 71, 154]. We confirmed it by conducting measurements on a commercial activated carbon from Kuraray and receiving 91 F/g and 45 F/cm^3 under the same conditions.

As was shown for 3-electrode measurements of TiC-CDC in the organic tetraethylammonium tetrafluoroborate electrolyte, as the synthesis temperature decreases below 500ºC and pore size decreases below 0.7 nm, the capacitance decreases. From simple geometrical considerations, this occurs because the pores are simply too small to be accessed by the electrolyte ions, which in this case are ~0.75 nm and ~0.8 nm for the cation and anion, respectively.

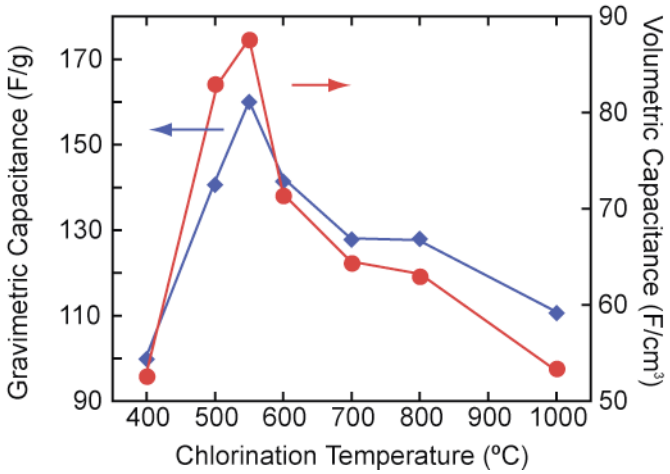

Figure 4.35: Specific gravimetric (F/g) and volumetric (F/cm^3) capacitances change versus the chlorination temperature for CDC electrodes tested in neat EMI-TFSI electrolyte at 60ºC. A standard activated carbon designed for organic electrolyte-based electrochemical capacitors reached 90 F/g and 45 F/cm^3 under the same experimental conditions.

As was done in the aqueous and organic electrolytes previously, the gravimetric capacitance was normalized by the specific surface area and plotted versus the CDC pore size (Figure 4.36). Figure 4.36 clearly points out the pore size effect. When the pore size decreases from 1.1 to 0.7 nm, the normalized capacitance increases, as was shown previously. A maximum in normalized capacitance is reached at ~0.7 nm – further decrease in pore size causes limitations in ion accessibility and a requisite decrease in the normalize capacitance. This pore size matches almost precisely the ion size of the electrolyte. The slightly smaller pore size indicates that the electrolyte, which has an aspect ratio less than one, most likely enters the pores with the longest dimension pointed down the length of the pore. Also, removing solvent effects gave the opportunity to definitively show that precisely matching the ion size with the pore size is the equation for maximizing performance.

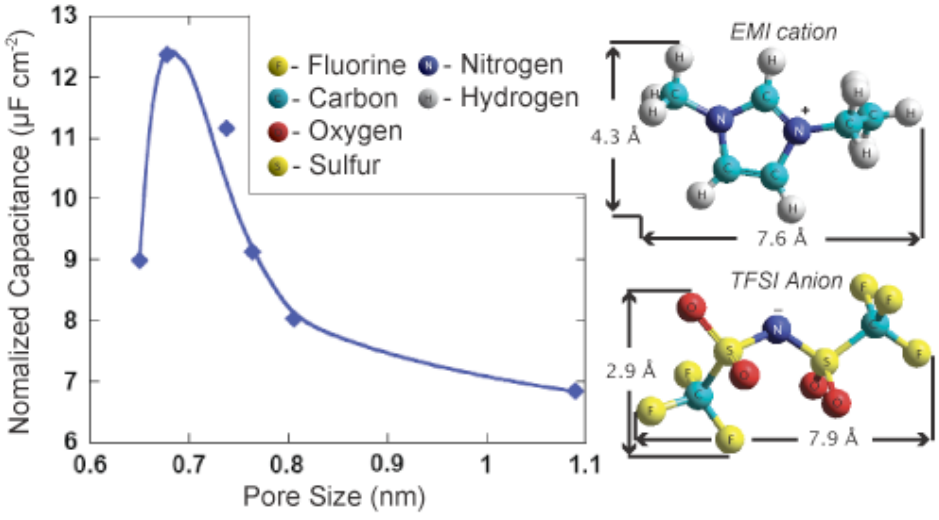

Figure 4.36: Normalized capacitance change versus pore size of TiC-CDC. [259]

4.3.4. Individual ion effect: 3-electrode cell for studying EMI^+ vs. $TFSI^-$ adsorption in TiC-CDCs

Like prior studies on CDC in $TEABF_4$ and aqueous electrolytes, the 2-terminal cell was modified to allow investigation of processes occurring at each electrode by inserting a silver quasi-reference electrode between the anode and cathode. Figure 4.37 shows the normalized capacitance of neat EMI-TFSI at both the anode and cathode versus the pore size of the TiC-CDC used.

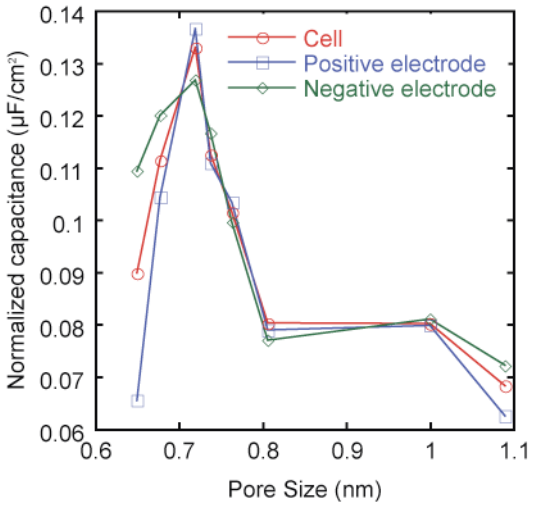

Figure 4.37: Normalized capacitance vs. pore size of the positive electrode, negative electrode and cell for TiC-CDC synthesized from 400ºC to 1000ºC in neat EMI-TFSI (Results collected by R. Lin)

Comparing the cell plot in Figure 4.37 with Figure 4.36, it is obvious that the shapes of the plots are nearly identical, showing that the 3-electrode cell represents the cell behavior very well. The normalized capacitance is relatively constant from the largest pore size studied, ~1 nm down to ~0.8 nm. At pore sizes between ~0.8 nm and ~0.75 nm, the normalized capacitance almost doubles from ~7.5 μF cm^{-2} to ~13.5 μF cm^{-2}. At pore sizes smaller than this, the normalized capacitance decreases as pores become inaccessible to the electrolyte, but are still large enough to be measured by gas molecules for SSA calculation. Unlike Figure 4.30, which shows the normalized capacitance of the anode and cathode of TiC-CDC in tetraethylammonium tetrafluoroborate diverging greatly at pore sizes less than ~0.75 nm, Figure 4.37 shows nearly identical normalized capacitance down below a pore size of ~0.7 nm. The difference in behavior is due to the difference in relative ion sizes between the anion and cation of tetraethylammonium tetrafluoroborate in Figure 4.30 and the anion and cation of EMI-TFSI in Figure 4.37. In $TEABF_4$, the anion is ~25% smaller than the cation (Figure 4.28), whereas the anion and cation are roughly the same size for EMI-TFSI (Figure 4.32). Interesting, though, because the EMI cation is ~5% smaller than the TFSI anion, when the pore size decreases below ~0.68 nm, the capacitance behavior of the positive electrode and negative electrode diverge, favoring the negative electrode and adsorption of the slightly smaller EMI cation. This shows the power of simply designing electrodes by matching the size of their pores to the size of the ions being used. Further, matching the size of the anion and cation seem to push this point even further.

Considering at the BF_4^- anion has higher capacitance (170 F/g) than both the EMI cation (158 F/g) and TFSI anion (165 F/g), but the cell capacitance of the EMI-TFSI ionic liquid is higher, it is evident that the lower capacitance of the $(CH_3CH_2)_4N^+$ cation is limiting.

Because of this, the electrode with the smallest capacitance most strongly influences the total capacitance. Therefore, not only is matching the ion size with the pore size a rational equation for maximizing capacitance, also, choosing ions of similar dimension (including solvent effects in traditional electrolytes) to match individual electrode capacitances maximizes the capacitance of the cell.

4.3.5. Effect of adding solvent to neat EMI-TFSI ionic liquid

To determine to what extent solvent plays on ion size selectivity in pores of different size, acetonitrile was added to our EMI-TFSI.

Electrochemical measurements on 1 M EMI-TFSI in acetonitrile are summarized in Figure 4.38. A maximum capacitance of 130 F/g is obtained for 800ºC TiC-CDC, with decaying capacitance at chlorination temperatures above and below this. Adding acetonitrile decreased the capacitance ~20% from the value in neat EMI-TFSI.

This decrease in capacitance of acetonitrile solvated EMI-TFSI below neat EMI-TFSI is probably due to a decreasing number of ions available for charge storage on the electrode surface because of dilution over the neat case, as well as an increase in the effective ion size, limiting the surface area available for charge storage. This latter point is also reflected in the shift of capacitance maximum occurring for TiC-CDC synthesized at

550ºC with a pore size of ~0.7 nm to 800ºC TiC-CDC with an average pore size of ~0.8 nm.

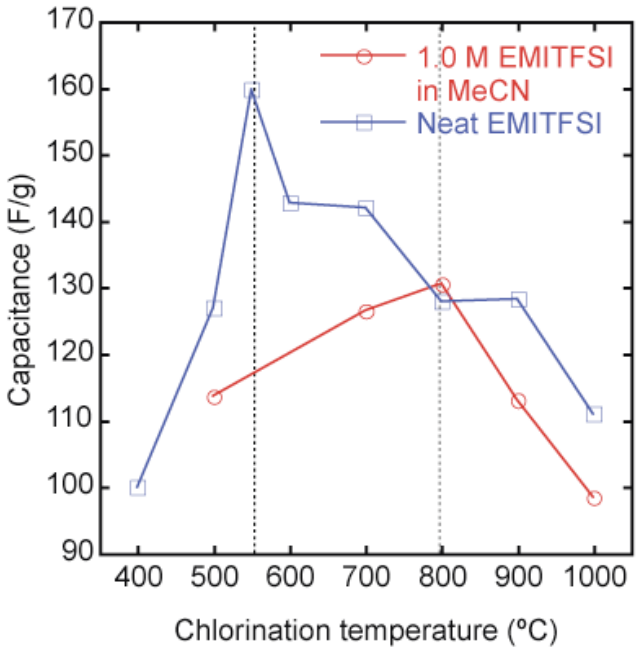

Figure 4.38: Capacitance versus chlorination temperature for TiC-CDC synthesized from 400ºC to 1000ºC in both neat EMI-TFSI and 1M EMI-TFSI in acetonitrile

The results are particularly interesting, because both the conductivity increases and the viscosity decreases in adding solvent to the neat ionic liquid. Though these results fit into our ion size – pore size correlation model well, predicting them without a great deal of insight is next to impossible.

4.4. Microelectrode studies on CDCs

4.4.1. Studies on CDCs in 1M H_2SO_4 – effect of pore size on capacitance – or, Hindsight: The way I should have done it

Improving the experimental electrochemical techniques substantially, from taking a few days for cell fabrication and testing to a few minutes or so could allow large enough datasets to be generated to potentially point theorists in a more proper direction. As an example of the speed of the CME technique, the study on a few CDCs shown in Section 0 was expanded to look at all CDCs studied in Section 4.2.3 (Figure 4.39). As seen in Figure 4.39, for different CDC precursors the capacitance has a different coupling with synthesis temperature. This is similar to what is seen in Figure 4.18. In general there is an increasing average current as the synthesis temperature decreases, until some critical value is reached. With further reduction in synthesis temperature there is a decrease in average current. It should be noted that these experiments were performed by Grady Betzel a first year undergraduate student under my supervision, with reliable data being generated after only a few hours of training. In contrast, the corresponding data in Figure 4.18 was collected over months by myself and because of the small intricacies in cell design, would require months of work by an experienced graduate student to duplicate.

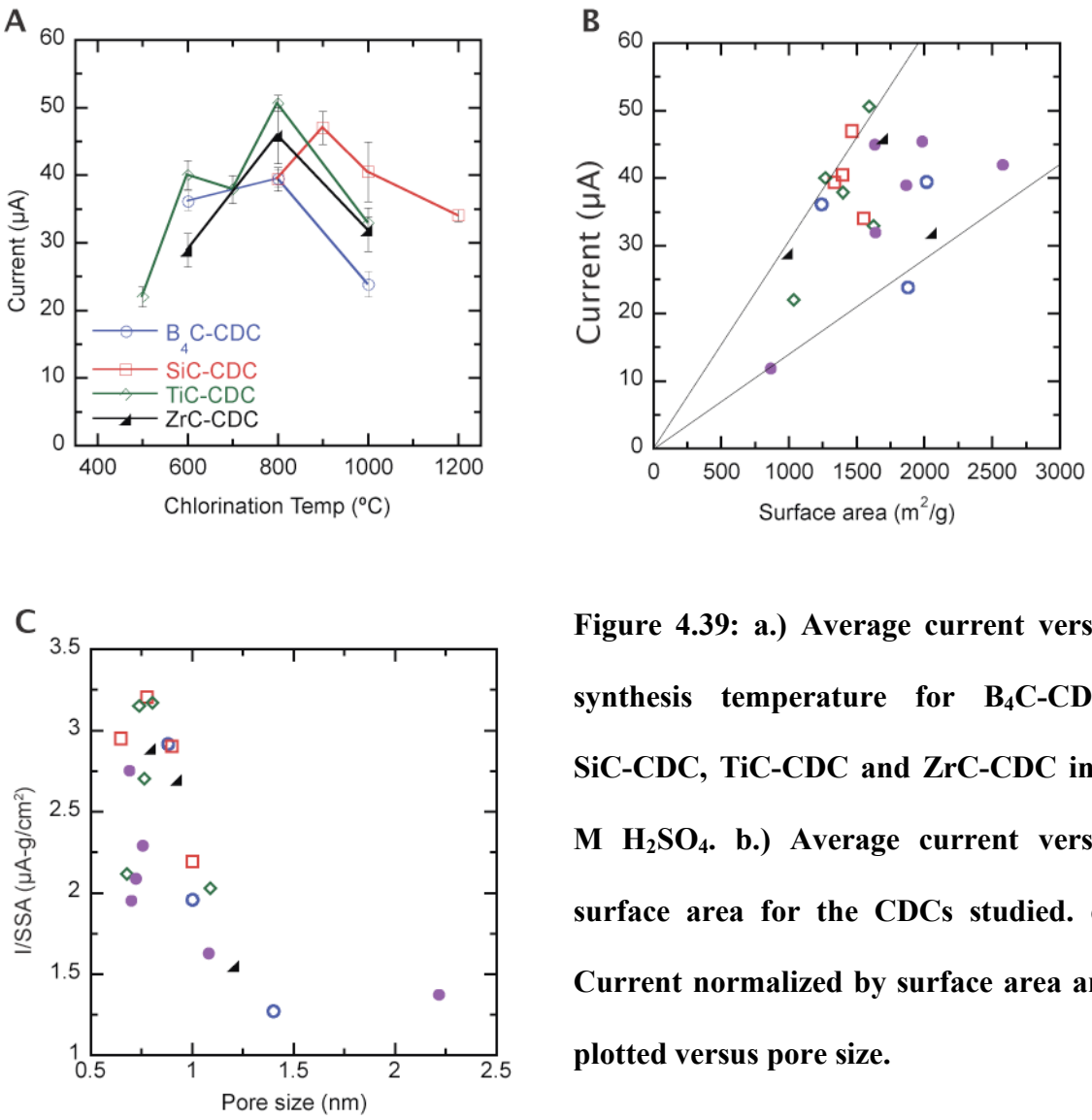

Figure 4.39: a.) Average current versus synthesis temperature for B_4C-CDC, SiC-CDC, TiC-CDC and ZrC-CDC in 1 M H_2SO_4. b.) Average current versus surface area for the CDCs studied. c.) Current normalized by surface area and plotted versus pore size.

Plotting the average current versus specific surface area, shows that, in general, capacitance (average current divided by scan rate, in this case) increases with increasing surface area, though there is a large amount of data scatter. Even when CDCs from individual precursors are considered individually, no real correlations can be made.

Of course, at this point we know that capacitance is a strong function of pore size in all the electrolytes studied, and probably ALL electrolytes. So following the methodology laid out in Sections 4.2.3 and 0, the average current for each CDC was normalized by its surface area and plotted versus its average pore size. As can be seen from Figure 4.39C, as the pore size decreases, there is an increasing normalized current for all CDC precursors studied. This small study shows the power of the CME technique to precisely replicate insights gained on full-sized cells, even nuanced behaviors that have taken years to fully develop. As an aside, too bad the CME technique was not an established technique in the beginning of my PhD studies – very much time could have been saved! ;-)

4.4.2. Simultaneously varying pore size and ion size - Alkyl chloride // TiC-CDC system study

Following work on controlling the CDC pore size and studying its effect on capacitance in a single electrolyte, work was extended using the CME technique to understand the effect of simultaneously varying the effective ion size and pore size. A similar study was conducted by Salitra [115] that showed K^+ had the smallest effective ion size of Li^+, Na^+ and K^+ and led to the largest capacitance, though more or less random carbon samples were chosen. For this study, TiC-CDC was chosen as the carbon material because it was the best-studied material and 1 M alkyl chloride electrolytes were used because there is ample data available on their properties. The effective ion size of Li^+, Na^+, K^+, Rb^+, and Cs^+ ions are given in [262].

Electrochemical measurements were made by doing cyclic voltammetry on a negatively polarized working electrode between the open circuit potential and 1 V vs. a platinum quasi-reference electrode at a scan rate of 50 mV/s. The current was averaged over the entire potential window scanned. Figure 4.40 shows the average current for TiC-CDC synthesized at 500ºC, 600ºC, 800ºC and 1000ºC in 1M electrolytes of LiCl, NaCl, RbCl and CsCl.

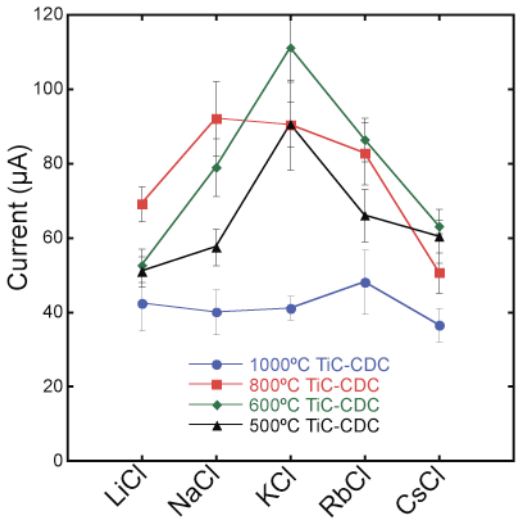

Figure 4.40: Average current obtained for LiCl, NaCl, KCl, RbCl and CsCl electrolytes with TiC-CDCs chlorinated between 500ºC and 1000ºC

Because the cells were negatively polarized, the cation should be adsorbed and have the largest contribution to capacitance. This allows us to monitor the effect of changing the ion size (Figure 4.40) on electrochemical properties. In moving from 1 M LiCl, which

has the smallest crystallographic ion size, through to 1 M CsCl, which has the largest crystallographic ion size, the electrochemical behavior differs depending on the synthesis temperature of the TiC-CDC. At the highest synthesis temperature, which has the largest pore size, all electrolytes have very similar electrochemical behavior. Essentially all of the pores are large enough to accommodate all of the ions and the conductivity of all of the electrolyte solutions is high enough to allow ions to completely percolate through the structure. As the synthesis temperature decreases to 800ºC, the average current for all electrolytes increases as the CDC pore size decreases. Also, the average current for NaCl, KCl and RbCl electrolytes are equivalent, while the average current for LiCl and CsCl being ~35% lower, though still higher than for 1000ºC TiC-CDC. Thus selectivity is beginning to be seen as the effective ion size and average pore size of the CDC are becoming commensurate. As the pore size decreases further, further selectivity is seen and for 1M KCl in the pores of 600ºC TiC-CDC, the average current is maximum. Decreasing the synthesis temperature, though increasing selectivity for KCl, decreases the maximum current seen.

4.4.3. $TEABF_4$ // TiC-CDC system study

For completeness, the microelectrode setup was also used to reproduce the results in Section 4.3.2. Figure 4.41a shows CVs of the 900°C-CDC sample at scan rates from 20 mV/s to 1 V/s, in 1.5 M $(CH_3CH_2)_4NBF_4$ electrolyte in acetonitrile solvent showing very good capacitive behavior, nearly identical to that of Figure 4.29. As the scan rate is increased to 1 V/s, there is very slight distortion of the CV's, but they remain capacitive in nature. In fact, the CV taken at 1 V/s on the CME is nearly identical to the CV taken at

20mV/s in a traditional cell. Surprisingly, even though the ionic conductivity of $(CH_3CH_2)_4NBF_4$ is around an order of magnitude less than for aqueous solutions, the capacitance behavior is preserved to ~1V!

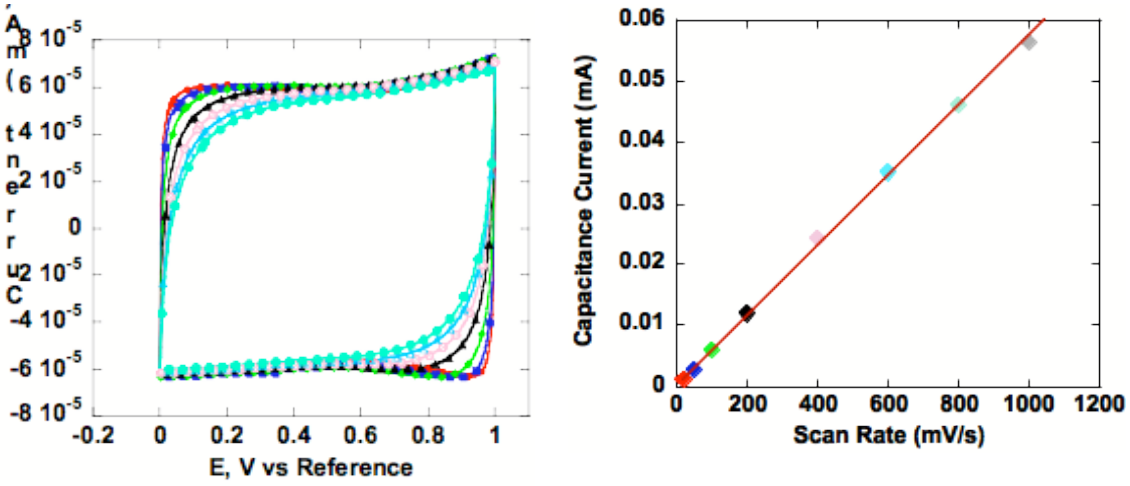

Figure 4.41: a.) Normalized CVs of the 900°C CDC sample in AN+1.5M TEA BF_4 electrolyte between 0 and +1.3 V/Ref at scan rate from 20 to 1000 mV/s and b.) the current vs scan rate plot. Currents were measured at the middle of the plateau at 0.5 V/Ref.

Figure 4.42 shows the CVs of the four CDC samples over the entire potential range traversed at positive and negative polarization. Two different potential ranges can be clearly identified in Figure 4.42, above and below the open circuit potential (which is within a few millivolts of zero for all samples). For positive polarizations, the CVs are

very rectangular-shaped. Likewise, when the potential scan is reversed, but polarization is still positive, there is little distortion in the CVs for all pore sizes.

At negative polarizations, the rectangular shape of the CV is lost for all samples except the 900°C cell, which has the largest pore size (1 nm). This inhomogeneous behavior persists even after the potential scan is reversed but polarizations remain negative. Also, it seems from Figure 4.42, that the smaller the pore size (the lower the synthesis temperature), the more distorted the CVs.

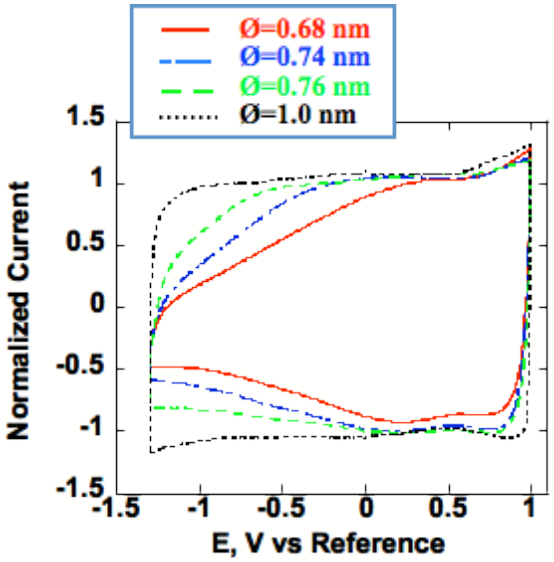

Figure 4.42: a.) CVs of CDC samples in AN+1.5M NEt_4BF_4 electrolyte between–1.3V/Ref. And +1V/Ref at the scan rate of 100 mV/s and b.) normalized CVs of the same samples.

To eliminate the possibility of kinetic effects due to poor ion transport in the porous structure, the experiments were repeated at a scan rate of 10 mV/s (Figure 4.43). The shape of the plots is preserved even at 10 mV/s: all CVs appear to be distorted and asymmetric, except for the largest pore size sample (900°C). This indicates that the

mechanisms governing plot shape are not kinetic in origin – this has 2 major implications. 1.) Narrow nanopores are accessible very quickly by largeish organic electrolyte ions and 2.) Any losses in performance seen at negative polarizations are not due to dynamic effects – this is a steady-state effect.

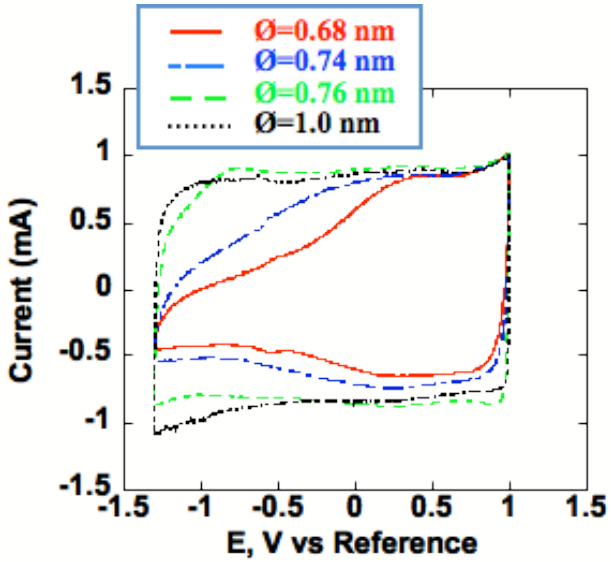

Figure 4.43: Normalized CVs of CDC samples in AN+1.5M NEt_4BF_4 electrolyte between–1.3V/Ref. And +1V/Ref. Scan rate: 10 mV/s.

Accordingly, the limitations observed cannot be linked with bulk electrolyte resistance or changing carbon resistance, and must be associated with ion transport in the carbon porous network external to any resistive effects. Taking into account the size of the solvated Et_4N^+ and BF_4^- ions in AN (1.3 nm and 1.16 nm respectively), these results confirm that ions must be at least partially de-solvated to enter these small pores, but there is some hindrance of transport.

4.5. Studies on monolithic CDC films

Since it was shown in a variety of electrolytes that pores significantly larger than the electrolyte ion were inefficient in energy storage, nanoporous monolithic CDC films were explored. CDC presents an ideal situation for a variety of reasons: 1.) good control over the microstructure - transforming the coating into the conductive carbide substrate means a perfect interface and 2.) the ability to utilize microfabrication to fabricate ECs (sputter TiC on patterned contacts, transform TiC to CDC, deposit electrolyte). Monolithic carbon foams in the form of aerogels [263] have shown promise, with capacitances in excess of 500 F/g [264] for very small samples, but the density of the samples is extremely low (pore volume of almost 2.5 cm^3/g). Once assembled, the large fraction of small pores does not contribute to energy storage and actually leads to bulk performance numbers lower than traditionally processed cells [265]. Also, the fragile films cannot be, at this point, directly fabricated on a current collector, which is the Holy Grail for industrial scale-up. Photoresist-derived carbons have been used in microelectromechanical systems (MEMS) [266], showing the potential for direct fabrication of carbon films on current collectors, exists, but the capacitance is very low.

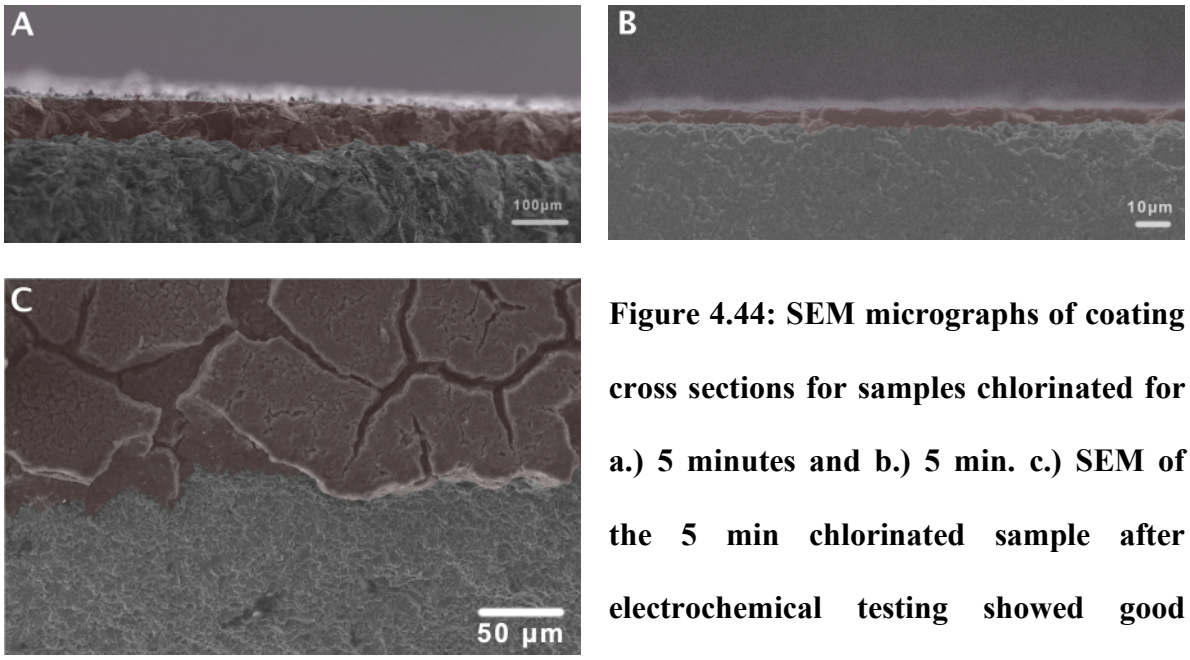

Figure 4.44: SEM micrographs of coating cross sections for samples chlorinated for a.) 5 minutes and b.) 5 min. c.) SEM of the 5 min chlorinated sample after electrochemical testing showed good adherence of the CDC film to the substrate with no large-scale evidence of spallation. The micrographs were artificially colored to accent the coating.

Bulk TiC pieces were cut to size and polished prior to being chlorinated for times ranging from 15 s to 5 min which led to coatings of ~2 µm to ~150 µm. SEM micrographs of ~75 µm (Figure 4.44 a) and ~5 µm (Figure 4.44 b) films show fairly uniform thickness and good adherence to the underlying TiC. 500ºC was chosen as the chlorination temperature because at lower synthesis temperatures the pore size is too small for effective ion storage but at synthesis temperatures larger than this the reaction kinetics are too fast to have good control over coating thickness. The precursors were also polished to be as thin as practically feasible (~300 µm) to minimize resistance.

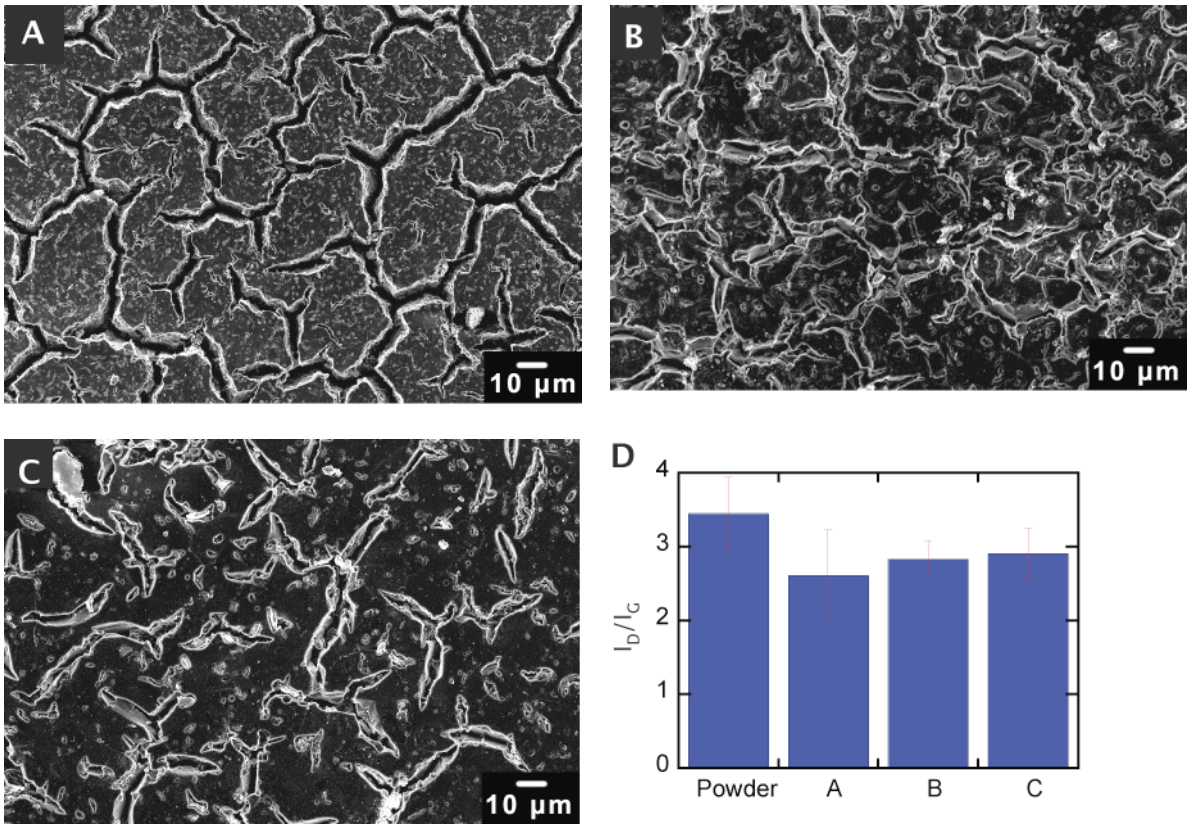

Figure 4.45: SEM micrographs of a.) ~120 µm, b.) ~50 µm and c.) ~2 µm coatings showing increasing microcracking with increasing coating thickness. d.) I_D/I_G ratio for the coatings. The labels in the bar graph correspond to the labels on the micrographs.

SEM micrographs of the film surface (Figure 4.45a-c) showed microcracking for all coating thicknesses due to stresses that develop in the film after Ti removal. The amount of microcracking increases with increasing coating thickness. Raman spectroscopy of the coating surface for the 3 different coating thicknesses (Figure 4.46d) shows that the I_D/I_G ratio decreases with increasing coating thickness indicating increasing ordering for thicker films at the surface. This is in line with what was observed in SEM – increasing relaxation of stresses at the surface for thicker films leads to higher levels of ordering.

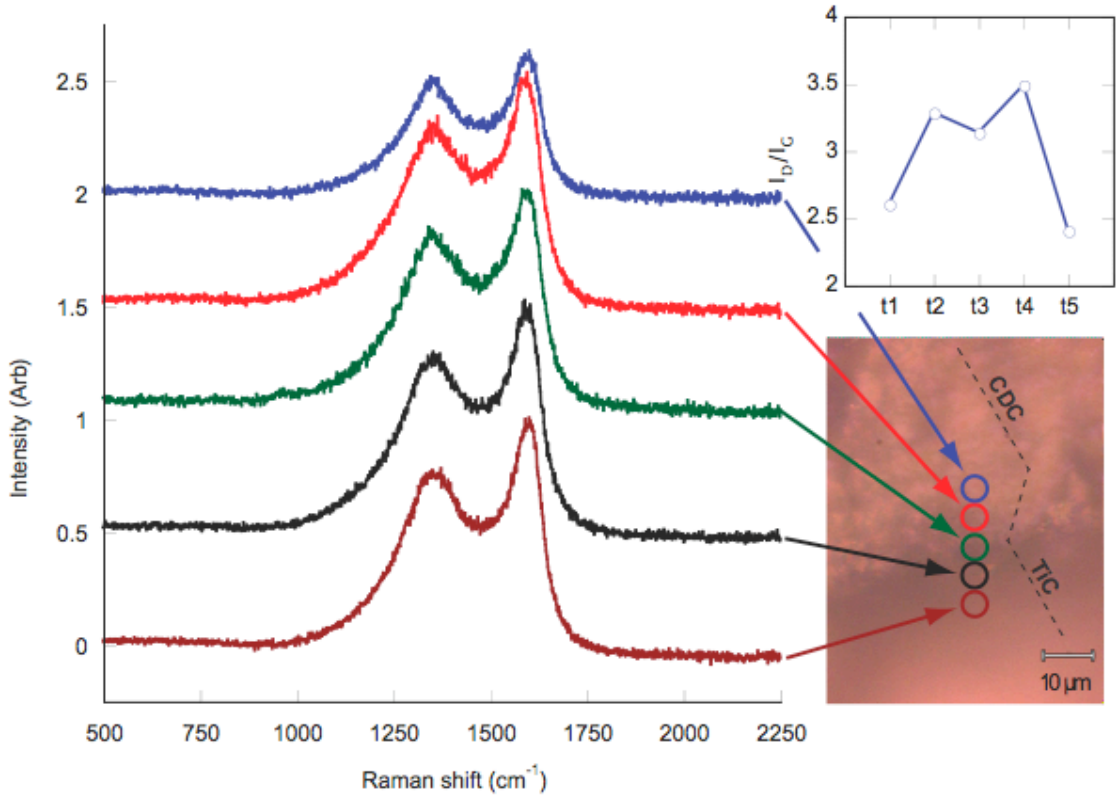

Figure 4.46: (L) Raman spectra taken across the cross-section of CDC at a fracture surface (shown in the micrograph on the bottom right). The I_D/I_G ratio (top right) of CDC changes across the fracture surface, but remains within the range of what is obtained on 500ºC TiC-CDC powders.

Raman microspectroscopy of a ~50 µm film (Figure 4.46) showed fairly uniform I_D/I_G ratio throughout the coating thickness. At the film surface, there seems to be a slightly larger amount of ordering, but in general, the coatings are all of very similar microstructure. This increased ordering at the surface is probably related to the microcracking shown previously.

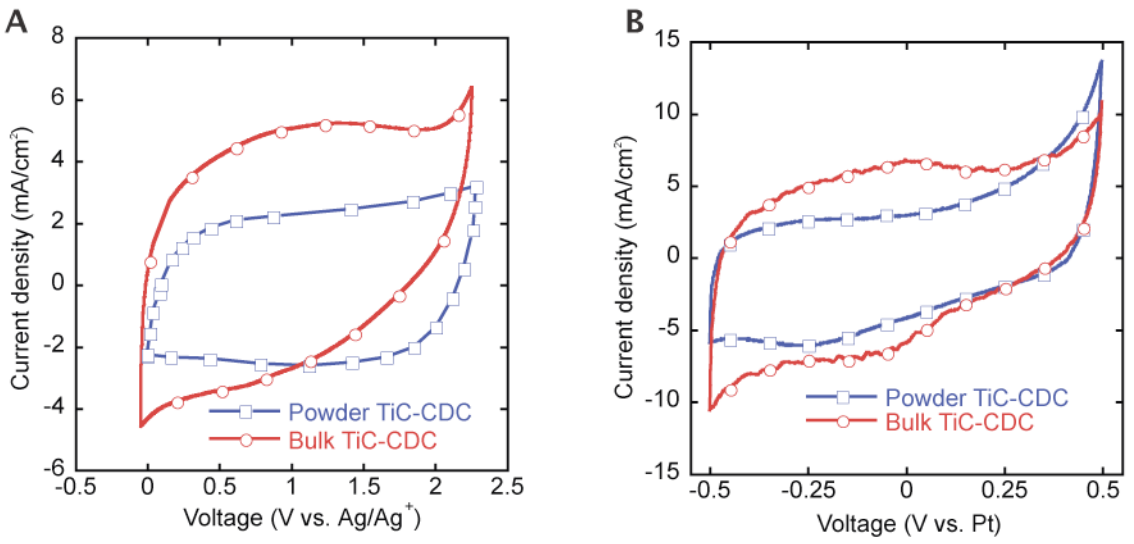

Figure 4.47: CVs for a.) ~50 µm film and ~50 µm traditional electrode in $TEABF_4$ and b.) ~50 µm film and ~50 µm traditional electrode in H_2SO_4.

Electrochemical measurements of CDC films were done in a 3-electrode configuration with a large overcapacitive counterelectrode and both 1 M H_2SO_4 (Figure 4.47 b) and (Figure 4.47 a) 1 M $TEABF_4$. CVs for 50 µm traditionally processed 500ºC TiC-CDC electrodes are also included for direct comparison. Both CVs show good non-Faradaic response, with voltage windows similar to powder electrodes. If th ere were a significant amount of impurities present due to chlorine and chlorides being trapped in the film after synthesis, there would be Faradaic currents, especially at the extents of cycling, because of chlorine making the IL acidic.

In $TEABF_4$ there are very minor current peaks at both of the switching potentials, which may be related to electrolyte decomposition. The peaks are minor, however, and decrease

with cycling. Interestingly, the shape of the CV is different for the forward sweep and backward sweep, which connects well with our ideas of pore accessibility, desolvation and effective ion sizes. During the positive sweep, BF_4^- ions penetrate into the finest pores and during the negative sweep, they must be replaced by larger TEA^+ cations, which is more difficult because of its larger size. Hence the slower saturation for the negative scan.

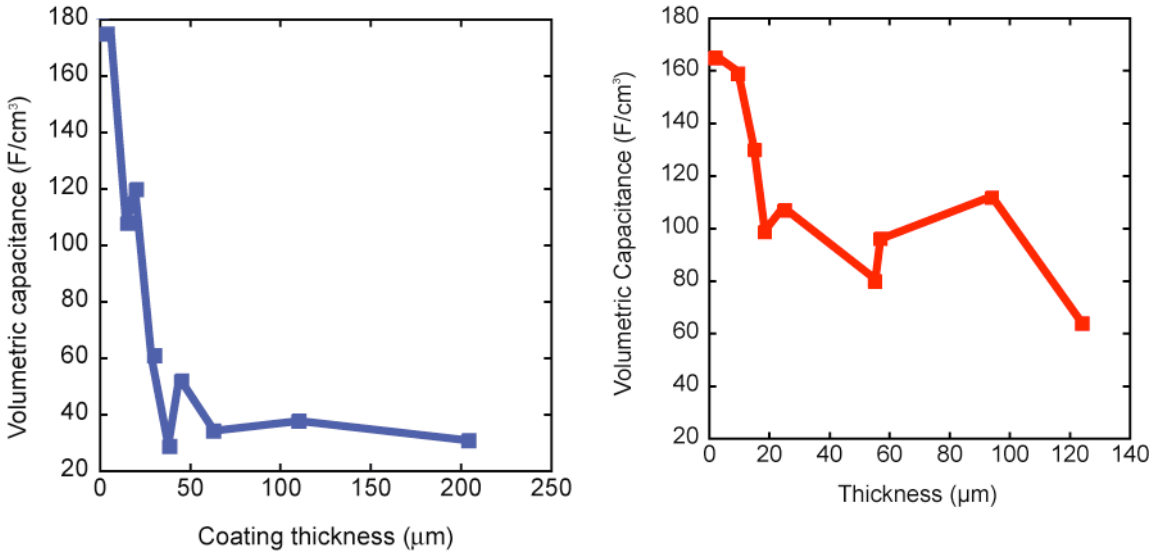

Figure 4.48: Volumetric capacitance for different film thicknesses in a.) $TEABF_4$ and b.) H_2SO_4

Volumetric capacitance was calculated for each of the different film thicknesses (Figure 4.48), as well as for a powder sample with the highest volumetric capacitance reported in literature in both electrolytes. For both $TEABF_4$ and H_2SO_4, the volumetric capacitance decreases with increasing coating thickness. This is especially pronounced in the organic

electrolyte, where there is a huge increase in volumetric capacitance as the film thickness decreases from 200 μm to ~2 μm. This decrease is most likely due to film failure as ions are inserted into the structure and it swells. Increased microcracking with increasing film thickness is evidence of particularly brittle films. Also, the larger ions in the organic electrolyte would cause more swelling, and hence more cracking, than the aqueous electrolyte.

Results for thin films are especially promising, though. It has been previously shown for SiC-CDC films [167] that dense coatings can be made to 200 μm, and prior work chlorinating sputtered amorphous TiC by Elizabeth Hoffman has shown that TiC-CDC can also be produced crack-free [267]. If for a non-optimized system, we were able to achieve double the capacitance ever reported for pure EDLCs in multiple electrolytes, continuing this work is certain to bring large rewards.

5. Discussion

Since beginning this project, it has evolved from a simple case of "let's try material X in application Y" and produced some novel results that have hopefully steered the direction of the community. Counting works in press, our *Science* paper already has nearly 50 citations, as an example of this. Groups have taken to independently modeling out results [247], and at least 1 full paper is devoted to repeating our experiments. From a technological standpoint, our patents have all been licensed for commercial development of the technology to Y-Carbon, which has partnered with Arkema for scaling up. The strongest evidence of the importance of this work is the January 2009 NSF Newsletter, which cites this work as the #2 most widely viewed NSF Discovery article of 2008. Acceptance by the general public is the true test. At this point, I am probably experiencing a common feeling amongst almost graduated graduate students, though – satisfaction at coming to the end of this experience and a bit of sadness that my baby has actually outgrown me… The fact remains, though, that what remains are some really interesting results that raise some equally interesting points.

Certainly, EDLCs are not a new concept, but judging by the fact that the understanding and research directions in the field have not substantially changed in the past half-century (besides trivialities like burning other nuts besides coconut shells and hoping the results are good), it is probably safe to say that the community is missing the big elephant standing in the room. Understandably, much of the difficulty relating to the study of

double-layer capacitance in carbon lies in the near impossibility to model the process fundamentally. This mostly is due to the amorphous microstructure of carbon and complex nature of the electrolyte, which cause researchers to idealize one or the other. In actuality, the carbon microstructure and electrolyte are coupled, as evidenced by the experimental data presented here showing a strong dependence of capacitance on pore size.

The first big elephant that needs to be properly addressed is the misconception that solvent molecules remain firmly attached to their ion wandering around inside of charged pores. In the case of aqueous electrolytes, which have solvation energies substantially higher than their non-aqueous counterparts, it is unclear to what extent solvent molecules are stripped from their ion, because porosity measurement techniques cannot probe such small dimensions. Certainly, however, because of their solvated size being larger than the CDC pore size, larger organic electrolyte ions must have their solvation shells removed. That means there exists at least some range of solvation energies that are lower than the energy gained by desolvating. What is this range? What effect does this have on measured capacitance? How can this understanding be built upon for developing improved materials?

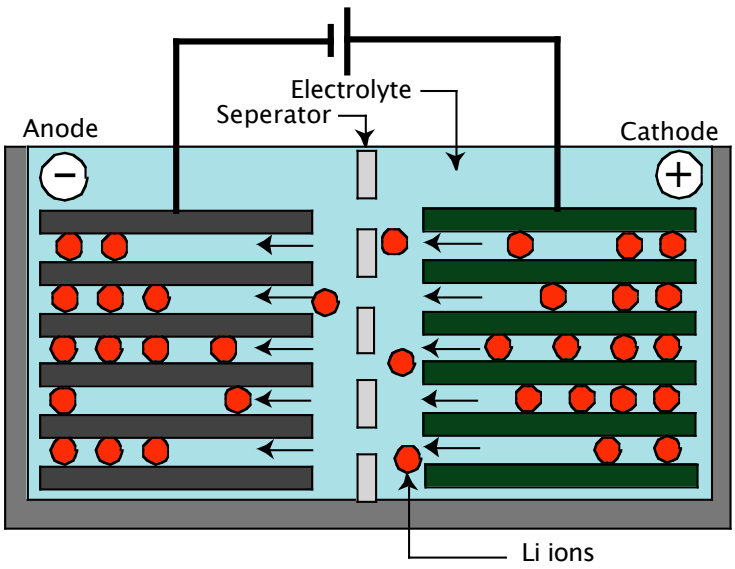

Figure 5.1: Schematic of Li-ion "rocking-chair" battery

Perhaps better understandings can be had by considering a system that is very close to ECs. The one clear case where ions are certainly desolvated is with lithium-ion batteries. Lithium batteries utilize Li^+ ions shuttling between intercalated graphite as the anode material, instead of lithium metal because of problems associated with dendritic growth of lithium during prolonged cycling causing short-circuiting (see, for example the large-scale recall of laptop batteries by Apple and Sony) and Li-containing transition metal oxides as the cathode material (Figure 5.1).

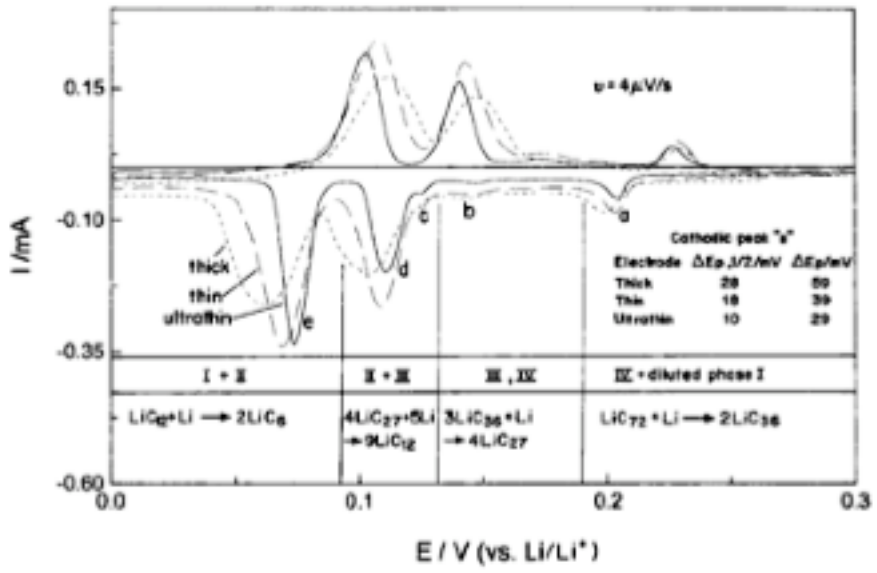

Figure 5.2: Slow scan cyclic voltammogram (SSCV) of ultrathin, thin and thick graphite anodes cycled between 0.3 V vs. Li/Li$^+$ and 0 V vs. Li/Li$^+$ [268]

Initially when the battery is assembled, the graphite anode does not contain any intercalated lithium ions. As current flows, there is initially only ion movement in the bulk solution as the voltage decreases linearally to ~1 V vs. Li/Li$^+$ (Figure 5.2). At ~2 V vs. Li/Li$^+$, *in situ* electrochemical STM measurements showed Li$^+$ attains a square planar array of 2D space group P2 [269]. Interestingly, the double-layer shown in Figure 5.3 is the same in plane configuration Li$^+$ takes when intercalated into carbon at LiC_{18}. Therefore, for non-Faradic current to flow at potentials more negative than ~2 V vs. Li/Li$^+$, there may be contributions from both a diffuse-type layer and more Li adsorbed on the surface (every 2nd graphite hexagon corresponds to the state seen in intercalated graphite). Indeed, at more negative potentials, it was seen that there is a thicker less

uniform layer on the surface that was attributed to SEI (a thin layer of oxidized electrolyte and bound lithium and both leads to irreversible loss of lithium, as well as passivates the graphite anode against further damage) formation, but surface nonhomogenaity did not allow visualization of a more dense compact layer. This is, however, direct visualization of partial desolvation, in that the Li^+ must sit at the electrode surface and on a specifically adsorbed layer of polarized solvent molecules.

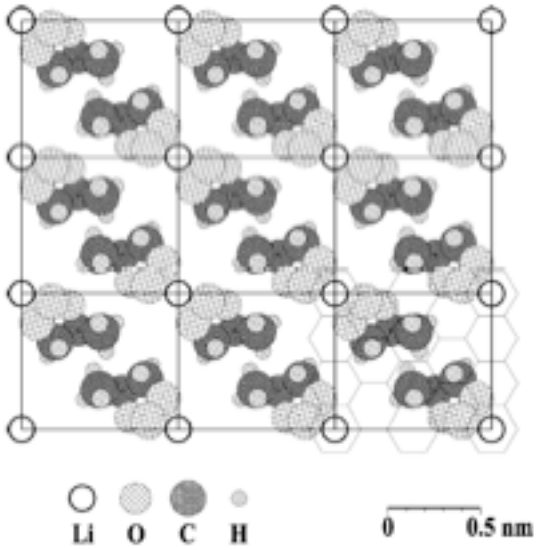

Figure 5.3: Schematic of the structure of Li^+ surrounded by 2 PC molecules solvating the ion in plane as determined by in situ electrochemical AFM at 2.15 V vs. Li/Li^+ [269]

Between ~1 V vs. Li/Li^+ and 0.2 V vs. Li/Li^+ on the first charging cycle, there is a plateau in the voltage versus time profile for a constant current measurement, indicative of SEI formation. The SSCV in Figure 5.2 is taken after SEI formation, which is why only capacitive currents are seen at potentials above 0.2 V vs. Li/Li^+. Below 0.2 V vs. Li/Li^+, there is a large voltage plateau that correlates with staged Li^+ insertion. From

SSCV, a reduction peak is visible close to 0.2 V vs. Li/Li^+ and an oxidation peak at slightly more positive potentials. This peak correlates with the initial intercalation of graphite with Li^+. Interestingly, lithium is not reduced inside of the graphite structure following

$$Li^+ + e^- \longrightarrow Li \tag{5.1}$$

and instead remains ionized. The ions center themselves at the center of a graphite hexagon, with the graphite layers changing stacking sequence from ABAB to AAAA to allow lithium epitaxy above graphite hexagon centers. At low currents and potentials close to 0.2 V vs. Li/Li^+, lithium intercalates into graphite in a regimented manner, with 4 layers of unintercalated graphite between each intercalated layer. At more negative potentials, though still positive of the reduction wave, there is continued insertion of lithium into intercalated graphite layers, probably until a composition dictated by epitaxy, as was shown in the in situ STM measurements (Figure 5.3).

The reduction waves just positive of 0.1 V vs. Li/Li^+ and ~0.05 V vs. Li/Li^+ in Figure 5.2 correspond to an increase in stage index – stage 4 has 4 layers of unintercalated graphite between layers of intercalated graphite, stage 3 has 3 layers of unintercalated graphite between layers of intercalated graphite, etc. The total integrated charge under the CV corresponds to 372 mA-h g^{-1}, which is every second graphite hexagon having a Li^+ ion centered over it and a stage 1 intercalation compound. Because of the good crystallinity of the system, it is very well characterized and may allow some parallels to be drawn with ECs.

The electrochemical processes occurring in lithinated graphite anodes are complex and do not follow standard Nernstian formalities. There is no formal phase change in lithium

and, instead, a large group of atoms have electrons added and withdrawn to preserve electroneutrality (LiC_{18} implies that 1 electron is localized over 18 carbons to screen the charge from 1 Li).

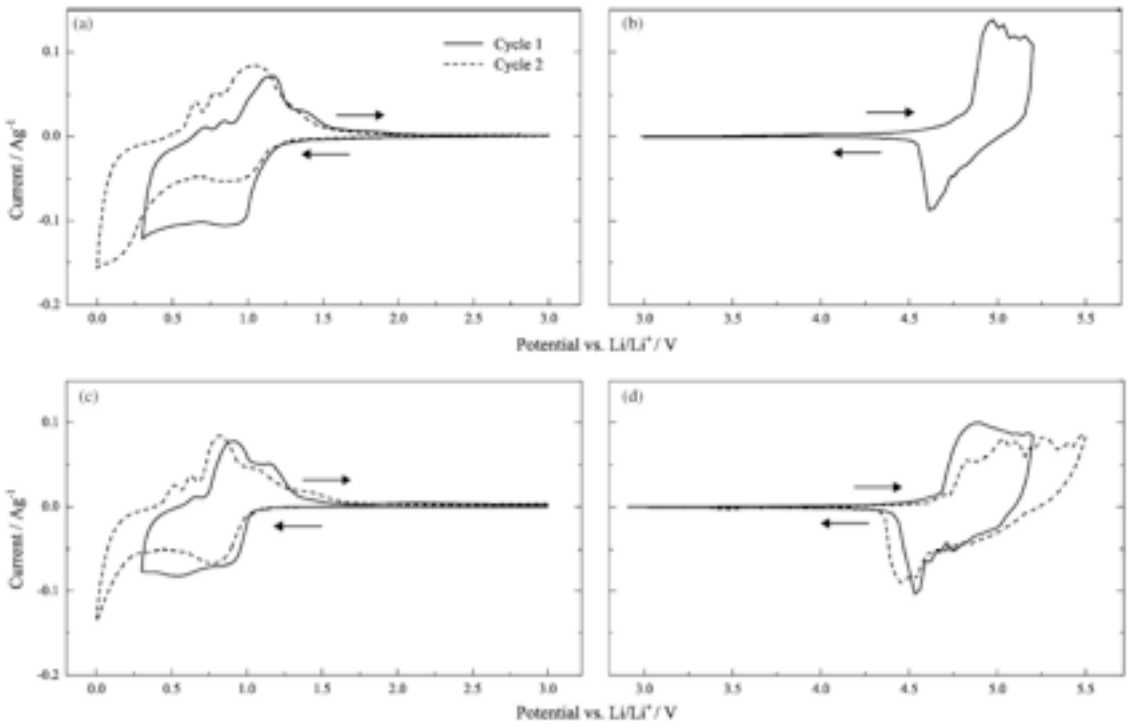

Figure 5.4: CV of $TEABF_4$ in a, b.) acetonitrile and c, d.) propylene carbonate [270]

When graphite is used as the anode and cathode in a nonaqueous EC electrolyte, $TEABF_4$, a much different voltammogram is obtained than typical EC behavior (Figure 5.4), though it is similar to that of Li intercalation (Figure 5.2) [270]. Because of the low surface area of graphite, very little current flows between ~1 V vs. Li/Li^+ and ~4.5 V vs. Li/Li^+. At potentials lower than 1 V vs. Li/Li^+ and higher than 4.5 V vs. Li/Li^+, there are

very defined reduction/oxidation peaks corresponding to insertion of TEA^+ and BF_4^-, respectively. Intercalation of these ions can be tracked using Raman spectroscopy [271] and XRD [270]. For both positive polarization greater than 4.17 V vs. Li/Li^+ (intercalaction of BF_4^-) and negative polarization less than 0.87 V vs. Li/Li^+ (intercalation of $(CH_3CH_2)_4N^+$), there is a splitting of the G-band due to a break in symmetry upon being intercalated. These bands can be assigned to interior E_{2g2}(i) vibrations (1578 cm^{-1}) of unintercalated graphite layers and bounding E_{2g2}(b) vibrations (1600 cm^{-1}) adjacent to intercalated layers. Plotting the intensity ratio of the E_{2g2}(i) band versus the E_{2g2}(b) band gives the ratio of unintercalated graphite layers to intercalated layers, or the stage number. Likewise, XRD can be used for calculating staging by tracking the disappearance of the (002) Bragg peak of graphite while it is intercalated and reappearance during deintercalation [272]. At potentials lower than 1 V vs. Li/Li^+, $(CH_3CH_2)_4N^+$ is intercalated up to a maximum stage 2 at potentials lower than 0.3 V vs. Li/Li^+ [271]. At potentials above 4.5 V vs. Li/Li^+, there is a mixture of stage 2 and stage 3 BF_4^- intercalation compound..

These results are in line with what would be expected, with $(CH_3CH_2)_4N^+$ being intercalated below 0.1 V vs. Li/Li^+ and Li^+ being intercalated at ~0.2 V vs. Li/Li^+, the former being much larger and requiring more lattice distortion in graphite, thus requiring lower potentials to insert. Like lithium intercalation, this process is decidedly non-Faradic, though the voltammograms show formal electron transfer steps.

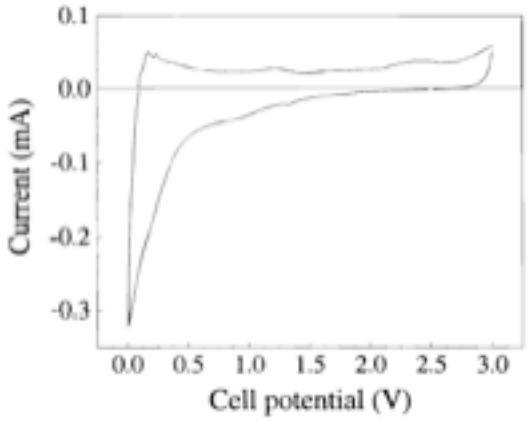

Figure 5.5: CV of lithium intercalation into SWNTs [273]

When disordered porous carbon is used as the anode material in Li-ion batteries, there are no defined redox peaks. Even in the case of SWNTs, which are decidedly more ordered, the redox peaks are suppressed (Figure 5.5). For lithium insertion, there is a continuously decreasing current from ~1 V vs. Li/Li^+ to 0 V vs. Li/Li^+, which looks similar to transients seen at the extents of cycling for EDLCs that were attributed to the distributed *RC* network within the pores [274].

This is attributed to 2 mechanisms, the well-known intercalation phenomenon, as well as interactions between Li^+ and H-passivated edge carbons [275]. Interestingly, Figure 5.5 was taken on most-likely H-free SWNTs and the mechanisms credited to Li interacting with H-passivated edge carbons are still present, namely large hysteresis between insertion and removal and Li and excess capacity above LiC_6. How can simple intercalation and ion accommodation be used to explain the observed behavior in the absence of H, then?

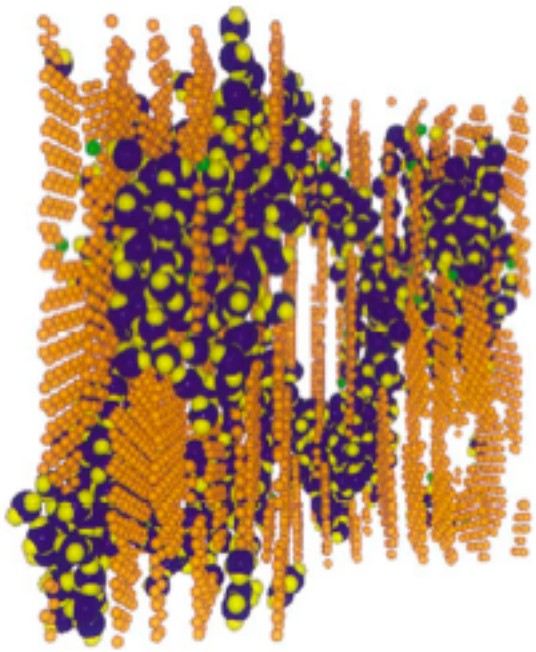

Figure 5.6: Reverse Monte Carlo (RMC) simulation of a disordered carbon structure filled with water molecules calculated from SAXS studies [276].

Figure 5.6 shows the rendered result of reverse Monte Carlo simulation of disordred carbon structures interacting with water molecules. The water molecules within the carbon pores are in a huge variety of different environments, with some being tightly bound within very small cavities approximating the size of the molecule and having a high number of carbon nearest neighbors to the case when water is adjacent to the graphite basal plane. In energetic terms, this is tantamount to gas phase adsorption phenomenon, whereby the highest binding energies for adsorption are found for the smallest pores and a continuum of energies exists between those of small pores and those of basal surfaces. Likewise, it would be expected that the potential where an ion

intercalates (adsorbs) would strongly depend on the local environment of the carbon around the ion.

To develop this idea slightly more, starting with the work of Kohlrausch [277] and most notably Warburg [278], electrochemistry has used the idea of equivalent circuits to model electrochemical phenomenon, specifically double-layers. The basis of these techniques involves using equations for electrical circuits applied to ionic motion and charge transfer. The main utility of this approach is, when combined with AC techniques that perturb the system with a small-amplitude sinusoidal voltage profile (typically 10 mV RMS, or so), to model the time dependence of electrochemical phenomenon. A prototypical circuit is constructed from resistors, capacitors and/or inductors that, when modulated under the same experimental conditions, repeats the behavior of the electrochemical cell. As in electrical circuit theory, resistance is completely in phase with the applied signal and capacitance is 90º out of phase. Using a frequency response analyzer, the AC signal received from the measurement can be split into a real impedance, *Z'*, that is in phase with the applied waveform and an imaginary impedance, *Z''*, that is out of phase with the applied waveform.

$$Z(\omega) = Z' - jZ'' \tag{5.2}$$

Therefore the entire response of the system is contained with the real and imaginary impedance terms. The typical behavior of a cell is exemplified by the Randles equivalent circuit, which has a resistor (representing the bulk solution resistance), in series with a parallel combination of a capacitor (representing the double-layer capacitance) and a general impedance element (similar to a “leaky capacitor”) that possesses information

about charge transfer. The major utility in utilizing this methodology lies in the ability to separate phenomena that occur at over different time scales. For instance double-layers assembling on a flat electrode and charge transfer occurring across the double-layer typically have differences in time constants of at least a century.

de Levie is credited with introducing transmission lines, instead of the general impedance element, Z_f, to model processes occurring inside of charged pores [33, 279]. The addition of more *RC* circuits to the distributed circuit element allows diffusion to be modeled semi-quantitatively, as the "leaky capacitor" is replaced by real, discreet circuit elements.

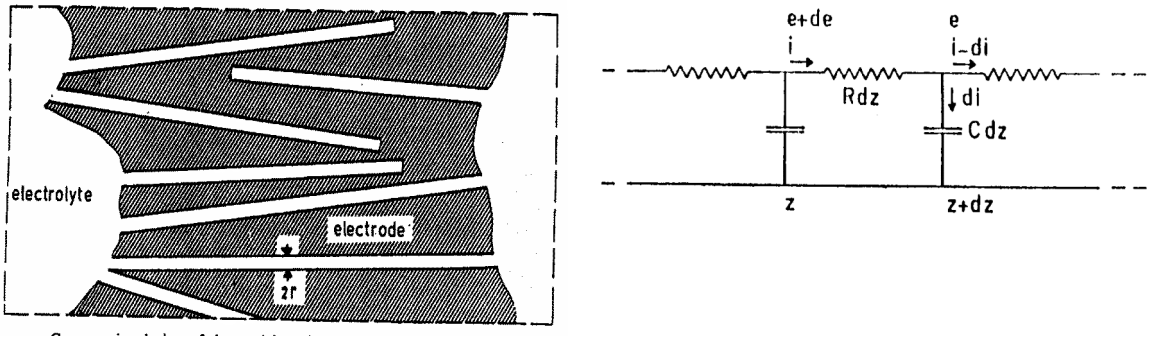

Figure 5.7: a.) Schematic of the pores of the transmission line model. b.) Circuit employed in de Levie's treatment, whereby a series of resistors and capacitors represents the increased resistance and increased capacitance as an ion moves down a pore.

The power of this method to fit an experimental impedance spectra is great, though assigning *R*'s and *C'*s to chemical events is not straightforward. As an example of this, consider the 2 impedance spectra of Figure 5.8. Figure 5.8 shows Nyquist plots of both electrochemical capacitors (Figure 5.8a) and lithium insertion (Figure 5.8b). The Nyquist plot is a convenient way to show impedance data with real impedance on the x-axis and imaginary impedance on the y-axis. The highest frequencies (kilohertz) are located at the lowest real and imaginary impedances, where the electric field is switching too fast for ions to move far. As the frequency decreases, time-dependent processes take precedence.

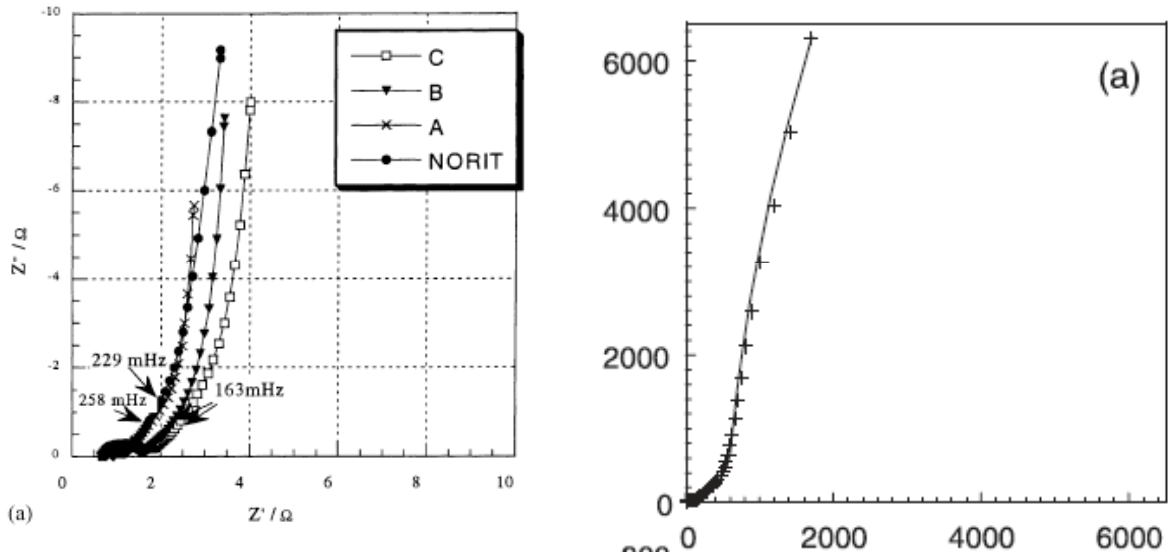

Figure 5.8: Nyquist spectra of a.) 4 EDLCs with different porous carbons [121] and b.) Li^+ insertion into SWNTs. Crosses represent experimental data points and the solid line is a fit to the equivalent circuit shown in Figure 5.9

There are 3 main regions of interest in the Nyquist plts. At the highest frequencies, there is a semi-circle. Classically, this is attributed to the double-layer, but in such porous electrodes, this is incorrect. Actually, this semicircle that has both capacitive and resistive components comes solely from poor electrode preparation [239]. It should be noted that the cell used in Figure 5.8b is the same cell used in Section 4.2.1 and is perfect for measuring steady-state behavior. This mumbo jumbo is only for illustrative purposes. At frequencies lower than the semicircle, there are 2 regions with constant slope, a transition region with ~45º slope and another with a near vertical slope. The former constitutes a so-called diffusion region and indicates a transition between resistive to charge storing. The final region corresponds to nearly pure charge storage.

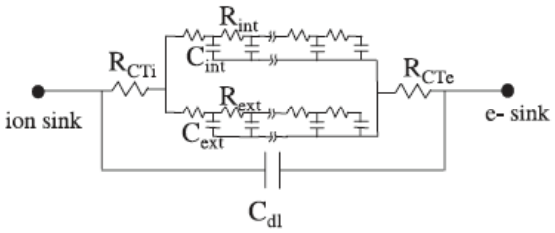

Figure 5.9: Equivalent circuit used to model EIS data. The two transmission lines in paralell represent the internal and external surfaces of an average SWNT rope. R_{ext} is the ionic resistance for alkyl ions to diffuse through the porosity of the buckypaper, while C_{ext} is the capacitance assoiated with the surface of the rope. R_{ext} is the resistance for ions to diffuse inside of a rope, while C_{int} is the internal capacitance of the rope. C_{dl} is the double layer capacitance at the macroscopic electrode/electrlyte interface. R_{CTi} and R_{CTe} are the charge transfer resistance for ions and electrons to reach that interface [237].

The equivalent circuit shown in Figure 5.9 was used to model the impedance spectra shown in Figure 5.8b. Two transmission lines representing lithium adsorbing on the external and internal nanotube surfaces are the key feature of this model. As shown in Figure 5.8b, the fit to the experimental data is good, especially in the low frequency limit. Curiously, however, the exact equivalent circuit fits the data shown in Figure 5.9b for an

electrochemical capacitor as well. Also, diffusion coefficients for lithium insertion into CDC [280] and EC ion movement [281] are both of the order of $10^{-9}cm^2/s$. So, the second, and probably largest elephant in the room is the question of whether intercalation and double-layer charging are of the same nature. The fact remains that in graphite there is pseudo-homogenous charge transfer at a defined potential, dictated by the ion being inserted, whereas excessive heterogeneity is seen in disordered carbons. How can we take advantage of the enormous capacity of lithium while preserving the rate capability of ECs, though?

The first much needed step required of the EC community is to get a grasp on the number of ions actually participating in charge storage. Raman spectroelectrochemistry can probe both the carbon as well as the electrolyte (in the case of $TEABF_4$) at all states of charge *in situ*. The resolution is still some several orders of magnitude lower than the size of a double-layer, so we cannot obtain detailed information about only the interface, but we can probe the local environment immediately adjacent to the electrode, and with micrometer-resolution, track ion concentrations immediately adjacent to the electrode.

Hardwick showed that the electrolyte concentration near the electrode decreases with increasing charge on the electrode [271]. Some 10 μm from the electrode surface, it was shown that the ion concentration can decrease to as much as 20% of the bulk solution value. The implications of this are twofold – 1.) more ions than previously thought are potentially involved in the double-layer process [103], and 2.) large electrolyte concentration gradients exist immediately adjacent to the electrode, which certainly limits

ionic conductivity. Reconciling either of these implications could bring a new level of understanding to next-generation energy storage devices.

6. Conclusions

- A systematic study of CDC produced from B_4C, Ti_2AlC, TiC, SiC, and ZrC at synthesis temperatures in the range of 400ºC to 1200ºC in electrochemical cells with aqueous electrolytes consisting of H_2SO_4, LiCl, NaCl, KCl, RbCl, and CsCl, TEA-BF_4 organic electrolyte in acetonitrile and propylene carbonate, as well as EMI-TFSI ionic liquid in both neat form as well as solvated by acetonitrile was done to investigate the coupling between electrolyte ion size and carbon pore size in carbon supercapacitors.

- To minimize artifacts from the test itself, 3 iterations of electrochemical cell design were done. The capacitance at a current density of 100 mA cm^{-2} was shown to increase by a factor of 4 in 1M H_2SO_4, from ~25 F/g to ~100 F/g and a factor of 2.5 in 1M $TEABF_4$ from ~20 F/g to ~50 F/g in going from the initial cell design to a more advanced cell design similar to the one developed at Paul Sabatier University and utilized etched current collectors treated with a conductive overcoat and 2 cm X 2 cm X ~100 μm electrodes. The improvement in performance in moving to a new cell was due to a lower ESR in the best cell design (0.4 Ω-cm^2 versus ~25 Ω-cm^2 in $TEABF_4$ and 1.2 Ω-cm^2 versus ~30 Ω-cm^2 in H_2SO_4), which enables better electron percolation throughout the carbon electrode. It is worth noting that the ESR value for the optimized cell using $TEABF_4$ electrolyte is on par with what is seen in commercially packaged devices.

- In general, as was seen in other studies of different activated carbons in supercapacitors, it was found that capacitance scales with surface area of CDC. Seemingly, as the surface area increases, there is a greater scatter in capacitance values, which was previously attributed to developing porosity too small to be accessed by electrolyte ions, though large enough to be accessed by gas probe molecules for surface area determination. In practice, however, it was found that increasing surface area in activated carbons is due more so to the creation of large pore volumes of larger pores.

- Taking some available literature data, normalizing the capacitance by the surface area within the developed porosity of the electrode and plotting it as a function of average pore size showed the opposite trend, decreasing normalized capacitance with increasing pore size. This showed that in moving from an average pore size of ~ 3 nm to ~ 0.7 nm, the normalized capacitance increased by a factor of 4, from 5 $\mu F/cm^2$ to a maximum of 20 $\mu F/cm^2$ (with an average value at ~1 nm of ~ 10 $\mu F/cm^2$). Because of the wide variety of precursors, however, there is a large amount of data scatter, which makes a systematic study using fine-tunable CDC timely.

- Systematic studies on various TiC-, B_4C-, ZrC- and SiC-CDCs showed the same trends as uncovered during the literature survey, namely increasing normalized capacitance from ~ 5 $\mu F/cm^2$ at an average pore size of 3 nm to ~ 10 $\mu F/cm^2$ at an average pore size of ~ 0.7 nm. The maximum gravimetric capacitance of nearly 200 F/g, for 800ºC TiC-CDC, is on par with the most advanced carbons in literature. Likewise, as the values for normalized capacitance are very close to the prior

activated carbons, albeit with far less data scatter, it shows CDC to be a good model system for both understanding global trends and producing high performance supercapacitors.

- As the solvated ion size of the sulfuric acid electrolyte used was smaller than the lowest resolvable pore size, work was extended to the larger $TEABF_4$ electrolyte in acetonitrile, which is widely used in commercial devices. In 2-terminal measurements of TiC-CDC samples synthesized in the temperature range 500ºC to 1000ºC in $TEABF_4$ (reporting the average behavior of the anion and cation inside of the CDC structure), the same behavior was found as seen in H_2SO_4. Decreasing the pore size from ~1.5 nm to ~0.7 nm increased the normalized capacitance from ~ 5 $\mu F/cm^2$ to ~14 $\mu F/cm^2$. This resulted in a gravimetric capacitance greater than 140 F/g, nearly 50% greater than commercially used carbons, and unsurpassed by other large-pore carbons.

- Addressing the behavior of each ion individually, it was shown that at an average pore size of 0.7 nm in TiC-CDC, there is a maximum capacitance of nearly 170 F/g for the BF_4^- anion at the cathode, which corresponds to a size intermediate between the solvated ion size (1.16 nm) and the desolvated ion size (0.48 nm). Similarly, at 0.75 nm, a pore size intermediate between the solvated size (0.67 nm) and desolvated size (1.30 nm) of the TEA^+ cation, the capacitance measured at the anode is a maximum of 125 F/g. This leads to two important points: 1.) each electrode must be tuned to a specific electrolyte ion individually, and 2.) the ions must be at least partially stripped of solvent molecules to enter the pores.

- Work was extended to a solvent-free ionic liquid, EMI-TFSI, to eliminate potential complications from solvation, and, indeed, the same trends were found. Capacitance is a maximum at the pore size corresponding to the ion size. Maximum capacitance of 155 F/g was measured for TiC-CDC having an average pore size of 0.68 nm. This is ~50% higher than anything else reported in literature, and with very stable cycling within the ~3 V window of EMI-TFSI, certainly leads to the highest energy density system out there.

- Addressing each ion separately, EMI^+ adsorption at the cathode and $TFSI^-$ adsorption at the anode lead to very similar dependence on pore size due to their similar ion sizes (0.76 nm vs. 0.79 nm, respectively). At the smallest pore sizes, however, there is some sieving effects as the ions are not precisely the same size.

- When acetonitrile is added to the neat EMI-TFSI, the maximum in capacitance is shifted to a larger pore size due to ion solvation effects.

- From various systematic studies on different families of electrolytes, it was shown that there is more energy to be gained utilizing carbons with pores matched to the ion size. Unfortunately, theory is not mature enough to offer a definitive answer as to why this effect is seen. Potentially, this effect can be explained by: 1.) higher density of ions within pores similar to their atomic dimensions due to electrostatic screening, or 2.) desolvation allows closer approach of ions to pore walls.

- Unfortunately, optimization still needs to be done to find the right couple between pore size and ion size and testing is lengthy. Using the cavity microelectrode (CME)

technique, it was shown that fast, but accurate studies can be made for identifying possible ion-pore couples as well as investigating transport limitation.

- Using the CME technique to study the coupling between 1M solutions of LiCl, NaCl, KCl, RbCl and CsCl and TiC-CDC with varying pore sizes showed that for larger pore sizes, the capacitance responses in electrolytes with different ion sizes are similar, though as the CDC synthesis temperature and thus the pore size decreases, capacitance becomes maximum for K^+ and falls off going up or down the alkali series. As the hydration energy is stronger for higher charge density Na^+ and Li^+, it would be expected that their hydrated ion size would be greater than K^+. Similarly, Cs^+ and Rb^+, with the same hydration number as K^+ would be much larger. Of course, effects from ion pairing and clustering cannot be discounted, though in terms of EC's is never talked about.

- Understanding that pores significantly larger than the effective ion size do not have large contribution to energy storage, work was extended to eliminate interparticle macroporosity by moving to porous CDC films on conductive TiC substrates. Even though the films showed microcracking, performance in both H_2SO_4 and $TEABF_4$ was excellent. In both electrolyte systems, the volumetric capacitance decreased with increasing coating thickness, probably due to increased failure of the coatings. For 2 μm coatings, the calculated volumetric capacitance in H_2SO_4 was 160 F/cm^3 and in $TEABF_4$, it was nearly 180 F/cm^3. In practical terms, this is more than a twofold improvement in capacitance in $TEABF_4$ compared to powder results.

- This work has identified the ion size to pore size correlation as the key criterion for increasing the capacitive energy storage and outlined directions for selection of carbon-electrolyte couples for electrochemical capacitors. Demonstration of the fact that at least partial desolvation of ions occurs in pores smaller that the solvated ion size raised an important fundamental issue about the structure of electrical double layer in confined space and at curved surfaces, which must addressed experimentally and theoretically in the future studies.

7. List of References

1. Arrow, K., Bolin, B., Costanza, R., Dasgupta, P., Folke, C., Holling, C.S., Jansson, N.-O., Levin, S., Maler, K.-G., Perrings, C. and Pimental, D., *Economic growth, carrying capacity, and the environment.* Science, 1995. **268**: p. 520-21.

2. Meyers, R.A. and Worm, B., *Rapid worldwide depletion of predatory fish communities.* Nature, 2003. **423**: p. 280-83.

3. Wilson, E.O., *The Future of Life*. 2002, New York, NY: Knopf. 256.

4. Leakey, R.E. and Lewin, R., *The sixth extinction: Patterns of life and the future of humankind*. 1996, New York, NY: Dantam Dell Publishing Group. 288.

5. Hubbert, M.K., *Nuclear energy and the fossil fuels.* Drilling and Production Practice, 1956. **95**.

6. Pfeiffer, D.A., *Eating Fossil Fuels*. 2004, Sherman Oaks, CA: From the Wilderness Publications.

7. Kunstler, J.H., *The Geography of Nowhere: The Rise and Decline of America's Man-Made Landscape*. 1994, New York, NY: Free Press. 304.

8. Agrawal, R., Singh, N.R., Ribeiro, F.H. and Delgass, W.N., *Sustainable fuel for the transportation sector.* PNAS, 2007. **104**: p. 4828-33.

9. Lovins, A.B. and Cramer, D.R., *Hypercars, hydrogen and the automotive transition.* Int. J. Vehicle Des., 2004. **35**: p. 50-85.

10. Kotz, R., Sauter, J.-C., Ruch, P., Dietrich, P., Buechi, F.N., Magne, P.A. and Varene, P., *Voltage balancing: Long-term experience with the 250 V supercapacitor module of the hybrid fuel cell vehicle Hy-Light.* J. Power Sources, 2007. **174**: p. 264-71.

11. Service, R.F., *New 'supercapacitor' promises to pack more electrical punch.* Science, 2006. **313**: p. 902-05.

12. Tickell, J., Tickell, K. and Roman, K., *From the Fryer to the Fuel Tank*. 2000, Portland, OR: Greenteach Publishing 130.

13. Bolund, B., Bernhoff, H. and Leijon, M., *Flywheel energy and power storage.* Renewable and Sustainable Energy Reviews, 2007. **11**: p. 235-58.

14. Linden, S.v.d., *Bulk energy storage potential in the USA, current developments and future prospects.* Energy, 2006. **31**: p. 3446-57.

15. Linden, D., ed. *Handbook of Batteries*. 2nd ed. 2001, McGraw-Hill: New York.

16. Conway, B.E., *Electrochemical Supercapacitors: Scientific Fundamentals and Technological Applications*. 1999: Kluwer.

17. Messenger, R.A. and Ventre, G.G., *Photovoltaic Systems Engineering*. Vol. 2. 2003, Boca Raton: CRC Press.

18. Amatucci, G., *High energy density hybrid battery/supercapacitor system.* US Patent 6,517,972, 2003.

19. Du Pasquier, A., Plitz, I., Menocal, S. and Amatucci, G., *A comparative study of Li-ion battery, supercapacitor and nonaqueous asymmetric hybrid devices for automotive applications.* J. Power Sources, 2003. **115**: p. 171-78.

20. Faggioli, E., Rena, P., Danel, V., Andrieu, X. and Mallant, R., *Supercapacitors for the energy management of electric vehicles.* J. Power Sources, 1999. **84**: p. 261-69.

21. Mastragostino, M. and Soavi, F., *Strategies for high-performance supercapacitors for HEV.* J Power Sources, 2007. **174**: p. 89-93.

22. Pell, W.G., Conway, B.E., Adams, W.A. and de Oliveira, J., *Electrochemical efficiency in multiple dischargerrecharge cycling of supercapacitors in hybrid EV applications* J. Power Sources, 1999. **80**: p. 134-41.

23. Pandolfo, A.G. and Hollenkamp, A.F., *Carbon properties and their role in supercapacitors.* J. Power Sources, 2006. **157**: p. 11-27.

24. Sullivan, F., *Ultracapacitors - global trends and markets*. 2005.

25. Kötz, R. and Carlen, M., *Principles and applications of electrochemical capacitors.* Electrochim. Acta., 2000. **45**: p. 2483-98.

26. Burke, A., *Ultracapacitors: Why, how, and where is the technology.* J. Power Sources, 2000. **91**: p. 37-50.

27. Beguin, F. and Frackowiak, E., *Nanotextured carbons for electrochemical energy storage*, in *Nanomaterials Handbook*, Y. Gogotsi, Editor. 2006, CRC Press: Boca Raton. p. 713-37.

28. Andrieu, X. and Poignant, P., *Electrical power supply circuit, in particular for portable appliances.* US Patent 6,061,577, 2000.

29. Simon, P. and Gogotsi, Y., *Materials for electrochemical capacitors.* Nat. Mater., 2008. **7**: p. 845-54.

30. Chmiola, J. and Gogotsi, Y., *Supercapacitors as advanced energy storage devices.* Nanotechnology Law and Business, 2007. **4**: p. 577

31. Pell, W.G. and Conway, B.E., *Peculiarities and requirements of asymmetric capacitor devices based on combination of capacitor and battery-type electrodes.* J. Power Sources, 2004. **136**: p. 334-45.

32. Conway, B.E., Birss, V. and Wojtowicz, J., *The role and utilization of pseudocapacitance for energy storage by supercapacitors.* J. Power Sources, 1997. **66**: p. 1-14.

33. Pell, W.G. and Conway, B.E., *Voltammetry at a de Levie brush electrode as a model for electrochemical supercapacitor behaviour.* J. Electroanal. Chem., 2001. **500**: p. 121-33.

34. Kim, Y.T., Tadai, K. and Mitani, T., *Highly dispersed ruthenium oxide nanoparticles on carboxylated carbon nanotubes for supercapacitor electrode materials.* J. Mater. Chem., 2005. **15**: p. 4915-21.

35. Jang, J.H., Machida, K., Kim, Y.T. and Naoi, K., *Electrophoretic deposition (EPD) of hydrous ruthenium oxides with PTFE and their supercapacitor performances.* Electrochim. Acta., 2006. **52**: p. 1733-41.

36. Macounova, K., Jirka, I., Trojanek, A., Makarova, M., Samec, Z. and Krtil, P., *Electrochemical behavior of nanocrystalline $Ru_{0.8}Me_{0.2}O_2$ (Me = Fe, Co, Ni) oxide electrodes in double-layer region.* J. Electrochem. Soc., 2007. **154**: p. A1077-A82.

37. Kim, I.H. and Kim, K.S., *Ruthenium oxide thin film electrodes for supercapacitors.* Electrochem. Solid. St. Let., 2001. **4**: p. A62-A64.

38. Mo, Y., Antonio, M.R. and Scherson, D.A., *In situ Ru K-edge X-ray absorption fine structure studies of electroprecipitated ruthenium dioxide films with relevance to supercapacitor applications.* J. Phys. Chem. B, 2000. **104**: p. 9777-79.

39. Chu, Y.S., Lister, T.E., Cullen, W.G., You, H. and Nagy, Z., *Commensurate water monolayer at the RuO_2(110)/water interface.* Phys. Rev. Lett., 2001. **86**: p. 3364-67.

40. Arbizzani, C., Mastragostino, M. and Meneghello, L., *Polymer-based redox supercapacitors: A comparative study.* Electrochim. Acta., 1996. **41**: p. 21-26.

41. Mastragostino, M., Arbizzani, C. and Soavi, F., *Conducting polymers as electrode materials in supercapacitors.* Solid State Ionics, 2002. **148**: p. 493-98.

42. Arbizzani, C., Mastragostino, M. and Soavi, F., *New trends in electrochemical supercapacitors.* J. Power Sources, 2001. **100**: p. 164-70.

43. Hwang, S. and Hyun, S., *Synthesis and characterization of tin oxide/carbon aerogel composite electrodes for electrochemical supercapacitors.* J Power Sources, 2007. **172**: p. 451-59.

44. Hu, C.C. and Cheng, C.S., *Ideally pseudocapacitive behavior of amorphous hydrous cobalt-nickel oxide prepared by anodic deposition.* Electrochem. Solid. St. Let., 2002. **5**: p. A43-A46.

45. Huggins, R.A., *Supercapacitors.* Philosophical Transactions: Mathematical, 1996. **354**: p. 1555-66.

46. Frackowiak, E. and Béguin, F., *Carbon materials for the electrochemical storage of energy in capacitors.* Carbon, 2001. **39**: p. 937-50.

47. Nagarajan, N. and Zhitomirsky, I., *Cathodic electrosynthesis of iron oxide films for electrochemical supercapacitors.* J. App. Electrochem., 2006. **36**: p. 1399-405.

48. Shinde, V.R., Mahadik, S.B., Gujar, T.P. and Lokhande, C.D., *Supercapacitive cobalt oxide (Co_3O_4) thin films by spray pyrolysis.* App. Surf. Sci., 2006. **252**: p. 7487-92.

49. Kalu, E.E., Nwoga, T.T., Srinivasan, V. and Weidner, J.W., *Cyclic voltammetric studies of the effects of time and temperature on the capacitance of electrochemically deposited nickel hydroxide.* J. Power Sources, 2001. **92**: p. 163-67.

50. Ragupathy, P., Vasan, H.N. and Munichandraiah, N., *Synthesis and characterization of nano-MnO_2 for electrochemical supercapacitor studies.* J Electrochem Soc, 2008. **155**: p. A34-A40.

51. Jow, J., Lee, H., Chen, H., Wu, M. and Wei, T., *Anodic, cathodic and cyclic voltammetric deposition of ruthenium oxides from aqueous $RuCl_3$ solutions.* Electrochim Acta, 2007. **52**: p. 2625-33.

52. Wohlfahrt-Mehrens, M., Schenk, J. and Wilde, P.M., *New materials for supercapacitors.* J. Power Sources, 2002. **105**: p. 182-88.

53. Suppes, G.M., Deore, B.A. and Freund, M.S., *Porous conducting polymer/heteropolyoxometalate hybrid material for electrochemical supercapacitor applications.* Langmuir, 2008. **24**: p. 1064-69.

54. Staiti, P. and Lufrano, F., *A study of the electrochemical behaviour of electrodes in operating solid-state supercapacitors.* Electrochim. Acta, 2007. **53**: p. 710-19.

55. Clemente, A., Panero, S., Spila, E. and Scrosati, B., *Solid-state, polymer-based, redox capacitors.* Solid State Ionics, 1996. **85**: p. 273-77.

56. Cebeci, F.C., Geyik, H., Sezer, E. and Sarac, A.S., *Synthesis, electrochemical characterization and impedance studies on novel thiophene-nonylbithiazole-thiophene comonomer.* J. Electroanal. Chem., 2007. **610**: p. 113-21.

57. Mi, H., Zhang, X., Ye, X. and Yang, S., *Preparation and enhanced capacitance of core-shell polypyrrole/polyaniline composite electrode for supercapacitors.* J Power Sources, 2008. **176**: p. 403-09.

58. Laforgue, A., Simon, P. and Fauvarque, J.F., *Chemical synthesis and characterization of fluorinated polyphenylthiophenes: Application to energy storage.* Synthetic Metals, 2001. **123**: p. 311-19.

59. Zheng, J.P., *The limitations of energy density of battery/double-layer capacitor asymmetric cells.* J. Electrochem. Soc., 2003. **150**: p. A484-A92.

60. Fan, Z., Chen, J., Cui, K., Sun, F., Xu, Y. and Kuang, Y., *Preparation and capacitive properties of cobalt-nickel oxides/carbon nanotube composites.* Electrochim Acta, 2007. **52**: p. 2959-65.

61. Lei, Y., Fournier, C., Pascal, J. and Favier, F., *Mesoporous carbon-manganese oxide composite as negative electrode material for supercapacitors.* Micropor. Mesopor. Mat., 2008. **110**: p. 167-76.

62. Li, H., Cheng, L. and Xia, Y.Y., *A hybrid electrochemical supercapacitor based on a 5 V Li-ion battery cathode and active carbon.* Electrochem. Solid. St. Let., 2005. **8**: p. A433-A36.

63. Kurzweil, P. and Chwistek, M., *Electrochemical stability of organic electrolytes in supercapacitors: Spectroscopy and gas analysis of decomposition products.* J. Power Sources, 2008. **176**: p. 555-67.

64. Hsieh, Y., Lee, K., Lin, Y., Wu, N. and Donne, S.W., *Investigation on capacity fading of aqueous MnO_2 NH_2O electrochemical capacitor.* J Power Sources, 2008. **177**: p. 660-64.

65. Hussain, A.M.P. and Kumar, A., *Enhanced electrochemical stability of all-polymer redox supercapacitors with modified polypyrrole electrodes.* J. Power Sources, 2006. **161**: p. 1486-92.

66. Lazzari, M., Mastragostino, M. and Soavi, F., *Capacitance response of carbons in solvent-free ionic liquid electrolytes.* Electrochem. Commun., 2007. **9**: p. 1567-72.

67. Conway, B.E. and Pell, W.G., *Power limitations of supercapacitor operation associated with resistance and capacitance distribution in porous electrode devices.* J. Power Sources, 2002. **105**.

68. Bard, A.J. and Faulkner, L.R., *Electrochemical Methods*. 2001, Hoboken, NJ: John Wiley & Sons.

69. Ohno, H., ed. *Electrochemical Aspects of Ionic Liquids*. 2005, Wiley Interscience: Hoboken, NJ. 392.

70. Izutsu, K., *Electrochemistry in Nonaqueous Solution*. 2002, Weinheim, Germany: Wiley-GmbH.

71. Balducci, A., Soavi, F. and Mastragostino, M., *The use of ionic liquids as solvent-free green electrolytes for hybrid supercapacitors.* Applied Physics A: Materials Science & Processing, 2006. **82**: p. 627-32.

72. Balducci, A., Dugas, R., Taberna, P.L., Simon, P. and Plée, D., *High temperature carbon–carbon supercapacitor using ionic liquid as electrolyte.* J. Power Sources, 2007. **165**: p. 922-27.

73. Shin, J., Henderson, W.A. and Passerini, S., *Ionic liquids to the rescue? Overcoming the ionic conductivity limitations of polymer electrolytes.* Electrochem. Commun., 2003. **5**: p. 1016-20.

74. Chojnacka, J., Acosta, J.L. and Morales, E., *New gel electrolytes for batteries and supercapacitor applications.* J. Power Sources, 2001. **97-98**: p. 819-21.

75. Bispo-Fonseca, I., Aggar, J., Sarrazin, C., Simon, P. and Fauvarque, J.F., *Possible improvements in making carbon electrodes for organic supercapacitors.* J. Power Sources, 1999. **79**: p. 238-41.

76. Ulbricht, M., *Advanced functional polymer membranes.* Polymer, 2006. **47**: p. 2217-62.

77. Andrieu, X., *Process for producing an electrolytic cell having a polymeric separator.* US Patent 6,270,928, 2001.

78. Gozdz, A.S., *Electrochemical cell comprising lamination of electrode and paper separator members.* US Patent App. 09/970,437, 2001.

79. Kejha, J.B., Smith, W.N. and McCloskey, J.R., *Lithium based electrochemical devices having a ceramic separator glued therein by an ion conductive adhesive* US Patent App. 10/516,986, 2002.

80. Nian, Y.R. and Teng, H., *Influence of surface oxides on the impedance behavior of carbon-based electrochemical capacitors.* J. Electroanal. Chem., 2003. **540**: p. 119-27.

81. Soffer, A. and Folman, M., *The electrical double layer of high surface porous carbon electrode.* J. Electroanal. Chem., 1972. **38**: p. 25-43.

82. von Helmholtz, H.L.F., *Studien über die elektrische grenzschichten.* Annalen der Physik, 1879. **243**: p. 337-82.

83. Trasatti, S. and Parsons, R., *Interphases in systems of conducting phases.* Pure & Appl. Chem., 1986. **58**: p. 437-54.

84. Broddd, R.J., Bullock, K.R., Leising, R.A., Middaugh, R.L., Miller, J.R. and Takeuchi, E., *Batteries, 1977 to 2002.* J. Electrochem. Soc., 2004. **151**: p. K1-K11.

85. Woolfe, G., *The supercap communication challenge.* Batteries and Energy Storage Technology, 2005. **3**: p. 107-13.

86. Arico, A.S., Bruce, P., Scrosati, B., Tarascon, J.-M. and Schalkwijk, W.V., *Nanostructured materials for advanced energy conversion and storage devices.* Nat. Mater., 2005. **4**: p. 366-77.

87. Chalk, S.G. and Miller, J.F., *Key challenges and recent progress in batteries, fuel cells, and hydrogen storage.* J. Power Sources, 2006. **159**: p. 73-80.

88. Tanimura, A., Kovalenko, A. and Hitata, F., *Molecular theory of an electrochemical double layer in a nanoporous carbon supercapacitor.* Chem. Phys. Lett., 2003. **378**: p. 638-46.

89. Ricketts, B.W. and Ton-That, C., *Self-discharge of carbon-based supercapacitors with organic electrolytes.* J. Power Sources, 2000. **89**: p. 64-69.

90. Becker, H.I., *Low voltage electrolytic capacitor*. 1957, U.S. Patent #2800616: U.S.A.

91. Rightmire, R.A., *Electrical energy storage apparatus*. 1962, US Patent # 3,288,641: USA.

92. Sharma, R.K., Oh, H., Shul, Y. and Kim, H., *Carbon-supported, nano-structured, manganese oxide composite electrode for electrochemical supercapacitor.* J. Power Sources, 2007. **173**: p. 1024-28.

93. Fang, W., Leu, M., Chen, K. and Chen, L., *Ultrafast charging-discharging capacitive property of RuO_2 nanoparticles on carbon nanotubes using nitrogen incorporation.* J Electrochem Soc, 2008. **155**: p. K15-K18.

94. Fang, W., Chen, K. and Chen, L., *Superior capacitive property of RuO_2 nanoparticles on carbon nanotubes incorporated with nitrogen.* Nanotechnology, 2007. **18**: p. 485716 (4pp).

95. Guang-lei, C., Xin-hong, Z., Lin-jie, Z., Thomas, A. and Muellen, K., *Carbon/nanostructured Ru composites as electrodes for supercapacitors.* New Carbon Mater, 2007. **22**: p. 302-06.

96. Long, J.W., Dening, B.M., McEvoy, T.M. and Rolison, D.R., *Carbon aerogels with ultrathin, electroactive poly(o-methoxyaniline) coatings for high-performance electrochemical capacitors.* J. Non-Cryst. Sol., 2004. **350**: p. 97-106.

97. Beguin, F., *Carbon materials for the electrochemical storage of energy in capacitors.* Carbon, 2001. **39**: p. 937-50.

98. Zhou, P., Li, B., Kang, F.Y. and Zeng, Y.Q., *The development of supercapacitors from coconut-shell activated carbon.* New Carbon Materials, 2006: p. 3214-17.

99. Dandekar, M.S., Arabale, G. and Vijayamohanan, K., *Preparation and characterization of composite electrodes of coconut-shell-based activated carbon and hydrous ruthenium oxide for supercapacitors.* J. Power Sources, 2005. **141**: p. 198-203.

100. Boos, D.L., *Electrolytic capacitor having carbon paste electrodes*. 1970, US Patent #3,536,963: USA.

101. Hamelin, A., in *Modern Aspects of Electrochemistry*, B.E. Conway, J.O.M. Bokris, and R. White, Editors. 1981, Plemum: New York.

102. Bockris, J.O.M. and Reddy, A.K.N., *Modern Electrochemistry 1: Ionics*, ed. J.O.M. Bockris. Vol. 2. 2003, New York: Springer.

103. Kastening, B., Hahn, M., Rabanus, B. and Heins, M., *Electronic properties and double layer of activated carbon.* Electrochim. Acta., 1997. **47**: p. 2789-800.

104. Gouy, G., Compt. Rend., 1910. **149**: p. 654.

105. Peirson, H.O., *Handbook of Carbon, Graphite, and Diamond*. 1994, Park Ridge, NJ: Noyes Publications.

106. Flandrois, S., *Battery Carbons*, in *Encyclopedia of Materials: Science and Technology*. 2001, Elsevier: Amsterdam. p. 484-88.

107. Kinoshita, K., *Carbon: Electrochemical and Physicochemical Properties*. 1988, New York: Wiley-Interscience.

108. Gogotsi, Y., *Carbon Nanomaterials*. 2006, Boca Raton, FL: CRC Press.

109. Baughman, R.H., Zakhidov, A.A. and deHeer, W.A., *Carbon nanotubes - the route toward applications.* Science, 2002. **297**: p. 787-92.

110. Subramoney, S., *Novel nanocarbons - structure, properties and potential applications.* Adv. Mater., 1998. **10**: p. 1157.

111. Bonnefoi, L., Simon, P., Fauvarque, J.F., Sarrazin, C. and Dugast, A., *Electrode optimization for carbon power supercapacitors.* J. Power Sources, 1999. **79**: p. 37-42.

112. Pan, H., Poh, C.K., Feng, Y.P. and Lin, J., *Supercapacitor electrodes from tubes-in-tube carbon nanostructures.* Chem Mater, 2007. **19**: p. 6120-25.

113. Lewandowski, A. and Galinski, M., *Practical and theoretical limits for electrochemical double-layer capacitors.* J Power Sources, 2007. **173**: p. 822-28.

114. Marsh, H. and Reinoso, F.R., *Activated Carbon*. 2005, Amsterdam: Elsevier.

115. Salitra, G., Soffer, A., Eliad, L., Cohen, Y. and Aurback, D., *Carbon electrodes for double-layer capacitors; I. Relations between ion and pore dimensions.* J. Electrochem. Soc., 2000. **147**: p. 2486-93.

116. Endo, M., Kim, Y.J., Takeda, T., Maeda, T., Hayashi, T., Koshiba, K., Hara, H. and Dresselhausb, M.S., *Polyvinylidene chloride-based carbon as an electrode material for high power capacitors with an aqueous electrolyte.* J. Electrochem. Soc., 2001. **148**: p. A1135-A40.

117. Endo, M., Takeda, T., Kim, Y.J., Koshiba, K. and Ishii, K., *High power electric double layer capacitor (EDLC's); from operating principle to pore size control in advanced activated carbons.* Carbon Sci., 2001. **1**: p. 117-28.

118. Kim, Y.T., Lee, B.J., Suezaki, H., Chino, T. and Abe, Y., *Preparation and characterization of bamboo-based activated carbons as electrode materials for electric double layer capacitors.* Carbon, 2006. **44**: p. 581-616.

119. Guo, Y., Qi, J., Jiang, Y.X., Yang, S., Wang, Z. and Xu,, *Performance of electrical double layer capacitors with porous carbons derived from rice husk.* Mater. Chem. Phys., 2003. **80**: p. 704-09.

120. Wu, F.-C., Tseng, R.-L., Hu, C.-C. and Wang, C.-C., *Physical and electrochemical characterization of activated carbons prepared from firwoods for supercapaictors.* J. Power Sources, 2004. **138**: p. 351-59.

121. Gamby, J., Taberna, P.L., Simon, P., Fauvarque, J.F. and Chesneau, M., *Studies and characterization of various activated carbons used for carbon/carbon supercapacitors.* J. Power Sources, 2001. **101**: p. 109-16.

122. Endo, M., Maeda, T., Kim, Y.J., Dresselhaus, M.S., Ohta, H., Inoue, T., Hayashi, T. and Nishimura, Y., *Morphology and organic edlc applications of chemically activated Ar-resin-based carbons.* Carbon, 2002. **40**: p. 2613-26.

123. Weng, T.C. and Teng, H., *Characterization of high porosity carbon electrodes derived from mesophase pitch for electric double-layer capacitors.* J. Electrochem. Soc., 2001. **148**: p. A368-A73.

124. Yang, K.L., Yiacoumi, S. and Tsouris, C., *Electrosorption capacitance of nanostructured carbon aerogel obtained by cyclic voltammetry.* J. Electroanal. Chem., 2003. **540**: p. 159-67.

125. Saliger, R., Fischer, U., Herta, C. and Fricke, J., *High surface area carbon aerogels for supercapacitors.* J. Non-Cryst. Sol., 1998. **225**: p. 81-85.

126. Adhyapak, P.V., Maddanimath, T. and Pethkar, S., *Application of electrochemically prepared carbon nanofibers in supercapacitors.* J. Power Sources, 2002. **109**: p. 105-10.

127. Huang, C.H., Wu, Y.P., Hu, C.C. and Li, Y., *Textural and electrochemical characterization of porous carbon nanofibers as electrodes for supercapacitors.* J. Power Sources, 2007. **172**: p. 460-67.

128. Shiraishi, S., Kurihara, H., Shi, L., Nakayama, T. and Oya, A., *Electric double-layer capacitance of meso/macroporous activated carbon fibers prepared by the blending method.* J. Electrochem. Soc., 2002. **149**: p. A855-A61.

129. Morishita, T., Soneda, Y., Tsumura, T. and Inagaki, M., *Preparation of porous carbons from thermoplastic precursors and their performance for electric double layer capacitors.* Carbon, 2006. **44**: p. 2360-67.

130. Fuertes, A.B., Pico, F. and Rojo, J.M., *Influence of pore structure on electric double-layer capacitance of template mesoporous carbons.* J. Power Sources, 2004. **133**: p. 329-36.

131. Vix-Guterl, C., Frackowiak, E., Jurewicz, K., Friebe, M., Parmentier, J. and Beguin, F., *Electrochemical energy storage in ordered porous carbon materials.* Carbon, 2005. **43**: p. 1293-302.

132. Prabaharan, S.R.S., Vimala, R. and Zainal, Z., *Nanostructured mesoporous carbon as electrodes for supercapacitors.* J. Power Sources, 2006. **161**: p. 730-36.

133. Liu, H.Y., Wang, K.P. and Teng, H., *A simplified preparation of mesoporous carbon and the examination of the carbon accessibility for electric double-layer formation.* Carbon, 2005. **43**: p. 559-66.

134. Li, H., Luo, J., Zhou, X., Yu, C. and Xia, Y., *An ordered mesoporous carbon with short pore length and its electrochemical performances in supercapacitor applications.* J Electrochem Soc, 2007. **154**: p. A731-A36.

135. Chen, J.H., Li, W.Z., Wang, D.Z., Yang, S.X., Wen, J.G. and Ren, Z.F., *Electrochemical characterization of carbon nanotubes as electrode in electrochemical double-layer capacitors.* Carbon, 2002. **40**: p. 1193-97.

136. Emmenegger, C., Maurona, P., Sudan, P., Wenger, P., Hermann, V., Gallay, R. and Zuttel, A., *Investigation of electrochemical double-layer (EDLC) capacitors electrodes based on carbon nanotubes and activated carbon materials.* J. Power Sources, 2003. **124**: p. 321-29.

137. Chunling, D., Xianyou, W., Qinghua, H. and Jun, L., *Porous carbide derived carbon.* Prog. Chem. (Chinese), 2008. **20**: p. 42-47.

138. Bleda-Martínez, M.J., Maciá-Agulló, J.A., Lozano-Castello, D., Morallon, E., Cazorla-Amoros, D. and Linares-Solano, A., *Role of surface chemistry on electric double layer capacitance of carbon materials.* Carbon, 2005. **43**: p. 2677-84.

139. Centeno, T.A. and Stoeckli, F., *The role of textural characteristics and oxygen-containing surface groups in the supercapacitor performances of activated carbons.* Electrochim. Acta., 2006. **52**: p. 560-66.

140. Frackowiak, E., Lota, G., Machnikowski, J., Vix-Guterl, C. and Beguin, F., *Optimisation of supercapacitors using carbons with controlled nanotexture and nitrogen content.* Electrochim. Acta., 2006. **51**: p. 2209-14.

141. Machnikowski, J., Grzyb, B., Weber, J.V., Frackowiak, E., Rouzaud, J.N. and Béguin, F., *Structural and electrochemical characterization of nitrogen enriched carbons produced by the co-pyrolysis of coal-tar pitch with polyacrylonitrile.* Electrochim. Acta., 2004. **49**: p. 423-32.

142. Kim, T., Lim, S., Kwon, K., Hong, S.-H., Qiao, W., Rhee, C.K., Yoon, S.-H. and Mochida, I., *Electrochemical capacities of well-defined carbon surfaces.* Langmuir, 2006. **22**: p. 9086-88.

143. Endo, M., Maeda, T., Takeda, T., Kim, Y.J., Koshiba, K., Hara, H. and Dresselhaus, M.S., *Capacitance and pore-size distribution in aqueous and nonaqueous electrolytes using various activated carbon electrodes.* J. Electrochem. Soc., 2001. **148**: p. A910-A14.

144. Hahn, M., Baertschi, M., Barbieri, O., Sauter, J.-C., Kotz, R. and Gallay, R., *Interfacial capacitance and electronic conductance of activated carbon double-layer electrodes.* Electrochem. Solid. St. Let., 2004. **7**: p. A33-A36.

145. Qu, D., *Studies of the activated carbons used in double-layer supercapacitors.* J. Power Sources, 2002. **109**: p. 403-11.

146. Kim, Y.J., Masutzawa, Y., Ozaki, S., Endo, M. and Dresselhaus, M.S., *PVDC-based carbon material by chemical activation and its application to nonaqueous EDLC.* J. Electrochem. Soc., 2004. **151**: p. E199-E205.

147. Gryglewicz, G., Machnikowski, J., Lorenc-Grabowska, E., Lota, G. and Frakowiak, E., *Effect of pore size distribution of coal-based activated carbons on double layer capacitance.* Electrochim. Acta., 2005. **50**: p. 1197-206.

148. Li, H., Xi, H.a., Zhu, S., Wen, Z. and Wang, R., *Preparation, structural characterization and electrochemical properties of chemically modified mesoporous carbon.* Micropor. Mesopor. Mat., 2006. **96**: p. 357-62.

149. Toupin, M., Bélanger, D., Hill, I.R. and Quinn, D., *Performance of experimental carbon blacks in aqueous supercapacitors.* J. Power Sources, 2005. **140**: p. 203-10.

150. Shi, H., *Activated carbons and double layer capacitance.* Electrochim. Acta., 1995. **41**: p. 1633-39.

151. Kim, Y.T., Masutzawa, Y., Ozaki, S. and Endo, M., *PVDC-based carbon material by chemical activation and its application to nonaqueous EDLC.* J. Electrochem. Soc., 2004.

152. Eliad, L., Salitra, G., Soffer, A. and Aurbach, D., *Ion sieving effects in the electrical double later of porous carbon electrodes: Estimating effective ion size in electrolytic solutions.* J. Phys. Chem. B, 2005. **105**: p. 6880-87.

153. Lin, C., Ritter, J.A. and Popov, B.N., *Correlation of double-layer capacitance with the pore structure of sol-gel derived carbon xerogels.* J. Electrochem. Soc., 1999. **146**: p. 3639-43.

154. Ania, C.O., Pernak, J., Stefaniak, F., Raymundo-Pinero, E. and Beguin, F., *Solvent-free ionic liquids as in situ probes for assessing the effect of ion size on the performance of electrical double layer capacitors.* Carbon, 2006. **44**: p. 3113-48.

155. Salitra, G., Soffer, A., Eliad, L., Cohen, Y.S. and Aurbach, D., *Carbon electrodes for double-layer capacitors I. Relations between ion and pore dimensions.* J. Electrochem. Soc., 2000. **147**: p. 2486-93.

156. Lozano-Castello, D., Cazorla-Amoros, D., Linares-Solano, A., Shiraishi, S., Kurihara, H. and Oya, A., *Influence of pore structure and surface chemistry on electric double layer capacitance in non-aqueous electrolyte.* Carbon, 2003. **41**: p. 1765-75.

157. Fernandez, J.A., Arulepp, M., Leis, J., Stoeckli, F. and Centeno, T.A., *EDLC performance of carbide-derived carbons in aprotic and acidic electrolytes.* Electrochim. Acta., 2008. **53**: p. 7111-16.

158. Groen, J.C., Peffer, L.A.A. and Perez-Ramirez, J., *Pore size determination in modified micro- and mesoporous materials. Pitfalls and limitations in gas adsorption data analysis.* Micropor. Mesopor. Mat., 2003. **60**: p. 1-17.

159. Leis, J., Arulepp, M., Kuura, A., Lätt, M. and Lust, E., *Electrical double-layer characteristics of novel carbide-derived carbon materials.* Carbon, 2006. **400**: p. 2122-29.

160. Lust, E., Janes, A. and Arulepp, M., *Influence of solvent nature on the electrochemical parameters of double layer capacitors.* J. Electroanal. Chem., 2003. **562**: p. 33-42.

161. Lust, E., Nurk, G., Janes, A., Arulepp, M., Permann, L., Nigu, P. and Moller, P., *Electrochemcial properties of nanoporous carbon electrodes.* Condens. Matter Phys., 2002. **5**: p. 307-27.

162. Gogotsi, Y., Nikitin, A., Ye, H., Zhou, W., Fischer, J.E., Yi, B., Foley, H.C. and Barsoum, M. W., *Nanoporous carbide-derived carbon with tunable pore size.* Nat. Mater., 2003. **2**: p. 591-94.

163. Yushin, G., Nikitin, A. and Gogotsi, Y., *Carbide Derived Carbon*, in *Nanomaterials Handbook*, Y. Gogotsi, Editor. 2006, CRC Press: Boca Raton. p. 237-80.

164. Mohun, W.A., *A novel amorphous carbon*, in *Proc. 4th biennial conf. Carbon*. 1959, Pergamon: Oxford. p. 443-53.

165. Mohun, W.A., *Mineral active carbon and process for producing same*. 1962, US Patent #3,066,099: US.

166. Kyutt, R.N., Smorgonskaya, E.A., Danishevskii, A.M., Gordeev, S.K. and Grechinskaya, A.V., *Structural studies of nanoporous carbon produced from silicon carbide.* Phys. Solid State, 1999. **41**: p. 808-10.

167. Ersoy, D.A., McNallan, M.J. and Gogotsi, Y., *Carbon coatings produced by high temperature chlorination of silicon carbide ceramics.* Mater. Res. Innov., 2001. **5**: p. 55-62.

168. Gogotsi, Y.G., I.-D. Jeon, M.J. McNallan., *Carbon coatings on silicon carbide by reaction with chlorine containing gases.* J. Mater. Chem., 1997. **7**: p. 1841.

169. Cambaz, Z.G., Yushin, G.N., Vyshnyakova, K.L., Pereselentseva, L.N. and Gogotsi, Y., *Conservation of shape during formation of carbide-derived carbon on silicon carbide nano-whiskers.* J. Am. Ceram. Soc., 2006. **89**: p. 509-14.

170. Jacobson, N.S., Gogotsi, Y.G. and Yoshimura, M., *Thermodynamic and experimental study of carbon formation on carbides under hydrothermal conditions.* Journal of Applied Chemistry, 1995. **5**: p. 595-601.

171. Nikitin, A. and Gogotsi, Y., *Nanostructured Carbide Derived Carbon*, in *Encyclopedia of Nanoscience and Nanotechnology*, H.S. Nalwa, Editor. 2003, American Scientific Publishers: Stevenson Ranch, CA. p. 553-74.

172. Yushin, G., Hoffman, E., Nikitin, A., Ye, H., Barsoum, M.W. and Gogotsi, Y., *Synthesis of nanoporous carbide-derived carbon by chlorination of titanium silicon carbide.* Carbon, 2005. **43**: p. 2075-82.

173. Hoffman, E.N., Yushin, G., Barsoum, M.W. and Gogotsi, Y., *Synthesis of carbide-derived carbon by chlorination of Ti_2AlC.* Chem. Mater., 2005. **17**: p. 2317-22.

174. Dash, R.K., Nikitin, A. and Gogotsi, Y., *Microporous carbon derived from boron carbide.* Micropor. Mesopor. Mat., 2004. **72**: p. 203-08.

175. Dimovski, S., Nikitin, A., Ye, H. and Gogotsi, Y., *Synthesis of graphite by chlorination of iron carbide at moderate temperatures.* J. Mater. Chem., 2004. **14**: p. 238-43.

176. Dash, R.K., Yushin, G. and Gogotsi, Y., *Structure and porosity analysis of microporous and mesoporous carbon derived from zirconium carbide.* Micropor. Mesopor. Mat., 2005. **86**: p. 50-57.

177. Hutchins, O., *Method for the production of silicon tetrachloride*. 1918, US Patent #1,271,713: US.

178. Boehm, H.P. and Warnecke, H.H., *Structural and molecular sieve properties of carbons prepared from metal carbides*, in *Proceedings of the 12th biennial conference on carbon*. 1975, Pergamon: Oxford. p. 149-50.

179. Dash, R., Chmiola, J., Yushin, G., Gogotsi, Y., Laudisio, G., Singer, J., Fischer, J. and Kucheyev, S., *Titanium carbide derived nanoporous carbon for energy-related applications.* Carbon, 2006. **44**: p. 2489-97.

180. Laudisio, G., Dash, R.K., Singer, J.P., Yushin, G., Gogotsi, Y. and Fischer, J.E., *Carbide-derived carbons: A comparative study of porosity based on small-angle scattering and adsorption isotherms.* Langmuir, 2006. **22**: p. 8945 -50.

181. Gogotsi, Y., Nikitin, A., Ye, H., Zhou, W., Fischer, J.E., Yi, B., Foley, H.C. and Barsoum, M.W., *Nanoporous carbide-derived carbon with tunable pore size.* Nat. Mater., 2003. **2**: p. 591-94.

182. Ersoy, D., McNallan, M.J. and Gogotsi, Y.G., *Carbon coatings produced by high temperature chlorination of silicon carbide ceramics.* , Mater. Res. Innovations, 2001. **5**: p. 55-62.

183. Zhang, J., Ekstrom, T.C., Gordeev, S.K. and Jacob, M., *Carbon with an onion-like structure obtained by chlorinating aluminum carbide.* J. Mater. Chem., 2000. **10**: p. 1039-41.

184. Jacob, M., Palmqvist, U., Alberius, P.C.A., Ekstrom, T., Nygren, M. and Lidin, S., *Synthesis of structurally controlled nanocarbons--in particular the nanobarrel carbon.* Solid State Sci., 2003. **5**: p. 133-37.

185. Weltz, S., McNallan, M. and Gogotsi, Y., *Carbon structures in silicon carbide derived carbon.* J. Mater. Process. Tech., 2006. **179**: p. 11-22.

186. Boehm, H.P., *The first observation of carbon nanotubes.* Carbon, 1997. **35**: p. 581-84.

187. Kravchik, A.E., Kukushikina, J.A., Sokolov, V.V. and Tereshchenko, G.F., *Structure of nanoporous carbon produced from boron carbide.* Carbon, 2006. **44**: p. 3263-68.

188. Leis, J., Perkson, A., Arulepp, M., Nigu, P. and Svensson, G., *Catalytic effect of metals of the iron subgroup on the chlorination of titanium carbide to form nanostructural carbon.* Carbon, 2002. **40**: p. 1559-64.

189. Kyutt, R.N., Smorgonskaya, E.A., Danishevski, A.M., Gordeev, S.K. and Grechinskaya, A.V., *Structural study of nanoporous carbon produced from polycrystalline carbide naterials: Small-angle X-ray scattering.* Phys. Solid State, 1999. **41**: p. 1359-63.

190. Kusunoki, M., Rokkaku, M. and Suzuki, T., *Epitaxial carbon nanotube film self-organized by decomposition of silicon carbide.* Appl. Phys. Lett., 1997. **71**: p. 2620-22.

191. Kusunoki, M., Suzuki, T., Hirayama, T., Shibata, J. and Kaneko, K., *A formation mechanism of carbon nanotube films on SiC (000-1).* Appl. Phys. Lett., 2000. **77**: p. 531-33.

192. Kusunoki, M., Suzuki, T., Kaneko, K. and Ito, M., *Formation of self-aligned carbon nanotube films by surface decomposition of silicon carbide.* Phil. Mag. Lett., 1999. **79**: p. 153-61.

193. Kusunoki, M., Suzuki, T., Honjo, C., Hirayama, T. and Shibata, N., *Selective synthesis of zigzag-type aligned carbon nanotubes on SiC (000-1) wafers.* Chem. Phys. Lett., 2002. **366**: p. 458-62.

194. Nagano, T., Ishikawa, Y. and Shibata, N., *Effects of surface oxides of SiC on carbon nanotube formation by surface decomposition.* Jpn. J. Appl. Phys., 2003. **42**: p. 1380-85.

195. Nagano, T., Ishikawa, Y. and Shibata, N., *Preparation of silicon-on-insulator substrate on large free-standing carbon nanotube film formation by surface decomposition of SiC film.* Jpn. J. Appl. Phys., 2003. **42**: p. 1717-21.

196. Yamauchi, T., Tokunaga, T., Naitoh, M., Nishigaki, S., Toyama, N., Shoji, F. and Kusunoki, M., *Influence of surface structure modifications on the growth of carbon nanotubes on the SiC (0001) surfaces.* Surf. Sci., 2006. **600**: p. 4077-80.

197. Harrison, J., Sambandam, S.N., Boeckl, J.J., Mitchel, W.C., Collins, W.E. and Lu, W., *Evaluation of metal-free carbon nanotubes formed by SiC thermal decomposition.* J. Appl. Phys., 2007. **101**: p. 104311.

198. Wang, S., Humphreys, E.S., Chung, S.-Y., Delduci, D.F., Lustig, S.R., Wang, H., Parker, K.N., Rizzo, N.W., Subramoney, S., Chiang, Y.-M. and Jagota, A., *Peptides with selective affinity for carbon nanotubes.* Nat. Mater., 2003. **2**: p. 196-299.

199. Botti, S., Asilyan, L.S., Ciardi, R., Fabbri, F., Lorety, S., Santoni, A. and Orlanducci, S., *Catalyst-free growth of carbon nanotubes by laser annealing of amorphous SiC films.* Chem. Phys. Let., 2004. **396**: p. 1-5.

200. Forbeaux, I., Themlin, J.-M. and Debever, J.-M., *High-temperature graphitization of the 6H-SiC (0001) face.* Surf. Sci., 1999. **442**: p. 9-18.

201. Cambaz, Z.G., Yushin, G., Osswald, S., Mochalin, V. and Gogotsi, Y., *Noncatalytic synthesis of carbon nanotubes, graphene and graphite on sic.* Carbon, 2008. **46**: p. 841-49.

202. Gogotsi, Y., Weltz, S., Ersoy, D.A. and McNallan, M.J., *Conversion of silicon carbide to crystalline diamond-structured carbon at ambient pressure.* Nature, 2001. **411**: p. 283-87.

203. Gogotsi, Y., Dash, R.K., Yushin, G., Yildirim, T., Laudisio, G. and Fischer, J.E., *Tailoring of nanoscale porosity in carbide-derived carbons for hydrogen storage.* J. Am. Chem. Soc., 2005. **127**: p. 16006-07.

204. Kotina, I.M., Lebedev, V.M., Ilves, A.G., Patsekina, G.V., Tuhkonen, L.M., Gordeev, S.K., Yagovkina, M.A. and Ekstrцm, T., *Study of the lithium diffusion in nanoporous carbon materials produced from carbides.* J. Non-Crystalline Solids, 2002. **299-302**: p. 815-19.

205. Kotina, I.M., Lebedev, V.M., Ilves, A.G., Patsekina, G.V., Tuhkonen, L.M., Gordeev, S.K., Yagovkina, M.A. and Ekstrom, T., *The phase composition of the lithiated samples of nanoporous carbon materials produced from carbides.* J. Non-Cryst. Sol., 2002. **299-302**: p. 820-23.

206. Yushin, G., Hoffman, E.N., Barsoum, M.W., Gogotsi, Y., Howell, C.A., Sandeman, S.R., Phlllips, G.J., Lloyd, A.W. and Mikhalovsky, S.V., *Mesoporous carbide-derived carbon with porosity tuned for efficient adsorption of cytokines.* Biomaterials, 2006. **27**: p. 5755-62.

207. Carroll, B., Gogotsi, Y., Kovalchenko, A., Erdemir, A. and McNallan, M., *Effect of humidity on the tribological properties of carbide-derived carbon (CDC) films on silicon carbide.* Tribo. Lett., 2003. **15**: p. 41-44.

208. Avarbz, R.G., Vartanova, A.V., Gordeev, S.K., Zjukov, S.G., Zelenov, B.A., Kravtjik, A.E., Kuznetsof, V.P., Kukusjkina, J.A., Mazaeva, T.V., Pankina, O.S. and Sokolov, V.V., *Process of manufacturing a porous carbon material and a capacitor having the same*. 1996, US Patent #5,876,787: U.S.A.

209. Dash, R.K., *Nanoporous carbons derived from binary carbides and their optimization for hydrogen storage*, in *Department of Materials Science and Engineering*. 2006, Drexel University: Philadelphia.

210. Chmiola, J., Yushin, G., Dash, R.K., Hoffman, E.N., Fischer, J.E., Barsoum, M. and Gogotsi, Y., *Double-layer capacitance of carbide-derived carbons in sulfuric acid.* Electrochem. Solid. St. Let., 2005. **8**: p. A357-A60.

211. Chmiola, J., Yushin, G., Gogotsi, Y., Portet, C., Simon, P. and Taberna, P.-L., *Anomalous increase in carbon capacitance at pore size below 1 nm.* Science, 2006. **313**: p. 1760-63.

212. Chmiola, J., Yushin, G., Dash, R. and Gogotsi, Y., *Effect of pore size and surface area of carbide-derived carbons on specific capacitance.* J. Power Sources, 2006. **158**: p. 765-72.

213. Hoffman, E.N., Yushin, G., Barsoum, M.W. and Gogotsi, Y., *Synthesis of carbide-derived carbon by chlorination of Ti_2AlC.* Chem. Mater., 2005. **17**: p. 2317-22.

214. Hoffman, E.N., Yushin, G., El-Raghy, T., Gogotsi, Y. and Barsoum, M.W., *Micro and mesoporosity of carbon derived from ternary and binary metal carbides.* Micropor. Mesopor. Mat., 2008. **112**: p. 526-32.

215. Janes, A., *Synthesis and characterisation of nanoporous carbide-derived carbon by chlorination of vanadium carbide.* Carbon, 2007. **45**: p. 2717-22.

216. Urbonaite, S., Wachtmeister, S., Mirguet, C., Coronel, E., Zou, W.Y., Csillag, S. and Svensson, G., *EELS studies of carbide derived carbons.* Carbon, 2007. **45**: p. 2047-53.

217. Urbonaite, S., Juarez-Galan, J.M., Leis, J., Rodriguez-Reinoso, F. and Svensson, G., *Porosity development along the synthesis of carbons from metal carbides.* Micropor. Mesopor. Mat., 2008. **113**: p. 14-21.

218. Chmiola, J., Yushin, G., Gogotsi, Y., Portet, C., Simon, P. and Taberna, P.-L., *Effect of pore size on electrochemical behavior of carbide derived carbon for supercapacitor applications*, in *231st ACS Spring Meeting*. 2006: Atlanta, GA, USA.

219. Chmiola, J., Yushin, G., Gogotsi, Y., Portet, C., Simon, P. and Taberna, P.L., *Anomalous increase in carbon capacitance at pore sizes less than 1 nanometer.* Science, 2006. **313**: p. 1760-63.

220. Rodriguez-Reinoso, F. and Sepulveda-Escribano, A., *Porous carbons in adsorption and catalysis*, in *Handbook of surfaces and interfaces of materials*, H.S. Nalwa, Editor. 2001, Academic: San Diego. p. 309-51.

221. Gordeev, S.K., Kukushkin, S.A., Osipov, A.V. and Pavlov, Y.V., *Self-organization in the formation of a nanoporous carbon material.* Physics of the Solid State, 2000. **42**: p. 2314-1317.

222. Maletin, Y.A., Strizhakova, N.G., Izotov, V.G., Mironova, A.A., Kozachkov, S.G., Danilin, V.G., Podmogilny, S.N., Arulepp, M., Kukusjkina, J.A., Kravtjik, A.E., Sokolov, V.V., Perkson, A., Leis, J., Zheng, J., Gordeev, S.K., Kolotilova, J.Y., Cederstrom, J. and C.L. Wallace, *A supercapacitor and a method of manufacturing such a supercapacitor*. 2002, Eurpoean Patent WO 02/39468.

223. Maletin, Y., Strizhakova, N., Kozachkov, S., Mironova, A., Podmogilny, S., Danilin, V., Kolotilova, J., Izotov, V., Konstantinovich, G.S., Aleksandrovna, J.K., Vasilevitj, V.S., Efimovitj, A.K., Perkson, A., Arulepp, M., Leis, J., Wallace, C.L. and Zheng, J., *Supercapacitor and a method of manufacturing such a supercapacitor*. 2004, US Patent #6,697,249.

224. Leis, J., Arulepp, M. and Perkson, A., *Method to modify the pore characteristics of porous carbon and porous carbon materials produced by this method*. 2004, European Patent WO/2004/094307.

225. Arulepp, M., Leis, J., Latt, M., Miller, F., Rumma, K., Lust, E. and Burke, A.F., *The advanced carbide-derived carbon based supercapacitor.* J. Power Sources, 2006. **162**: p. 1460-66.

226. Erdemir, A., Kovalchenko, A., McNallan, M.J., Weltz, S., Lee, A. and Gogotsi, Y., *Effects of high-temperature hydrogenation treatment on sliding friction and wear behavior of carbide-derived carbon films.* Surface & Coatings Technology, 2004. **188-189**: p. 588-93.

227. Yushin, G., Dash, R., Jagiello, J., Fischer, J.E. and Gogotsi, Y., *Carbide-derived carbons: Effect of pore size on hydrogen uptake and heat of adsorption.* Ad. Funct. Mater., 2006. **16**: p. 2288-93.

228. Yushin, G.N., Hoffman, E.N., Nikitin, A., Ye, H.H., Barsoum, M.W. and Gogotsi, Y., *Synthesis of nanoporous carbide-derived carbon by chlorination of titanium silicon carbide.* Carbon, 2005. **43**: p. 2075-82.

229. Zagotta, W.N., *Permutations of permeability.* Nature, 2006. **440**: p. 427-29.

230. *Practical laboratory information*. Lange's Handbook of Chemistry, ed. J.A. Dean. 1999, New York: McGraw-Hill.

231. Rouquerol, J., Avnir, d., Fairbridge, C.W., Everett, D.H., Haynes, J.H., Pernicone, N., Ramsay, J.D.F., Sing, K.S.W. and Unger, K.K., *Recommendations for the characterization of porous solids.* Pure & Appl. Chem., 1994. **66**: p. 1739-58.

232. Sing, K.S.W., Everett, D.H., Haul, R.A.V., Moscou, L., Pierotti, R.A., Rouquerol, J. and Siemieniewska, T., *Reporting physisorption data for gas/solid systems.* Pure & Appl. Chem., 1985. **57**: p. 603-19.

233. Brunauer, S., Emmett, P. and Teller, E., *Adsorption of gasses in multimolecular layers.* J. Am. Chem. Soc., 1938. **60**: p. 309-19.

234. Laudisio, G., Dash, R.K., Singer, J.P., Yushin, G.N., Gogotsi, Y. and Fischer, J.E., *Carbide-derived carbons: A comparative study of porosity based on small-angle scattering and adsorption isotherms.* Langmuir, 2006. **22**: p. 8945-50.

235. Wu, N.L. and Wang, S.Y., *Conductivity percolation in carbon-carbon supercapacitor electrodes.* J. Power Sources, 2002. **110**: p. 233-36.

236. Yoon, S., Jang, J.H., Ka, B.H. and Oh, S.M., *Complex capacitance analysis on rate capability of electric-double layer capacitor (EDLC) electrodes of different thicknesses.* Electrochim. Acta., 2005. **50**: p. 2255-62.

237. Claye, A., Fischer, J.E. and Métrot, A., *Kinetics of alkali insertion in single wall carbon nanotubes: An electrochemical impedance spectroscopy study.* Chem. Phys. Lett., 2000. **330**: p. 61-67.

238. X-miao, L., Rui, Z., Liang, Z., Dong-hui, L., Wen-ming, Q., Jun-he, Y. and Li-cheng, L., *Impedance of carbon aerogel/activated carbon composites as electrodes of electrochemical capacitors in aprotic electrolyte.* New Carbon Materials, 2007. **22**: p. 153-58.

239. Portet, C., Taberna, P.L., Simon, P. and Laberty-Robert, C., *Modification of al current collector surface by sol-gel deposit for carbon-carbon supercapacitor applications.* Electrochim. Acta., 2004. **49**: p. 905-12.

240. Taberna, P.L., Portet, C. and Simon, P., *Electrode surface treatment and electrochemical impedance spectroscopy study on carbon/carbon supercapacitors.* Appl. Phys. A, 2006. **82**: p. 639-46.

241. Chmiola, J., Dash, R., Yushin, G. and Gogotsi, Y., *Effect of pore size and surface area of carbide derived carbon on specific capacitance.* J. Power Sources, 2006. **158**: p. 765-72.

242. Hoffman, E.N., *Max−phase carbide derived carbons for environmental applications*, in *Materials Science and Engineering*. 2006, Drexel: Philadelphia.

243. Permann, L., Lätt, M., Leis, J. and Arulepp, M., *Electrical double layer characteristics of nanoporous carbon derived from titanium carbide.* Electrochim. Acta., 2006.

244. Jagiello, J. and Thommes, M., *Comparison of dft characterization methods based on N_2, Ar, CO_2 and H_2 adsorption applied to carbons with various pore size distributions.* Carbon, 2004. **42**: p. 1227-32.

245. Chmiola, J., Yushin, G., Dash, R.K., Hoffman, E.N., Fischer, J.E., Barsoum, M.W. and Gogotsi, Y., *Double-layer capacitance of carbide derived carbons in sulfuric acid.* Electrochemical and Solid State Letters, 2005. **8**: p. A357-A60.

246. Flandrois, S. and Simon, B., *Carbon materials for lithium-ion rechargeable batteries.* Carbon, 1999. **37**: p. 165-80.

247. Huang, J., Sumpter, B.G. and Meunier, V., *Theoretical model of nanoporous carbon supercapacitors.* Angewandte Chemie, 2007. **46**: p. 1-6.

248. Dzubiella, J. and Hansen, J.P., *Electric-field-controlled water and ion permeation of a hydrophobic nanopore.* Journal of Chemical Physics, 2005. **122**: p. 23706-10

249. Oshkubo, T., Konishi, T., Hattori, Y., Kanoh, H., Fujikawa, T. and Kaneko, K., *Restricted hydration structures of Rb and Br ions confined in slit-shaped carbon nanospaces.* J. Am. Chem. Soc., 2002. **124**: p. 11860-61.

250. Carrillo-Tripp, M., Saint-Martin, H. and Ortega-Blake, I., *Minimalist molecular model for nanopore selectivity.* Phys. Rev. Lett., 2004. **93**: p. 168104.

251. DiLeo, J.M. and Maranon, J., *Hydration and diffusion of cations in nanopores.* J. Mol. Struct., 2004. **729**: p. 53-57.

252. Chmiola, J., Largeot, C., Taberna, P.-L., Simon, P. and Gogotsi, Y., *Desolvation of ions in subnanometer pores, its effect on capacitance and double-layer theory.* Angewandte Chemie, 2008. **47**: p. 3392-95.

253. Tarascon, J.-M. and Armand, M., *Issues and challenges facing rechargeable lithium batteries.* Nature, 2001. **414**: p. 359-67.

254. McKinnon, W.R., *Insertion electrodes I: Atomic and electronic structure of the hosts and their insertion compounds*. Solid-State Electrochemistry, ed. P.G. Bruce. 1995, New York: Cambridge University Press.

255. Yang, L. and Garde, S., *Modeling the selective partitioning of cations into negatively charged nanopores in water.* J. Chem. Phys., 2007. **126**: p. 18706.

256. Yang, C.-M., Kim, Y.-J., Endo, M., Kanoh, H., Yudasaka, M., Iijima, S. and Kaneko, K., *Nanowindow-regulated specific capacitance of supercapacitor electrodes of single-wall carbon nanohorns.* J. Am. Chem. Soc., 2007. **129**: p. 20-21.

257. Tanimura, A., Kovalenko, A. and Hirata, F., *Structure of electrolyte solutions sorbed in carbon nanospaces, studied by the replica RISM theory.* Langmuir, 2007. **23**: p. 1507-17.

258. Tanimura, A., Kovalenko, A. and Hirata, F., *Molecular theory of an electrochemical double layer in a nanoporous carbon supercapacitor.* Chem. Phys. Lett., 2003. **378**: p. 638-46.

259. Largeot, C., Portet, C., Chmiola, J., Taberna, P.-L., Gogotsi, Y. and Simon, P., *Relation between the ion size and pore size for an electric double-layer capacitor.* J. Am. Chem. Soc., 2008. **130**: p. 2730-31.

260. Portet, C., Taberna, P.L., Simon, P. and Flahaut, E., *High power density electrodes for carbon supercapacitor applications.* Electrochim. Acta., 2005. **50**: p. 4174-81.

261. Taberna, P.L., Simon, P. and Fauvarque, J.F., *Electrochemical characteristics and impedance spectroscopy studies of carbon-carbon supercapacitors.* J. Electrochem. Soc., 2003. **150**: p. 292-300.

262. Conway, B.E., *Electrolyte solutions: Solvation and structural aspects.* Annu. Rev. Phys. Chem., 2007. **17**: p. 481-528.

263. Bordjiba, T., Mohamedi, M. and Dao, L.H., *Synthesis and electrochemical capacitance of binderless nanocomposite electrodes formed by dispersion of carbon nanotubes and carbon aerogels.* J. Power Sources, 2007. **172**: p. 991-98.

264. Bordjiba, T., Mohamedi, M. and Dao, L.H., *New class of carbon-nanotube aerogel electrodes for electrochemical power sources.* Adv Mater, 2008. **20**: p. 815-19.

265. Bonnefoi, L., Simon, P., Fauvarque, J.F. and Sarrazin, C., *Electrode compositions for carbon power supercapacitors.* J. Power Sources, 1999. **79**: p. 37-42.

266. Srikanth Ranganathan, R.S.a., *Photoresist-derived carbon for microelectromechanical systems and electrochemical applications.* J. Electrochem. Soc., 2000. **147**: p. 277-82.

267. Hoffman, E.N., Yushin, G., Wendler, B.G., Barsoum, M.W. and Gogotsi, Y., *Carbide-derived carbon membrane.* Mater. Chem. Phys., 2008. **112**: p. 587-91.

268. Aurbach, D., Markovsky, B., Weissman, I., Levi, E. and Ein-Eli, Y., *On the correlation between surface chemistry and performance of graphite negative electrodes for Li ion batteries.* Electrochim. Acta., 1999. **45**: p. 67-86.

269. Zhu, L., Hommet, F., Salace, G., Claude-Montigny, B. and Metrot, A., *STM observation of the electro-adsorption of lithium ions onto graphite and of the ensuing solid electrolyte interphase formation.* Surf. Sci., 2002. **512**: p. 84-96.

270. Ruch, P.W., Hahn, M., Rosciano, F., Holzapfel, A., Kaiser, H., Scheifele, W., Schmitt, B., Novák, P., Koetz, R. and Wokaun, A., *In situ X-ray diffraction of the intercalation of $(C_2H_5)_4N^+$ and BF_4^- into graphite from acetonitrile and propylene carbonate based supercapacitor electrolytes*, in *Electrochim Acta*. 2007. p. 1074-82.

271. Hardwick, L.J., Hahn, M., Ruch, P., Holzapfel, M., Scheifele, W., Buqa, H., Krumeich, F., Novak, P. and Kotz, R., *An in situ raman study of the intercalation of supercapacitor-type electrolyte into microcrystalline graphite.* Electrochim. Acta., 2006. **52**: p. 675-80.

272. Ruch, P.W., Hahn, M., Rosciano, F., Holzapfel, M., Kaiser, H., Scheifele, W., Schmitt, B., Novak, P., Kotz, R. and Wokaun, A., *In situ X-ray diffraction of the intercalation of $(C_2H_5)_4N^+$ and BF_4^- into graphite from acetonitrile and propylene*

carbonate based supercapacitor electrolytes. Electrochim. Acta., 2007. **53**: p. 1074-82.

273. Claye, A., Fischer, J.E., Huffman, C.B., Rinzler, A.G. and Smalley, R.E., *Solid-state electrochemistry of the Li single wall carbon nanotube system.* J. Electrochem. Soc, 2000. **147**: p. 2845-52.

274. Gagnon, E.G., *The triangular voltage sweep method for determining double-layer capacity of porous electrodes.* J. Electrochem. Soc., 1975. **122**: p. 521-25.

275. Pananek, P., Radosavljevic, M. and Fischer, J.E., *Lithium insertion in disordered carbon-hydrogen alloys: Intercalation vs covalent binding.* Chem Mater, 1996.

276. Brennan, J.K., Bandosz, T.J., Thomson, K.T. and Gubbins, K.E., *Water in porous carbons.* Colloids and Surfaces A: Physicochemical and Engineering Aspects, 2001. **187**.

277. Kohlrausch, F., Pogg. Ann., 1873. **148**: p. 143.

278. E.Warburg, Ann. Phys., 1901. **6**: p. 125.

279. de Levie, R., *On the nature of porous charged interfaces.* Electrochim. Acta., 1963. **8**: p. 751-80.

280. Kotina, I.M., Lebedev, V.M., Ilves, A.G., Patsekina, G.V., Tuhkonen, L.M., Gordeev, S.K., Yagovkina, M.A. and Ekstrom, T., *Study of the lithium diffusion in nanoporous carbon materials produced from carbides.* J. Non-Cryst. Sol., 2002. **299-302**: p. 815-19.

281. Zuleta, M., Bursell, M., Bjornbom, P. and Lundblad, A., *Determination of the effective diffusion coefficient of nanoporous carbon by means of a single particle microelectrode technique.* J. Electroanal. Chem., 2003. **549**: p. 101-08.

Appendix A: Abbreviations

AC	Alternating current
BET	Brunauer, Emmet and Teller
BF_4	Tetrafluoroborate anion
CDC	Carbide derived carbon
CME	Cavity microelectrode
CV	Cyclic voltammetry
DC	Direct current
DFT	Density functional theory
DI	Deionized
EC	Electrochemical capacitor
EDLC	Electric double-layer capacitor
EDS	Energy dispersive X-ray spectroscopy
EIS	Electrochemical impedance spectroscopy
EMI	1-ethyl-3-methyl immidazolium
ESR	Equivalent series resistance
FWHM	Full width at half maximum
HEV	Hybrid electric vehicle
ICE	Internal combustion engine
MEMS	Microelectromechanical systems
MPG	Miles per gallon

MWCNT	Multi-walled carbon nanotube
NLDFT	Non-local density functional theory
NMAC	Natural material activated carbon
OD	Outer diameter
PTFE	Polytetrafluroethylene
PVDF	Polyvinylidene fluoride
PZC	Point of zero charge
RMS	Root mean square
SAXS	Small-angle X-ray scattering
SEM	Scanning electron microscopy
SMAC	Synthetic material activated carbon
SOHIO	Standard Oil of Ohio
SSA	Specific surface area
SWNT	Single wall carbon nanotube
TEA	Tetraethylammonium cation
TEM	Transmission electron microscopy
TFSI	bis-(trifluoromethanesulfonyl)imide
XRD	X-Ray diffraction

Appendix B: Symbols

A	Area	(m^2)
C	Capacitance	(F)
C_ϕ	Adsorption capacitance	(F)
C_{total}	Total capacitance	(F)
$C_{positive}$	Capacitance of positive electrode	(F)
$C_{negative}$	Capacitance of negative electrode	(F)
d	Charge separation distance	(m)
γ	Surface tension	(N/m)
E	Energy	(J)
e	Electron charge	(1.602×10^{-19} C)
ε	Dielectric constant	(Unitless)
ε_0	Dielectric permittivity	(8.85×10^{-12} F/m)
g	Gravitational force	(9.8 m/s^2)
$g\theta$	Lateral interaction term	(Unitless)
$\overline{G}^R$	Bulk solution Gibbs free energy	(J/mol)
$\overline{G}^S$	Interfacial Gibbs free energy	(J/mol)
σ_i^M	Surface charge density	(m^{-2})
k	Boltzman's constant	(1.38×10^{-23} J/atom-K)
m	Mass	(kg)

n_i^{σ}	Excess number of surface electrons	(Unitless)
n_i^{S}	Excess number of surface ions	(Unitless)
n_i^{R}	Excess number of bulk ions	(Unitless)
n_i	Concentration of electrolyte at x	(M)
n_i^{0}	Bulk electrolyte concentration	(M)
ϕ	Potential	(V)
P	Pressure	(Pa)
q	Charge	(C)
R	Gas constant	(8.31 J/mol-K)
r_c	Critical drop radius	(m)
S	Entropy	(J/K)
T	Temperature	(K)
t_{max}	Time of mercury drop residence	(s)
$\bar{\mu}_i$	Electrochemical potential	(J/mol)
V	Voltage	(V)

Vita

John Chmiola spent his first few years of life as the oldest son in a military family. Fresh out of high school in 1980, his young father joined the Army and his kid parents started a new life in King City, CA, where John was born on October 25th, 1980. His family later traveled with the military to live in Amberg, Germany, and finally Fort Carson, CO, before calling Wilkes-Barre, PA home. LEGO's and tree forts gradually gave way to, BMX bikes and Hardcore/Punk music as teenage rebellion required a rallying cry – 4130 Chromolly is probably the key reason why he chose Materials Science, in fact. After learning how microstructure affects the properties of steels and aluminums, his research interests broadened. Now John's bike has 27" wheels, instead of 20" wheels and he still thinks that steel is better than aluminum. Fast loud music, even to this day, reminds him that just because something is accepted does not make it right. And the louder you yell, the more likely someone will agree.

John graduated with a B.S. in Dept. of Materials Science and Engineering from Drexel University in 2004 with the 2nd highest GPA and the best senior design project in the University. This was only the 2nd time in the history of this competition that someone from the Materials Science & Engineering Department won this award. Exceedingly pleased with Drexel, he decided to stay to pursue a Ph.D. after his B.S. studies. During his tenure, he was awarded a number of national fellowships, the DOEd GAANN Fellowship, the NSF IGERT Fellowship and most notably the NSF GRFP Fellowship, as

well as numerous internal Research Awards at Drexel and numerous Best Poster awards at international conferences.

Thankfully, the research was highly successful, with more than 15 journal articles, 1 book chapter and 2 review articles published or in preparation. Additionally, 4 patents were licensed and are being actively developed by Y-Carbon, LLC who has partnered with Arkema Chemical. This project allowed John to travel all over the world presenting results, namely, Mexico, Canada, and Germany, among many domestic presentations as well as a healthy international collaboration with the group of Patrice Simon at the University Paul Sabatier. The research was also accepted outside of the immediate field, as evidenced by an NSF Discovery Article written about our research being the 2nd most viewed article on NSF sponsored research in 2008 (being surpassed only by an article on Google).